

Development and Evaluation
of a Test System
for the Quality Assurance
during the Mass Production
of Silicon Microstrip Detector Modules
for the CMS Experiment

Von der Fakultät für Mathematik, Informatik und Naturwissenschaften
der Rheinisch-Westfälischen Technischen Hochschule Aachen
zur Erlangung des akademischen Grades eines
Doktors der Naturwissenschaften
genehmigte Dissertation

vorgelegt von

Torsten Franke

aus Rudolstadt

Berichter: Universitätsprofessor Dr. rer. nat Günter Flügge
Universitätsprofessor Dr. rer. nat. Joachim Mnich

Tag der mündlichen Prüfung: 04. Juli 2005

Diese Dissertation ist auf den Internetseiten der Hochschulbibliothek
online verfügbar.

Zusammenfassung

Der CMS Detektor (Compact Moun Solenoid) ist einer von vier Großdetektoren, die im Rahmen des LHC Projektes (Large Hadron Collider) am Europäischen Zentrum für Elementarteilchen-Physik (CERN) errichtet werden. Der innere Spurdetektor von CMS basiert vollständig auf Silizium-Streifen-Sensoren. Mit einer sensitiven Fläche von insgesamt 198 m^2 wird er bei seiner Fertigstellung der weltweit größte, je gebaute Spurdetektor seiner Art sein. Für seinen Zusammenbau werden etwa 16.000 sogenannte Module benötigt, die jeweils aus den Silizium-Streifen-Sensoren, der Ausleseelektronik und einer Tragestruktur bestehen. Die Modulproduktion wird in einer Kooperation von zahlreichen Instituten und Unternehmen bewerkstelligt. Für die Gewährleistung eines zuverlässigen Betriebs der Module unter extremen Strahlenbelastungen sind umfassende Tests aller Komponenten notwendig.

Ein wichtiger Beitrag zur Qualitätssicherung der Module wird durch die Bereitstellung eines Testsystems aus Aachen geleistet, das neben umfassenden Tests der Auslese-Elektronik auch Auskunft über möglich Fehler der Sensoren geben kann. Dieses Testsystem wird im Rahmen der Modul-Produktion in mehr als 20 beteiligten Instituten in Europa und den USA eingesetzt.

Die automatisierte Überprüfung der Module erfordert eine spezielle Auslese- und Analysesoftware. Diese Software sowie alle Komponenten des Testsystems und deren Funktionsweisen werden in der vorliegenden Arbeit beschrieben.

Ein Fehlerfindungsalgorithmus wurde implementiert, der die genommenen Daten auf charakteristische Signaturen verschiedener Typen von Modul-Fehlern untersucht. Eine zuverlässige Identifizierung fehlerhafter Streifen eines Moduls ist wichtig im Hinblick auf entsprechende Reparaturmaßnahmen und die Beurteilung der Eignung eines Moduls für die Verwendung im Spurdetektor.

Es wird ausführlich erklärt, wie die Tests bestimmt wurden, die am besten zur Identifizierung eines Modulfehlers geeignet sind und wie der Fehlerfindungsalgorithmus optimiert wurde, um dessen Zuverlässigkeit, unabhängig vom verwendeten Test-Setup, zu verbessern. Anhand der Daten von über 500 Modulen mit bekannten Fehlern wurde die Eignung der gewählten Methoden überprüft.

Dabei wurden alle Fehler gefunden und in über 90 % der Fälle korrekt identifiziert. Gleichzeitig wurden weniger als 0,02 % der unbeschädigten Kanäle als fehlerhaft markiert. Die Beurteilung der Eignung eines Moduls erwies sich als nahezu unabhängig vom speziellen Test-Setup und ergab in ca. 96 % der Fälle das gleiche Resultat für Module, die mehrfach getestet wurden.

Insgesamt wurden 0,3 % defekte Streifen gefunden und ca. 98 % der Module als geeignet zur Verwendung im CMS-Detektor klassifiziert.

Abstract

The Compact Muon Solenoid (CMS) is one of four large-scale experiments that is going to be installed at the Large Hadron Collider (LHC) at the European Laboratory for Particle Physics (CERN). For CMS an inner tracking system entirely equipped with silicon microstrip detectors was chosen. With an active area of about 198 m^2 it will be the largest tracking device of the world that was ever constructed using silicon sensors. The basic components in the construction of the tracking system are approximately 16,000 so-called modules, which are pre-assembled units consisting of the sensors, the readout electronics and a support structure. The module production is carried out by a cooperation of number of institutes and industrial companies. To ensure the operation of the modules within the harsh radiation environment extensive tests have to be performed on all components.

An important contribution to the quality assurance of the modules is made by a test system of which all components were developed in Aachen. In addition to thorough tests of the readout electronics and it enables the detection of many faults of the silicon sensor it is connected to. It is used in more than 20 different institutes in Europe and the USA which participate in the module production.

The application of the test system for automated tests of modules requires a dedicated readout and analysis software. The software and all components of the test system will be explained in detail in this thesis.

Different types of faults on a module show a significant behaviour in particular tests. A dedicated fault finding algorithm searches for these signatures. A safe identification of faulty channels and a reliable information on the respective type of fault is important. It facilitates the reparation and enables the assessment of the appropriateness of a module for the insertion into the tracker. It will be explained which approach was used to find the most appropriate tests for that purpose and how the fault finding algorithm was optimized to give reliable results independent of the specific test setup. Finally, the algorithm is used for the qualification of more than 500 repeatedly measured modules with known failures to verify its suitability.

All faulty channels are found and more than 90 % of the faults are correctly identified. At the same time less than 0.02 % of good channels are wrongly flagged as faulty. The assessment of the module quality is nearly independent of the particular setup and can be reproduced in about 96 % of the cases of repeatedly measured modules.

In total, less than 0.3 % of the channels are faulty and about 98 % of all modules are suited for the construction of the tracker.

Contents

1	Introduction	1
1.1	The Large Hadron Collider	2
1.2	The CMS Experiment	2
1.3	The Silicon Strip Tracker	5
2	The CMS Silicon Tracker Modules	9
2.1	Energy Loss due to Ionization	9
2.2	The Function Principle of a Silicon Strip Detector	12
2.3	Design Goals and Operation Principles	14
2.3.1	Depletion Voltage	15
2.3.2	Leakage Current	16
2.3.3	Trapping of Signal Charge	17
2.3.4	Detector Capacitances	17
2.3.5	Annealing and Reverse Annealing	18
2.4	Layout of the CMS Silicon Microstrip Sensors	19
2.5	The CMS Silicon Strip Tracker Modules	20
2.5.1	Design of the Module Mechanics	20
2.5.2	The Front-End Hybrid	21
2.5.3	The APV Chip	23
2.5.4	The MUX Chip	27
2.5.5	The TPLL Chip	27
2.5.6	The DCU Chip	28
2.6	Possible Module Faults	29
2.6.1	Problems in the Sensor Production	29
2.6.2	ASIC and Hybrid Problems	32
2.6.3	Module Production and Handling Problems	33
3	The APV Readout Controller System	35
3.1	System Overview	36
3.2	The ARC Board	36
3.2.1	Trigger Generation	38
3.2.2	Data Acquisition	40
3.2.3	Slow Control	41
3.3	The Front-End Adapter	42
3.3.1	Functions	43

3.3.2	Versions of the Front-End Adapter	43
3.4	The LED Controller	45
3.4.1	The LED Controller Board	45
3.4.2	The Choice of the LEDs	46
3.4.3	The Transmission of Light to the Sensors	47
3.5	The High Voltage Controller	48
3.6	The Single Module Test Box	50
3.7	Cold Box Setup	52
3.7.1	The Cold Box Design	52
3.7.2	Cold Box Control	53
3.8	Multi Board Setup	54
3.9	The ARC System in the Module Production	55
4	The APV Readout Controller Software	57
4.1	Software Structure	58
4.2	Data Acquisition in ARCS	58
4.3	The Initialization	59
4.4	The Monitoring Panel	60
4.5	Automated Test Procedures	61
4.6	The ROOT File	62
4.7	Data Analysis in ARCS	63
5	The Automated Test Procedures in ARCS	67
5.1	The I-V Test	67
5.1.1	Data Acquisition Procedure	67
5.2	The Noise Test	68
5.2.1	Data Acquisition Procedure	68
5.2.2	The Noise Calculation in General	68
5.2.3	The Noise Calculation in ARCS	70
5.3	The Pulse Shape Test	73
5.3.1	Data Acquisition Procedure	74
5.3.2	Pre-Analysis of the Pulse Shape Data	76
5.4	The Gain Test	78
5.4.1	Data Acquisition Procedure	78
5.4.2	Pre-Analysis of the Gain Test Data	79
5.5	The Pipeline Test	79
5.5.1	Data Acquisition Procedure	80
5.5.2	Pre-Analysis of the Data	81
5.6	The LED Test	83
5.6.1	Data Acquisition Procedure	83
5.6.2	Pre-Analysis of the LED Test Data	84
5.7	The Pinhole Test	84
5.7.1	Function Principle of the Pinhole Test	84
5.7.2	Data Acquisition Procedure	87
5.7.3	Pre-Analysis of the Data	88

5.8	The Backplane Pulse Test	89
5.8.1	Data Acquisition Procedure	89
5.8.2	Pre-Analysis of the Backplane Pulse Data	90
5.9	The Functional Test	90
6	The Signatures of Faults in Module Tests	93
6.1	The Signature of Open and Missing Bonds	93
6.2	The Signature of Short-Circuited Channels	98
6.3	The Signature of Pinholes	100
6.4	The Signature of Dead Channels	102
6.5	The Signature of Defective Inverters	103
6.6	The Signature of Defective Pipeline Cells	104
6.7	Noisy Channels	104
6.8	Micro-Discharges	106
6.9	Unknown Faults	106
6.10	Summary Table of Signatures	106
7	The Optimisation of the Fault Finding Algorithm	109
7.1	Motivation for the Analysis	110
7.2	Preparation of the Analysis	111
7.2.1	The Dataset	111
7.2.2	Fault Classification	111
7.2.3	Processing of the Measured Data	113
7.2.4	Weighting of the Data	116
7.3	Evaluation of the Separation of Faults	116
7.3.1	Distance Criterion	116
7.3.2	Overlap Criterion	118
7.4	Results of the Analysis	120
7.4.1	Tests for the Safe Identification of Opens	120
7.4.2	The Separation of Pitch Adapter-Sensor-Opens from Sensor-Sensor-Opens	123
7.4.3	Tests for the Safe Identification of Short-Circuits	124
7.4.4	Tests for the Safe Identification of Dead Channels	126
7.4.5	Tests for the Safe Identification of Pinholes	127
7.4.6	The Separation of Dead Channels and Pinholes	129
7.4.7	Identification of Defective Inverters	130
7.4.8	Identification of Defective Pipeline Cells	131
7.5	Determination of Stable Noise Cuts	132
7.5.1	The Noise Analysis	133
7.6	The Updated Fault Finding Algorithm	136
7.6.1	Flagging of Bad Channels	137
7.6.2	Analysis of the Flags	138
7.6.3	Grading	141
7.7	The Evaluation of the Fault Finding Efficiency	141
7.7.1	Identification of Pinholes	142

7.8	Assessment of the Stability of the Grading	142
7.9	Assessment of the Module Quality	144
8	Conclusion	145
A	Addendum to the Fault Finding Algorithms	147
A.1	The first version of the fault finding algorithm	147
A.2	Cut Values for the new Fault Finding Algorithm	149
B	Additional Plots and Figures	155
B.1	Characteristics of the LED induced Leakage Current	155
B.2	The Timing of the Backplane Pulse	156
B.3	The Signal-to-Noise Ratio	157
B.4	Preferred Decay Channels for the Search for the Higgs Boson	158
B.5	Branching Ratios and Cross Sections	159
C	Module Sizes and Quantities	161
D	Addendum to the APV Chip	163
D.1	The APV Internal Common Mode Correction	163
D.2	APV Register Values	164

Chapter 1

Introduction

Despite the great success of the Standard Model of Particle Physics in the description of nature, there are still open questions. One of the most important problems is the question for the origin of mass. The Standard Model predicts masses of zero for fermions and the quanta of the weak interaction, the W and Z -boson. Instead of being massless the bosons are among the heaviest known particles. To circumvent this problem the so-called Higgs mechanism was postulated. Masses of particles are explained by their coupling with an additional scalar field with a non-vanishing vacuum expectation value. As a consequence of the Higgs mechanism, an additional particle — the Higgs boson — must exist, of which the mass m_H is not predicted by the model.

Former particle physics experiments such as LEP ¹ were not able to detect the Higgs boson directly, but determined a lower limit for the Higgs mass at $114.4 \text{ GeV}/c^2$ [1]. Theoretical considerations combined with observations in other experiments constrain an upper limit of approximately $1 \text{ TeV}/c^2$. With the *Large Hadron Collider (LHC)* particles of this mass and beyond can be produced.

Though the mass of the Higgs boson is unknown, its decay channels (if it exists) are predictable. The decay products vary over the whole particle spectrum since a decay in heavier particles is enabled if m_H is larger. Among the great variety of possible final states only those are of interest for a discovery of the Higgs boson, that have distinctive signatures with respect to the much more frequently “ordinary” interactions (background) that also occur in proton-proton-collisions. In the mass range below $200 \text{ GeV}/c^2$ for example, the decays $H \rightarrow \gamma\gamma$ ($m_H \approx 130 \text{ GeV}$) or $H \rightarrow ZZ \rightarrow \mu^+ \mu^- \mu^+ \mu^-$ ($m_H \approx 180 \text{ GeV}$) have such clear signatures. Nonetheless also decays with a worse signature but higher probability of occurrence (higher cross section) have to be considered, e.g. $H \rightarrow b\bar{b}$.

A detector experiment must be designed to recognise all different signatures covering the whole range of potential Higgs masses. Of course, the search for the Higgs boson is only the most prominent example of the spectrum of envisaged physics analyses. Further main goals of the LHC project are the investigation of b and t -physics phenomena and the search for potential supersymmetric particles.

¹LEP: *Large Electron Positron Collider*.

1.1 The Large Hadron Collider

The Large Hadron Collider (LHC) is a particle accelerator that will access a new range of energy for the elementary particle physics. It will be located in the tunnel of the former LEP experiment at CERN². As from 2007 two beams of protons, each accelerated to 7 TeV kinetic energy, will circulate in two separate rings with 27 km circumference in opposite directions. Dipole magnets with a field of 8.4 T are necessary to force the protons on their orbit. At four different points the rings intersect and protons collide every 25 ns with a centre-of-mass energy of 14 TeV. Around these four interaction points large detectors are built, to measure the particles produced in the collision.

Two of these detectors are dedicated to a specific field of physics. The ALICE³ detector is envisaged to investigate collisions of heavy ions, which are also accelerated by the LHC for certain periods per year, to search for the quark-gluon-plasma, a postulated state of matter occurring at very high densities of strongly interacting particles. The LHC-b⁴ detector is dedicated to precise measurements of CP violation and rare decays in events including b -quarks.

The other two experiments, ATLAS⁵ and CMS⁶, are designed as multi-purpose detectors for the investigation of a wide field of Standard Model processes and new physics, such as Higgs decays and the search for supersymmetric particles. As the postulated cross sections of most of these processes are small, a very high luminosity \mathcal{L} is needed for the observation of rare events. The LHC is designed for a luminosity of $\mathcal{L} \approx 10^{33} \text{ cm}^{-2}\text{s}^{-1}$ during the first years of operation (low luminosity phase) and a luminosity of $\mathcal{L} \approx 10^{34} \text{ cm}^{-2}\text{s}^{-1}$ later (high luminosity phase).

1.2 The CMS Experiment

The CMS experiment (see figure 1.1) is a typical multi purpose detector. It is particularly optimized with respect to the registration of decay products of the Higgs bosons in a mass range between 100 GeV and 1 TeV. From the interaction point to the outside it is instrumented with

- a vertex detector based on silicon pixel sensors,
- a tracking detector based on silicon microstrip sensors,
- an electromagnetic calorimeter,
- a hadron calorimeter,
- a superconducting magnet, and

²CERN: Organisation Européenne pour la Recherche Nucléaire, primarily the abbreviation of Conseil Européenne pour la Recherche Nucléaire.

³ALICE: *A Large Ion Collider Experiment*.

⁴LHC-b: *Large Hadron Collider Beauty Experiment*.

⁵ATLAS: *A Toroidal LHC ApparatuS*.

⁶CMS: *Compact Moun Solenoid*.

- a muon detector system integrated into the iron return yoke of the magnet.

The whole detector has a length of 22 m and a diameter of 14.6 m and a mass of about 12,500 tons.

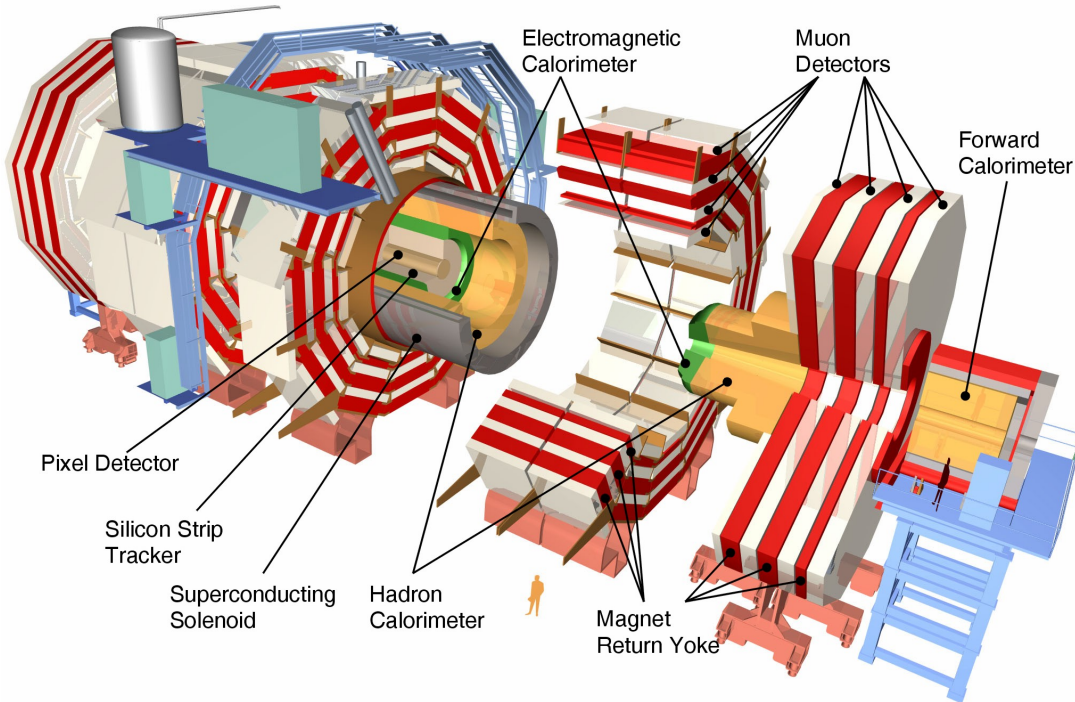


Figure 1.1: Overview of the CMS Detector.

During the high luminosity phase about 20 proton-proton interactions will occur every 25 ns, each time producing about 1000 tracks of charged particles. Thus the design of the whole detector required the development of extremely radiation hard detector devices with a high granularity. The short bunch crossing time of 25 ns sets the scale for the time resolution of all detector components and readout electronics.

Purpose and design of each sub-detector will be briefly explained in the following paragraphs.

The Muon Detectors

Muons are decay products of many physics processes the LHC is designed for. An efficient muon detection is for example of interest with respect to measurements in the Higgs decay channel $H \rightarrow ZZ^* \rightarrow \mu^+ \mu^- \mu^+ \mu^-$. The muon system is the outermost part of the detector since muons are the only charged particles that are able to traverse the inner detector components without a significant energy loss. The muon detection in the barrel region is based on drift tubes while the strong variations of the magnetic field in the end cap regions necessitates the use of cathode strip chambers. In addition both regions are equipped with resistive plate chambers for fast trigger signals [2].

The Magnet System

The magnet used in CMS is a superconducting solenoid of about 12.5 meter length and a diameter of about 6 meter, providing a uniform magnetic field of 4 T [3]. The strong magnetic field accompanied by a high resolution tracking system allows for a good momentum resolution of high energetic charged particles. The magnetic flux is returned via an iron yoke of 1.8 m thickness which is instrumented with the muon detectors. The size is chosen such that the tracking detectors and the calorimeters are housed inside the volume of the solenoid to reduce the radiation absorbing material in particular in front of the calorimeters. The system of magnet and muon system gives the detector its name.

The Hadron Calorimeter

In combination with the electromagnetic calorimeter the hadron calorimeter measures quark, gluon and neutrino directions and energies by measuring the direction of particle jets and of the missing transverse energy flow [4, 5]. The hadron calorimeter consists of an inner barrel region, an outer barrel region, two end caps and two very forward calorimeters. Inner barrel and end caps are inside the solenoid whereas the outer barrel resides inside the return yoke of the magnet. The forward calorimeter is located beyond the return yoke of the magnet in about 12 m distance from the interaction point.

The hadron calorimeter is a sampling calorimeter. In the barrel and end cap regions it consists of passive absorber plates interleaved with active readout components. The absorber plates are made of copper of 6 cm thickness. The active material are 4 mm thick plastic scintillator tiles read out using wavelength-shifting plastic fibres. The forward calorimeter uses quartz fibres as active medium embedded in a copper absorber matrix.

The Electromagnetic Calorimeter

The electromagnetic calorimeter plays an essential role in the investigation of the Higgs decay mode $H \rightarrow \gamma\gamma$ by detecting the two photons. It is also important for the measurement of electrons and positrons of large transverse momenta, since these particles are clear signatures for many interesting decays (e.g. semi-leptonic t -quark decays).

The electromagnetic calorimeter is composed of about 83,000 lead tungstate (PbWO_4) crystals of about 23 cm length and 2.2×2.2 cm cross section. The crystals have a fast scintillation time of about 15 ns and a small Molière radius of 2.2 cm. The latter aspect allows a good separation of adjacent showers. The comparably small light yield is amplified by avalanche photo diodes [6].

The Tracking Detector

As this thesis deals with components of the silicon strip tracker, this part will be explained in more detail in section 1.3.

The Vertex Detector

The innermost tracking detector is a silicon pixel detector. It consists of two barrel layers (*TPB* in figure 1.2) and two end caps at each side (*TPE*). Due to charge sharing effects between quadratic pixels of $150 \times 150 \mu\text{m}^2$ size a hit resolution at the level of $15 \mu\text{m}$ can be obtained in both coordinates [7]. This is necessary for a precise determination of impact parameters and three dimensional vertex reconstruction needed for the tagging of long-lived particles like *b*- or *c*-quarks and τ -leptons. For detecting *t*-quark decays, Higgs or SUSY particles *b*-tagging in particular plays an important role.

1.3 The Silicon Strip Tracker

As the name implies, the main purpose of the tracker is the determination of tracks. It is entirely based on silicon microstrip sensors [8]. In order to minimize radiation damages (cf. chapter 2.3) the whole tracker is operated at a temperature below 0°C .

Tracker Design

The overall structure of the silicon strip tracker, in the following denoted as tracker, is divided into barrel and end cap parts (see figure 1.2). The barrel part is subdivided into a 4-layer inner barrel (*TIB*) and a 6-layer tracker outer barrel (*TOB*) region. Both end caps are sectioned into inner disc regions (*TID*) consisting of 3 discs and the outer end caps (*TEC*) consisting of 9 discs. The tracker has a length of 5.5 m and an outer diameter of 2.2 m. It covers the range of pseudo-rapidity⁷ up to $|\eta| = 2.5$. An area of about 198 m^2 is covered with active silicon detectors. On completion it will be the largest tracking device of the world, that was ever built based on silicon detectors only.

The active detector components are single sided silicon strip sensors with a strip length of about 10 cm and a strip pitch of about $100 \mu\text{m}$. The sensors will be explained in detail in chapter 2. The choice of detectors with a larger sensitive area with respect to the pixels is justified by its general benefit for the reduction of readout channels and a significantly lower track density. At a distance of 60 cm from the interaction point 0.01 tracks/cm^2 are expected instead of 1 track/cm^2 at 10 cm distance [9].

The smallest units in the construction of the tracker are the so-called modules (cf. chapter 2.4). Modules are pre-assembled devices consisting of the sensors, the readout electronics and a support structure. In total, about 16,000 modules have to be built. The strip direction in the barrel region is chosen in parallel to the beam axis. In the end cap region the strips point at the beam axis. Depending on their position in the tracker modules are equipped with sensors of different geometries.

Track positions can be determined only perpendicular to the strips. To improve the spatial resolution along the strips some of the modules are mounted back-to-back with “stereo modules” to form a double sided module. In case of stereo modules the sensors are rotated by 5.6 degree with respect to “normal modules”. Figure 1.3 shows a

⁷The pseudo-rapidity η is defined as $\eta = -\ln(\tan \frac{\theta}{2})$, where θ is the polar angle with respect to the beam axis.

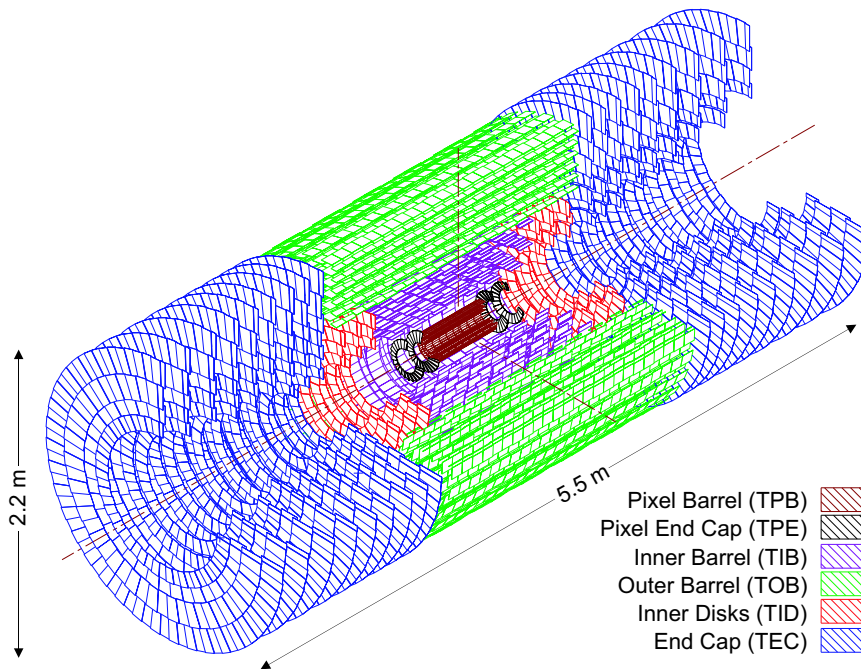


Figure 1.2: General view of the CMS tracker and its substructures.

longitudinal cut through a quarter of the tracker. The positions of double sided modules are marked in red.

Modules are integrated in higher-level structures to facilitate the assembly and enable an easier maintenance in case of defects. These structures are called *rods* (for the TOB), *shells* (TIB), *discs* (TID). In case of the TEC, the *petal* structures hold modules of up to seven different rings that are needed to equip one disc. Examples are shown in figure 1.4. All supply cables, high precision mounting points, and the cooling system are integrated in these structures. In addition they carry opto-hybrids which transform analogue electrical signals from the silicon sensors into analogue optical signals. The transmission of optical signals avoids a deterioration of electrical signals during the transmission over long cables in a strong magnetic field.

A silicon based tracker fulfils the requirement for a fast response and a very precise hit resolution. The application of standard production techniques enables a comparably low price. low costs. Its major disadvantage is the large amount of material that is introduced in front of the calorimeters by the silicon itself but also by support structures, supply cables and cooling system components.

Momentum Measurement

In a magnetic field the momentum of a charged particle can be derived from the curvature of its track. Interesting proton-proton-interactions are characterized by large transverse momenta (i.e. perpendicular to the beam axis) of secondary particles. Thus the design of the tracker and the direction of the magnetic field are chosen such that the transverse momentum p_t can be measured with a high resolution at the expense of

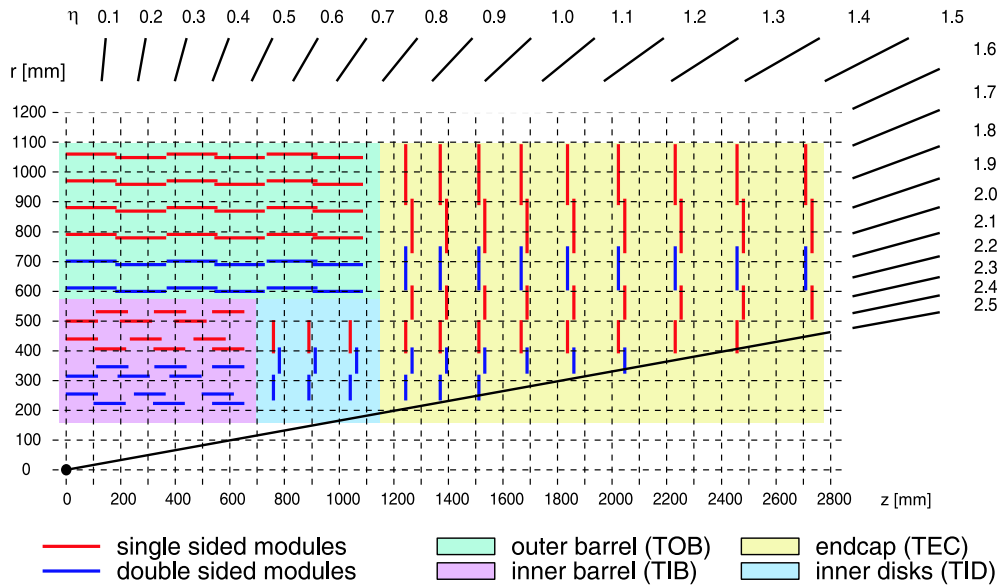


Figure 1.3: Longitudinal cut through a quarter of the CMS silicon strip tracker. The tracker covers a pseudo-rapidity range up to $|\eta| = 2.5$ (from [10]).

a worse resolution⁸ for the longitudinal momentum p_t . The higher the accuracy of the measurements of the r and φ coordinates, the better is the p_t -resolution.

In the barrel region the resolution is very good in r and φ , whereas it is good in φ but worse in r for the end caps. Therefore the transverse momentum resolution $\Delta p_t/p_t$ degrades for larger values of η (see figure 1.5).

An acceptable resolution for the longitudinal momentum is achieved due to the three dimensional space points provided by the double sided modules.

Trigger and Data Acquisition

Due to the enormous collision rate a pre-selection is indispensable, to store only the most interesting events. This task is performed by a multi-level trigger system.

The tracker signals are read out only after the reception of a level-1 trigger (occurring with a frequency of about 100 kHz). The level-1 trigger decision is based on the signals of the fastest detector components, mainly the electromagnetic calorimeter and the resistive plate chambers of the muon system. The time needed for this decision is about 3.2 μ s. Thus the front-end electronics attached to the silicon microstrip modules of the tracker has to store the informations on detected signals for at least this time period (see chapter 2.4).

The higher level trigger stage will reduce the number of selected events furthermore, finally resulting in a rate of about 100 events per second, that are stored. This still corresponds to 100 MByte data per second which requires also new techniques of data handling and analysis.

⁸The measurement of p_t also benefits from the fact that the sum $\sum p_t$ of all particles is known to be zero prior to the collision, whereas the longitudinal momenta of the interacting quarks are not known.

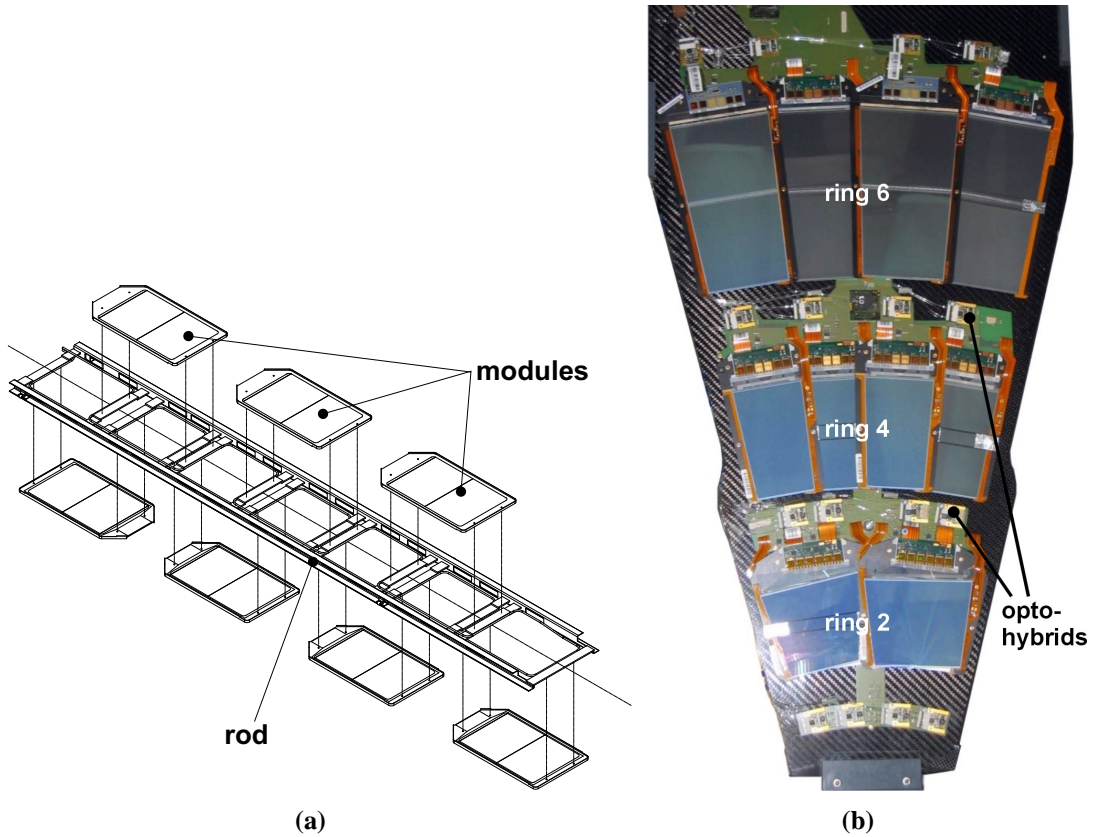


Figure 1.4: (a) Sketch of a rod, the support structure for TOB modules (from [7]). (b) Photograph of a wedge-shaped petal for the TEC. Only three of the seven rings are visible. Modules of the remaining four rings are mounted at the backside to cover the full area of the petal with sensors. Though only two ring 2 modules are visible, there are four modules (two pairs of back-to-back modules) mounted as indicated by the number of opto-hybrids (from [11]).

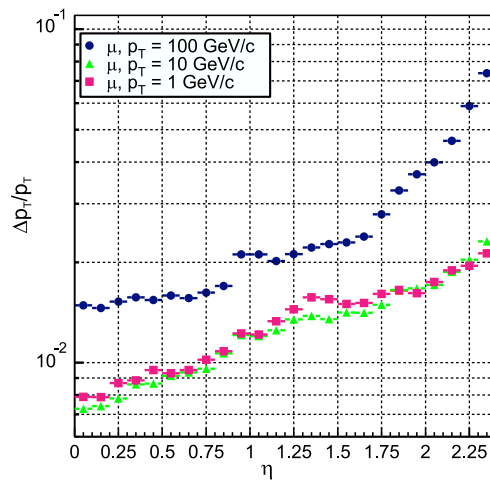


Figure 1.5: The transverse momentum resolution of the tracker for muons of different energies. For larger values of $|\eta|$ the resolution degrades (from [9]).

Chapter 2

The CMS Silicon Tracker Modules

This chapter gives a short introduction to the principles of particle detection using a silicon microstrip detector. The design of the sensors for the CMS experiment will be motivated and explained. The front-end electronics necessary to readout the silicon microstrip sensors will be introduced in more detail to provide useful fundamentals for later chapters. The assembly of sensors, front-end electronics and the support structure to a *module* will be described.

2.1 Energy Loss due to Ionization

Charged particles passing any material lose energy due to ionization along their trajectory in the material. The mean differential energy loss $-dE$ per distance dx can be calculated. The resultant formula for charged, heavy particles (i.e. all but electrons) is the *Bethe-Bloch-Formula* (cf. [12]) that, including corrections, reads as follows:

$$-\frac{dE}{dx} = 2\pi N_a r_e^2 m_e c^2 \rho \frac{Z}{A} \frac{z^2}{\beta^2} \left[\ln \left(\frac{2 m_e \gamma^2 v^2 W_{max}}{I^2} \right) - 2\beta^2 - \delta - 2\frac{C}{Z} \right] \quad (2.1)$$

with the constants:

- N_a : Avogadro's number = $6.022 \times 10^{23} \text{ mol}^{-1}$,
- r_e : classical electron radius = $2.817 \times 10^{-13} \text{ cm}$,
- m_e : electron mass,
- c : speed of light,

the properties of the incident particle:

- z : charge of incident particle in units of the electron charge e ,
- $\beta = v/c$, the velocity of the incident particle,
- $\gamma = 1/\sqrt{1-\beta^2}$,

and the material dependent values:

- ρ : density of absorbing material,
- Z : atomic number of absorbing material,
- A : atomic weight of absorbing material,
- W_{max} : maximum energy transfer in a single collision,
- I : mean excitation potential,
- δ : density correction,
- C : shell correction.

The density correction δ takes the shielding of the charge of the incident particle due to atomic polarization effects into account. This effect plays a role only for high velocities of the incident particle and reduces the mean differential energy loss. The shell correction C has to be considered for low velocities only. At low velocities the assumption of a stationary atomic electron with respect to the incident particle as used in the deduction of formula (2.1) is no longer valid. The mean excitation potential I depends on atomic number. According to [12], the dependence of the ratio I/Z can be approximated by:

$$\frac{I}{Z} = 12 + \frac{7}{Z} \text{ eV} \quad (Z < 13) \text{ and } \frac{I}{Z} = 9.76 + 58.8 Z^{-1.19} \text{ eV} \quad (Z \geq 13). \quad (2.2)$$

The Bethe-Bloch function according to equation (2.1) in various materials is shown in figure 2.1 as a function of $\beta\gamma$.

Recent measurements of I/Z are presented in [13]. With all corrections the Bethe-Bloch formula describes the energy loss for heavy, charged particles with an accuracy of a few percent in a range from several MeV up to the critical energy¹. Above the critical energy Bremsstrahlung becomes the dominant mechanism for the energy loss.

In the low energy regime, the shape is dominated by the $1/\beta^2$ factor, whereas for high energies the function follows mainly the logarithmic term, since γ is still increasing with increasing energy while β and v converge. In between at $\beta\gamma \approx 3$, there is a region of minimum energy loss due to ionization. The energy loss for particles of higher kinetic energy is close to that minimum value. That justifies to call particles of these respective energies *minimum ionizing particles* (MIPs).

The energy loss of electrons and positrons is different from that of heavy particles. They can be deflected significantly when interacting with atomic electrons and the maximum energy transfer in a single collision can be as high as $W_{max} = T_e/2$, where T_e denotes the kinetic energy of the incident electron. Furthermore the identity of the incident electron and the electrons it ionizes has to be regarded for electrons.

Since the energy loss in a single collision process can vary widely due to high energetic primary electrons (see figure 2.3 c)), the total energy loss in a material of given thickness can fluctuate a lot as well. For thin layers of material, the probability

¹The critical energy is defined as the energy at which the energy loss due to ionisation equals the energy loss due to Bremsstrahlung. The critical energy depends on the mass of the incident particle and the material [13, 14].

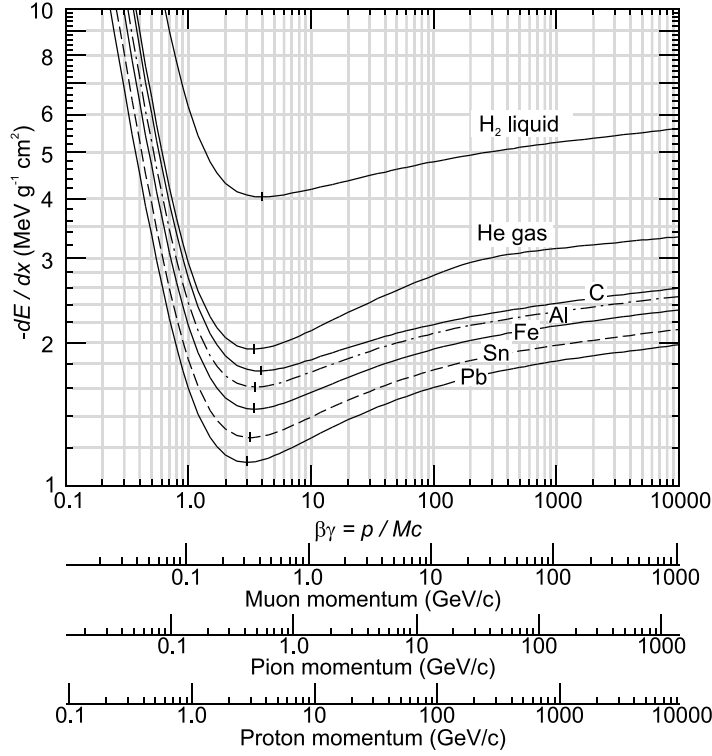


Figure 2.1: Mean energy loss rate in various material according to the Bethe-Bloch formula. Independent from the respective material the minimum ionization corresponds to a value of $\beta\gamma \approx 3$. In practice most relativistic particles have mean energy loss rates close to that minimum and can thus be regarded as minimum ionizing particles (from [13]). Note, that the energy loss is measured in the common unit of $\text{MeV g}^{-1} \text{cm}^2$. It can be obtained from formula (2.1), by division of the energy loss $-dE/dx$ by ρ .

distribution function $f(\Delta E; x)$ describing the distribution of energy loss ΔE within a thickness x is usually called the *Landau distribution*.

Examples of this function for silicon of different thicknesses are shown in figure 2.2. It depicts the asymmetric shape of the Landau distribution, where the most probable energy loss for a given detector thickness is significantly smaller than the mean energy loss. For detector calibration purposes, the most probable energy loss is much more relevant than the mean energy loss, since it requires only the measurement of a part of the energy loss distribution. According to [14] a feasible fit function giving a reasonable approximation of the Landau Distribution is given by:

$$f(\Delta E; x) = \frac{1}{\sqrt{2\pi}} \cdot \exp \left[-\frac{1}{2} \left(\frac{\Delta E - \Delta E^{mp}}{\kappa \rho x} + \exp \left(-\frac{\Delta E - \Delta E^{mp}}{\kappa \rho x} \right) \right) \right] \quad (2.3)$$

where ΔE is the actual energy loss, ΔE^{mp} is the most probable energy loss, x is the thickness of the absorber, ρ the density, and $\kappa = 2\pi N_A r_e^2 m_e c^2 z^2 \cdot Z/A \cdot 1/\beta^2$.

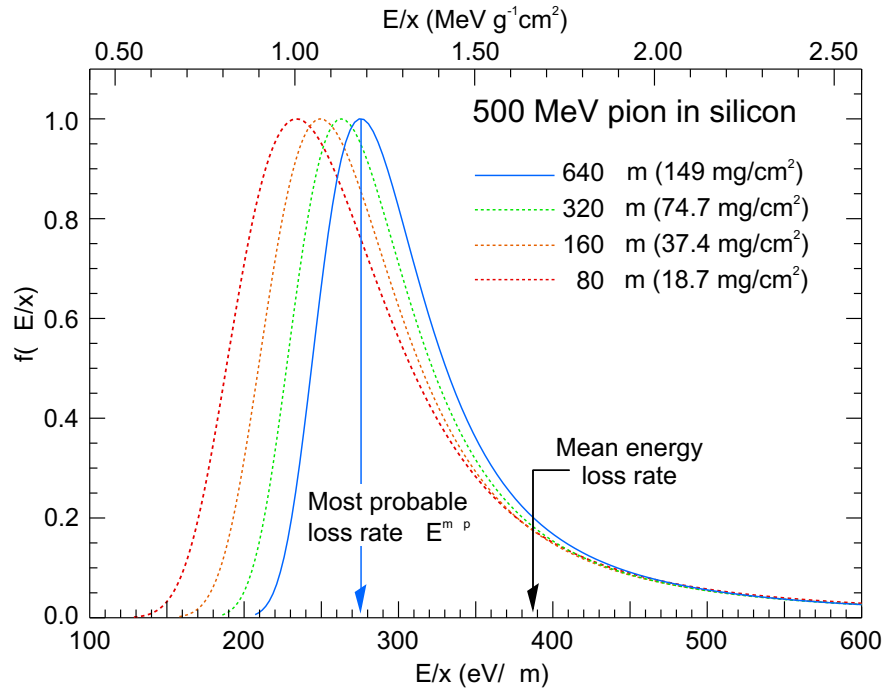


Figure 2.2: Recent calculation of “Landau” distributions for 500 MeV pions in silicon of various thickness, normalized to unity at the most probable value. (from [13]).

2.2 The Function Principle of a Silicon Strip Detector

In the most simple approach, a p-n junction can be described by two doped silicon pieces of n-type (with a respective acceptor density N_A) and p-type (donor density N_D) joined very closely together forming a diode.

If a n-type silicon “contacts” a p-type one, a gradient evolves in the electron and hole densities which causes electrons and holes to migrate into the p-type and n-type, respectively. This process leaves the n-type with a positive net space charge due to unneutralized holes and donor atoms and causes at the same time the p-type silicon to be negatively charged due to surplus electrons. The evolving electric field between these two charged regions counteracts the migration and stops it finally. This *space charge region* gets depleted of free charge carriers. Although regular diodes have more complicated doping density distributions and are not formed by simply contacting the two pieces, the main dependencies can be deduced from this simple model. An overview of the subject and more extensive descriptions respectively can be found in the literature (e. g. [12] and [15]).

If an external voltage V_{bias} with the same sign compared to the electric field in the space charge region is applied to the electrodes of the diode (so-called reverse bias) the width of the space charge region increases. Only a very small leakage current flows in the reversely biased p-n junction. This effect makes the depleted p-n junction usable as a particle detector.

If a charged particle traverses the p-n junction it creates electron-hole pairs along its track as depicted in figure 2.3 (a). In a silicon sensor of 320 μm a MIP loses about

260 eV per μm , while on average 3.6 eV are needed to create an electron-hole pair. Thus in total about 23,000 electron-hole pairs are generated by the passage of a MIP. The charges of the respective sign move in the direction given by the electric field. Within some 10 ns charge pulses are induced in both electrodes of the diode which can be used to indicate the crossing of a particle. This principle can be extended to a precise position detector if segmented electrodes are used.

The segmented electrodes work like many different neighbouring diodes and give a position information according to the position of the diodes hit by the traversing particle. This is depicted in figure 2.3 (b) and (c).

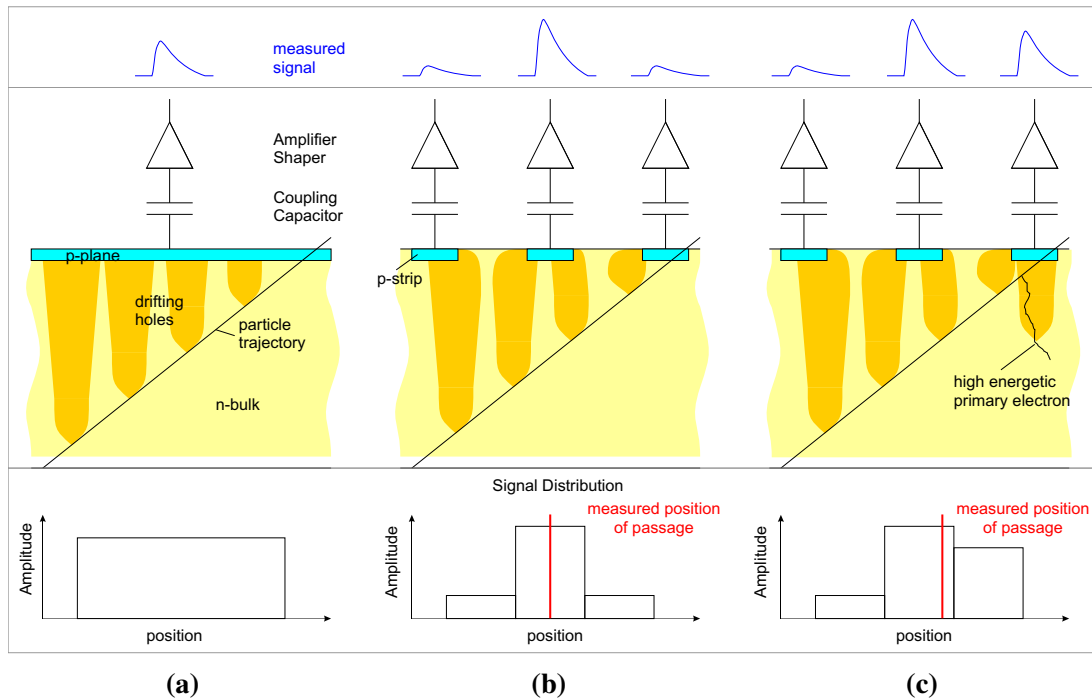


Figure 2.3: Principle of the particle detection using a reversely biased diode. (a) Charges created by an ionizing particle drift to their respective electrode and induce a signal, that indicates the passage of a particle. (b) Charges drifting to neighbouring electrodes induce signals whose height is a measure for the amount of charge drifting to the respective electrode. By weighting the signals the spatial resolution can be improved to values below the size/width of the segments. (c) High energetic primary electrons can create charges and thus signals in regions far away from the particle's track. Thereby the spatial resolution gets deteriorated. High energetic primary electrons are responsible for the long tail of the Landau Distribution.

For a particle detector highly doped p^+ -strips embedded in a low doped n-bulk are used. Due to the difference in doping concentration ($N_A \gg N_D$) the holes in a comparably small volume (in CMS ≈ 20 to $50 \mu\text{m}$ wide, $\approx 1 \mu\text{m}$ thick) can compensate electrons coming from a large fraction of the n-bulk (80 to $205 \mu\text{m}$ wide, 300 to $500 \mu\text{m}$ thick). This causes the space charge region to expand almost completely in the n-bulk.

The width W of the space charge region can be approximated by (cf. [16]):

$$W \approx \sqrt{2 \epsilon_0 \epsilon_r \rho \mu V_{bias}} , \quad (2.4)$$

with ϵ_0 being the dielectric constant, ϵ_r being the material specific dielectric constant, ρ being the material resistivity and μ being the majority charge carrier density (μ_e in case of the n-bulk).

The width W increases proportional to $\sqrt{V_{bias}}$ until the full detector thickness D is finally reached. The dedicated bias voltage is called depletion voltage V_{depl} . The depletion voltage V_{depl} according to equation (2.4) is given by:

$$V_{depl} = \frac{W^2}{2 \epsilon_0 \epsilon_r \rho \mu} = \frac{e D^2 N_{eff}}{2 \epsilon_0 \epsilon_r} , \quad (2.5)$$

with $N_{eff} = N_D - N_A$ being the effective doping concentration and e the electron charge. For the right hand side of equation (2.5) the relation $1/\rho = e N_{eff} \mu_e$ was used.

Since the charge associated with the depletion zone depends on the voltage, one can consider the p-n junction as a capacitance which can be expressed as a function of V_{bias} (cf. [16]):

$$C(V_{bias}) = \epsilon_0 \epsilon_r \frac{A}{W(V_{Bias})} = A \cdot \sqrt{\frac{e \epsilon_0 \epsilon_r N_{eff}}{2 V_{bias}}} . \quad (2.6)$$

If the detector is fully depleted, the capacitance saturates and reaches a final value of $C = \epsilon_0 \epsilon_r \cdot A/D$. The point of saturation can be used to determine the depletion voltage.

2.3 Design Goals and Operation Principles of CMS Silicon Microstrip Sensors

The choice of the sensor parameters for the CMS silicon strip sensors such as the overall size, the strip pitch, the doping concentration etc. represents a compromise between many, partially conflicting demands. The sensors have to provide the best possible signal-to-noise ratio, a low power dissipation, a low material budget and a good two track separation. Although a signal distribution over numerous channels is preferable to achieve a good spatial resolution, a smaller number of strips hit by a particle reduces the amount of data to be processed. This helps to avoid overstraining the capabilities of the readout system which is designed to handle the data of approximately ten million strips. In addition, the total number of strips per sensor must be a multiple of 128 because of the readout electronics used.

But the most striking factor is the requirement for radiation hardness. Radiation induced damages modify the behaviour of all sensor properties and thus the whole design has to be well balanced to guarantee the operation of the sensors up to the maximum accumulated flux to be expected.

Under the high integrated flux of up to 1.6×10^{14} 1-MeV-neutron-equivalents per cm^2 the n-bulk is going to be damaged by non ionizing energy loss which causes the following changes to the silicon lattice of the sensor:

- displacement of lattice atoms, leading to interstitials (atoms between regular lattice sites) and vacancies (empty lattice sites),
- nuclear interactions (e. g. neutron capture and nucleus transmutation),
- secondary processes from high energetic displaced lattice atoms and defect clusters from cascade processes, respectively.

The radiation defects generate new energy levels in the band gap between valence and conduction band. The effects of these defects are manifold and in general not beneficial for the detector performance. The quantities described in the following sections 2.3.1 to 2.3.5 are of major significance. A more detailed description of the sensor design for silicon sensors in vast radiation fluences can be found in [17].

2.3.1 Depletion Voltage

Original dopants such as boron or phosphorus can be captured in new defect complexes which causes the loss of their original function as acceptors or donors. This changes the effective doping concentration. The dependency of the doping concentration on the fluence can be well described by models which attribute the observed behaviour to an interplay of donor and acceptor removal and the creation of new defects behaving effectively like donors and acceptors (cf. [15]). On average newly created defects behave more acceptor like and thus the effective doping becomes more and more p-type with increasing radiation doses. This is shown in figure 2.4, where an originally n-type silicon wafer gets virtually intrinsic before its type is finally reversed to p-type (*type inversion*) by radiation induced radiation damages.

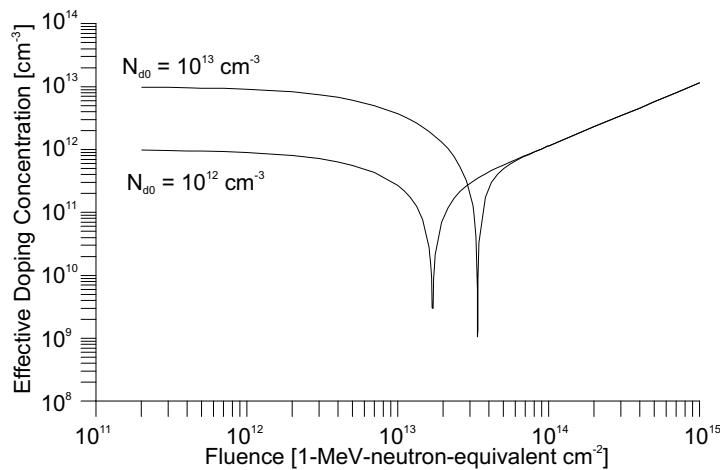


Figure 2.4: Calculated effective doping concentration vs. high-energy proton fluence for silicon with two different initial doping concentrations. After very high fluences the difference in doping concentration becomes negligible (from [18]).

One consequence of this type inversion is, that the depletion voltage also takes its minimum value at the point of lowest doping concentration (cf. equation (2.5)) and rises later linearly with the accumulated fluence.

Impact on the Sensor Design: According to equation (2.5) a higher resistivity of the material results in a lower depletion voltage. On the other hand using low resistivity material (higher initial dopant concentration) delays the type inversion and thus enables to operate the detector at lower depletion voltages after ten years of irradiation at LHC (cf. [19]).

Thus the resistivity is lower (~ 1.5 to 3.25 k Ω cm) for the sensors used in the inner region and higher (~ 4 to 8 k Ω cm) for sensors instrumenting the outer parts of the CMS tracker.

A low depletion voltage is not only of interest with respect to the high voltage stability, but also the achievable spatial resolution benefits from a lower depletion voltage. The charge diffusion is wider and can spread over more strips compared to a higher voltage.

The sensors used in CMS are designed to have a depletion voltage of below 400 V after ten years of LHC operation.

2.3.2 Leakage Current

An energy level between the valence and conduction band introduced by radiation damages enables electron and hole emission as well as electron and hole capture, as denoted in figure 2.5.

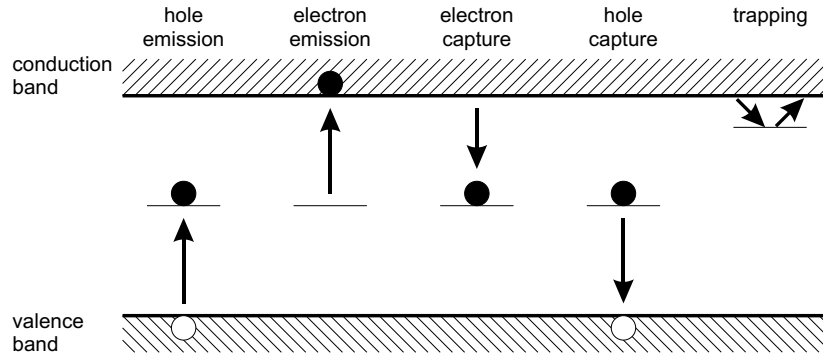


Figure 2.5: Additional generation processes are enabled by energy levels in the band gap: hole emission and electron emission. Additional recombination processes are also permitted like electron capture and hole capture. In a depletion region the conduction band is underpopulated so generation processes dominate (from [18]).

The emission of electrons and holes is responsible for the leakage current of a reverse biased detector. The transition probability is exponentially dependent on the difference of energy levels between two states. As the creation of both electrons and holes is required, defects with energy levels close to the middle of the band gap are most effective in generating leakage currents. The leakage current I^{rad} after irradiation rises linearly with the fluence and can be parameterized according to the equation

$$I_{rev}^{rad} = I_0 + \alpha \Phi V \quad (2.7)$$

where Φ is the fluence, I_0 is the leakage current before irradiation, V is the detector volume, and α is a damage coefficient which depends on the type of particle and the

fluence (cf. [18]). Furthermore the coefficient α and thus the reverse bias I_{rev} current depend strongly on the temperature T if the generation current dominates:

$$I_{rev}(T) \propto T^2 e^{-\frac{E}{2k_B T}}. \quad (2.8)$$

Here k_B is the Boltzmann constant and E is the effective activation energy which is ≈ 1.15 eV for unirradiated silicon and can reach values of ≈ 1.2 eV for radiation damaged silicon [18].

Impact on the Sensor Operation: The only way to keep the leakage currents low is to cool the device (see also 2.3.5).

2.3.3 Trapping of Signal Charge

Energy levels in the band gap capture charge and release it after a delay that depends on the depth of the energy level. This effect is called *trapping* (see figure 2.5). If the leakage current takes low values, almost all traps in the space charge region are unoccupied. If electron/hole pairs are generated by a passing particle, the charge carriers may be trapped and get released too late to contribute to the measured signal.

Impact on the Detector Operation: This problem of signal trapping can be partially extenuated by a higher bias voltage (*over-depletion*).

2.3.4 Detector Capacitances

The total capacitance of a detector strip is the sum of the backplane capacitance and the inter-strip capacitance. Radiation damages change the dielectric properties of the insulating oxide and the bulk material and thereby the capacitances. The diligent choice of sensor properties with respect to the capacitances is essential for the noise behaviour and the signal division between adjacent strips.

Impacts on the Sensor Design: In this case there are two major impacts on the choice of sensor parameters:

(1) Orientation of the Silicon Crystal Lattice: For detectors one usually uses n-type silicon of $1 \text{ k}\Omega \text{ cm}$ to $10 \text{ k}\Omega \text{ cm}$ with the lattice orientation $\langle 111 \rangle$ because it gives the highest energy loss (cf. [16], p. 16). On the other hand it turned out that silicon with $\langle 100 \rangle$ lattice orientation has less dangling bonds² than standard $\langle 111 \rangle$ silicon, leading to a suppression of surface defects. Thereby the inter strip capacitance is not changed significantly after the exposure of the sensors to ~ 3.1 to 4.3×10^{14} protons/cm² i.e. 1.5 to 2.0×10^{14} 1 MeV neutron equivalents, resulting in an acceptable

²If a silicon atom has less than four neighbours, e. g. in a defect structure it is said to have “dangling bonds”.

low capacitive noise after irradiation which is the dominant noise contribution at an operating temperature of $-10\text{ }^{\circ}\text{C}$ for the CMS tracker (cf. [19], [20]).

(2) Width-to-Pitch Ratio: All sensors used in the CMS experiment have a width-to-pitch ratio of 0.25. The meaning of the values width and pitch is depicted in figure 2.6. The choice of the pitch is driven by the achievable two particle separation. For the given pitch the width-to-pitch ratio represents a compromise between mainly three requirements (cf. [20]):

- The *charge collection efficiency* through the coupling capacitor between p^+ -implant and the aluminium strip determines the signal height. It saturates for values of $w/p > 0.2$.
- The requirement of *high voltage stability* disfavours too small values of the width-to-pitch ratio since high electric fields are more probable to occur at narrow p^+ -implants.
- The lowest *noise* and the best *signal-to-noise ratio* can be obtained with a small width (best value for $w/p \approx 0.06$) since the strip capacitance is low in that case.

The total strip capacitance per length of a readout strip is approximately a function of the width-to-pitch ratio w/p only. This can be explained by the observation that a decrease in the backplane capacitance with increasing detector thickness is compensated by an increase in the inter-strip capacitance. The total strip capacitance C_{tot} per unit length can be parametrized as [20]:

$$C_{tot} = \left(0.8 + 1.7\frac{w}{p}\right) \text{ pF/cm} \quad (2.9)$$

In the outer regions of the CMS tracker module strip lengths up to 20 cm are used which effects additional capacitive noise. To obtain an acceptable signal-to-noise ratio it is possible, according to equation (2.9), to gain a higher signal by enlarging the thickness of a detector without worsening the noise behaviour which is independent of the detector thickness.

2.3.5 Annealing and Reverse Annealing

After the exposure to radiation the silicon is not in a stable state, since defects caused by radiation can roam around in the lattice. They may transform thereby into other more stable defect types. Thus the properties of the detector change on a longer time scale. At room temperature one can observe an *annealing* that takes place within some hours up to some weeks. It manifests itself in terms of a decreasing effective doping concentration, and so it has beneficial impacts on the leakage current, depletion voltage etc..

But the transformation of defects in the silicon crystal continues such, that on a time scale of months, the effective doping concentration increases again. This effect is called *reverse annealing*. It dominates on long time scales and impairs the detector performance.

Impact on the Sensor Operation: Fortunately the reverse annealing can be suppressed virtually completely if the detector is kept at low temperatures. This is the main reason why the CMS silicon tracker will be operated at temperatures below 0 °C besides the advantages of low temperatures for the leakage current (see 2.3.2).

2.4 Layout of the CMS Silicon Microstrip Sensors

A figure presenting the schematic design of a silicon microstrip sensor as used in the CMS experiment is shown in figure 2.6.

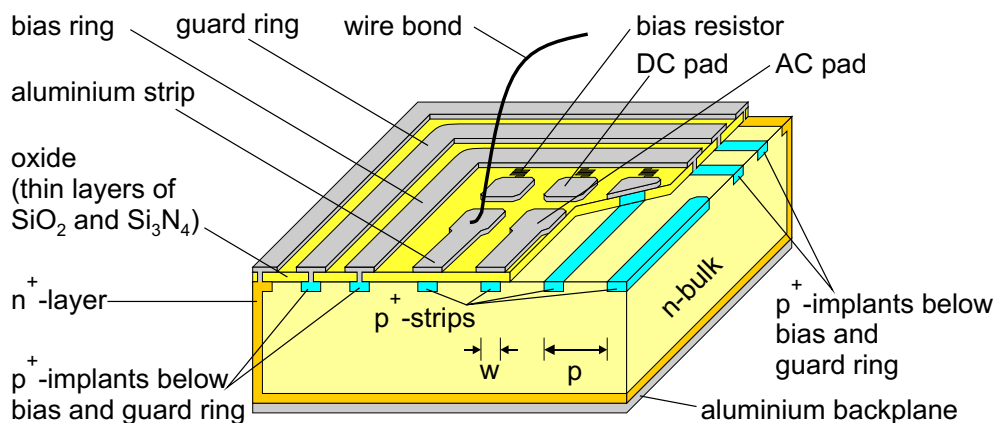


Figure 2.6: Schematic design of a silicon microstrip detector as used in the CMS experiment.

The reversed biased p-n junction serving as sensitive region is formed between the p⁺-strips and the n-type bulk. The back side of the detector consists of a uniformly metallized n⁺-layer providing the necessary ohmic contact between the bulk and the aluminium layer.

The n⁺-layer surrounds the sensor at the edges in order to keep the space charge region away from the highly damaged cutting edges. This implantation, covered by an aluminium layer, helps to protect the sensitive area from charges created at the cutting edge.

The p⁺-strips are separated from the overlying aluminium strips by multiple layers of SiO₂ and Si₃N₄ providing the dielectric for the capacitors made of each pair of p⁺- and aluminium strips. These capacitors serve as coupling capacitors for the signal induced by the movement of electrons and holes in the sensor after the passing through of an ionizing particle. The width of the aluminium strips is larger by about 15 % compared to the width of the p⁺-implants, in order to shift regions of high electric field from the low resistivity n-bulk to the highly resistive oxide layer, thus reducing the risk of electrical breakdown.

The sensitive area is surrounded by two rings of p⁺-implants, both covered by an aluminium layer. The bias ring is connected to ground and thus used to bias the implanted p⁺-strips via metallized probe pads (DC pads). The connection is established by wiggled shaped poly-silicon bias resistors. The guard ring is left floating and helps to degrade the electric field between the n⁺-implantation at the sensor edges and the

	thin sensors	thick sensors
vendor	HPK	STM and HPK
thickness	$320 \mu\text{m} \pm 20 \mu\text{m}$	$500 \mu\text{m} \pm 20 \mu\text{m}$
flatness	100 μm over total sensor length	
dicing accuracy	$\pm 20 \mu\text{m}$	
implant precision	$\pm 1 \mu\text{m}$	
crystal lattice orientation	$\langle 100 \rangle$	
resistivity μ	1.5 . . 3.25 k Ω cm	4 . . 8 k Ω cm
bias resistors	$1.5 \pm 0.5 \text{ M}\Omega$	
width-to-pitch ratio	0.25	
pitch	80 . . 158 μm	122 . . 205 μm
width of p ⁺ -implant	20 . . 39 μm	30 . . 51 μm
width of aluminium	28 . . 51 μm	40 . . 67 μm

Table 2.1: Parameters of the silicon sensors used in CMS (source [21]).

bias ring. The ring geometry with round corners helps to avoid discharges while operating the device at high voltages.

The positive high voltage for the reverse bias is applied via the aluminium back-plane.

The modules for the CMS Silicon Strip Tracker are manufactured by two vendors, HPK³ and STM⁴. HPK is responsible for all thin and parts of the thick sensors while STM is responsible for the remaining thick sensors. The properties of the sensors are summarised in table 2.1.

2.5 The CMS Silicon Strip Tracker Modules

The sensors and the associated front-end readout electronics are mounted on light carbon fibre based support structures, to built up the *modules*. These modules facilitate the installation into larger structures. In total 15,148 modules (plus approximately 10 % spares) have to be produced. The following subsections describe the support structure and the front-end electronics in more detail.

2.5.1 Design of the Module Mechanics

Modules for the inner barrel, the inner disks and ring 1 to 4 of the end caps are equipped with one sensor, modules of the outer barrel and rings 5 to 7 of the end caps have two sensors. In the latter case the strips of the sensors are electrically connected via wire bonds.

³HPK: *Hamamatsu Photonics K.K.*, 325-6, Sunayama-cho, Hamamatsu City, 430-8587 Japan. URL <http://www.hamamatsu.com>.

⁴STM: *ST Microelectronics*, 39, Chemin du Champ des Filles, C. P. 21, CH 1228 Plan-Les-Ouates, Geneva, Switzerland. URL www.st.com.

The support structure provides the necessary stability to the sensors and carries the readout electronics. The material amount for the support structures has to be minimized to keep the total amount of material within the tracker volume small. In case of the inner barrel modules, it consists of a graphite frame that surrounds the sensor on all sides. The support structure for the one-sensor-modules of the end cap is an U-shaped frame of graphite. For the two-sensor-modules of the end cap a similar U-shaped support structure is obtained by gluing two carbon fibre legs on a graphite cross piece (see figure 2.7(a)) which holds the front-end electronics.

The graphite fulfils the requirements of high stiffness, low mass, and efficient heat removal from the sensors. In addition, it is sufficiently radiation hard and has approximately the same coefficient of thermal expansion as silicon. Remaining differences in the thermal expansion have to be compensated by the glue which has to be chosen wisely to comply with requirements for radiation hardness, a very good thermal conductivity, and thermal stability.

Sensors and front-end hybrids (see chapter 2.5.2) are glued to the frames by high precision assembly robots, so-called *gantries* [22]. In total, seven centres (*gantry centres*) are responsible for the assembly of all modules. Positioning precisions of approximately 30 μm are required and obtained with a high yield for the plane perpendicular to the strip direction (see e. g. [23]).

A *pitch adapter* is used to adjust the various pitches of the sensors to the APV pitch width of 44 μm . Besides that it allows to place the heat producing electronics further away from the sensors.

In order to bring the bias voltage to the backplane of the sensors, a thin metallized Kapton⁵ foil is connected with electrically conductive glue to the backplane. The return line is a thick line on the pitch-adapter connecting the bias ring on one side and the hybrid ground on the other side.

The module is mounted on larger substructures using only four points, two of which being high precision bushings, allowing for a mounting with an accuracy of less than 100 μm . Common to all mounting points is, that they are at the same time used as thermal contact to the cooling pipes running through the petal, rods, and discs, respectively. The clamps close to the sensors are therefore implemented as special heat collector pieces (see [24]).

2.5.2 The Front-End Hybrid

The front-end hybrid is utilized to supply the various ASIC⁶ chips used for readout and support tasks with the required voltages of 1.25 V and 2.50 V, respectively. A number of different material compositions have been investigated with respect to radiation hardness, low mass, low bending at changing temperature and good heat transfer from the power consuming ASICs to the heat collecting mounting points [25]. Since the number of front-end hybrid equals the number of modules, the mass production suitability is an important aspect in the choice of the final design. Thus constraints come

⁵Kapton is a trademark of DuPont. DuPont Building, 1007 Market Street, Wilmington, DE 19898, USA.

⁶ASIC: Application Specific Integrated Circuit.

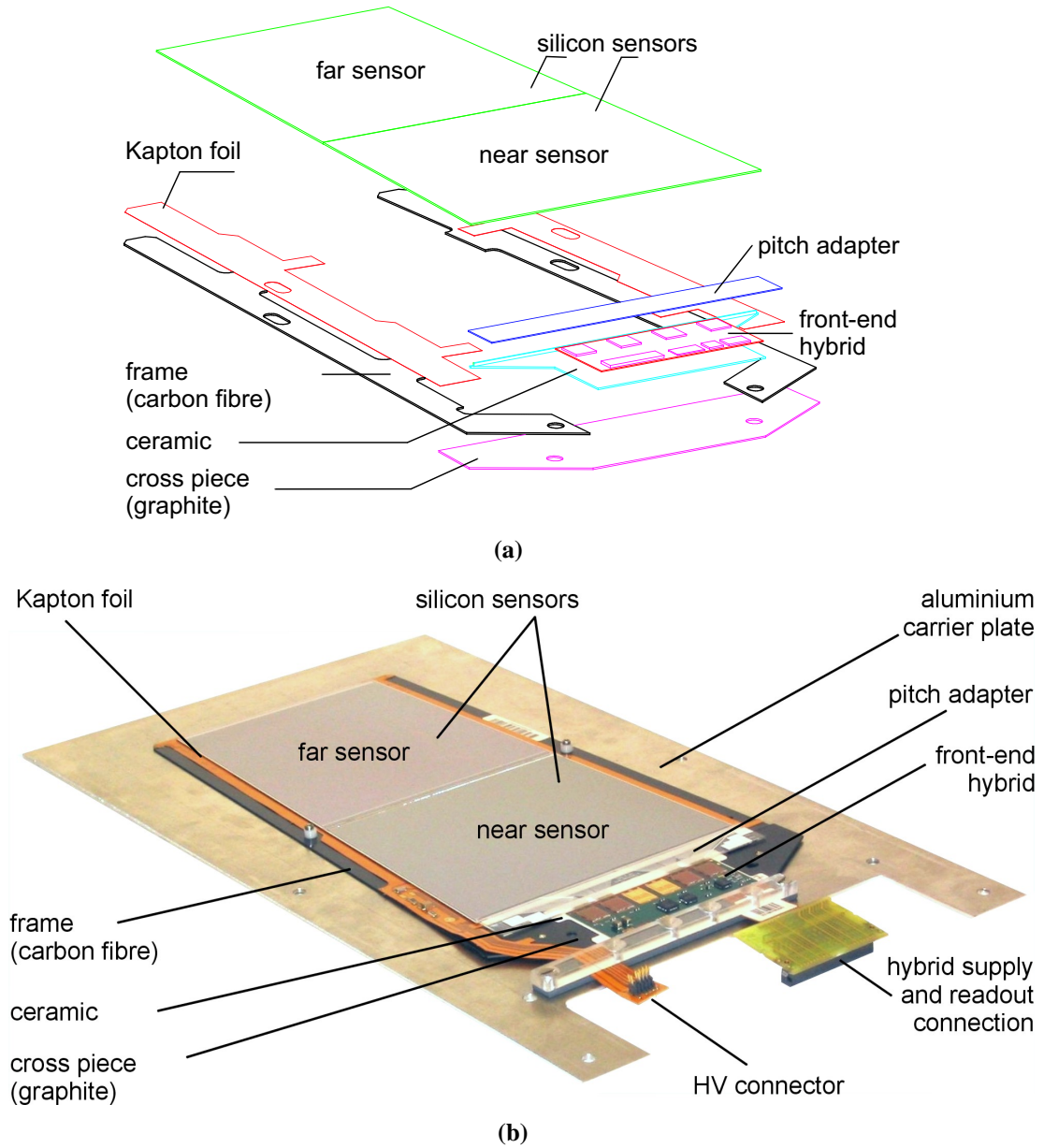


Figure 2.7: (a) Exploded view of a ring 6 TEC module. (b) Photograph of a ring 6 TEC module mounted on an aluminium carrier to facilitate the handling during the tests.

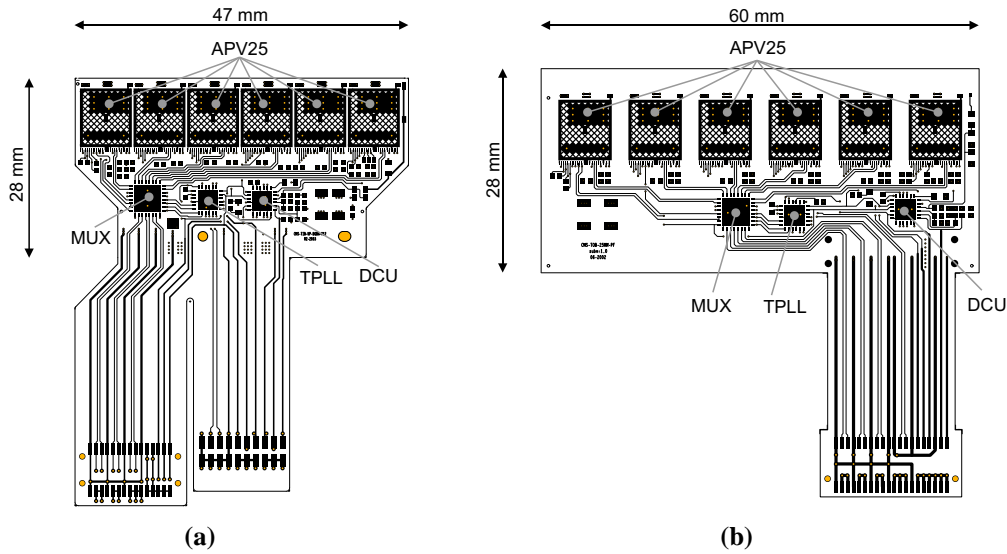


Figure 2.8: (a) The high density layout for TIB and TID hybrids, (b) the slightly larger circuit for TOB and TEC (from [25]).

also from the assembly robots which require very thin, flat, rigid, and light hybrids. A description of the final design can be found in [26]. In total, twelve different types of hybrids have to be produced, while essentially two major designs exist which are illustrated in figure 2.8.

A front-end hybrid houses four or six APV25-S1 chips, used for the data acquisition, and three auxiliary chips: one multiplexer chip (MUX), one chip for the trigger decoding (TPLL), and one chip for the surveillance of environment variables (DCU). These chips are glued on preassigned positions on the hybrid. The electrical connections between ASIC and circuit path are done by wire bonds. The different chips and their functionality are described in the following sections.

2.5.3 The APV Chip

The APV25-S1⁷ chips represent the main components of a front-end hybrid. The APV25 chip is the result of a long development effort at the Rutherford Appleton Laboratory⁸. It is fabricated in a 0.25 micron CMOS process to take advantage of the radiation tolerance, low noise and power consumption, and high circuit density which can be achieved [27]. For a proper operation the APV requires a connection to a 40 MHz clock line and two operation voltages of 1.25 V and 2.5 V (plus ground). Under standard operation conditions it consumes approximately 2.81 mW per channel, including the power dissipation of external resistors [28].

⁷The full name APV25-S1 indicates the main function principle (*Analogue Pipeline Voltage mode*), the production process (0.25 micron features size) and the revision number (*S1*). For better readability it will be referred to as APV25 or simply APV.

⁸Instrumentation Department, CCLRC Rutherford Appleton Laboratory, Chilton, Didcot, Oxfordshire, OX11 0QX, Great Britain.

Signal Processing

One APV chip comprises 128 inputs for signals coming from the capacitively coupled aluminium strips of a sensor (see figure 2.6). The charge signals get amplified by low noise amplifiers and transformed into a voltage step (see figure 2.9).

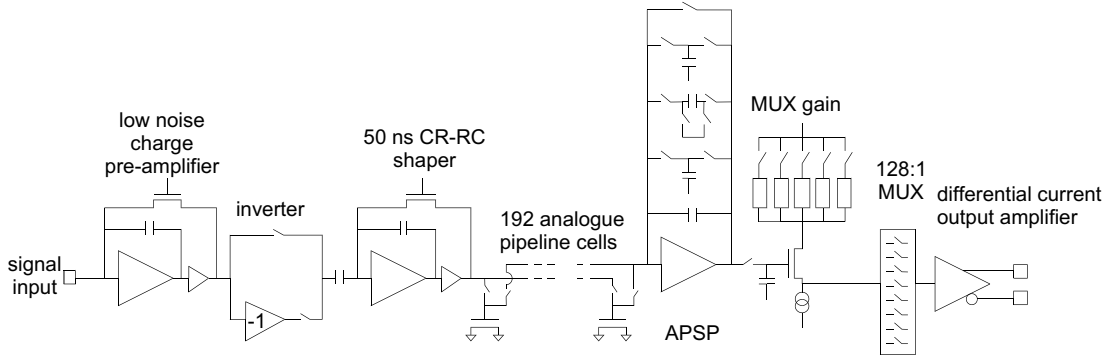


Figure 2.9: Block diagram of one channel of an APV25 chip (based on [27]).

Depending on whether positive or negative charge arrives at the input, the APV facilitates the inversion of the signal. This is necessary to enable the measurement over the largest possible range of signals which is only possible for positive signals. The next unit is a CR-RC shaper with a peaking time of 50 ns. The shaped voltage pulses are then continuously sampled every 25 ns. The sampled charge is stored in an analogue pipeline consisting of 192 switched capacitor elements per channel. The specific pipeline cell envisaged for writing is determined by a write pointer. The pipeline permits to store the signal for more than 4 μs and to process up to 32 or 10 triggers, in peak and deconvolution mode, respectively (see next section). If no trigger is received within 4.8 μs the pipeline cells become overwritten.

On a trigger signal, the specific pipeline column chosen for read out is marked by a read pointer. Read pointer and write pointer are separated by an adjustable *latency*. The charges stored in the 128 pipeline capacitors belonging to the respective clock cycle are routed to the 128:1 multiplexer before leaving the APV.

Operation Modes

The APV comprises an *Analogue Pulse Shape Processor* (APSP) that allows to return data with different peaking times. Three different modes of operation are available for the APSP. When a trigger is received by the APV either one or three pipeline columns are reserved for readout, depending on the operation mode of the APV.

In *peak mode* the signal stored in one pipeline cell is routed to the succeeding processing steps. Two hits within 25 ns cannot be disentangled, since the shaping time of 50 ns entails an overlap of two closely succeeding shaped signals.

To circumvent this problem, the *deconvolution mode* (abbreviatory *dec mode*) was introduced. The principle of the deconvolution is, that although signals of any appearance are smoothed by the shaper, the final (deconvoluted) shape still depends on

the appearance of the original signal which can be restored from the shaped pulse. In case of a CR-RC shaper with a peaking time τ and sampling intervals Δt , the original signal can be restored by a weighted summation of three subsequent samples of the shaped pulse. With $\tau = 50$ ns, $\Delta t = 25$ ns and $x = \Delta t/\tau = 1/2$, the weights can be calculated to [29]

$$\begin{aligned} w_1 &= e^{\left(\frac{x-1}{x}\right)} = 1.213 \\ w_2 &= -\frac{2}{x \cdot e} = -1.472 \\ w_3 &= \frac{1}{x \cdot e^{x+1}} = 0.446 \end{aligned} \quad (2.10)$$

The APV uses multiples of these weight values ($w_1 : w_2 : w_3 = 1.457 : -1.759 : 0.534$) to get in deconvolution mode approximately the same pulse height as in peak mode. The process of weighted summation is depicted in figure 2.10.

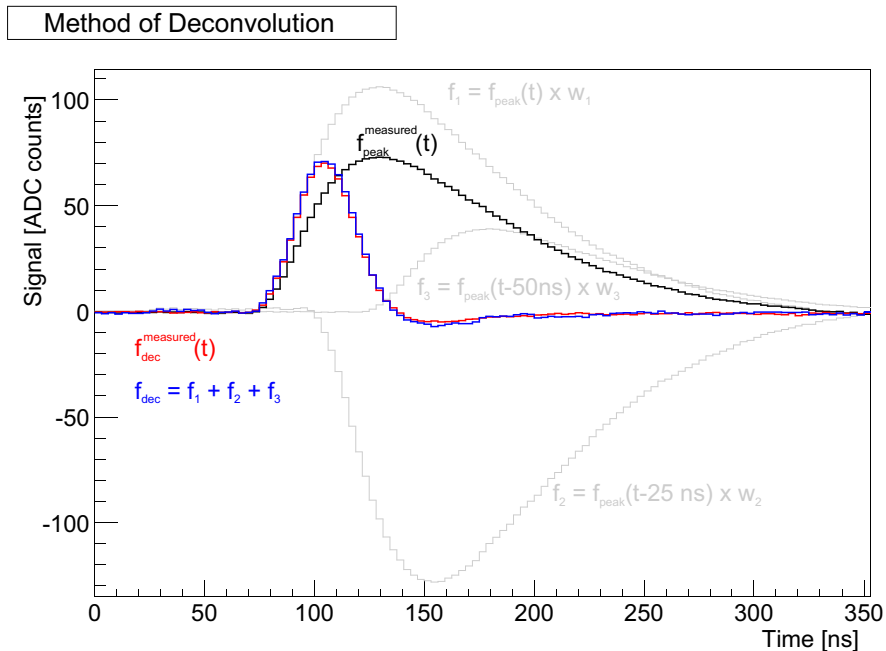


Figure 2.10: The principle of the APV deconvolution explained with measured data in peak and deconvolution mode: The deconvoluted pulse f_{dec} (blue line) can be calculated from the measured pulse in peak mode $f_{peak}^{measured}(t)$ (black line) by the weighted sum of three values shifted by 25 ns (light grey lines). A measured pulse shape $f_{dec}^{measured}(t)$ in deconvolution mode of the same strip is shown for comparison (red line).

In the APV chip, the weights are realized in the APSP in fixed capacitances of values $C_1 = 0.61$ pF, $C_2 = 2.04$ pF, and $C_3 = 1.69$ pF. If the chip receives a trigger signal in deconvolution mode, it takes four clock cycles until the data is relayed to the succeeding electronics [30].

In the first clock cycle C_1 gets loaded, in the second C_2 , and in the third cycle C_3 . The fourth cycle is used to release the charge of all three capacitances and feed it into the APV internal multiplexer.

Since the deconvolution logic introduces additional noise, the deconvolution mode is foreseen to be used at high event rates only, expected in the high luminosity phase of LHC. The peak mode can always be used when the data rates are sufficiently low. In this mode, the signal-to-noise ratio is maximized and the non-linearity of the signal is minimized.

A third operation mode is implemented in the APV, called *multi* or *three sample mode*. It returns the data of the same three succeeding pipeline cells used for the deconvolution, but without the weighted summation.

APV Data Frames

A typical APV dataset is shown in figure 2.11. It consists of a digital header of 12 bit length. The first three bits are used to indicate the beginning of the header. They are followed by 8 bits decoding the pipeline address⁹ (in case of deconvolution mode the address of the first of the three cells) and an error bit. If the error bit is set to 0 this indicates that either a *FIFO error* (APV received more trigger than it can work off) or a *Latency Error* (Pipeline read and write pointer are separated by a number differing from the adjusted latency) occurred.

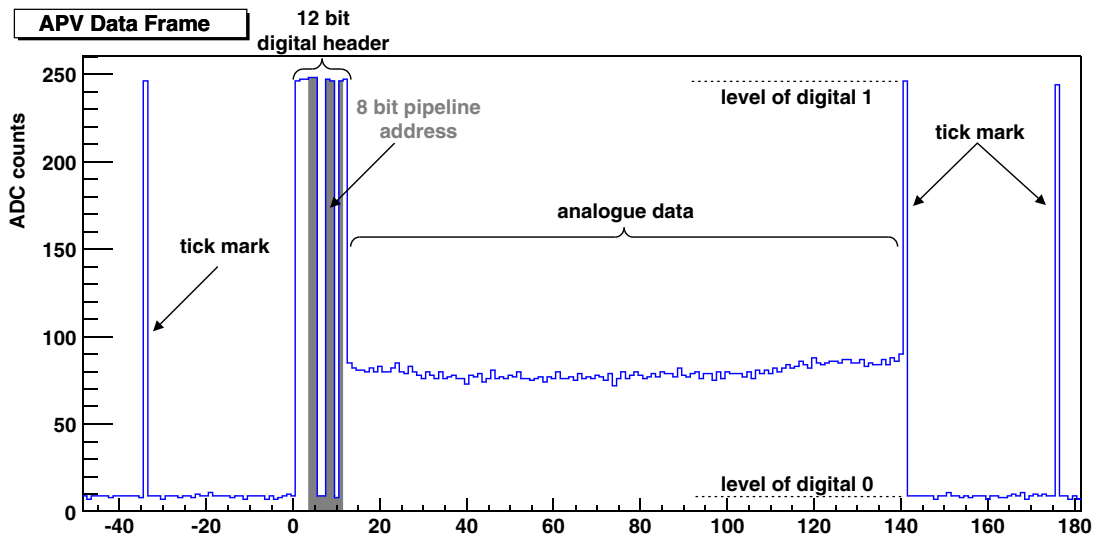


Figure 2.11: A typical APV Data frame. Entries 1 to 12 make up the 12-bit header. They are interpreted as digital 0 if the value is low, and as digital 1 if the value is high. Bits 1 to 3 mark the beginning of the header, bits 4 to 11 the pipeline address, bit 12 indicates an error if it is low. Entries 13 to 140 represent the (digitized) analogue data. The entries at -34 , 141 , 176 are the so-called tick marks.

After the error bit, the 128 analogue data corresponding to the 128 strips are transmitted. A data sample is always terminated by a tick mark (a digital 1).

⁹In fact the 8 bits in the header are not the pipeline addresses, since the pipeline addresses are coded in a so-called grey code. This is done to minimize switching noise e. g. if all bits have to be altered by switching from pipeline cell 127 (binary 0111.1111) to 128 (binary 1000.0000).

If no data is present only a tick mark is sent every 35 clock cycles in order to keep the synchronization with the DAQ system.

Slow Control

Many operation conditions of the APV can be adjusted via a two wire serial interface, conform to the Philips I²C standard [31]. In total, 17 registers can be used to influence e. g. the operation mode, the latency, the pedestal, and currents and voltages for the preamplifier, shaper, APSP, and multiplexer [32]. The access to all these parameters is necessary to allow for chip tuning under various conditions (temperature, strip capacitance) but mainly to enable counter measures to the expected degradation caused by radiation damages.

An especially important feature of the APV, adjustable via I²C, is the built in calibration circuit for the injection of a defined amount of charge into groups of APV inputs. A more precise description of the calibration circuit is given in chapter 5.3.

Trigger Patterns

The standard trigger¹⁰ for data output is a 1 followed by at least two zeroes, e. g. 100. But there are additional trigger patterns to initiate auxiliary functions. If the APV receives two trigger signals in two subsequent clock cycles (trigger pattern 11, this is interpreted as a calibration request, i. e. as a command to release a charge pulse from the chip internal calibration circuit. The trigger sequence 101 activates a chip reset.

2.5.4 The MUX Chip

The MUX chip interfaces as manifold 2:1 multiplexer between the APVs and the subsequent components in the readout chain, in order to minimize the number of readout channels. It multiplexes the analogue data of a pair of APVs onto a single differential line. The currents output by the APVs are converted into voltages via eight resistors. Each of the resistors with a resistance of 400 Ω can be connected in parallel to a selectable number of others, thus giving resistances between 50 and 400 Ω . The number of connected resistors determines the signal height arriving at the opto-hybrids and can thus be used to adapt to the dynamic range of the lasers of the opto-hybrid. The resistors are switched via an 8 bit register, accessible via the chip internal I²C interface.

2.5.5 The TPLL Chip

Within the tracker of the CMS experiment, the clock and level 1 trigger information are encoded in one signal as shown in figure 2.12(a). This minimizes the bandwidth and the power requirements of the transmission system [33]. On the other hand it requires a dedicated circuit to decode the trigger and the clock signal, to make both suited for

¹⁰A trigger signal is denoted by a 1, while no trigger in a clock cycle means a 0.

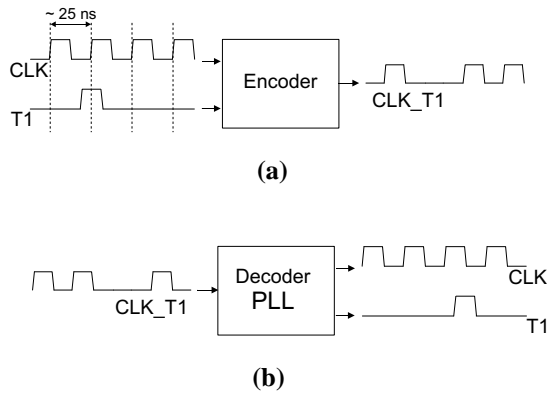


Figure 2.12: (a) Clock (CLK) and level 1 trigger (T1) are encoded in a single signal. (b) The TPLL decodes the signal and distributes trigger and clock as two separate signals to the ASICs on the hybrid.

the APV and the MUX. This is done by the TPLL¹¹ chip as indicated in figure 2.12(b). To allow for an accurate measurement of analogue data from the APV the time jitter must not exceed 0.5 ns.

In addition to clock recovery and trigger decoding it also serves to compensate clock delays introduced by the runtime of the signal on cables of different lengths and the different times of flight of particles coming from the interaction point.

2.5.6 The DCU Chip

The DCU chip serves as *Detector Control Unit*. The monitoring functions are three-fold: surveillance of the sensor leakage current, of the APV power supply voltages ($V_{1.25}$ and $V_{2.50}$ with nominal values of 1.25 V and 2.50 V, respectively), and of hybrid and sensor temperatures. In addition, the DCU possesses a uniquely writeable 24 bit identifier, intended to allow for the safe identification of any module in the tracker. The DCU block diagram is shown in figure 2.13.

The sensor leakage current is monitored using a sensing resistor (R_S). The DCU houses two temperature and power supply independent constant current sources of 10 and 20 μA respectively. The 10 μA source is used to drive a thermistor near the APVs. The voltage drop over the thermistor is measured and used to determine the temperature on the hybrid. According to the same principle the temperature of the sensor(s) is measured. For that purpose, two thermistors are positioned at the backside of the silicon sensor(s), both connected in parallel and driven by the 20 μA current source. A third temperature measurement inside the DCU is carried out by monitoring the voltage derived from a self-biased current source whose current is proportional to the absolute temperature.

¹¹TPLL: Tracker Phase Locked Loop, the name describes the principle of clock phase locking via a feedback loop. The TPLL comprises a voltage controlled oscillator (VCO), whose oscillation frequency is adjustable via a voltage. The phase shift between incoming and outgoing clock signals is measured and transformed into a voltage. This voltage is feed back for the adjustment of the VCO voltage.

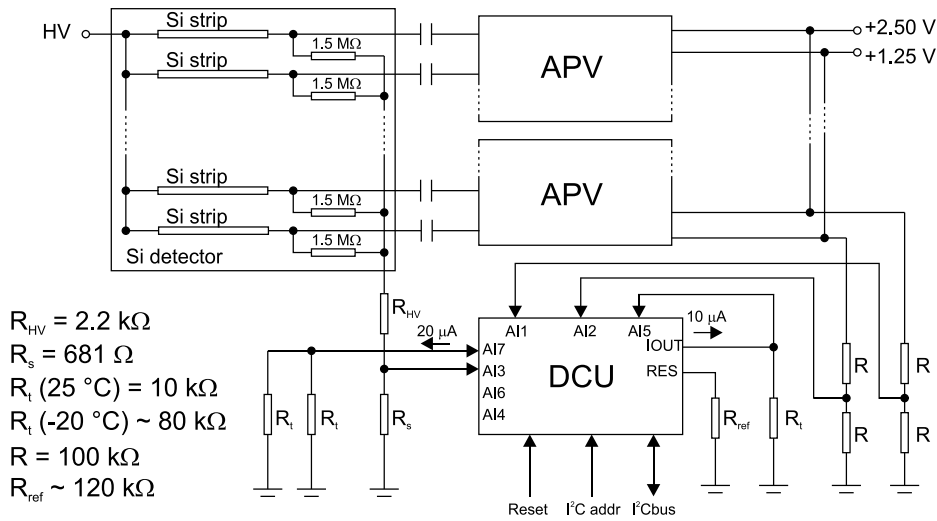


Figure 2.13: DCU block diagram (from [34], some resistor values adapted).

The APV power supply voltages $V_{1.25}$ and $V_{2.50}$ are maintained using two external resistive dividers.

All analogue measurements are converted into digital values by a 12 bit analogue-to-digital converter. The conversion results as well as the identifier are readable via an I²C interface.

The total power of one DCU consumption is about 35 mW [34].

2.6 Possible Module Faults

As described in the previous sections, the production of the CMS Silicon Strip Tracker modules is a very challenging task. Virtually all components are close to the limit of what is technically feasible in a large scale production. Therefore a broad spectrum of failures and flaws occurred during several module pre-production lines and the commencing mass production. They can be characterized with respect to their origin as problems of the sensor production, problems of the ASIC and the hybrid production and problems which occurred during the module assembly, module handling and finally in the operation of the completed module. Some typical problems and failures which concern a significant number of modules are explained in the following subsections.

2.6.1 Problems in the Sensor Production

As mentioned in section 2.4, the sensors for the CMS silicon tracker are delivered by two different vendors, Hamamatsu Photonics K.K. and ST Microelectronics, responsible for the production of thin (320 μm) and thick sensors (500 μm), respectively. The specifications of the sensors are determined by the CMS collaboration, while the production process is left to the companies. Thus sensors with slightly different properties were delivered to the CMS collaboration. All sensors are tested carefully in the quality

test centres¹² [19]. A sensor test usually includes the measurement of the I-V curve in the range from 0 to 550 V and the C-V curve in the range of 0 to 350 V. Both measurements provide information about the performance of a sensor. In addition, four parameters are measured for every strip:

- The single strip current I_{Strip} by measuring the current between the backplane and the DC pad while the bias ring and the DC pad are at 0 V (to short-circuit the bias resistor) and the backplane is biased with 400 V.
- The poly-silicon resistor value R_{Poly} by measuring the resistance between bias ring and DC pad.
- The dielectric current I_{Diel} by measuring the current flowing between AC and DC pad at 10 V.
- The coupling capacitance C_{AC} between the aluminium strip and the subjacent p⁺-strip which is intentionally short-circuited to one neighbouring p⁺-strip, by measuring the inductive reactance at a frequency of 100 Hz. In that way short-circuited strips are measured as two capacitors in parallel and the resulting value is twice the correct one.

Characteristic deviations of nominal test results in one or more of the above mentioned tests can be attributed to certain sensor failures.

A high total leakage current does not influence the detector performance significantly but is taken as an indicator of problems. Thus sensors with a leakage current of more than 10 μ A are rejected. The C-V curve shows a kink at a certain voltage which indicates the complete depletion of the sensor. It can thus be used to monitor the resistivity of the sensor (cf. equation (2.6)). A significantly higher strip current will induce a higher noise on the affected strip and might make it unusable for a reliable signal detection. Accordingly such channels appear in later noise measurements (cf. chapter 5.2) as *noisy channels*¹³.

A particular subtype of noisy channels are channels with *micro-discharges*. Micro-discharges are attributed to small, localized peaks in the electric field inside the sensor which cause an avalanche effect. Such field deformations can be due to a physical damage of the sensor surface (see figure 2.14(a)). Thereby the strip current can be dramatically increased, resulting in a very large noise.

The measurement of the dielectric current is used for the identification of *pinholes* which are contacts between the p⁺-strip and the corresponding aluminium strip due to a defective oxide layer. According to the type of contact, pinholes can be classified as *resistive pinholes* (if there is a ohmic contact between aluminium strip and subjacent p⁺-strip) or as *threshold pinholes* (if the contact is established only if the potential difference between aluminium strip and subjacent p⁺-strip exceeds a certain value).

¹²Since an expensive probe station is needed to test the silicon sensors, in the CMS collaboration only five *quality test centres* (QTCs) are in charge of the quality control for the whole production.

¹³The noise of a channel depends on many different aspects, e. g. the shielding of the module, the common mode of the whole APV and the crosstalk to other channels and the bias ring. All terms will be explained in later chapters.

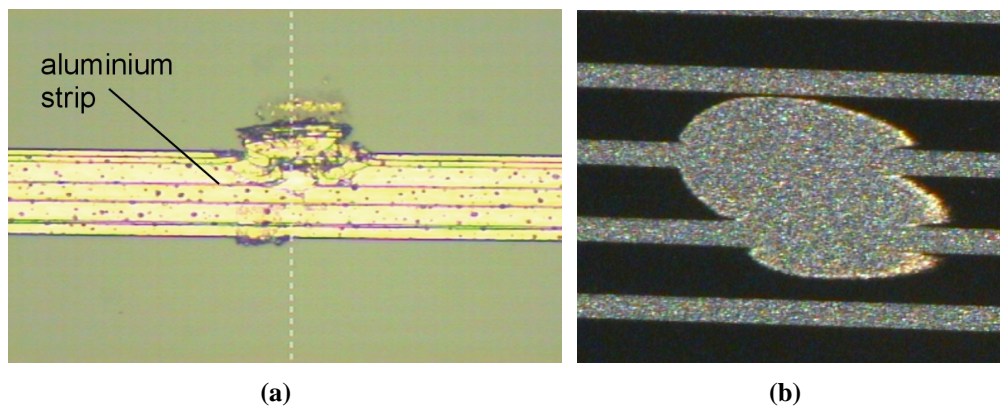


Figure 2.14: (a) Microscopic view of a channel with a very high noise (from [35]). The damage effectuates a micro-discharge effect. (b) microscopic view of a short-circuit between two aluminium strips (from [36])

The coupling capacitance has twice the value of normal channels if two neighbouring aluminium strips are *short-circuited* (see figure 2.14(b)) and can thus be used to indicate this particular type of faults. Resistive pinholes will also show up in the C_{AC} test. Sensor faults are visualized in figure 2.15.

In some cases a smaller coupling capacitance can be attributed to defects in the metallization of the aluminium strip. Such defects are denoted as *mid-sensor-opens*, since their behaviour equals in many properties those of open bonds (see section 2.6.3). A microscopic view of a mid-sensor-open is shown in figure 2.16(a).

Sensor failures like noisy strips, pinholes, and short-circuits are not repairable and it depends on the number of these failures whether the affected sensors are accepted or not. A fraction of 1 % bad strips per sensor is allowed.

Although the grand total of sensors from both vendors fulfilled the aforementioned criteria (cf. [37]) several other serious problems were found on the sensors from ST Microelectronics. In particular, the long term stability of the leakage current was not satisfactory. Furthermore, parts of the aluminium on the sensor surface which were not passivated showed corrosion effects (denoted as dots and stains, cf. [38]) after the biased sensors were exposed for a short period to environments with a relative

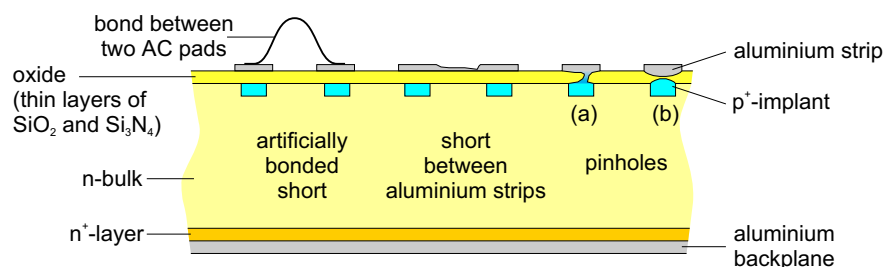


Figure 2.15: Visualization of sensor failures. For test purposes short-circuits can be created via a bond connection between two adjacent AC pads. Pinhole (a) represents a resistive pinhole, (b) represents a threshold pinhole with a damaged oxide layer.

humidity of more than 40 %. Along with many other smaller problems and a generally lower production yield, it was thus decided in 2004 to hand the production of the thick modules over to Hamamatsu.

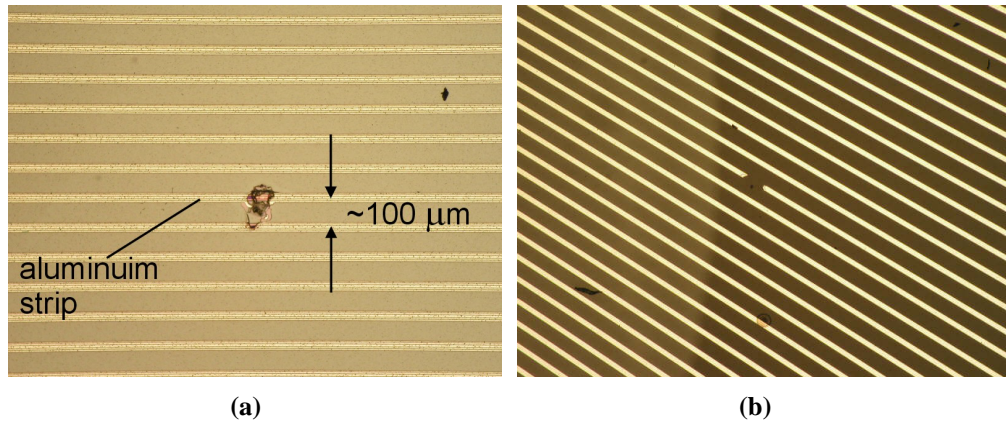


Figure 2.16: (a) Microscopic view of a mid-sensor-open. The missing aluminium line enables the view on the underlying oxide layer. (b) Microscopic view of an open line on the pitch adapter (in the centre of the picture). The glass substrate appears black due to the underlying graphite cross piece.

2.6.2 ASIC and Hybrid Problems

As explained in section 2.5.2, the front-end hybrid is a four layer printed circuit board with a complex structure of different materials to meet all electrical, mechanical and mass production related requirements. After some months of mass production of the hybrids a very subtle but serious problem was found. The vias¹⁴ between different hybrid layers were badly metallized such that under certain circumstances the connection between both layers failed and the hybrid did not work properly. The whole hybrid production had to be stopped and hybrids produced so far are thenceforward treated as suspicious. The problem could be finally solved by a more careful production process but the whole hybrid production was relaunched with about half a year delay.

All problems concerning the ASIC designs are virtually solved. Minor problems like single *defective pipeline cells* of an APV (with approximately 25,000 pipeline cells) are acceptable. In some cases, the input amplifier or the shaper of a single APV channel does not work. As this problem causes a behaviour similar to a saturated amplifier¹⁵ such channels are denoted as *saturated channels* or *dead channels*. In some cases the signal amplification in modes with activated inverter is significantly different from the amplification with deactivated inverter. Such failures are summarized by the term *defective inverters*.

¹⁴“Via” is the name for a connection between two layers of a printed circuit board. A via is a hole (drilled or shot with a laser) through the insulation layer between two layers with conductor paths whose inner side is metallized to establish the electrical connection between two layers.

¹⁵In this context a saturated amplifier means an amplifier which is not operated at its operating point.

ASICs with more serious problems like a *broken I²C part* are usually sorted out to avoid glueing them on hybrids. The wire bonds which connect the ASICs with the hybrid, are a possible source of error. In some cases this causes a failing *I²C* communication. Due to the redundant design of the bond wiring and a severe quality control in the hybrid test practically no hybrid with bad ASIC bonds was incorporated in a module.

2.6.3 Module Production and Handling Problems

The next critical step in the module production is the assembly of the different components, with an accuracy of 20 to 50 μm . A possible source of error is a lack of positioning precision. In fact, some modules with worse precision have been produced. The mistakes could be almost completely attributed to problems with the gantry robots (cf. section 2.5.1). Depending on the degree of mismatch, modules with a lower mechanical precision are provisionally put aside as spares. As the final understanding of the true position of a module within a tracker will mainly be based on particle tracks, one has to correct on misalignments anyway. Thus it might be possible to use these modules in the final tracker.

The final step of the module production is the sensor bonding. Depending on the number of sensors and the number of strips per sensor, between 512 and 1536 wire bonds have to be made to establish the electrical connection from pitch adapter to sensor and from sensor to sensor. Polluted bond pads might cause a wire bond to loosen after a short time period. Also bond parameters like the force used to press a wire bond against the bond pad during the welding can influence the stability and lifetime of a wire bonding (cf. [39]). It has been demonstrated that high forces on the bond pad can also create pinholes. If a strip on a sensor is known to be affected by a pinhole, this strip is not going to be bonded. In case of two short-circuited strips, it is often advisable to bond only one of the strips. This doubles the signal collected by one APV input when a charged particle traverses the sensor, while the noise is in general less affected. By this means, the spatial resolution is worse for the benefit of an improved signal-to-noise ratio (cf. B.3). If a strip has a very high noise, in particular if it affects its neighbours or even the whole APV, this strip has to be un-bonded. Some rare cases occurred where the aluminium lines on the pitch adapter were cut due to scratches or impurities during the application of the aluminium on the glass substrate (see figure 2.16(b)).

Either way, in the end a certain number of strips will have either *open bonds* or *missing bonds* (see figures 2.17(a), 2.17(b)), which can be furthermore separated according to their position into *pitch adapter-sensor-opens* and *sensor-sensor-opens*. All types of open or missing bonds are also denoted as *opens*. Since all bond pads allow between two and four trials, in many cases one can try to re-bond an open bond. During the whole production and during all tests the modules have to be handled very carefully. Dust is a common problem which can be avoided most effectively by producing, testing, and storing all modules in a clean environment.

All possible module faults mentioned above are summarized in table 2.2.

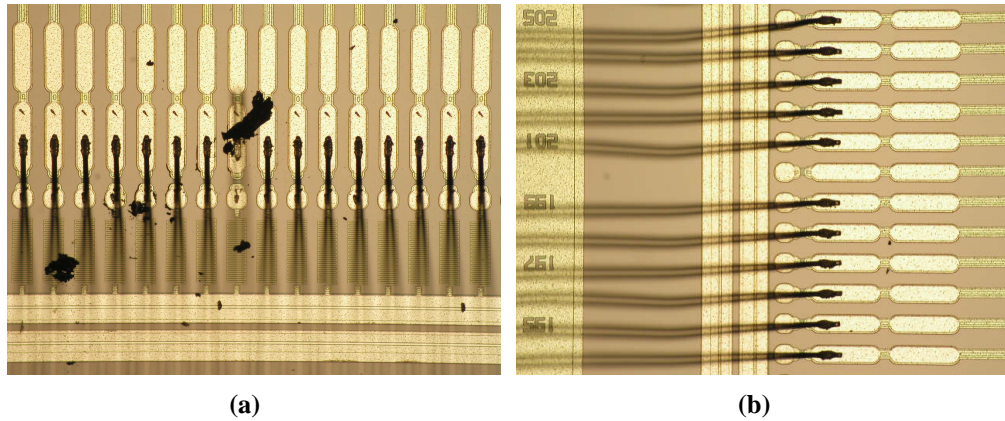


Figure 2.17: (a) Microscopic view of an open bond. A polluted bond pad inhibited a stable bond connection. The loosened bond is only visible out of focus due to the small depth of field of the microscope. (b) Microscopic view of a missing bond. In this particular case the wire bond was left out on purpose due to a known pinhole on the corresponding strip.

Overview of Different Types of Faults	
Type of Fault	Origin
Noisy Channels	e. g. a higher strip current
Micro-Discharge	avalanche effects due to localized peaks of the electric field inside the sensor
Resistive Pinhole	ohmic connection between p^+ -implant and aluminium strip
Threshold Pinhole	damaged insulation layer between p^+ -implant and aluminium strip; a breakthrough occurs at large potential differences
Short-Circuits	ohmic connection between two or more adjacent aluminium strips.
Defective Pipeline Cells	failures in the production of the ASIC
Saturated/Dead Channels	defective APV input amplifier or a defective transmission line to the pipeline cells
Defective Inverters	a defective inverter stage of a channel of the APV
Broken I ² C Part	failures in the production of the ASIC
Failing I ² C Communication	either failures in the production of the ASIC or missing bonds between hybrid and ASIC
Mid-Sensor-Opens	severe damage (cut) of an aluminium strip such that only a part of the strip is connected to the APV input
Missing or Open Bonds	polluted bond pads, bad parameters for the bonding robot or deliberately removed bonds due to a severe failure on the strip

Table 2.2: Overview of possible module faults and their respective origins.

Chapter 3

The APV Readout Controller System - A Test System for Hybrids and Modules

The APV Readout Controller system (ARC system) and all extensions presented here were developed by the III. Physikalisches Institut B, RWTH Aachen. The core of the system is the ARC board, a printed circuit board based on the SRDAPV readout board [40], a development made by the same institute for the AMS-01¹ experiment. The ARC board was designed in 2000, including many additional features purpose-built for the requirements of the CMS silicon strip tracker front-end hybrids and modules.

The board is foreseen to be used in a *test system* for the quality assurance during the mass production [41]. It is limited in terms of high readout rates, occurring e. g. in a test beam experiment.

A first series of ten ARC boards (see section 3.2) was produced in January 2001 and distributed to the collaborating institutes. A first version of a dedicated readout software (ARCS, see chapter 4) was also available at that time.

The ARC board mainly uses customary standard electronics components and can thus be provided at a comparably low price on a short time scale in sufficient numbers. Consequentially it became the official test system for hybrid tests in 2001.

A significant fraction of the first series of ARC boards was used to produce FHIT² systems, devices dedicated for hybrid tests in the hybrid factories (see also 5.9). The FHIT system uses function groups of the ARC board for the slow control and data readout of the hybrids.

A second series of 20 ARC boards was finished in May 2001. Due to the easy handling of hard- and software, concurrent with its suitability to test modules as well as hybrids, it was decided in 2002 to use the ARC system also as the official module

¹The Alpha Magnetic Spectrometer (AMS-01) was an astro particle space experiment on a space shuttle mission in 1998. It was equipped with a silicon tracker which was read out with the predecessor of the APV25, the APV6.

²FHIT: *Front-End Hybrid Industrial Tester*, is a development by the Université Catholique de Louvain la Neuve. Informations about the FHIT system are available at [42].

test system within the CMS module production.

The appropriateness of the ARC system for module tests was even improved by a redesign of the ARC front-end adapter (ARC FE-M, see section 3.3), the interface between the ARC board and the module/hybrid.

Since June 2001, an LED controller board (LEP16, see section 3.4) for additional module tests with external light signals was available, including the necessary software support. Since November 2002, compatible high voltage controllers (DEPP, see section 3.5) became available and were distributed to the collaborating institutes.

The ARC system provides the option to be used also in a synchronously running multi-board setup. Therefore a complete tracking system for low rates can be built up, e. g. as a cosmic muon hodoscope.

In total, 105 ARC boards, 60 front-end adapters of the first type, 120 front-end adapters of the redesigned type, 59 HV controller, and 39 LED controllers were built up to the end of 2004 and distributed to more than 20 institutes.

The following sections will give a system overview and subsequently a detailed description of the hardware components of the ARC system and its compatible extensions.

3.1 System Overview

The ARC system can be operated as a basic system, used for the readout of one or two hybrids at a time, or as an extended system, suited for complete module qualification. A common PC acts as a device to control all system parameters and for data storage via the ARC software (cf. chapter 4). The connection between PC and ARC system is made by a flat cable which is connected to an interface card within the PC on the one side and to one or more ARC boards on the other side.

The ARC board is the central component of any ARC system. It provides all tools necessary to read out and control all ASICs on the front-end hybrids. The connection between the ARC board and the hybrid under test is done via a front-end adapter whose main functions are the amplification of readout signals, the conditioning of control signals, and the monitoring of state variables nearby the hybrid. The front-end adapter is connected to one hybrid port of the ARC board by a flat cable. The connection to the hybrid is established by a passive adapter card, the Hybrid-to-VUTRI adapter card³ which was developed at CERN.

An overview of all components is shown in figure 3.1. A detailed description of the components is presented in the following sections.

3.2 The ARC Board

The ARC board, shown in figure 3.2, is a six layer printed circuit board in double Euro format (160 × 233 mm). It is supplied by two voltages, -5 V and $+5$ V, requiring cur-

³Due to different hybrid layouts, different layouts of this adapter card are necessary to be able to use a common readout hardware for the various hybrid types.

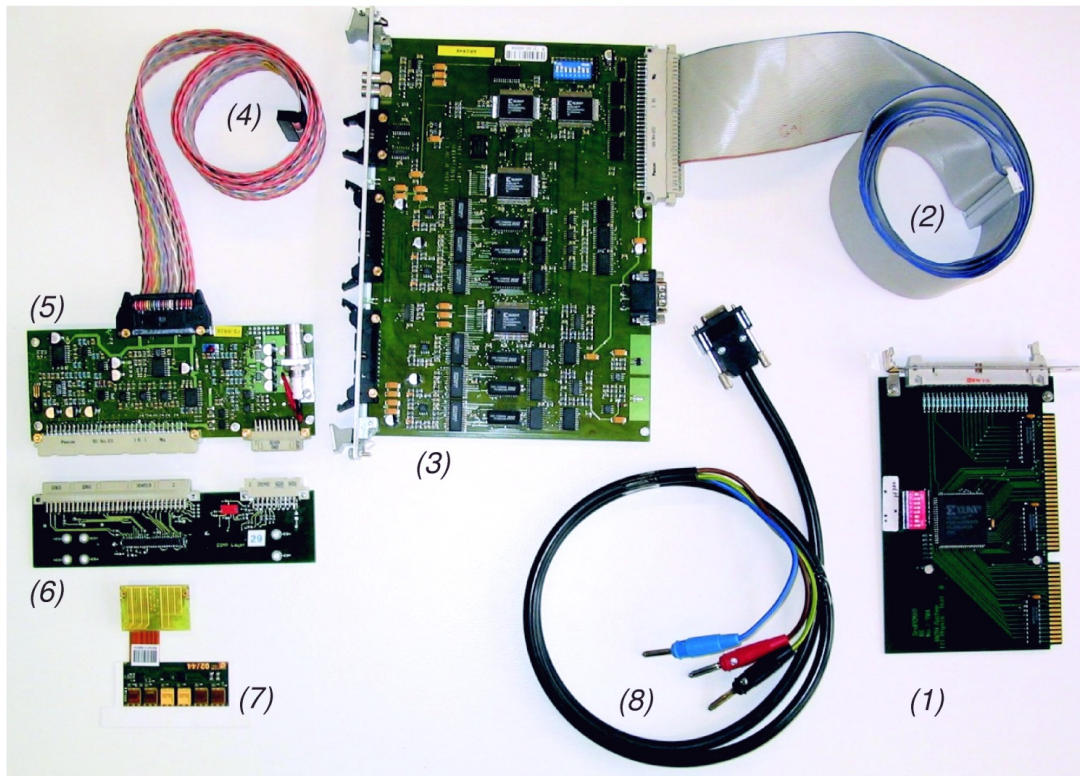


Figure 3.1: Photograph of a complete ARC setup: (1) PCMIIO Interface, to be plugged into an ISA slot of the PC motherboard, (2) 50 pin flat cable, (3) ARC board, (4) 26 pin twisted pair flat cable, (5) ARC front-end adapter, (6) Hybrid-to-VUTRI adapter card, (7) front-end hybrid, (8) power supply cable for the ARC board.

rents of approximately 60 mA and 1.4 A, respectively. The connection is established by a D-Sub9 connector⁴.

The communication with the PC is performed according to the PCMIIO bus protocol which is an adaptation of the ISA bus protocol. The bus provides three control lines, six address lines and 16 bidirectional data lines. The transmission of signals between PC and ARC board is established by a 50 pin flat cable, being plugged in a 64 pin HI-CON⁵ VG connector at the backside of the board. The remaining 14 pins of the connector are used instead of the D-Sub9 connector to supply the voltages if the board is used in a crate.

Control commands from the PC can be written into eight different registers on the ARC board, allowing the adjustment of all necessary board parameters. Up to 256 boards can be addressed by one bus. The distinction between different devices is done by selectable addresses, to be set by a DIL⁶ switch on the ARC board.

One ARC board features the readout of two hybrids or modules at a time. Clock and trigger are generated only once per ARC board (see section 3.2.1). All function

⁴D-Sub9: 9 pole connector, sub-miniature type D.

⁵HI-CON is a product line of the Pancon GmbH, Siemensstr.7, 61267 Neu-Anspach, Germany.

⁶DIL: Dual In Line.

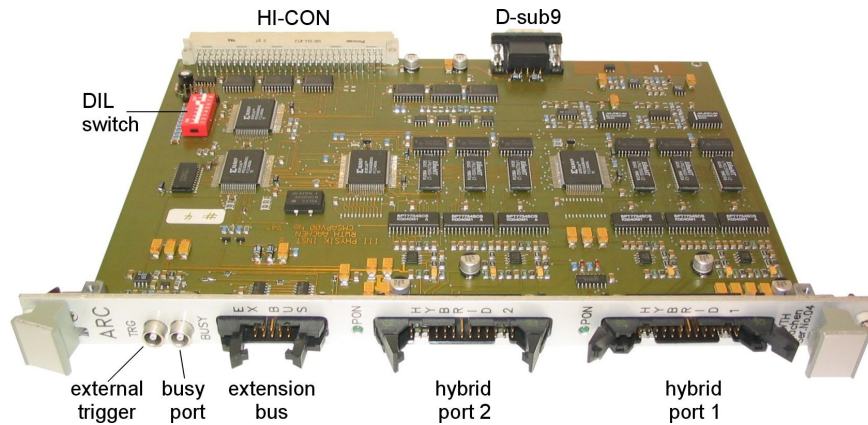


Figure 3.2: Photograph of an ARC board.

groups concerning the readout (see section 3.2.2) and slow control (see section 3.2.3) of a hybrid are implemented twice. In particular two ports are foreseen for the connection to the respective ARC front-end adapter (hybrid port 1, port 2 in figure 3.2).

The whole trigger and readout logic is implemented in the firmware of four PLDs⁷. This provides the opportunity to introduce new or remove obsolete functionalities if this is indicated by advanced testing experience. For tests using external signals, a dedicated LEMO⁸ socket for external trigger signals (TRG in figure 3.2) is available, accepting NIM⁹ signals. The operating status of the ARC board during data sampling and processing can be queried from a socket (BUSY).

Furthermore the ARC boards can be used in a multi board setup, for synchronous, parallel operation of several ARC boards. To obtain a synchronous readout, one master board delivers clock and trigger signals, while the remaining slave boards accept these signals from the master. The transfer of these signals is done via low voltage differential signals (LVDS) transmitted on a 10 pin flat cable connecting the extension bus sockets (EX-BUS) of all ARC boards (see also section 3.8).

3.2.1 Trigger Generation

As stated in chapter 2.5.5, the hybrids require both clock and trigger to be encoded in one signal. A trigger signal appears as a missing clock pulse. The TPLL chip on the hybrid decodes these missing clock pulses as trigger signals and routes clock and trigger information to the MUX and the APV chips, respectively.

The ARC board permits to send complex series of trigger signals in the required format. For that purpose, an adjustable *trigger sequencer* is used. It can store any *trigger pattern* consisting of two times 8 bit length (high byte and low byte), separated by an adjustable number of up to 255 zeros (so-called *spacer*). Trigger pattern and

⁷PLD: Programmable Logic Device.

⁸LEMO: The LEMO GmbH is a factory producing connectors with a special push-pull locking mechanism which are wide spread in electronic applications. LEMO GmbH, Hanns-Schwindt-Str. 6, 81829 München, Germany.

⁹NIM: Standardized Nuclear Instrument Module logic signal.

spacer length are tunable by the ARC software.

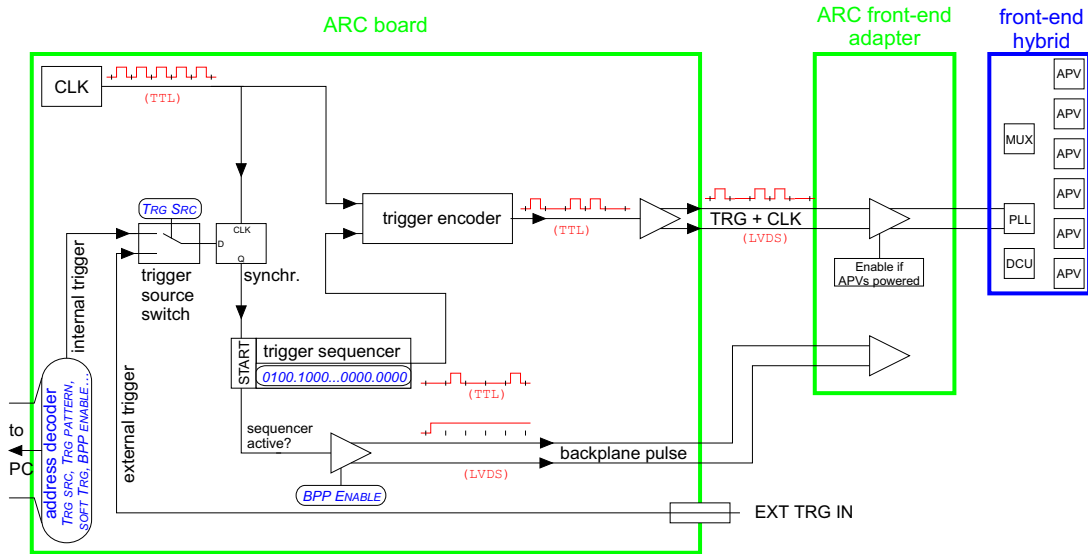


Figure 3.3: Block diagram of the trigger generation on the ARC board. For the sake of simplicity, only one front-end adapter for one front-end hybrid is drawn. The trigger function block is implemented only once per ARC board. The backplane pulse signal is also distributed to both front-end adapters but concerns only module tests. Board settings which are adjustable by software are encircled by oval boxes.

The ARC board features a 40 MHz crystal oscillator needed for the generation of the clock signal. Trigger signals can be released either by an *external trigger* pulse (NIM pulse) received via the TRG socket or the extension bus, respectively, or per software (*internal trigger*). The trigger source is adjustable by software. Any trigger signal received by the ARC board from the activated trigger source will be synchronized to the board internal 40 MHz clock. With the next rising edge of the clock the trigger signal is sent to the trigger sequencer. Thereupon the sequencer sends the predefined trigger pattern according to the timing given by the clock.

Clock and trigger signals are then synchronously fed into a trigger encoder which creates CMS-like clock signals with the disguised trigger signals. To drive the signal over longer lines it is converted from TTL¹⁰ standard to LVDS standard. To provide steep edges at the input of the TPLL it is refreshed on the front-end adapter. To avoid supplying the APV chips with power via the trigger line while they are switched off, the trigger line is activated only if the APVs are powered. The whole chain of trigger generation is illustrated in the block diagram in figure 3.3.

Two hybrids being connected to one ARC board receive exactly the same synchronous trigger signals. A different timing between both hybrids can be achieved nonetheless by an appropriate setting of the APV latency (see chapter 2.5.3).

One feature related to the trigger generation is the generation of the *backplane pulse* (BPP). The backplane pulse is a short voltage pulse capacitively injected upon

¹⁰TTL: Transistor-Transistor Logic.

the high voltage supply line¹¹ which is used for the depletion of the silicon sensors of a module. Thus it concerns only module tests (see chapter 5.8) and was enabled only by a redesign of the front-end adapter (see section 3.3.2). The backplane pulse starts at the same time the trigger sequencer gets started. It ends when the trigger sequence is finished. Accordingly the backplane pulse has a duration between 16×25 ns (minimum) and 271×25 ns (maximum trigger spacer).

3.2.2 Data Acquisition

As explained in section 2.5.4, the analogue data from two neighbouring APVs are multiplexed by the MUX chip onto a single line. For a hybrid with 6 APVs thus 3 multiplexed datasets have to be transferred from the MUX to the readout system. The signals are transferred as differential voltage signals. On the ARC front-end adapter, closest possible to the hybrid, the signals get amplified.

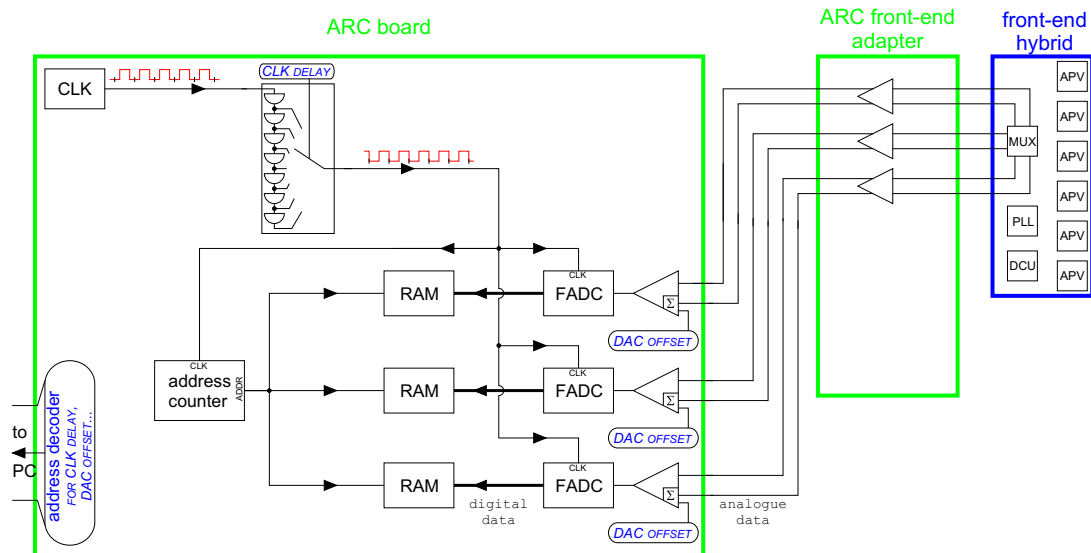


Figure 3.4: Block diagram of the data sampling chain. For the sake of simplicity, only the parts belonging to one hybrid port are sketched. Board settings which are adjustable by software are encircled by oval boxes.

On the ARC board, these signals are fed into an 8-bit FADC¹². To trim the analogue data to the operating range of the FADC, the ARC board permits the addition of an offset to one of the differential lines. The respective DAC¹³ value is selectable in the ARC software.

Within the FADC, the analogue data are sampled every 25 ns. Since all analogue data have to be sampled at their plateau value if procurable, the timing has to be tunable

¹¹Since the pulse is coupled on the positive high voltage line which is connected to the backplane of the silicon sensor(s), it is called the “backplane pulse”.

¹²FADC: *Flash Analogue to Digital Converter*.

¹³D/A converter: *Digital to Analogue Converter*, also DAC.

(depending e. g. on the runtime of the signals on cables). It is thus possible to vary the sampling point in time (*CLK delay*) in 10 steps of 1.7 ns.

The digitised data from the FADC are then written into an 8-bit RAM¹⁴ module with a depth of 8192 entries¹⁵. The switching from one RAM entry to the next is controlled by an address counter that runs with the same shifted clock as the FADC, to have a fixed time relation between data sampling and storage.

The tuning of the timing of all components of the readout chain was one of the most challenging parts in the development of the ARC board, since a whole write cycle consists of an intricate sequence of read/write prohibition, switching to next RAM address, and read/write permission within only 25 ns.

A block diagram of the data sampling sequence is shown in figure 3.4

3.2.3 Slow Control

The third major function group implemented on the ARC board is the slow control. The slow control is used to access all ASIC operation parameters and for the monitoring of state variables of the system. A block diagram of the slow control part is shown in figure 3.5.

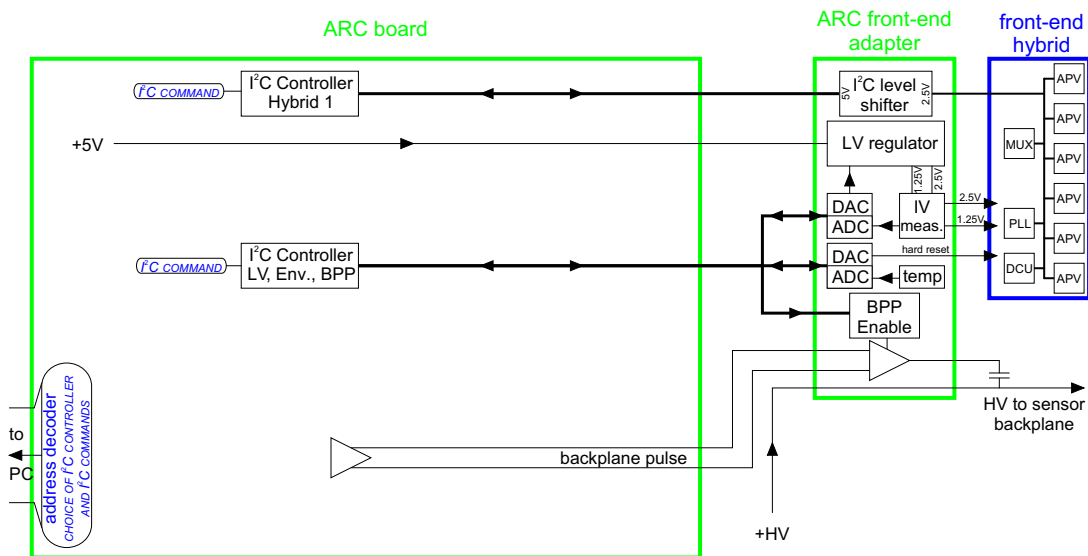


Figure 3.5: Block diagram of the slow control. For the sake of simplicity, only the parts belonging to one hybrid port are sketched. Board settings which are adjustable by software are encircled.

The ARC board houses in total three I²C bus controllers. Two of these controllers are intended for operating all I²C devices on each hybrid. Although all hybrid devices follow the I²C protocol there is a difference in the levels of digital ones and zeroes which is 0 and 2.5 V for the hybrid ASICs and 0 and 5 V for customary I²C devices,

¹⁴RAM: Random Access Memory.

¹⁵To maximise the data acquisition rate only a fraction of the 8192 entries are used. In general, it is sufficient to sample about 500 values.

respectively. Therefore signal levels sent by the corresponding I²C bus controller to the hybrid have to be halved, while signals in the other direction have to be doubled. This task is performed by the I²C *level shifter* on the front-end adapter. The third I²C bus controller is used to control the environment variables of the setup. It is connected to three I²C -accessible devices per front-end adapter.

Two of these devices are combined 8 bit D/A and A/D¹⁶ converters, equipped with four analogue inputs and one analogue output. The first device is intended for low voltage control while the second one measures several temperatures and the humidity. Moreover the D/A converter part of the latter one facilitates a power off/on reset¹⁷ for the hybrid.

The third device is a digital input/output device. Only one output is used to enable the backplane pulse. The various functions of all three I²C devices are listed in table 3.1.

first ADC/DAC device	
ADC channel 1	current at 1.25 V line
ADC channel 2	current at 2.50 V line
ADC channel 3	voltage at 1.25 V line
ADC channel 4	voltage at 2.50 V line
DAC output	voltage control at 1.25 V and 2.50 V line
second ADC/DAC device	
ADC channel 1	DCU thermistor current
ADC channel 2	temperature sensor (optional)
ADC channel 3	humidity on front-end adapter
ADC channel 4	temperature on front-end adapter
DAC output	hybrid power on/off reset
Input/Output device	
enabling of the backplane pulse	

Table 3.1: Functions of the I²C accessible system state monitoring devices mounted on an ARC front-end adapter (ARC FE_M).

3.3 The Front-End Adapter

All components of the readout and slow control that would suffer from voltage drops along the supply lines are located close to the hybrid on the front-end adapter. At the beginning of ARC development in 2000 some specifications of the hybrid operation were not yet fixed. The placement of all components needed to adapt to changes in the hybrid design are housed on the front-end adapter. Thereby an expensive exchange

¹⁶A/D converter: Analogue to Digital Converter, also ADC.

¹⁷Power off/on Reset: A special reset command is sent to all ASICs on the hybrid. The effect is the same as if the power for all ASICs would be switched off and afterwards on again. All ASICs get powered and run with their default settings.

of the whole ARC board could be avoided, as all hybrid specifications were fixed in 2001.

3.3.1 Functions

The front-end adapter was designed to be able to operate an ARC based test system some distance (≈ 1 m) away from the test objects. It facilitates the *amplification* of analogue signals coming from the hybrid and the *reprocessing* of digital signals coming from the ARC board. To reduce the influence of voltage drops, the voltage and currents supplying the hybrid are also measured and monitored on the front-end adapter. An adjustable *voltage controller*, supplied by the ARC board with 5 V, provides the two hybrid voltages of 1.25 and 2.50 V. Voltages in a range of 1.05/2.1 V to 1.3/2.6 V are adjustable while the ratio of both is always one half. Additionally the hybrid is protected against over current by a safety fuse. The low voltage regulation produces a considerable amount of heat as a side-effect.

The front-end adapter houses an *I²C level shifter* to transform standard I²C signals (0 and 5 V) to the hybrid specific signals between 0 and 2.5 V and vice versa.

Furthermore it accommodates three active devices being accessible via I²C: two combined A/D and D/A converters and a configurable digital Input/Output device, whose functions are summarised in table 3.1. Since all of these devices are custom-ary I²C devices, they are all conform to the I²C standard. In total, six devices are available in case two front-end adapters are connected to an ARC board. The distinction between the devices is made by different I²C addresses. These addresses can be set only by dedicated solder pads on the adapter. Only two combinations of address triples are used in practice to facilitate the identification of front-end adapters belonging to different hybrid ports by the ARC software.

3.3.2 Versions of the Front-End Adapter

Two versions of front-end adapters have been produced. Both versions are 4-layer printed circuit boards. The first version, available from 2001 to 2002, consisted of two printed circuit boards of 72 mm \times 72 mm size, mounted onto each other in a sandwich structure. The upper one housed all active components for the trigger transmission, signal amplification and slow control. The lower part contained the low voltage regulation.

The design was well suited for hybrid tests and facilitated the usage of this adapter in cooling tests, where the heat producing part could be left outside the cold environment, thus relaxing the requirements for the cooling plants. In contrast to this advantage, it required laborious efforts to obtain a reasonable grounding of the modules (see e. g. appendix E.2 in [41]). Secondly the design suffered from the fact that the connection to the hybrid had to be established via a very fragile NAIS¹⁸ connector or by

¹⁸NAIS: a series of connectors from Matsushita Electric Works, Ltd. 1048, Kadoma, Kadoma-shi, Osaka 571-8686, Japan. http://www.naisweb.com/e/connecte/con_eng/.

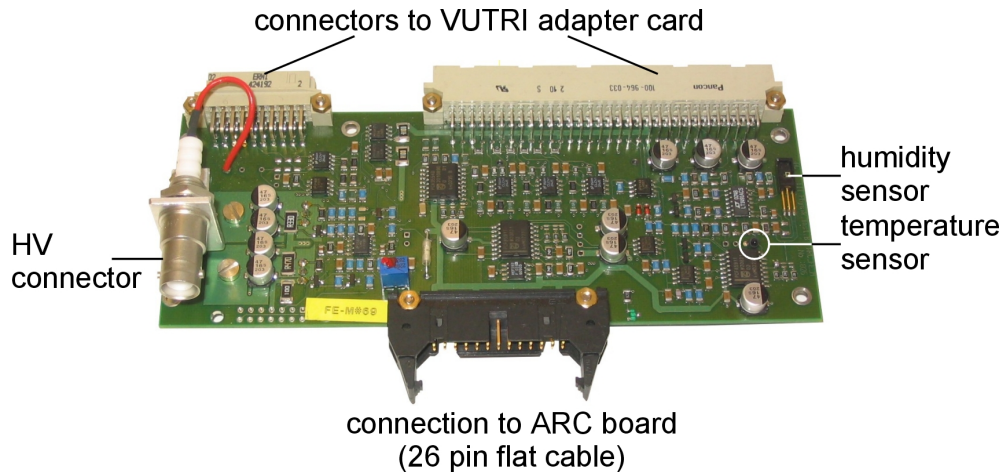


Figure 3.6: Photograph of an ARC front-end adapter especially suited for module tests (ARC FE_M).

a more robust ERNI¹⁹ connector, that required additional adapter cards which were not available in sufficient numbers. Different hybrid layouts (see figure 2.8) complicated a common solution for connection and grounding furthermore. As common interface cards for the different hybrid types, the *Hybrid-to-VUTRI adapter* cards, were developed at CERN, a redesign of the ARC front-end adapter was advisable. The Hybrid-to-VUTRI adapter card includes a high voltage socket as well as lines for the interconnection of the thermistors at the backplane of the sensors to the DCU.

Consequently a modified front-end adapter, the ARC FE_M²⁰, compatible to the Hybrid-to-VUTRI adapter card became available in January 2003. It consists of only one printed circuit board of size 63 mm × 162 mm (see figure 3.6).

The combination of the Hybrid-to-VUTRI adapter card with the ARC FE_M allows for an easy and save handling of the modules in the purpose-built module test box (see section 3.6). It turned out that the degradation of the analogue APV signals, due to longer distances the signals have to cover, is negligible for hybrids and modules, whereas the mitigation of the common mode (cf. chapter 5.2) is substantial [43].

In contrast to its predecessor, the new ARC FE_M is equipped with two sensors, to measure humidity and temperature of the setup environment (cf. table 3.1). The high voltage connection including the grounding is also integrated in the design. A completely new feature enabled by the new design is the backplane pulse. Although the backplane pulse should be more attributed to the ARC board, it is only possible to supply this signal to the silicon sensor backplane with the ARC FE_M, because the first version of the front-end adapter does not support this feature.

¹⁹ERNI: ERNI is the provider of the connector. ERNI Elektroapparate GmbH, Seestraße 9, 73099 Adelberg, Germany. <http://www.erni.com>.

²⁰ARC FE_M: The M in the name indicates that this adapter is designed to be used mostly for module tests.

3.4 The LED Controller

The basic ARC system described so far can be extended by a LED controller *LEP16* to provide the opportunity to test modules with externally generated signals. Signals are created when the light shines on the detector and excites electron-hole pairs in the detector volume.

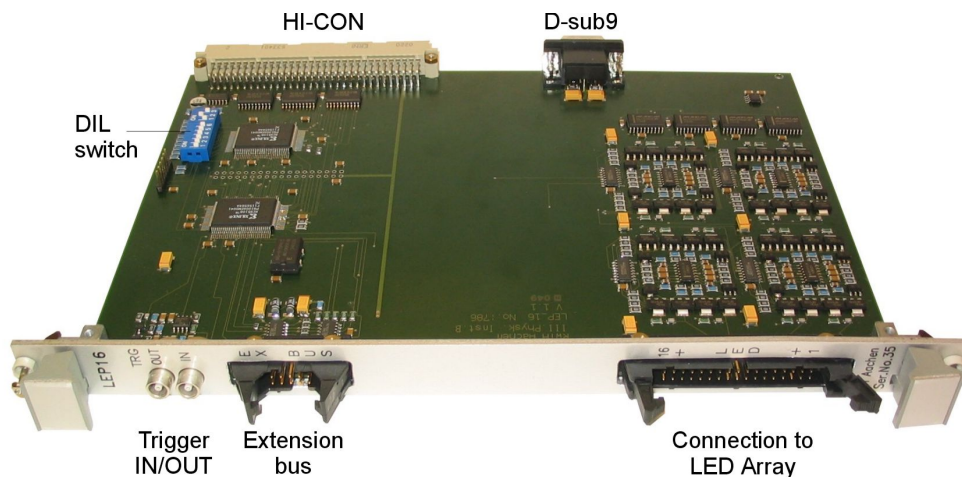


Figure 3.7: Photograph of a LED controller board LEP16.

3.4.1 The LED Controller Board

The LEP16 board, shown in figure 3.7, is a six layer printed circuit board in double Euro format. Like the ARC board it is powered by -5 V and $+5\text{ V}$ and all communication is done via the PCMIO bus. Accordingly the board is equipped with the same D-Sub9 and VG connectors as the ARC board. The board specific address for the distinction from other devices can be set via a ninefold DIL switch.

The LEP16 board has five registers to configure and control all board operations. The controller drives 16 LEDs with operating voltages of up to 5 V . The *intensity* of all LEDs can be adjusted via dedicated 8-bit DACs. The DACs determine the current generated by a current source in a range of 0 to 100 mA (see figure 3.8). This current is fed either into the LEDs or a resistor. Each LED can be switched on or off separately. Due to the characteristics of the LEDs, there is a nearly linear relation between the adjusted current and the adjusted current through the LED (see figure B.1, appendix B). If all LEDs are fully powered, an LED board requires slightly more than $16 \times 100\text{ mA} = 1.6\text{ A}$ on the $+5\text{ V}$ line.

Two major operation modes are supported by the LEP16 board, in which the LEDs are either *continuously* powered or *pulsed* on a trigger. This trigger can originate from three different sources. As in case of the ARC board, it is possible to trigger the board by *software*, by an *external* NIM pulse, or via the extension bus if the LEP16 board acts in slave mode. A third option is the *auto-repeat mode*. In the auto-repeat mode, the board perpetually generates trigger signals. The *repetition rate* ν_{rep} is adjustable in

a *clock divider* via an 8-bit register, holding a value n , according to the equation (3.1):

$$\nu_{rep} = \frac{40 \text{ MHz}}{512 \cdot (1 + n)}, \quad (3.1)$$

thus allowing rates between 300 Hz and 80 kHz. The *pulse length* is the same for all LEDs and can be adjusted in multiples of 25 ns steps in a range of 25 to 1600 ns.

When a trigger signal is received, it gets synchronized to the board internal 40 MHz clock. The synchronized signal is fed into a pulse length controller. Depending on the selected pulse length this controller switches the permanently flowing current onto the LEDs by fast differential amplifiers. This configuration allows to obtain fast switching times with a comparably slow current source.

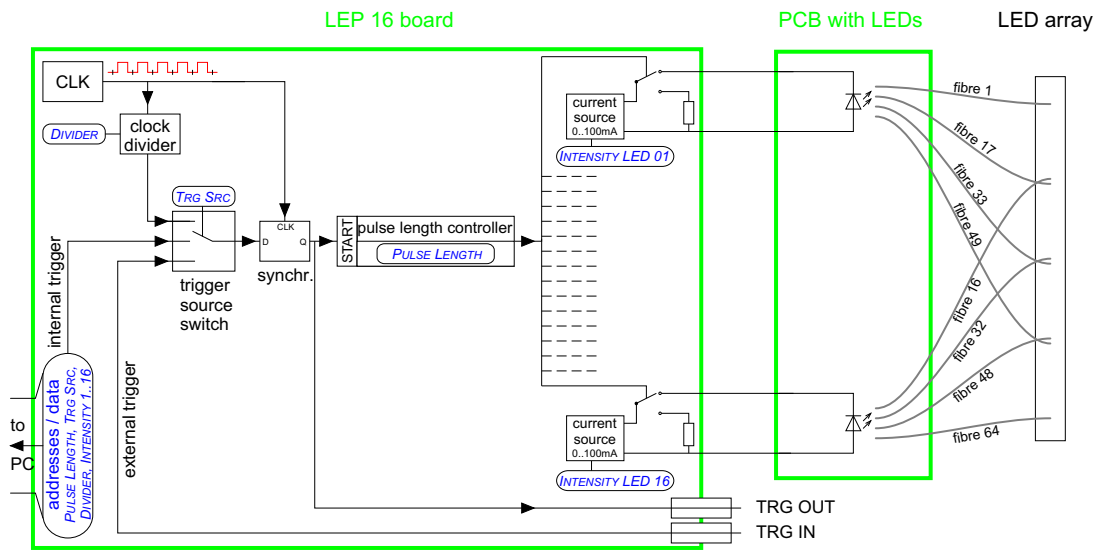


Figure 3.8: Block Diagram of a LED controller board LEP16.

Any trigger signal is also present on a trigger output to enable data acquisition time correlated to the light emission of the LEDs. Furthermore the LEP16 board can be operated in master or slave mode. In the first case the LEP16 board delivers clock and trigger information to other ARC system devices, in the latter case the clock and trigger information are delivered by another board operating in master mode.

3.4.2 The Choice of the LEDs

The LEDs used have to meet the requirements of a fast rising time, an appropriate wavelength, and a low price. Infrared LEDs of type OSRAM²¹ SFH 4501 were finally chosen, featuring a rising time of approximately 10 ns and a wavelength of 950 nm. Light with this wavelength has a penetration depth of approximately 50 μm in silicon. Electron-hole pairs are therefore mainly excited in the regime close to the sensor surface.

²¹OSRAM GmbH, Hellabrunner Straße 1, 81543 München, Germany. URL <http://www.osram.de>

Tests with LEDs of other wavelengths were also made. LEDs emitting light in the visible regime are also available to low prices. The intensities are sufficiently high and the rising times are short enough for all testing purposes. The disadvantage of these LEDs is the significantly smaller penetration depth of only some μm . This causes the release of all the charges in the uppermost region of the detector which is a bad approximation of real traversing MIPs.

LEDs with 1050 nm have an average penetration depth of approximately 400 μm . They are in principle better suited to imitate traversing particles but the collected signal is about a factor of ten smaller compared to the OSRAM LEDs.

3.4.3 The Transmission of Light to the Sensors

To avoid electrical crosstalk during the illumination with light, introduced by the LED supply current, the light is guided to the modules by *optical fibres* of about 1 m length. To allow for a reasonable link between LEDs and fibres, the LEDs are soldered on a small printed circuit board which is attached to the LEP16 board via a 34 pin twisted pair flat cable (16 \times 2 lines for the LEDs, 2 additional ground lines). An aluminium block with 16 holes is mounted on the printed circuit board, to hold the LED heads (see figure 3.9).

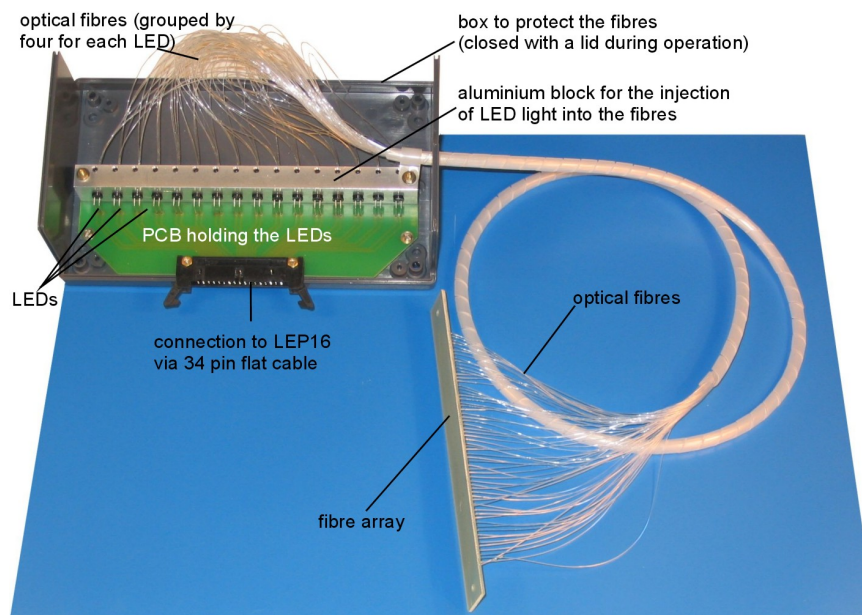


Figure 3.9: Printed circuit board, optical fibres and fibre array.

Four optical fibres with a diameter of 0.5 mm are glued in front of each LED head into the other open end of the hole, to pick up the light and to guide it to the other end of the fibre. In total, 64 optical fibres are used to illuminate the sensors. The fibres are arranged in a 64 \times 1 array, with a distance of 2 mm between two adjacent fibres. This array has to be mounted above the sensor surface. The total length of the array of 126 mm is sufficient to cover all types of sensors. The fibres connected to one LED are always separated by 15 other fibres, e. g. fibre 1, 17, 33, and 49. This partition

guarantees that two fibres belonging to one LED never illuminate strips belonging to the same APV. By this means, a signal saturation of the APVs is avoided.

The fibres are polished at both ends to enhance the injection of light into the fibres as well as the decoupling out of the fibres at the other end facing the sensor. The currents induced in a sensor due to illumination with the optical fibres can be compared to the direct illumination with a LED. From these measurements one can estimate, that only about 1–3 % of the light emitted by the LEDs reaches the sensor in the chosen design. Nonetheless this amount is sufficient to generate currents of 200 to 400 μA , depending on the particular fibre array and the illuminated sensor area. This is high enough for all testing purposes.

3.5 The High Voltage Controller

The high voltage controller DEPP²², shown in figure 3.10, is a four layer printed circuit board, in double Euro format as the ARC and LEP16 boards. It is equipped with two ports to supply two modules with the high voltage required to deplete the silicon strip sensors.

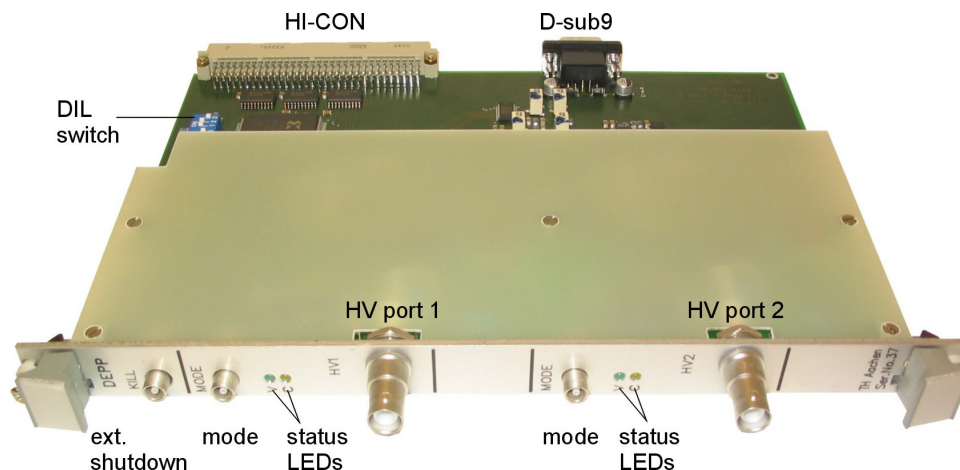


Figure 3.10: Photograph of a high voltage controller board DEPP. For reasons of safe handling the high voltage part is covered with an insulating plate.

The controller is fully compatible to the other ARC system components. The address switches, the connections to the PCMIO bus, and the power supply are identical to the ARC and the LEP16 board.

The controller offers three registers which are used to set different operation modes, to set current and voltage values, and to monitor the supplied voltages and currents.

The voltage supplied by the DEPP is floating. For that purpose, the high voltage and low voltage parts have to be completely decoupled on the board. The power between both sections is transmitted by a 1:150 transformer. To allow for a transformation the low DC voltage is chopped with a frequency of 180 kHz. Therefore voltages of

²²DEPP: *DE*pletion *P*ower Controller. The name indicates its usage as a device to deplete silicon sensors.

more than 600 V can be generated from the 5 V the board is supplied with. The sense lines measuring the high voltage and the current are decoupled from the low voltage part by insulation amplifiers. A block diagram of the DEPP voltage regulation circuit is shown in figure 3.11.

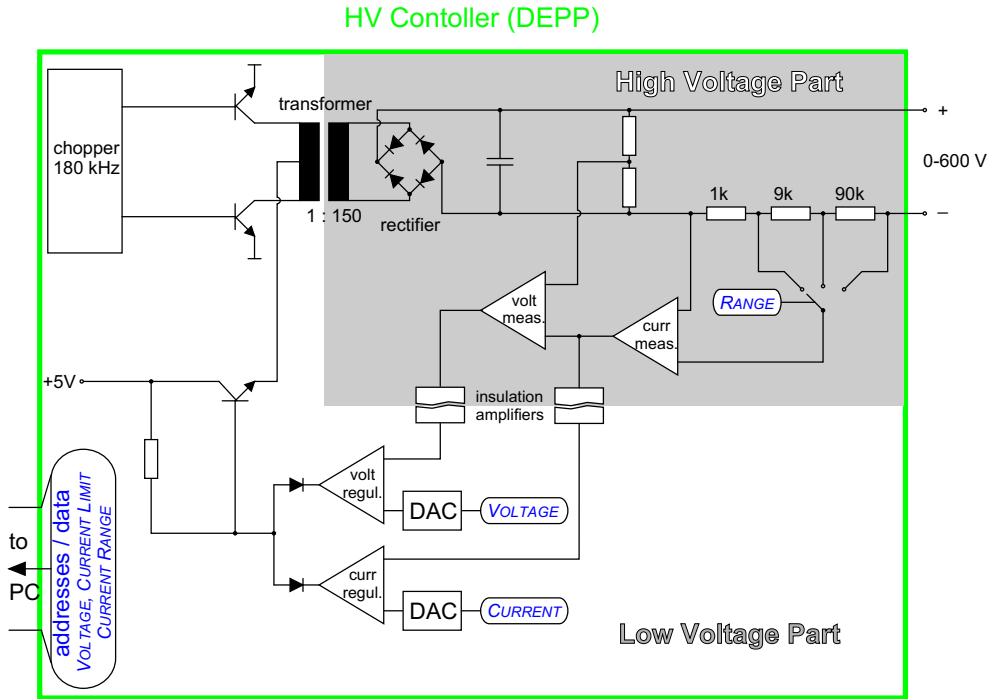


Figure 3.11: Block Diagram of the high voltage controller board DEPP. Board settings which are adjustable by software are encircled by oval boxes.

Both high voltage ports can be switched on and off separately. Voltages can be adjusted and measured by 12-bit DACs and ADCs respectively, in steps of 0.15 V in a range of 0 to 614.25 V. Current limits and supplied current values can be set and measured by 12-bit DACs and ADCs. Three different current ranges are available to allow very precise measurements of low currents as well as measurements of very high currents. Ranges and resolutions are summarised in table 3.2.

voltage adjustment/measurement		
	Range	Resolution
	0...614.25 V	0.15 V
current adjustment/measurement		
	Range	Resolution
Range 1	0...10.24 μ A	0.25 nA
Range 2	0...102.4 μ A	2.5 nA
Range 3	0...1024 μ A	25 nA

Table 3.2: The voltage and current ranges and resolutions of the DEPP board.

If for a particular test object the current exceeds the current limit set in the DEPP

board, the voltage will be decreased until the current falls below the threshold. This *current regulation mode* is indicated by a yellow light at the front panel of the controller. In contrast to that, a green light indicates the *voltage regulation mode*.

The maximum deviation between adjusted and supplied value is below 1 V. The safe operation of a silicon detector at high voltages requires a slow ramp up of the voltage of at most 10 V/s. This *ramping* has to be controlled by delays within the software.

For other applications than module tests, the DEPP provides the additional option to shut down the voltage immediately. This shut-down can be triggered either by an over-current or by an external shut-down signal received on the KILL socket of the DEPP.

3.6 The Single Module Test Box

To enable a safe and fast testing of a large number of modules in an environment providing the best possible electrical performance, a dedicated test box was developed²³. A photograph of a test box is shown in figure 3.12.

The box is built completely of aluminium and consists of a robust bottom plate, a chunk to carry the front-end adapter and a lid. Two oblong blocks of non-conducting plastic bars with slots on the side facing each other are mounted on the bottom plate to hold the module carrier. The fibre array is attached to these plastic bars at a distance of about 5 mm above the sensor. The box design was driven by the following aspects: *Grounding*: The grounding can be optimized by avoiding ground loops²⁴ and the use of short and thick cables with short signal running times and low resistances. Bottom plate, aluminium chunk, lid and the minus pole of the floating high voltage supply line are connected to the ground points provided by the ARC FE_M. The ground connection provided to the front-end hybrid of the module is also connected to the ground points on the front-end adapter. The module carrier plate is left floating. Its potential is determined by the contact to the graphite legs which are also connected to ground. The width of the common mode distribution (see chapter 5.2.3) was found to be the best measure to estimate the quality of the grounding. It is significantly reduced compared to the old test box design (compare [41]).

Light protection: To measure the thermally created leakage current one has to suppress any leakage current introduced by other types of electron-hole excitation, e. g. excitation by light. Therefore the whole setup is covered by an aluminium lid. Additionally all edges of the lid are surrounded by opaque drapery.

Protection against externally induced noise by electromagnetic radiation: Additional noise can be introduced by any type of high-frequency radiation which is omnipresent in a laboratory equipped with PCs, monitors, readout hardware etc. The lid of the setup closes the Faraday cage around the module under test. To improve the tightness

²³The test box was designed by Jan Olzem, I. Physikalisches Institut B, RWTH Aachen, and later slightly modified with respect to the noise performance.

²⁴If a point is connected electrically to ground via more than one connection, this is called a *ground loop*.

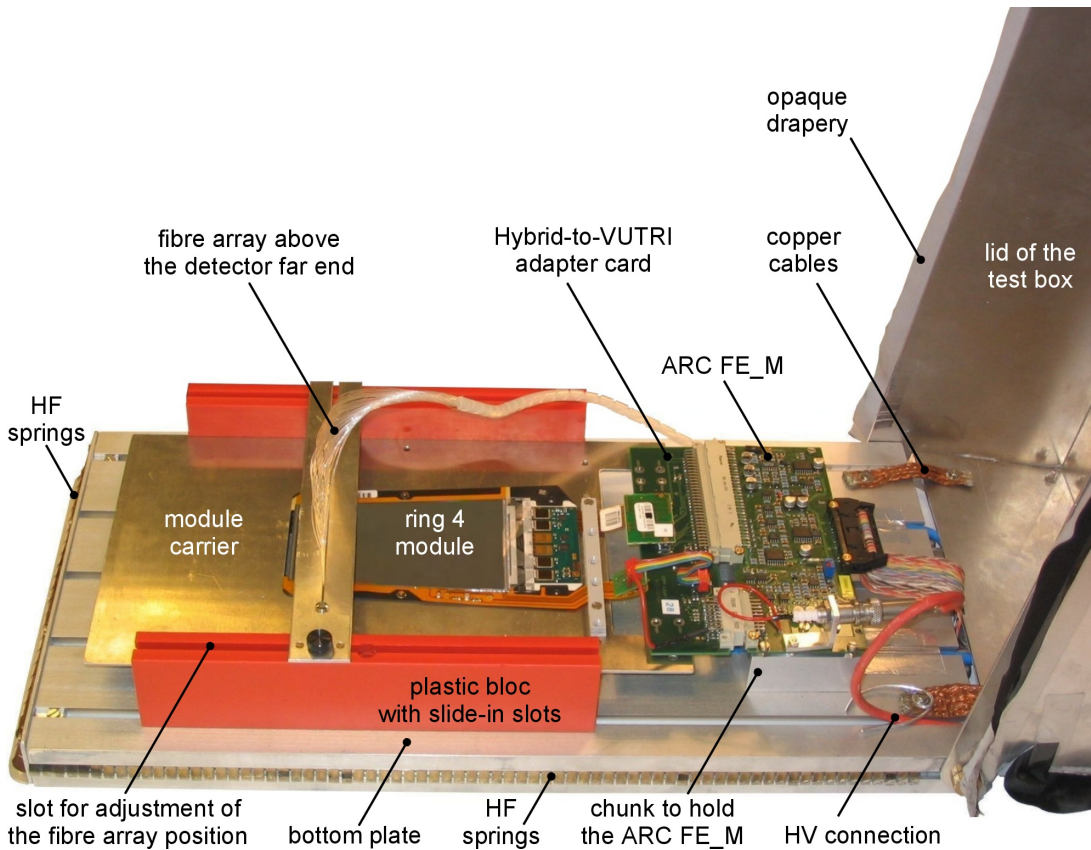


Figure 3.12: The test box used for single module tests. The feed pipes for the nitrogen are covered by the module carrier and thus not visible in the picture.

of the box with respect to high frequent radiation three sides of the bottom plate are surrounded by HF springs²⁵, while at the hinge-joint side the connection is established by two thick copper cables.

Safe handling of the modules: The slots in the plastic bars allow to slide in the modules very smoothly and provide sufficient fixation of the module during the test. Care is nonetheless indispensable during the plugging of the hybrid adapter card and the establishment of the high voltage connection, since these actions have to take place close to the front-end hybrid.

Relocatable fixation for the fibre array driven by the LEP16 board: A slot on the top side of the plastic bars allows to adjust the position of the array depending on the different lengths of the modules. This feature is especially of interest if modules of various geometries have to be tested. Since the ARC system and the setup performance had to be tested with as many different geometries as possible, this feature was of particular importance for the setup.

Dry air flow: To suppress surface currents flowing near the sensor edges it is recommended to do the tests in a dry air or nitrogen atmosphere with a relative humidity of

²⁵HF springs: *High Frequency* springs. The type used for the test box is usually used to shield sensitive electronics in racks.

less than 30 %. The test box comprises two 6 mm tubes which can be both flushed at the same time via a distributor outside of the box. Both tubes let the gas escape underneath the far end of the module, with respect to the hybrid and the ARC FE_M. This ensures that the sensor is exposed to the dry environment for a reasonably long time before the humidity sensor on the front-end adapter notifies a sufficiently low humidity.

3.7 Cold Box Setup

In order to enable module tests in a cold environment and to perform long term tests, a dedicated cold box setup was designed, including the cold box itself plus hardware and software for the temperature regulation and monitoring. The readout of the module data is done by the ARC hardware and software. Tests using the LED controller LEP16 are not possible since the lead-through and the handling of the fibres in the cold box would be too involved. The components of this setup will be described shortly in the next sections. Very detailed information of all components can be found in [43].

3.7.1 The Cold Box Design

A photograph of the cold box setup is shown in figure 3.13.

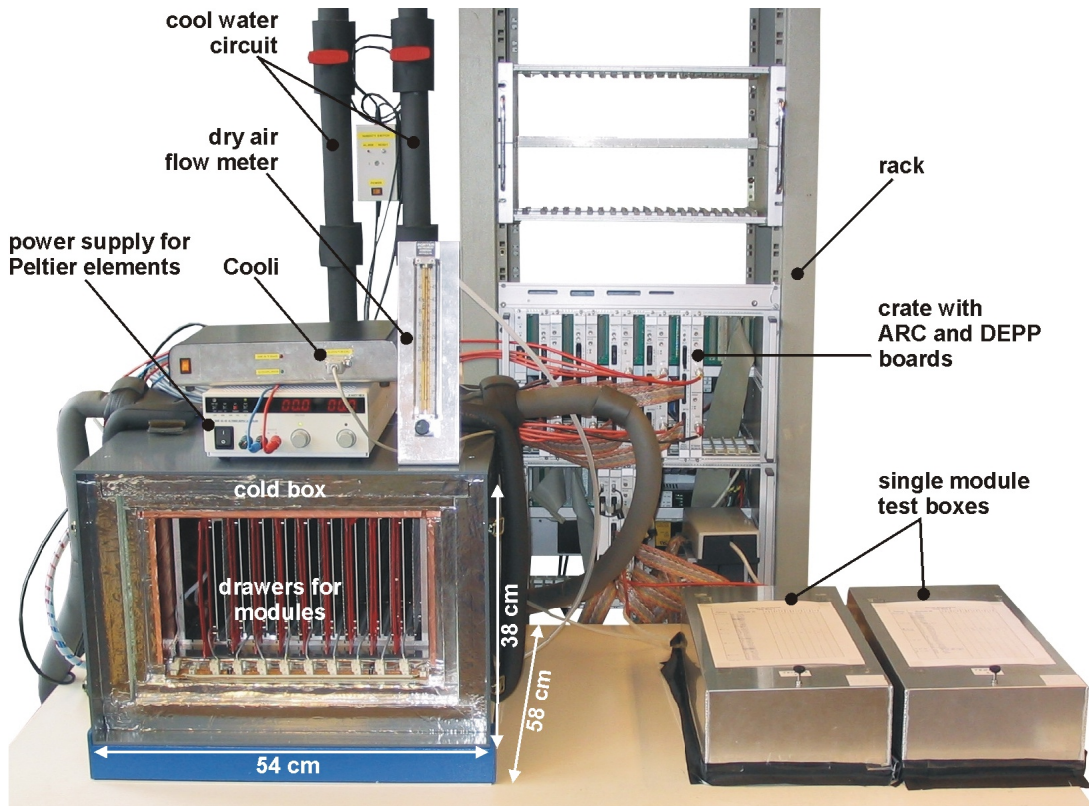


Figure 3.13: The cold box setup. At the right side also two single module test boxes are visible.

Its outer dimensions are $38 \times 54 \times 58 \text{ cm}^3$ (H \times W \times D). The cold box can cool down up to ten modules simultaneously. The cooling is done by two Peltier elements [44], one at the top and the second at the bottom of the cold box. They have a cooling power of up to 300 W each, depending on the temperature difference between both sides of the element. Heat dissipated from the inner part of the box is supplied to a cool water circuit. The insulation is established by 8 cm thick layers of Styrodur[®] C²⁶. To reduce externally induced noise due to electromagnetic radiation, the inner sides of the insulation are laminated with a copper foil to form a Faraday cage. In order to protect the modules from depositing frost due to solidifying humidity, the cold box is flushed with nitrogen during the whole time of cooling. A sophisticated pipe distribution system was thus implemented in the bottom side of the cold box.

The ten modules are read out by a system of five ARC boards which are connected to the modules by special extension boards through the backplane of the box.

The inner part of the box is made up of an aluminium cage which provides the thermal contact between the Peltier elements and the metal drawers in which the modules are placed during the tests. The cage is designed to be as light as possible to reduce the load to the cooling system, thus accelerating the time needed for cooling.

The tasks of the metal module drawers are manifold. Firstly they ensure a further shielding of the modules. Secondly they facilitate the handling of the modules within the box because all plug connections can be done outside the box. For that purpose, each drawer is equipped with a Hybrid-to-VUTRI adapter card which is tightly mounted in the drawer. Having installed a module outside the cold box in such a drawer, it can easily be pushed—with the adapter card first—into the proper counterpart of the extension board in the backplane. All drawers contain Copper-Beryllium springs to improve the thermal contact to the module carrier plate. The drawers are designed with the smallest additional amount of material, e. g. by using perforated aluminium plates. The perforated aluminium plates also facilitate the drying of the modules due to the nitrogen flow. Furthermore a Dallas sensor (cf. [45]) is part of each module drawer to measure the temperature inside.

3.7.2 Cold Box Control

The current flowing through the Peltier elements determines the amount of dissipated heat and thus the temperature inside the box. For this reason, the temperature in the box can be regulated by the Peltier current.

The large amount of heat of up to 600 W has to be dissipated at voltages below 24 V and requires therefore a power supply suited for high currents. This power supply must also provide a slow control interface to be able to set voltages and currents by appropriate signals defined in a cold box software. The chosen *Xantrex XHR 33-33*²⁷

²⁶The type used for the cold box are named 2800 CS and 3035 CS. Both are provided by the producer BASF, BASF Aktiengesellschaft, 67056 Ludwigshafen, Germany. URL http://www2.basf.de/basf2/html/plastics/englisch/pages/schaum/styrodur_techinfo.htm

²⁷Xantrex Technologies Inc., 8999 Nelson Way, Burnaby, BC, Canada V5A 4B5. URL <http://www.xantrex.com>

fulfils the current and voltage requirements and provides a RS-232 interface²⁸.

In addition to the Dallas sensors in the module drawers the cold box comprises two Sensirion sensors [46] which measure the temperature with an accuracy of better than 0.1 K²⁹ and the relative humidity to better than 0.1 %. Some further Dallas sensors inside the cold box determine environment parameters like the temperature of the Peltier elements. Both types of sensors are driven and read out by the *Cold Box Control Serial Interface* (Cooli), a dedicated interface built by the III. Physikalisches Institut B, RWTH Aachen. Values from these sensors are used for the regulation which is implemented in the ACDC³⁰ software. The ACDC software is written completely in LabVIEW³¹ and uses an adjustable PID regulation³² for the evaluation of the appropriate current. The calculated values are sent to the Cooli which routes it to the Peltier power supply.

The ACDC software cannot only send temperature data to the ARC software by an UDP³³ connection. It can even start measurements inside the ARC software as a part of a large long term test via a TCP/IP³⁴ connection. Both programs are usually running on two different networked PCs to improve the operation stability.

3.8 Multi Board Setup

In a multi board setup it is possible to run all boards with a synchronous clock. This can be achieved by switching one board to the *master mode*, while all other boards are operated in the *slave mode*. The clock of the master and also the trigger signals are then distributed to the slave boards via the extension bus. If the master board starts to send its trigger pattern, a signal is sent to all slave boards. The slave boards will send the trigger patterns stored in their trigger pattern buffer with a delay of 16 clock cycles with respect to the master board. This delay has to be compensated by either adapting the trigger pattern or the latency of the APVs.

An application of the multi board setup is a cosmic muon hodoscope consisting of five CMS silicon strip modules. This hodoscope was built up for the track prediction for a time projection chamber in the context of the International Linear Collider Experiment (see [47] and [48]).

²⁸RS-232: Recommended Standard 232, standardised serial interface of a personal computer

²⁹The accuracy of less than 0.1 K is only a repetition accuracy. This means if the sensor indicates the same temperature value in two different measurements the actual temperature difference in both measurements is less than 0.1 K.

³⁰ACDC: Aachen Cooling Device Control.

³¹LabVIEW is a graphical interface for the programming language “G”, invented by the National Instruments Corporation, 11500 North MoPac Expressway, Austin, Texas, USA.

³²PID regulation: Proportional, Integral, Differential regulation. A certain type of data evaluation, used to determine the optimum Peltier power supply current to reach a certain temperature in a very short time.

³³UDP: Unreliable Datagram Protocol.

³⁴TCP/IP: Transmission Control Protocol/Internet Protocol.

3.9 Usage of the ARC System in the Silicon Strip Module Production

The production of the CMS silicon strip tracker modules is distributed over many different locations (see figure 3.14). Partly finished modules are shipped several times from one to an other centre. Each component and the assembled module is labelled with a unique identification number (ID). The IDs are stored in the tracker database. Each shipment from one centre to another as well as all test results have to be transmitted by an XML file to the database. This is done to keep track of all parts that are used for the construction of the tracker.

The ARC system is used for all tests concerning the front-end electronics between the production of the hybrids in the industry and the integration of modules into larger structures. A completed module cannot be disassembled without a significant risk for the module components. Thus it is necessary to retest the hybrids or modules after a transport in the receiving centre to spot production problems and damages as early as possible. Thereby the number of defective modules can be minimized and expenses can be saved.

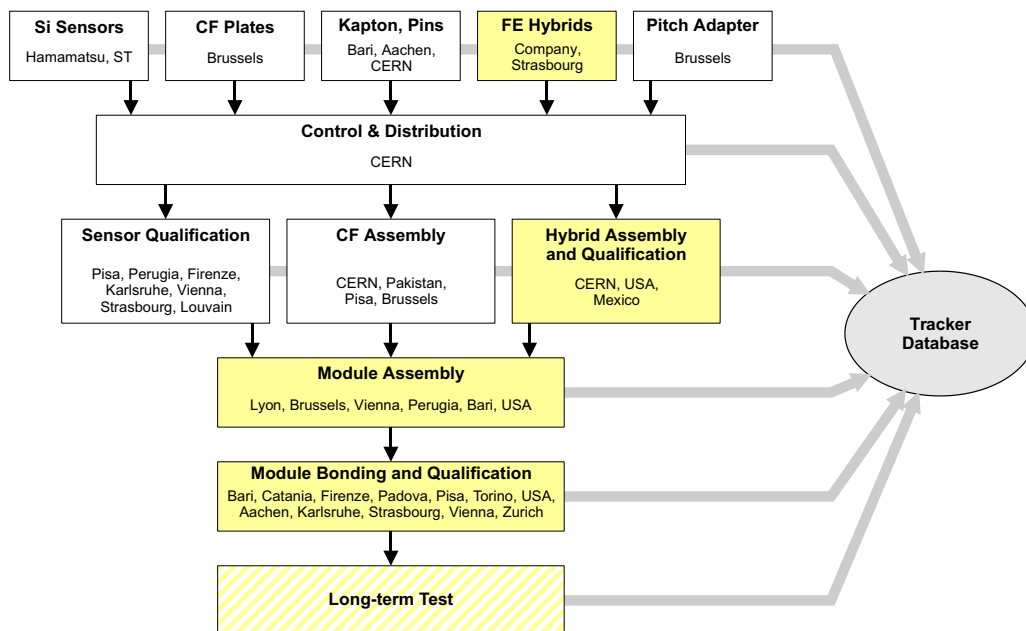


Figure 3.14: The production flow of silicon microstrip modules for the CMS tracker (according to [41]). Production steps that make use of ARC tests are filled in yellow. At each step test results or assembled components have to be reported to the central tracker database.

In the *industry* the ARC system is used with some additional hardware components in the FHIT system. Several ARC systems are utilized in *hybrid test stations*, for the qualification of hybrids after they are connected to the pitch adapter via wire bonds. In *module assembly centres* the sensors and hybrids with pitch adapter are glued on the support structure by the gantry robots. A short functionality test with the ARC

system prior to the assembly ensures that only fully functioning hybrids are used. In the *module bonding and qualification centres* the most extensive tests with the ARC system are made. In addition to the verification of the hybrid functioning also sensor and bonding failures can be found (cf. chapter 5 to 6). Defective strips can either be rebonded or unbonded on purpose.

Furthermore, many modules are tested at low temperatures in so-called *long term tests* for a period of about three days. Two different systems are utilised for that purpose. One of the systems is based on the ARC system (cf. section 3.7 and [43]), the other one is based on a setup that uses components similar to the final CMS tracker readout system³⁵.

In all steps, except the hybrid tests in the industry, automatic tests are performed with a specific ARC software which is explained in detail in chapter 4.

³⁵Long term tests of single modules are of particular interest in the commencing mass production. If these tests show that no severe problems occur at low temperatures, they can be skipped for the benefit of the mandatory long term tests of substructures, where many modules are tested at once.

Chapter 4

The APV Readout Controller Software

This chapter describes the functionality of the APV Readout Controller Software – ARCS.

The development of a dedicated ARC software started at the time the completion of the very first ARC board, as it became clear that it would be very difficult to refine and maintain the existing test readout program (cf. [49]). To achieve an easy to use test software, it was decided to build a software based on LabVIEW with embedded DLL¹ calls. The DLL functionality itself is based on C++ code. A first version of the software was released in March 2001, only two months after the completion of the first limited-lot ARC board production series. The first year of development concentrated on the implementation of comfortable interfaces to access all board features and all hybrid ASICs. A first version of a fast test for the industrial hybrid production was released. During the second year the extension from a hybrid to a module test system was achieved by the integration of the LED and high voltage controllers. A number of automated tests for different test procedures were also drafted and implemented. Feedbacks from a growing community of ARCS users helped to improve many tests. The third year brought significant improvements with respect to the handling of the data. Thenceforward all measured results were stored in ROOT² files. The incorporation of the ROOT software package allowed a detailed analysis of the test results at runtime. To create database compatible XML³ files a second software package was included, the XERCES⁴ package. An important step concerning steady, consistent measurement data was made by the automation of test sequences. The development during the fourth year focused on the analysis and combination of the numerous test results to subsume them to a trustworthy fault identification. The fast test, originally foreseen to be a fast

¹DLL: *Dynamic Link Library*. DLLs are linked with the executable program only at runtime. This allows to use the DLL functionality by several programs and to replace only the DLL in case of problems instead of the whole program which is of particular importance for larger software projects.

²ROOT is an object oriented data analysis framework. It is written completely in C++. It is freely available (<http://root.cern.ch>) and wide spread in the high energy physics community.

³XML: *EXtensible Markup Language*. It is an enhancement of the hypertext markup language (HTML). In contrast to HTML XML allows the definition of individual document types.

⁴XERCES is a package for XML parsing and generation. It is provided by The Apache Software Foundation, 1901 Munsey Drive, Forest Hill, MD 21050-2747, U.S.A. (<http://xml.apache.org/index.html>).

hybrid and ASIC test for the industrial hybrid production became a detailed ASIC and slow control test including a sophisticated data interpretation.

The field of application for the ARC software along with the ARC hardware is wide. It is used for all tests concerning the hybrid functionality, in particular at CERN. The version used there, is adapted to examine the behaviour of hybrids at temperatures down to $-25\text{ }^{\circ}\text{C}$ and to monitor the quality of all hybrids attached to pitch adapters before they are mounted on modules.

Immediately after bonding the sensors to the pitch adapter, so as soon as the hybrid electronics is linked to the sensor, the ARC system acts as a module test system. Its main purpose is to detect bad strips which influence the electrical behaviour of single strips and to identify their specific type. After the bonding at the bonding centres the module is sent to the integration centres where the larger substructures are assembled. There the module is shortly retested with the ARC system before it is incorporated into larger substructures.

The software is designed to perform all measurements and give an instructive fault identification with only a few number of handles.

The following sections of this chapter give an overview of the general software structure. Chapter 5 will explain all the automated test procedures in detail.

4.1 Software Structure

The programming code of the ARC software can be divided into two major parts:

- The *graphical user interface*, designed to receive user commands and for the graphical, acoustical, and textual output of test results, warnings, or other types of information. This part is completely implemented using LabVIEW.
- All *accesses to the ARC hardware*, including the data sampling and the slow control, as well as the subsequent *data analysis* is completely implemented using C++. The programming code is compiled to build a DLL which is linked to the LabVIEW code.

The LabVIEW part is compiled to a so-called LabVIEW application. LabVIEW applications have the advantage of being executable with a freely available runtime engine. Thus it is not necessary to purchase an expensive LabVIEW license to run ARCS. Since this runtime engine is available only for Windows⁵, ARCS is running on this platform only.

4.2 Data Acquisition in ARCS

The flow of information between the different software parts is visualized in figure 4.1.

Any action performed by the software is initiated by an action on the graphical user interface. The associated function call is first processed within the LabVIEW part

⁵Windows is a registered trademark of the Microsoft Corporation, One Microsoft Way, Redmond, WA 98052-6399, USA.

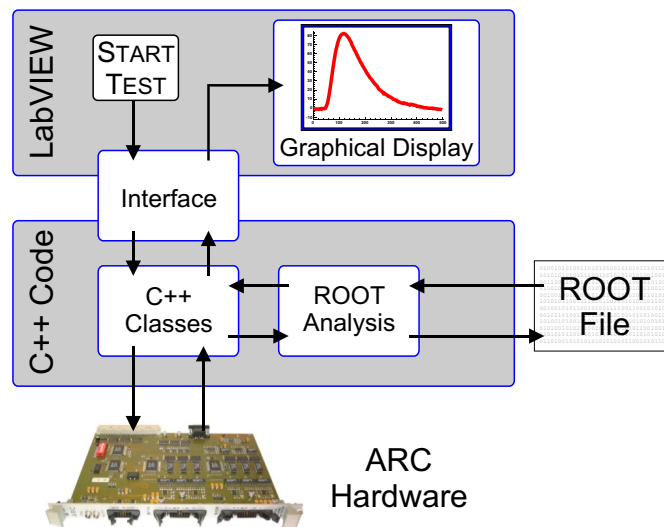


Figure 4.1: The general software structure of the ARC software. Pushing a **START TEST** button in the LabVIEW graphical interface initiates the data acquisition in the C++ code. Measured data are analysed in the ROOT framework and finally stored in a ROOT file. Furthermore the results are displayed in the LabVIEW graphical interface.

of the software. The function parameters are transferred to the C++ code. Within the C++ code the commands are distributed to a number of sub-procedures which start mostly with an access to the hardware⁶. In case of an automated test (cf. section 4.5) measured data are stored in the data containers in the memory until the end of all hardware accesses. Then the data samples are analysed, either by C++ routines or—if the analysis is more elaborate—with the ROOT package. All analysis results are written to one module specific ROOT file (cf. section 4.6) while the most expressive results are passed to the LabVIEW user interface to give information about the test results.

4.3 The Initialization

The first phase after launching the software is the initialization phase. This phase includes a scan for all ARC system components (ARC boards, LED controllers, and HV controllers) announced to the software by a configuration file. All components are distinguished by their corresponding addresses, set by the specific DIL switch on each board. If the predefined address does not belong to a board of the stated type a warning appears.

All ARC boards undergo a detailed *self test* (cf. section 5.9). A scan is performed for each I²C controller of an ARC board, to find all I²C devices which are connected to the respective controller. By this means, one can identify the I²C devices on the ARC front-end adapter used for the LV regulation and monitoring. Thus the software

⁶All types of hardware devices are represented by C++ classes.

detects the potential absence of a front-end adapter. The scan also identifies all ASIC devices on the front-end hybrid(s).

In case of a successful initialization the operator has to enter the module/hybrid identification number which is going to be assigned to the test object and the ROOT file. Afterwards, the initialization is finished and the operator attains to the monitoring mode.

4.4 The Monitoring Panel

The monitoring panel is the default display after the initialization. It serves two major purposes.

Firstly, and this is the main purpose, it allows the experienced user a sophisticated cause study in case of any problem that cannot be addressed to an ordinary fault. Among other things, it allows to repeat the initialization phase for a module. All I²C registers of all ASICs on a front-end hybrid can be set by convenient graphical interfaces. ARC board specific parameters, such as the trigger pattern, can be adjusted.

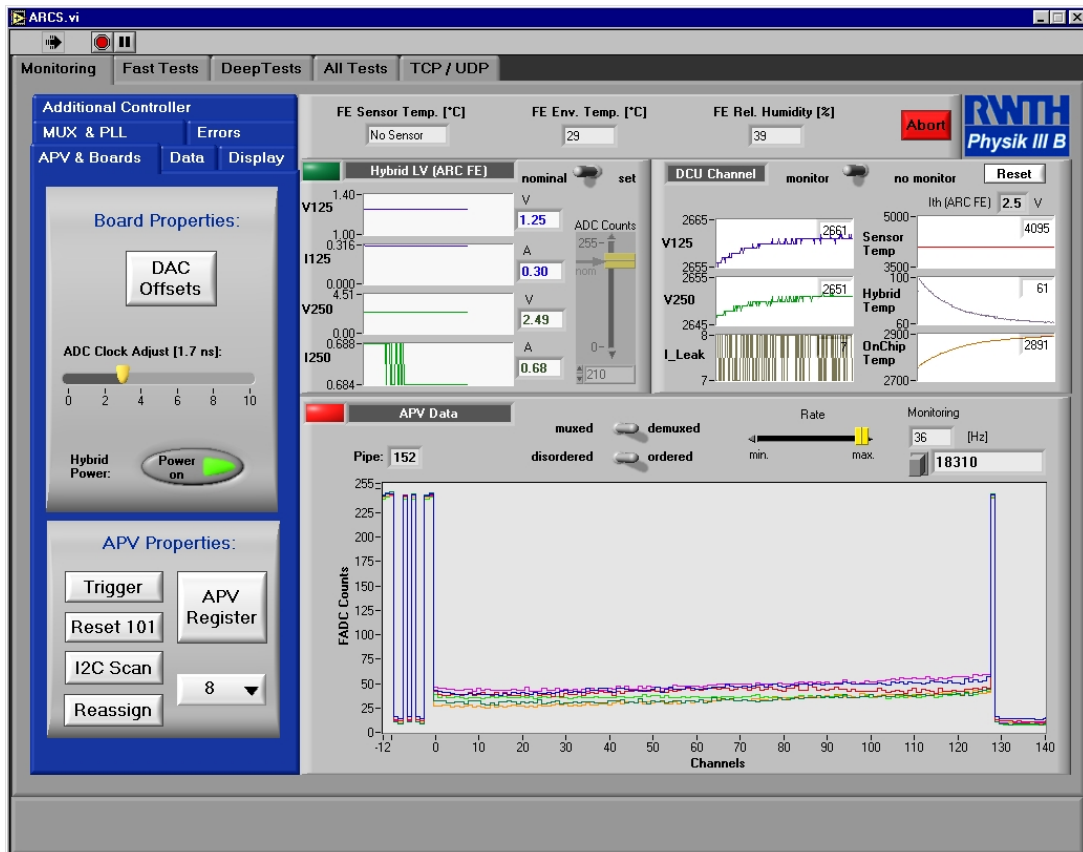


Figure 4.2: A screenshot of the monitoring panel of ARCS.

Dedicated graphical user interfaces can be launched for the LED controller as well as for the HV controller. They facilitate the comprehensive configuration of all opera-

tion parameters of both controllers which are described in chapters 3.4 and 3.5. Each of these interfaces is designed to control all connected controllers of a type.

Furthermore the monitoring panel provides graphical and numerical indicators for the monitoring of environmental parameters like hybrid currents, hybrid voltages, temperature, humidity, and DCU values. Excesses of (tunable) hybrid current or voltage limits are indicated by an optical warning signal.

Secondly, it gives the user an impression of the functioning of a chosen module under test. A functioning data acquisition is indicated by a rapidly updating display of APV frames. Problems in the data acquisition like asynchronously running APVs or header errors are visible in the display and additionally indicated by warning lights.

A screen shot of the monitoring panel of ARCS is shown in figure 4.2

4.5 Automated Test Procedures

The tests used for the qualification of hybrids or modules are highly automated. This applies to the data acquisition, the setting of test parameters, and the analysis of the measured data. For the assessment of module properties, a number of tests have been implemented in which data are acquired and pre-analysed automatically. These tests are described in detail in chapter 5. Different tests have different potentials to spot certain types of faults. For the qualification of a module, it is hence necessary to perform at least a minimum subset of tests⁷. This subset of tests determines the *standard module test*. For that purpose, ARCS comprises the so-called *all-test sequence*. During the all-test sequence, a number of specified tests with specific test parameters are performed automatically. The tests to be performed can be determined in a configuration file. Specific test parameters are read from a further configuration file. The automation guarantees the uniformity of test results in the sense that

- all relevant tests, needed to qualify a module, are made,
- all tests are performed with the appropriate settings.

During the all-test sequence, automated tests can be performed sequentially in the order given in table 4.1. The stated number of events represent mostly the settings used for a standard module test. Tests performed in a standard module test are marked separately. The time consumption for a standard module test is of the order of 25 minutes.

In general, all tests can be performed with a selectable number of events⁸ and in four different APV modes: peak mode with the inverter being switched on or off, or deconvolution mode with the inverter being switched on or off. Only some very specific tests utilizing additional controllers (pinhole test, LED test) are performed in only one APV mode.

⁷Feasible tests for a module qualification, test parameters, and environment parameters are specified in [50].

⁸The term *event* is here and in the following used in the meaning of reading out an APV frame on a trigger. It is neither used in the sense of a particle physics interaction nor in the sense of a detection of a charged particle traversing the silicon sensor(s).

order	test	acquired data	APV modes	part of standard module test	time consumption
1st	I-V test	0–450 V (45 steps)	–	yes	5:30 min
2nd	functional test	test dependant	–	yes	1:20 min
3rd	pedestal, noise, common mode	5000 events	all 4	yes	~ 2:00 min (4 × 0:30 min)
4th	pulse shape test	50 events/point	all 4	yes	~ 2:40 min (4 × 0:40 min)
5th	pipeline test	50 events/point	all 4	yes, only peak inv. on	~ 18:00 min (4 × 4:30 min)
6th	gain test	100 events/point	all 4	no	~ 2:20 min (4 × 0:40 min)
7th	backplane pulse test	100 events/point	all 4	no	~ 1:00 min (4 × 0:15 min)
8th	LED test	100 events/point	peak, inv. on	no	~ 0:30 min
9th	pinhole test	5 events/point	peak, inv. off	yes	~ 3:00 min

Table 4.1: Time consumptions for an all-test sequence with typical test parameters. The time data refer to a data acquisition with 700 MHz Pentium III personal computer.

4.6 The ROOT File

The data measured in a single test or in the automated test sequences can be stored in a ROOT file. The ROOT file is structured in directories. The base directory is a record (see figure 4.3). All tests in one record are considered as a coherent set of data, containing e. g. all data acquired at a specific date.

A record contains subdirectories for tests performed in different APV operation modes. A new record is created

- if a new all-test sequence is started,
- if data of a test in a certain APV mode are already present in the recent record to avoid overwriting the results of a previous test.

In the first case *consistent datasets* are created, i. e. the data of all specified tests are in one record. In the latter case data can be spread over several records if one of the measurements was done twice.

Each record contains four subdirectories for the storage of data measured in different APV operation modes. In addition, each record contains an “environment” subdirectory, a “header” subdirectory, and two subdirectories for module tests which are

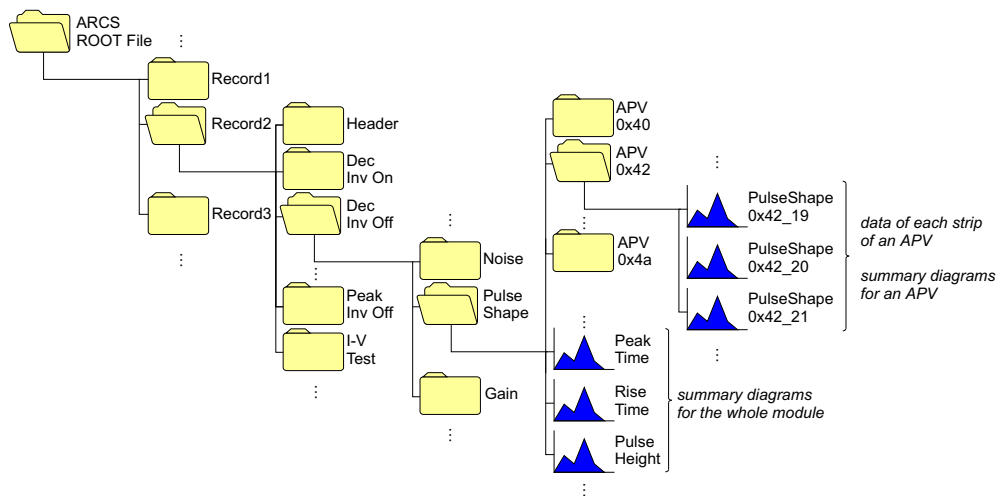


Figure 4.3: Illustration of the structure of the ARCS ROOT file.

not attributable to a specific APV operation mode (I-V test, functional test). Environment and header directory contain environmental information (e. g. temperature and humidity of the setup) and parameters of general interest (module specific identification number, version number of ARCS, date of test). The results of the tests are filled in specific subdirectories according to the APV operation mode the test was performed with. Each of these test specific directories contains subdirectories where the data of each APV (APV_0x40, APV_0x42, . . . , APV_0x4a) are stored. In addition, the most significant test results are summarised in diagrams which display the test results of the whole module are comprised in the test specific subdirectory.

4.7 Data Analysis in ARCS

The data analysis is intended for the search for typical signatures in the acquired data stored in the ROOT file. Certain signatures are used to identify a certain type of fault. The analysis should only be started after the results of certain tests are available in the ROOT file. This is expedient since in many cases a number of tests are needed for a safe identification of a certain type of fault.

Grading of Modules

The analysis has to assess the suitability of a module for the application in the CMS experiment. This suitability is expressed in a module *grading*. The criteria for this grading are defined independently from the specific method of data analysis (cf. [50]). They can be subdivided into

- *Criteria assessing strip-by-strip measurements:*
A module is grade A if the module has less than 1 % bad channels. A module is grade B if the module has between 1 % and 2 % bad channels. In both cases the

leakage current at 450 V $I_{Leak}(450\text{ V})$ has to be below $10\text{ }\mu\text{A}$ per sensor. Any module with more the 2 % bad channels is grade C.

- *Criteria assessing the module as a whole:*

A module is graded C if $I_{Leak}(450\text{ V}) > 10\text{ }\mu\text{A}$ per sensor. Moreover, a module is graded AF (BF) if it is a grade A (B) module and if $I_{Leak}(450\text{ V}) > 5 \cdot I_{DB}(450\text{ V})$, where $I_{DB}(450\text{ V})$ is the leakage current at 450 V from the sensor database. If the functional tests discovers a serious problem in the functioning or communication with an ASIC on the front-end hybrid, the module is also graded C.

Modules of grade A and B can be immediately used for the assembly of the tracker. Modules of grade A are used in regions close to the interaction point, with a higher density of particle tracks. If possible, modules of grade B are used in the outer regions of the tracker, where the density of particle tracks is lower and a worsened spatial resolution is tolerable. Modules of grade AF, BF, or C are used only in case of a lack of modules, if the respective position would stay unoccupied.

Analysis Sequence

The data analysis is decoupled from the data acquisition. It is performed by the so-called *XML Parser*, a program part that is integrated in the ARC software but also available as a standalone application. A decoupled analysis facilitates the re-analysis of data if the growing experience indicates that the data should be treated differently to improve the reliability of the data analysis. Only data in one record (cf. chapter 4.6) of the ROOT file are used for the analysis, since these data belong to one run of a module test.

The general flow of data between different program parts during the data analysis is illustrated in figure 4.4. Any analysis is initiated by an action in the graphical user

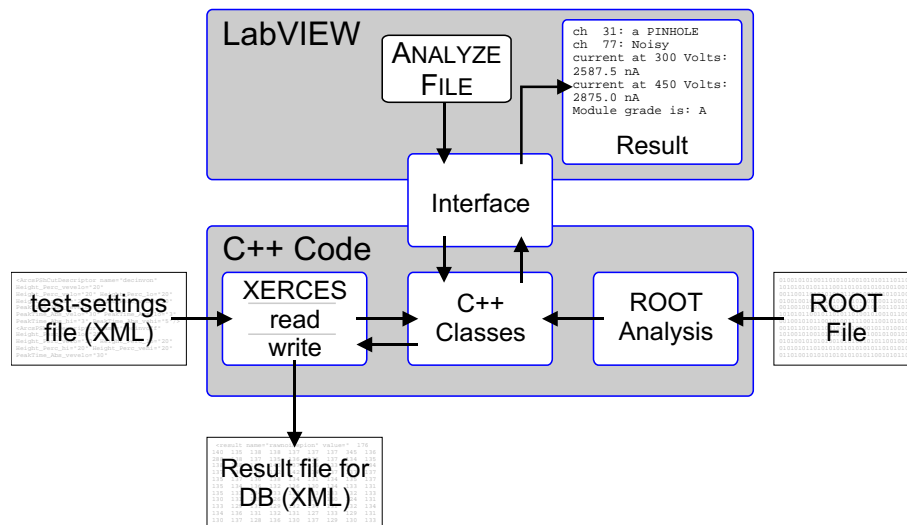


Figure 4.4: Principal overview of the data analysis part of the ARC software, the XML parser.

interface. Only the name of the ROOT file, the number of the record, and the name of a test-settings file are transferred to the C++ part. The C++ part includes the whole evaluation algorithm. The datasets needed for the evaluation are read from the corresponding record of the ROOT file. The limits used for the definition of the tolerable range of accepted values in a certain test are read from the test-settings XML file using the XERCES package. In case of an excess of such a limit, a definite *flag* for the respective channel is created. All channels with such a flag are considered as bad or faulty channels. After a whole sequence of single test evaluations, the respective flags can be combined. All ordinary faults show characteristic excesses in certain subset of tests. Thereby the type of fault can be determined. Chapter 7 will describe in detail how the data analysis works within the ARC software and which approach was used to optimize the limits as well as the combination algorithm. Any problem found during the analysis is reported in a textual output in the graphical user interface.

To transfer the most significant results to the CMS tracker database a special XML template file is filled. This file contains

- the specific module/hybrid identification number,
- environmental parameters, such as temperature and humidity of the setup,
- a link to the test-settings file used,
- exclusive results of single significant tests,
- a list of the faulty channels including their respective type,
- results of the ASIC functionality tests, and
- a final general grading of the module or hybrid.

The generated XML file can be transferred to the database with the *Big Browser* [51] database interface software.

Chapter 5

The Automated Test Procedures in ARCS

This chapter describes the data acquisition and data evaluation of all automated tests implemented in the ARC software.

5.1 The I-V Test

The I-V test is intended to assess the quality of the sensors as a whole. The leakage current is an important parameter with respect to the load expected for the high voltage power supplies in the final CMS experiment. Furthermore it is the major source of heat for the sensors, in particular after strong irradiation. Thus, it should be as low as possible.

5.1.1 Data Acquisition Procedure

The I-V test quantifies the total leakage current of a module as a function of the voltage applied. The power supply as well as the current measurements are performed with the DEPP high voltage controller (cf. chapter 3.5). To get significant test data it is recommended to keep the relative humidity below 30 % during the test and to do the test at room temperature (cf. equation (2.8)). The sensor has to be kept in a dark environment to suppress photon induced leakage current. The voltage is varied in up to 600 equally spaced voltage steps, starting at the minimum voltage. The current is measured at each step.

Between two steps the voltage is ramped up slowly, without exceeding a ramping speed of 10 V/s. After reaching a voltage step the software waits an adjustable time period (about five seconds) to allow for a stabilisation of the leakage current. This is necessary in particular at low voltages, where the capacitance of the detector increases with increasing bias voltage and gets charged up by the leakage current. After this holding time the leakage current is measured once. Thereafter the voltage is ramped to the next step. At the maximum voltage (600 V at most) the current is measured twice with a longer holding time between both measurements. This is done to observe

potential current fluctuations at the maximum voltage. After the test the voltage is not ramped down to zero. Since the I-V test is in general the first test to be performed it is more convenient to set a final voltage, appropriate for all subsequent tests.

An important aspect in the implementation of the I-V test was the protection of the sensor(s) from over-current. Thus a current limit determines the maximum current during the tests. In general, this maximum is 10 μA or below to enable the DEPP to be operated with its *best current resolution* (cf. table 3.2). In case of an excess of this maximum the voltage is ramped down to 0 V.

To learn how significant the excess was and to get the data of all other tests to assess the module quality, the measurement is repeated with a higher current limit and a worse current resolution (if the current limit exceeds 10 μA). This second limit represents the *maximum tolerable current* which can flow without impairing the detector. Only if this limit is exceeded before the maximum voltage is reached, the I-V test is finally aborted. In this case all further tests are skipped.

5.2 The Noise Test

The knowledge of the noise is important with respect to the expected performance of the detector. This performance can be quantified by the *signal-to-noise ratio* (cf. appendix B.3). The terms signal and noise will be specified in the following section (equations (5.6), (5.7)).

A more detailed analysis of the signal-to-noise ratio which makes use of the ARC system can be found in [52].

5.2.1 Data Acquisition Procedure

During the noise test a specified number of events are measured. For each event a randomly triggered pipeline cell is read. From the APV frames read (see figure 2.11) in event n the corresponding raw data belonging to channel ch are extracted. Subsequently these raw data are denoted as $RD_{ch,n}$.

5.2.2 The Noise Calculation in General

The *pedestal* P_{ch} of channel ch is determined by the mean value read from a certain channel, averaged over all events, from $n = 1$ to the total number of events N :

$$P_{ch} = \frac{1}{N} \cdot \sum_{n=1}^N RD_{ch,n}. \quad (5.1)$$

A typical pedestal of an APV is shown in figure 5.1. In general, the pedestal is not flat. This affects the operation of the modules in the tracker, since the dynamic ranges of channels with different pedestal vary by some percent. In most cases this feature can be further compensated by a shift of all pedestal values which is achieved by an adaptation of the APV register VPSP (cf. D.2).

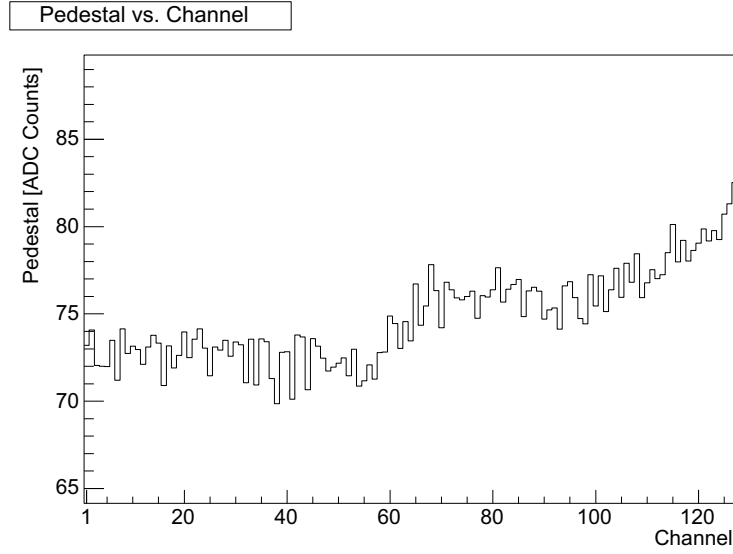


Figure 5.1: A typical pedestal of an APV. The pedestal is not flat. The y-axis uses ADC counts, measured with the 8-bit FADCs on the ARC board. On this axis the dynamic range of the APV reaches from approximately 5 ADC counts to 250 ADC counts.

The *raw noise* RN_{ch} of channel ch is the RMS¹ of the deviations of the raw data from the pedestal, calculated according to the equation:

$$RN_{ch} = \sqrt{\frac{\sum_{n=1}^N (RD_{ch,n} - P_{ch})^2}{N}}. \quad (5.2)$$

This noise computation discounts the fact that the average value of all channels of one APV can vary significantly from event to event. Such variations can be caused by e. g. small fluctuations on the power supply lines of the APV. The deviation of the average

$$AV_n = 1/128 \cdot \sum_{ch=1}^{128} RD_{ch,n} \quad (5.3)$$

over all channels of an APV in a single event n , from the average over all channels of an APV in all events

$$AV_{all} = 1/N \cdot \sum_{n=1}^N AV_n = \frac{1}{128} \cdot \sum_{ch=1}^{128} P_{ch}, \quad (5.4)$$

is in general called the *common mode* of event n and denoted as CM_n :

$$CM_n = AV_n - AV_{all}. \quad (5.5)$$

The *signal* $S_{ch,n}$ is defined as the difference between the common mode corrected raw data and the pedestal

$$S_{ch,n} = (RD_{ch,n} - CM_n) - P_{ch}. \quad (5.6)$$

¹RMS: The Root Mean Square of N measurements m_i , $i = 1 \dots N$ is defined as $RMS = \sqrt{\frac{1}{N} \sum m_i^2}$.

Thus the *common mode corrected noise* CMN_{ch} is given by:

$$CMN_{ch} = \sqrt{\frac{\sum_{n=1}^N (S_{ch,n})^2}{N}}. \quad (5.7)$$

A calculation according to equations (5.1) to (5.7) requires to keep *all* raw data in memory until the measurement is completed. This is of particular concern if computations are performed for many thousands of events and many modules in parallel. To save memory a calculation was implemented that approximates all aforementioned properties. The next section discusses this approximation.

5.2.3 The Noise Calculation in ARCS

The programming code used in ARCS for the calculation of pedestal, noise and common mode corrected noise is basically identical to the code used for the calculation of these quantities in the ORCA analysis package².

In ARCS a preliminary pedestal value $P_{ch,n}$ is calculated in each event and is updated with every new event according to

$$P_{ch,n} = \frac{P_{ch,(n-1)} \cdot (n-1) + RD_{ch,n}}{n}, \quad (5.8)$$

where $P_{ch,(n-1)}$ and $P_{ch,n}$ denote the preliminary pedestal values³ of channel ch based on the data of $(n-1)$ and n events respectively.

Therefore the noise computation starts only after the first 20 % of the events, when a stable pedestal value is established. The raw noise calculated in the event $(n-1)$, is used to determine the noise in the n -th event according to

$$RN_{ch,n}^2 = \frac{RN_{ch,(n-1)}^2 \cdot (n - 0.2 \cdot N - 1) + (RD_{ch,n} - P_{ch,n})^2}{n - 0.2 \cdot N}, \quad (5.9)$$

where $RN_{ch,(n-1)}$ and $RN_{ch,n}$ denote the raw noise of channel ch calculated after the $(n-1)$ -th and n -th event respectively.

Also the common mode is approximated with respect to this pedestal. In ARCS the common mode in event n is approximated by

$$CM_n = AV_n - AV_{1\dots n}, \quad (5.10)$$

where $AV_{1\dots n}$ is the average over all channels and all n events

$$AV_{1\dots n} = \frac{1}{128} \sum_{ch=1}^{128} P_{ch,n}, \quad (5.11)$$

²ORCA: *Object-oriented Reconstruction for CMS Analysis*, is a framework used for the reconstruction of collision events in the CMS detector. The code piece used for ARCS is identical to the `Apv_Analysis` in an ORCA 5 release written by Valery Zhukov, IEKP Karlsruhe.

³Apart from rounding errors the relations $P_{ch,n} \xrightarrow{n \rightarrow N} P_{ch}$ and $P_{ch,N} \equiv P_{ch}$ hold for all N .

and AV_n the average over all channels in event n (cf. equation (5.3)). Similar to equation (5.6) the signal $S_{ch,n}$ can be determined by

$$S_{ch,n} = RD_{ch,n} - CM_n - P_{ch,n}. \quad (5.12)$$

The computation of the common mode corrected noise $CMN_{ch,n}$ resembles the one of the raw noise:

$$CMN_{ch,n}^2 = \frac{CMN_{ch,(n-1)}^2 \cdot (n - 0.2 \cdot N - 1) + S_{ch,n}^2}{n - 0.2 \cdot N}, \quad (5.13)$$

where the result of event $(n - 1)$ is used to determine the result for event n .

Nonetheless, in ARCS the situation is bit more complicated. Instead of using all 128 channels of an APV for the common mode definition, the calculation is done in four groups of 32 neighbouring channels. Thus one has to distinguish between four values $CM_{n,g}$ for the four possible groups g . It turned out that this effort is advisable to get lower and flatter noise figures.

To compute the common mode correctly bad channels are excluded, since e. g. very noisy channels with large fluctuations affect the average of a whole group significantly. Therefore a single channel is excluded from the common mode correction if

$$|S_{ch,n}| > 4 \cdot CMN_{ch,n}, \quad (5.14)$$

$$\text{or } |S_{ch,n}| > 4 \cdot \frac{\sum_{ch=1}^{128} |S_{ch,n}|}{128}. \quad (5.15)$$

In both cases the channel is marked as noisy in the respective event. The number M_n of marks, counted until event n , is compared to the total number of events used so far for the noise calculation. If $M_n > 0.2 \cdot (n - 0.2 \cdot N)$, i.e. if the channel is marked as noisy in more than 20% of all cases, the channel is also neglected in the common mode correction. A further criterion can cause the exclusion of a channel from the common mode correction. This criterion is based on the consideration of the deviation $CMN_{ch,n} - \langle CMN_n \rangle$ of the common mode corrected noise of a channel from the average common mode corrected noise $\langle CMN_n \rangle$ of all channels:

$$|CMN_{ch,n} - \langle CMN_n \rangle| > 5 \cdot \sqrt{\frac{\sum_{ch=1}^{128} (CMN_{ch,n} - \langle CMN_n \rangle)^2}{128}}. \quad (5.16)$$

The common mode values in event n determined that way are recorded in a histogram with a bin width of 0.01 ADC counts for each group g of 32 neighbouring strips. Examples of common mode histograms for different APV modes and types of modules are depicted in figure 5.2.

For such a histogram one can determine the RMS of all entries. The respective value

$$WCM_g = \sqrt{\frac{\sum_n CM_{n,g}^2}{n}}, \quad (5.17)$$

with $CM_{n,g}$ being rounded according to the bin size, is (in this thesis) denoted as the *width of the common mode distribution of group g* . The bin wise sum of the histograms

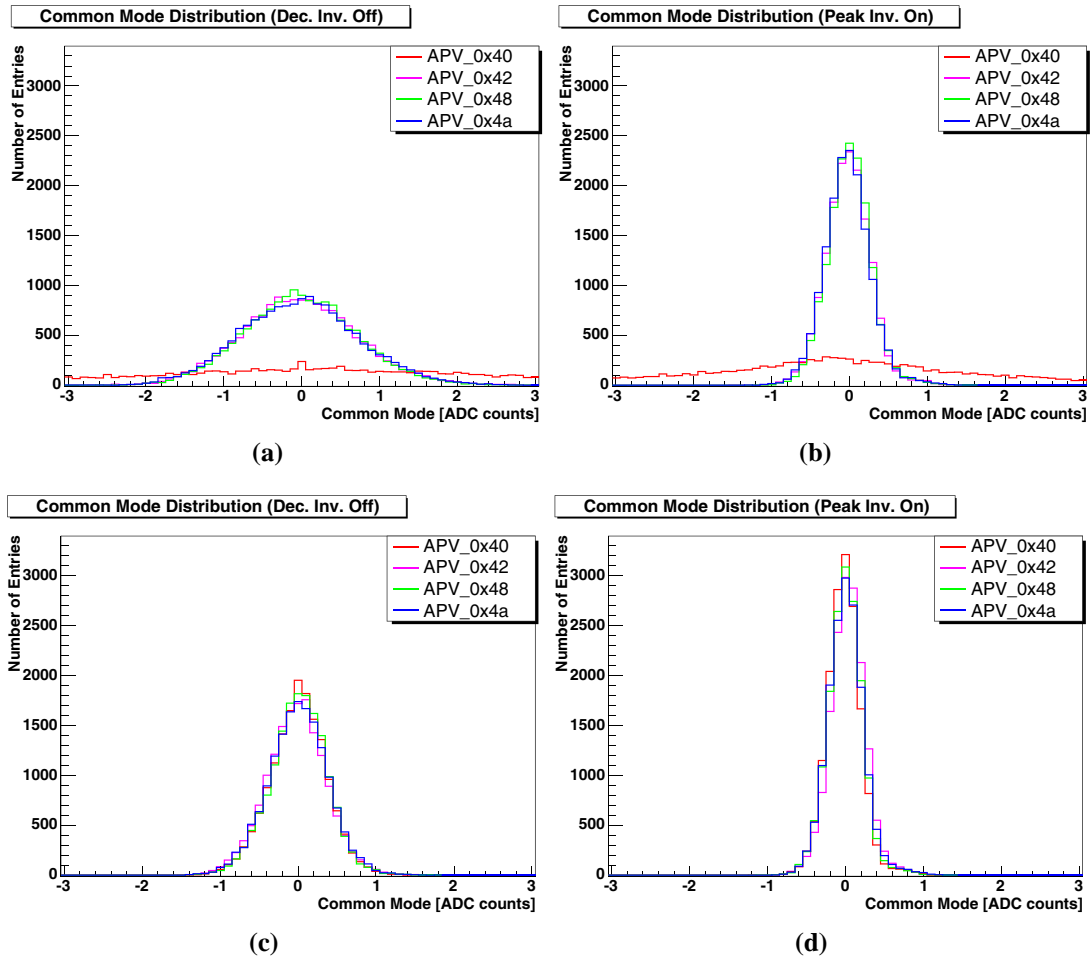


Figure 5.2: Common mode distributions. (a) A ring 6 module, deconvolution mode, inverter off. (b) The same ring 6 module, peak mode, inverter on. In both figures one APV (APV_0x40) has a large width of the common mode distribution. (c) and (d) The same measurements for a ring 3 module.

of the four common mode computation groups results in a fifth histogram. The RMS of that histogram is, though a bit oversimplifying, denoted as the *width of the common mode distribution*⁴ WCM .

All common mode histograms plus histograms for the pedestal, the raw noise, and the common mode corrected noise are stored in the ROOT file. The calculation of pedestal, noise, and common mode corrected noise is very fast. In particular it allows to query the values of all quantities simultaneous to the data acquisition, without any extra calculation. In ARCS all quantities are queried once per second. The results are displayed in the graphical user interface to enable the operator to assess pedestal and noise values already at runtime.

Both, the exact calculation and the approximated calculation converge to the same

⁴The term is equivalent to frequently used term common mode noise. In this thesis the term “width of common mode distribution” is used to have a clear conceptual discrimination from the common mode corrected noise.

value, as depicted in figure 5.3 showing the common mode corrected noise of a single

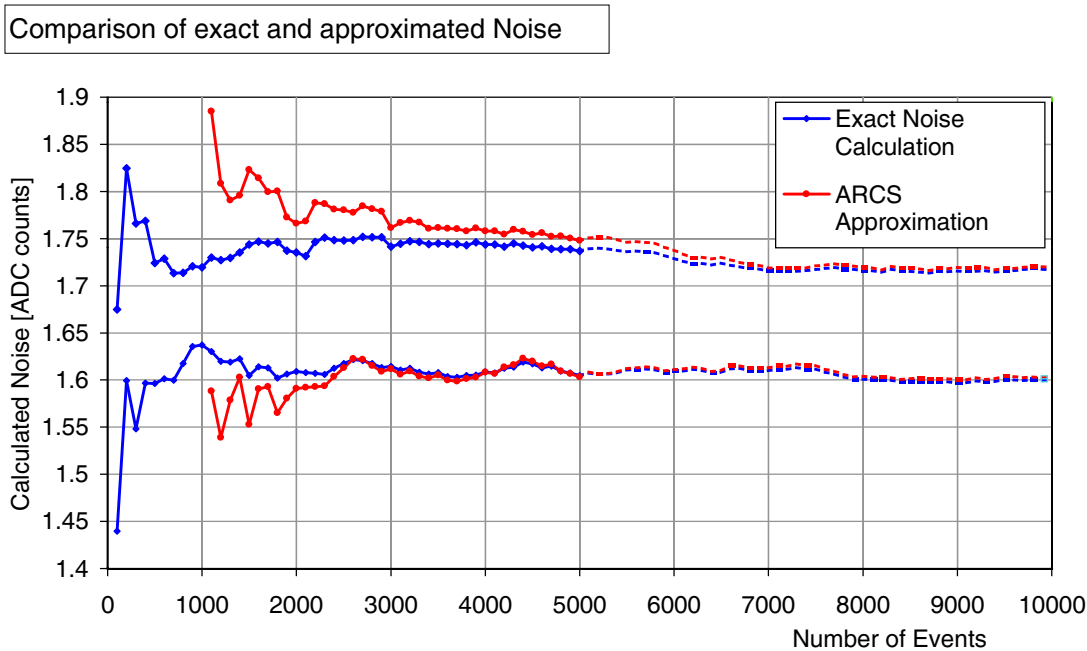


Figure 5.3: Comparison of the convergence of exact and approximated noise computation for two different channels. The approximated noise calculation starts only at 1,000 events, the point it would start in ARCS if 5,000 events were foreseen for the measurement. The noise results after every 100th event are displayed. After some thousands of events both values deviate less than 1%. Therefore 5,000 events are an advisable number to get a reliable, calculation independent result of the noise calculation. A larger number of events improves the agreement between both measurements furthermore, as indicated by the dashed lines from 5,100 to 10,000 events.

channel. The deviation between exact value and approximated values is of the order of 1% after some thousands of events. A comparison of the complete noise figures of an APV according to both types of calculations is shown in figure 5.4.

5.3 The Pulse Shape Test

The pulse shape test is one of the most complex tests with respect to the data acquisition procedure and the analysis of the measured data. It makes use of the APV internal calibration logic. The shape of the pulses is measured and evaluated. The purpose of the pulse shape test is threefold. First, it tests the calibration logic of the APV. Second, with a functioning calibration logic, the best point in time for the sampling of data from the respective module type can be deduced. Third, the test is the most sensitive one with respect to the capacitance connected to the APV input. This capacitance affects the measured shape noticeably. It is therefore suited to indicate module faults like open bonds, short-circuits, and pinholes, that change the strip capacitance.

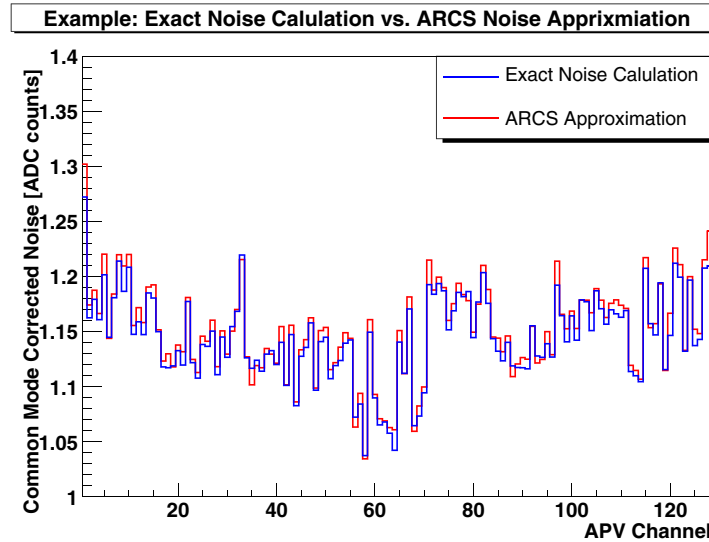


Figure 5.4: Comparison of exact noise computation and ARCS approximation after 5000 events. The average difference between the two measurements of a single channel are well below 1 %.

5.3.1 Data Acquisition Procedure

If the APV is running in the appropriate mode (Calibration Inhibit Off, cf. table D.1) a calibration signal is generated if the APV receives a trigger sequence containing the series 001100 (calibration request 11 with two preceding and two succeeding zeros). Since the APV calibration uses flip-flop circuits, the signal polarity switches with every calibration request. Thus a dummy request has to be generated between two measurements of a calibration signal, to get only pulses of the same polarity. The calibration pulse is a δ -like charge pulse injected in one of eight groups of APV channels. Each calibration group G ($G=0 \dots 7$) consists of 16 channels, all of which being separated by seven channels belonging to other groups, so for instance channels 1, 9, 17, 25... 113, 121 belong to one calibration group⁵. Therefore one has to switch at least seven times from one group to the other (APV register CDRV) to inject charge at least once in each channel. The pulses are amplified, shaped, and sampled by the APV (see section 2.5.3) and the results are stored in the pipeline capacitors.

If the APV receives a trigger like 00100, shortly after the calibration request (before the data are overwritten), the stored signal can be read. To read the pipeline cells containing the pulse data, an exact adjustment of trigger and latency is needed. An additional 0, preceding the trigger signal 1, delays the trigger signal by 25 ns. This can be balanced by increasing the latency by 1. During the pulse shape test a constant trigger pattern is used. Reading data from pipeline cells further in the past, thus requires a larger latency value. Therefore also the LATENCY register of the APV has to be changed several times to measure the full pulse. Up to 20 LATENCY steps are possible.

⁵In a more mathematical way one could say that all channels ch to which applies $ch \bmod 8 = G$ are members of group G , with G being an integer between 0 and 7.

To scan the pulse in more detail eight intermediate steps are possible per adjusted latency value to sample the calibration pulse in steps of 3.125 ns. Instead of shifting the trigger signal with respect to the clock, this is achieved by an adjustment of the time of calibration injection (APV register CSEL).

The whole acquisition sequence looks as follows:

1. A certain *latency* is *adjusted*. The pedestal P_{ch}^{lat} is measured under conditions where no calibration charge is injected (10 events).
2. For a chosen latency the appropriate *intermediate time step* is adjusted. This is done for all eight steps.
3. For a chosen latency and intermediate time step a *calibration group* G is chosen. This is done for all eight calibration groups.
4. For a chosen latency, intermediate step and calibration group G , a specified number of events is acquired. The average of these measurements $M_{ch}^{lat,csel}$ is the measured point of the pulse for the respective channel.

The *signal* $S_{ch}^{lat,csel}$ is in principle the difference between the measured point of the pulse signal $M_{ch}^{lat,csel}$ and the pedestal P_{ch}^{lat} . But due to an APV internal (partial) common mode correction the channels belonging to groups $\neq G$ perform a kind of “counter motion” when a signal is injected into group G . With respect to their pedestal (measured with no calibration pulse being present) they recognise a signal of opposite sign, compared to the channels hit by the calibration pulse. This opposite signal stems from a shift of the baseline of the APV (analogy to the common mode). Therefore the true signal amplitude for a channel of group G is

$$S_{ch}^{lat,csel} = M_{ch}^{lat,csel} - P_{ch}^{lat} - CM_G^{lat,csel}, \quad (5.18)$$

where $CM_G^{lat,csel}$ is the counter motion, that is calculated similar to equation (5.5):

$$CM_G^{lat,csel} = \frac{1}{112} \cdot \sum_{\{ch; ch \bmod 8 \neq G\}} (P_{ch}^{lat} - M_{ch}^{lat,csel}). \quad (5.19)$$

In addition to the signal $S_{ch}^{lat,csel}$ the signals $XT_{ch}^{lat,csel} = (M_{ch}^{lat,csel} - P_{ch}^{lat,csel})$ on the two neighbouring channels ($ch = n - 1, n + 1$) and the two next-to-neighbouring channels ($ch = n - 2, n + 2$) are measured whenever channel n is hit by a calibration signal. This is done to measure conspicuous *crosstalk* effects between two neighbouring and next-to-neighbouring channels, respectively.

The pulse shape test is comparably time consuming due to the large number of points to be measured per channel and due to many slow control accesses to the APV registers during the data acquisition.

5.3.2 Pre-Analysis of the Pulse Shape Data

A typical result of a pulse shape measurement in peak mode is shown in figure 5.5(a) together with the measured crosstalk on its two neighbours and two next-to-neighbours.

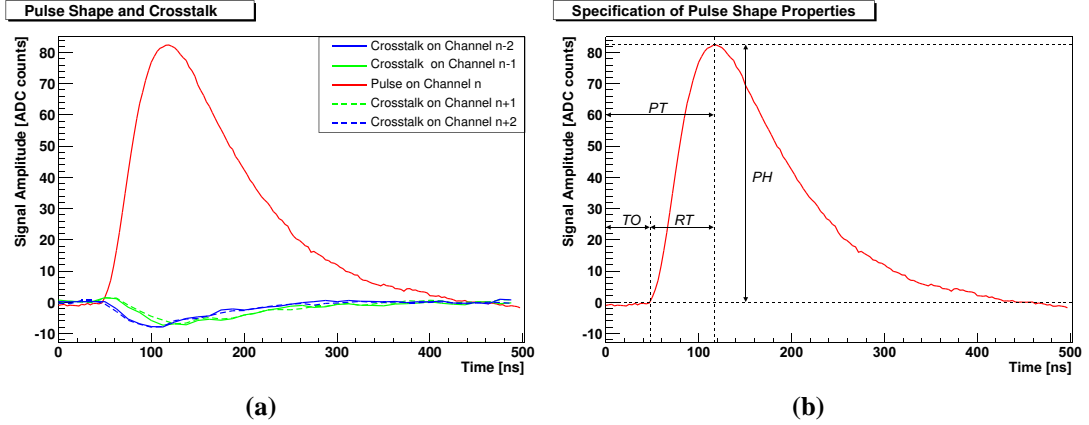


Figure 5.5: (a) Pulse shape and crosstalk in peak mode. the figure represents a measurement where the calibration pulse was injected into channel n . The green and blue curves demonstrate how the (next-to-)neighbouring strips are affected by a pulse injection into channel n . (b) The definition of pulse shape properties which are obtained from a fit.

Only the pulse shape datasets are analysed in detail using the ROOT framework. For each channel, in total four properties which describe the pulse, are extracted from the data with a fit⁶:

- The *pulse height* PH_{fit} is the extremal amplitude of the fitted shape (maximum if inverter is switched off, minimum if inverter is switched on).
- The *time offset* TO_{fit} describes the time between the start of the measurement and the intersection of the fitted curve with the zero line.
- The *rise time* RT_{fit} specifies the time between the intersection of the fitted curve with the baseline and the moment of the extremal amplitude.
- The *peak time* PT_{fit} is defined as the time that elapses between the start of the measurement and the moment of the extremal amplitude. $PT = TO + RT$.

Pulse height PH_{meas} and peak time PT_{meas} can also be obtained from the datasets as the extreme value and moment of extreme value.

Fit on the Peak Mode Data: In case of the peak mode the function

$$f_{peak}^{shape}(t) = PH_{fit} \cdot \frac{t - TO_{fit}}{RT_{fit}} \cdot \exp\left(1 - \frac{t - TO_{fit}}{RT_{fit}}\right), \quad (5.20)$$

⁶There is no error calculated for the single points the fit has to match. In such a case ROOT assumes a standard error of 1 for each point.

is used to fit the data. In [41] it was shown that this fit function describes the measured shape of the calibration signal for values of the APV register VFS below 120 only. Since standard test setting specify a VFS value of 60, this plays no role for standard module tests (cf. table D.3).

Fit on the Deconvolution Mode Data: Since the calibration signals in deconvolution mode are almost symmetrical, a Gaussian function can be used for the fit:

$$f_{dec}^{shape}(t) = PH_{fit} \cdot \exp\left(-\frac{1}{2} \cdot \frac{(t - PT_{fit})^2}{\sigma^2}\right). \quad (5.21)$$

Here the rise time is approximated as $RT_{fit} = PT_{fit} - 2.3 \cdot \sigma$. The quality of this fit is nearly independent of the APV register Vfs.

To prevent a fit from failing dramatically, only the region of ± 20 ns (deconvolution mode) and ± 30 ns (peak mode) around the extremal value is fitted. The extremal values PH_{meas} and their positions PT_{meas} are determined before the fit, based on the measured datasets. PT_{meas} is used as a starting point for the fit algorithm (so-called seed). If $|PH_{meas}| < 10$ ADC counts, no fit is applied at all. In that case, the pulse is treated as a flat line. In addition, it is required that the deviation between PH_{meas} and PH_{fit} does not exceed 10 ADC counts. If this is not the case the seed of the fit is varied with a small random offset and the fit is tried again. If necessary this procedure is repeated up to 200 times. If a reasonable match between PH_{meas} and PH_{fit} is not even obtainable this way, e. g. if a channel is extremely noisy, the pulse is also treated as a flat line and all properties are set to zero, to indicate a serious problem. This random variation procedure reduces the number of bad fits from $\mathcal{O}(1$ per module) to $\mathcal{O}(1$ per 100 modules).

The fitted pulse heights, peak times, and rise times are entered in diagrams vs. the channel number and stored in a ROOT data file. Typical results of such a pulse height and peak time measurement for a single APV are shown in figure 5.6.

The pulse height figure is not as flat as the peak time figure. This is caused by a voltage drop along the supply lines of the APV preamplifiers which affects the amplification, but not the time constants of the amplifier. A structure which recurs with every eighth channel is nonetheless visible in both pictures. This structure stems from slight differences in the injection circuits for the eight different calibration injection groups.

If a channel has a strong crosstalk with a channel hit by the calibration signal, an amplitude having the same sign as the calibration signal will be measured. For the determination of that sign it is sufficient to determine the sum over all crosstalk measurements of a channel. This sum has a different sign than channels without crosstalk which show the characteristic counter motion.

To save time the pulse shape is not measured over its full length, in general. Data are taken only in a region of about 50 to 100 ns before and 50 to 100 ns after the expected time of maximum amplitude.

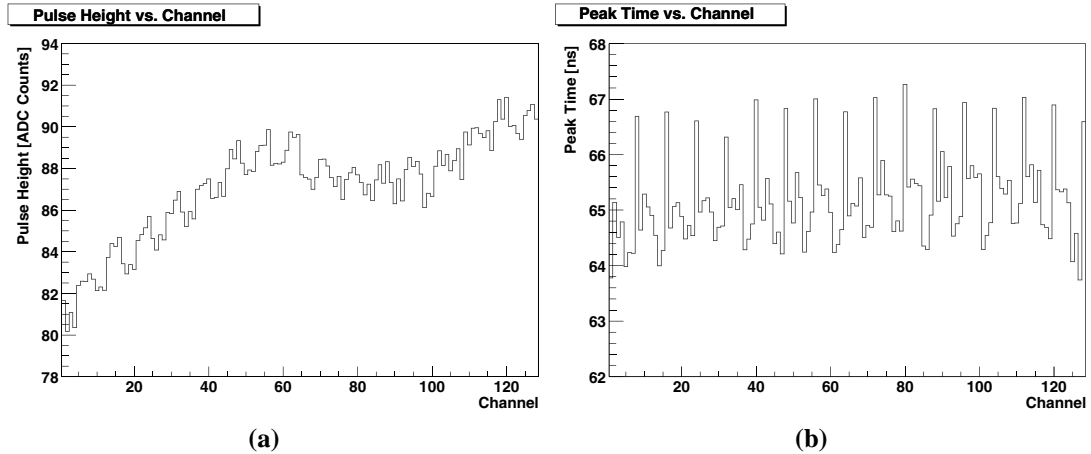


Figure 5.6: (a) A typical diagram of a pulse height measurement. A slight slope and the typical eight strip substructure are visible. The former is due to a voltage drop in the bias lines of the APV preamplifiers, the latter originates in the calibration circuit itself which injects a pulse in groups of 16 channel per APV. (E. g. channel 3, 11, 19, 27... are in one injection group.) (b) A typical peak time measurement of the same APV (here in peak mode). No slope is observable, but the eight strip substructure is well pronounced.

5.4 The Gain Test

The gain test is performed to measure the linearity of the gain of the APV input amplifiers. For this purpose a certain number of increasing charge pulses are injected by the calibration injection circuits of the APV. Ideally, the measured signals should lie on a straight line. The linearity of the amplification is important for the correct computation of the charge centre of gravity (see figure 2.3). A bad linearity worsens the spatial resolution or, if the linearity is bad in general but obeys a known relation, require a correction.

5.4.1 Data Acquisition Procedure

The calibration signal for different amounts of injected charge is sampled at a *fixed point in time* close to the maximum of the calibration pulse⁷. The amount of charge is determined via the ICAL register of the APV. The relation $n_{elec} = 625 \times ICAL$ holds, with n_{elec} being the number of electrons injected per channel. An accurate proportionality between adjusted ICAL value and injected charge is warranted up to an amount equivalent to 3 MIPs (corresponding to ICAL=120, cf. [53]). Using the APV calibration circuit requires to switch from one calibration group of 16 channels to the other groups, using the CDRV register of the APV (cf. section 5.3.1). Thus the whole data acquisition sequence looks as follows:

⁷As the position of that maximum is slightly dependent on the hybrid/module type, it is not guaranteed that the maximum is exactly met.

1. A certain ICAL value is set to inject a certain amount of charge with every calibration request. This is done for a number of equally spaced points between a minimum and maximum calibration signal.
2. For a chosen amount of charge injection one has to switch through all eight calibration groups to measure the signal on all channels for a specified number of events.

The signal measured for a channel belonging to a group hit by the calibration pulse has to be corrected for the counter motion of the unaffected channels. This correction is equivalent to the one explained in equations (5.18) and (5.19).

Unlike in the pulse shape test, channels neighbouring a channel hit by the calibration signal are not considered. A further difference is, that the flip-flops of the calibration logic are triggered such that the measured signals are always positive, independent of the inverter setting.

5.4.2 Pre-Analysis of the Gain Test Data

The datasets measured represent points in a plane spanned by the calibration charge (ICAL value) and the measured signal. A linear fit function

$$f(I_{cal}) = SL \cdot I_{cal} + OS \quad (5.22)$$

is applied to the data (see figure 5.7(a)), with I_{cal} representing the ICAL value, SL the slope of the fitted curve and OS its offset (intersection point with the ordinate). The fit routine also returns a χ^2 value⁸. This χ^2 value can be used to assess the linearity of the data.

A typical result of a gain slope measurement is shown in figure 5.7(b). As in all measurements facilitating the calibration logic, a structure recurring with every eighth channel is visible. A slope comparable to the one of the pulse height (see figure 5.6) can be seen. This matches the expectation, since both measurements are affected by the voltage drop along the supply lines of the APV preamplifiers.

5.5 The Pipeline Test

In all other tests mentioned in this chapter, datasets are distinguished only with respect to the channel they are assigned to. In fact the data are read from 192 different pipeline cells belonging to the respective channel. Averaging all measurements for a channel could hide defective pipeline cells which might either be dead, very noisy, or have a significantly different pedestal. The test was implemented to find such cells.

⁸The χ^2 is based on the assumption of a single point error of 1. This assumption is made since no error is specified.

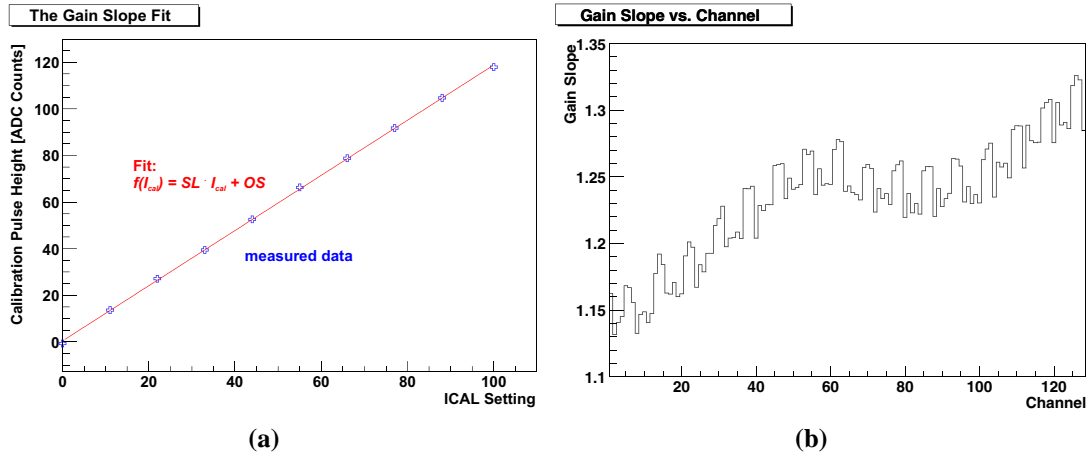


Figure 5.7: (a) A linear fit is applied to the data points measured during a gain test. (b) A typical result of a gain slope measurement. A slope comparable to the one of the pulse height measurement (see figure 5.6(a)) is visible. In fact the data belong to the same APV of the same module, operated in the same mode.

5.5.1 Data Acquisition Procedure

The pipeline test consists of two different measurements. The first one is an adapted pedestal and noise test. The second one measures the signal from a pipeline cell hit by the calibration pulse. This gives a good criteria for dead channels.

Pipeline Pedestal and Pipeline Noise

To permit the acquisition of data from a specific pipeline cell it is necessary to reset both the read and the write pointer of the APV pipeline. This is obtained by a reset 101 sequence on the trigger line. Upon processing of the reset the write pointer is switched from one pipeline column to the following one every 25 ns, beginning at column 0⁹. With a delay defined in the APV LATENCY register the pipeline read pointer follows. If the trigger, a single 1, follows the reset 101 with a *fixed time distance* (which has to be larger than the adjusted LATENCY) *only one specific pipeline column PC* will be triggered, according to the relation

$$PC = N_{ckl} - \text{LATENCY} - C ,$$

where N_{ckl} is the number of clock ticks (number of zeros) between reset and trigger and C is a constant time needed within the APV to process the reset. In ARCS a fixed latency is used. The access to the desired pipeline column is thus regulated by means of an adaptation of the spacer of the trigger pattern. The trigger pattern

$$\underbrace{101}_{\text{reset}} \underbrace{0.0000}_{\text{highbyte}} . \underbrace{(PC + 23)}_{\text{spacer}} . \underbrace{0000.000}_{\text{lowbyte}} \underbrace{1}_{\text{trigger}}$$

⁹The pipeline column addresses range from 0 to 191.

is used to access the pipeline column PC in peak mode ($PC = 0 \dots 191$). In deconvolution mode the 23 has to be replaced by a 21.

For an adjusted spacer the measurement is repeated for a specified number of events. Since this procedure has to be repeated for all 192 pipeline columns the test is very time consuming (cf. table 4.1). The number of events sampled per pipeline cell is thus quite low ($\mathcal{O}(10 - 100)$).

The Pipeline Calibration Amplitude Test

The pipeline calibration amplitude test measures the calibration pulse height at a fixed point in time of the pulse, close to the maximum of the pulse, as in the gain test (cf. section 5.4). To access a specific pipeline column it uses the same principle as the pedestal and noise pipeline test. The high byte of the trigger pattern contains again the reset 101 used to reset read and write pointer of the APV matrix. The decisive difference is, that the low byte contains the calibration request 11 and the trigger 1. The whole trigger sequence used is

$$\overbrace{00\ 10.1\ 000}^{\text{highbyte}} \cdot \overbrace{(PC + 19)}^{\text{spacer}} \cdot \overbrace{\underbrace{11}_{\text{cal. req.}}\ 00.000\ \underbrace{1}_{\text{trigger}}}^{\text{lowbyte}}, \text{ in peak mode}$$

and

$$0101.0000. (PC + 19) .1100.0001, \text{ in deconvolution mode.}$$

Constant CSEL and LATENCY values are set throughout the test (LATENCY = 4 and 7 in peak mode and deconvolution mode respectively). These settings ensure a sampling of the calibration signal close to its maximum in all APV modes. Since no space was left in the trigger pattern an additional dummy calibration request has to be sent after the aforementioned trigger sequence to toggle the calibration injection flip-flops.

5.5.2 Pre-Analysis of the Data

Pedestal and Noise Data

The raw data for each pipeline cell are treated like the raw data of a single channel in the pedestal and noise approximation algorithm described in section 5.2.3. This algorithm returns a pedestal and common mode corrected noise value for each pipeline cell. Since the number of events used in the test is very low, the noise calculation starts only after the first 30 % of the events. The results are stored in a *matrix*. An example of a noise matrix of an APV is shown in figure 5.8(a). Comparably large fluctuations are evident even for an individual channel. They can be smoothed only at the expense of a higher number of events per cell and a much longer testing time. The test can thus only be used to find cells with a significantly different noise.

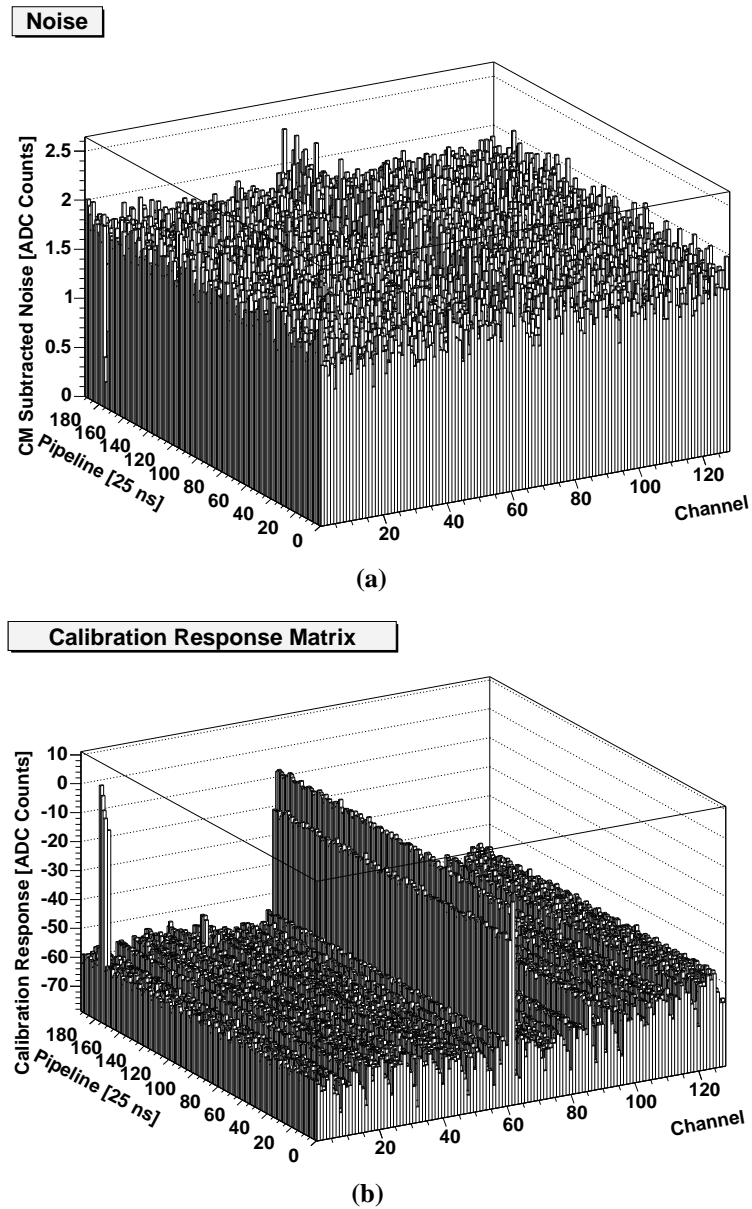


Figure 5.8: (a) Example of a noise matrix. The pipeline cells of column 163...166 of channel 1 have significantly lower noise. (b) Example of a calibration amplitude matrix of the same APV. Since the results origin from a measurement with activated inverter, the signals are negative. The pipeline cells of column 163...166 of channel 1 show only very small response to the calibration pulse and can thus be called dead cells. All pipeline cells of channels 61 and 62 show only a small response to the calibration signal. But in this case a short-circuit, present between both strips, is the reason.

Pre-Analysis of the Pulse Amplitude Data

The average calibration amplitude for each pipeline cell is stored in a calibration amplitude matrix. Dead cells show no or only a weak response to a calibration pulse injection. An example of a calibration amplitude pipeline matrix is shown in figure 5.8(b).

5.6 The LED Test

The idea of the LED test is, to have a measurement with signals coming from an external source which is independent from the APV internal calibration logic. For that purpose, the test makes use of the LED controller LEP 16 (cf. chapter 3.4). A signal in terms of a short infrared light pulse can be induced everywhere along a strip by a proper adjustment of the fibre array above the sensor(s) perpendicular to the strip direction (see figure 3.12). The measured signal size should be independent of the position of the fibre array. If it is not so, this can be an indicator for a problem along the strip between the APV and the position of the fibre array. In principle the test is thus suited to determine the position of an open bond or a mid-sensor-open along a strip quite exactly. Anyway, it is too involved to move the fibre array during a test. Since other tests provide the same information without any mechanical movement, the LED test is mainly used for reasons of redundancy. The fibre array is in general positioned furthest away from the hybrid, about 5 mm above the sensor.

5.6.1 Data Acquisition Procedure

Charge signals have to be of a short duration to be recognised as signals. Thus the LED Controller has to be operated in *pulsed mode*. During the LED test the LEP 16 runs in *auto-repeat mode* and delivers the *trigger signal for the ARC board* via a LEMO cable connecting the respective trigger ports of both boards.

The duration of the pulse is adjusted to 500 ns with a rate of about 400 Hz. Thus the impact of the illumination on the total leakage current of the module is negligible. The sampling point of the data is 100 ns after firing the LEDs, when the light emission has reached a stable value¹⁰. This is done to measure in some time delay from the rising edge of the light pulse and to be more independent of the runtime of the trigger signals over the cable. Due to the APV internal common mode correction it is not possible to measure a signal on all channels at a time. Therefore only one LED illuminates the detector during the data acquisition in a single event through four optical fibres. Due to the distribution of the LED light to four separate optical fibres, strips belonging to one APV are exposed to the light of one fibre at most.

At the beginning of the test the pedestal value P_{ch}^{dark} is determined for each channel ch , while the detector is not illuminated. Then the first LED is switched on and a given number of events are sampled. For each channel the pedestal P_{ch,LED_1} is computed, specifying the average data measured while LED_1 illuminated the detector with pulsed

¹⁰The nominal rise time of the LED signal is 10 ns.

light. Then the first LED is switched off, the second is switched on, and the pedestal values P_{ch,LED_2} are determined, and so forth.

The data acquisition ends when all pedestals P_{ch,LED_i} , $i = 1 \dots 16$, corresponding to the 16 LEDs, are measured.

5.6.2 Pre-Analysis of the LED Test Data

For each of the LEDs the signal S_{ch,LED_i} is computed, that was present when the respective LED shone, according to the definition

$$S_{ch,LED_i} = \begin{cases} 0 & , \text{ if } P_{ch,LED_i} - P_{ch}^{dark} \leq 6 \\ P_{ch,LED_i} - P_{ch,dark} & , \text{ else.} \end{cases} \quad (5.23)$$

This definition removes very small signals to facilitate later fits¹¹. Such a signal S_{ch,LED_i} for a fixed i and $ch = 1 \dots 128$ is illustrated in figure 5.9(a).

Due to the in general Gaussian-like shape of the signal a Gaussian function can be used to fit the signal data. An evolved algorithm treats cases where the light pulse shines only on some edge channels of an APV. In such a case also a parabolic fit is used, if the χ^2 of the Gaussian fit is unsatisfactory. From the fit function one can extract the expected signal S_{ch,LED_i}^{fit} for a channel ch illuminated by LED i .

An envelope curve can be defined for both, the measured and the expected signals, if the maximum for all 16 LEDs is determined for each channel:

$$Env_{ch} = \max\{S_{ch,LED_i}; i = 1 \dots 16\}, \text{ for the measured signals,} \quad (5.24)$$

$$Env_{ch}^{fit} = \max\{S_{ch,LED_i}^{fit}; i = 1 \dots 16\}, \text{ for the expected signals.} \quad (5.25)$$

The difference between both envelopes should be close to zero because the measured signal should almost agree with the expectation. A significant difference is an indicator of a defect channel.

5.7 The Pinhole Test

5.7.1 Function Principle of the Pinhole Test

As the name of the test implies, this test is dedicated to the detection of pinholes. If a pinhole is present on a strip, the APV input and the p⁺-implant of that strip are connected via the aluminium strip and the pinhole itself. If the resistance of the pinhole is small, the APV input potential is thus forced to match the potential $V_{p^+,ch}$ of the corresponding p⁺-implant.

¹¹If a value is 0, this value is ignored in the fit routine, whereas a value $\neq 0$ would influence the fit. An open, for example, between the fibre array position and the hybrid would avoid the recognition of a signal in the corresponding channel. One would thus measure a signal S_{ch,LED_i} close to zero, where a higher signal would be expected. To predict the expected signal correctly the channel must be disregarded.

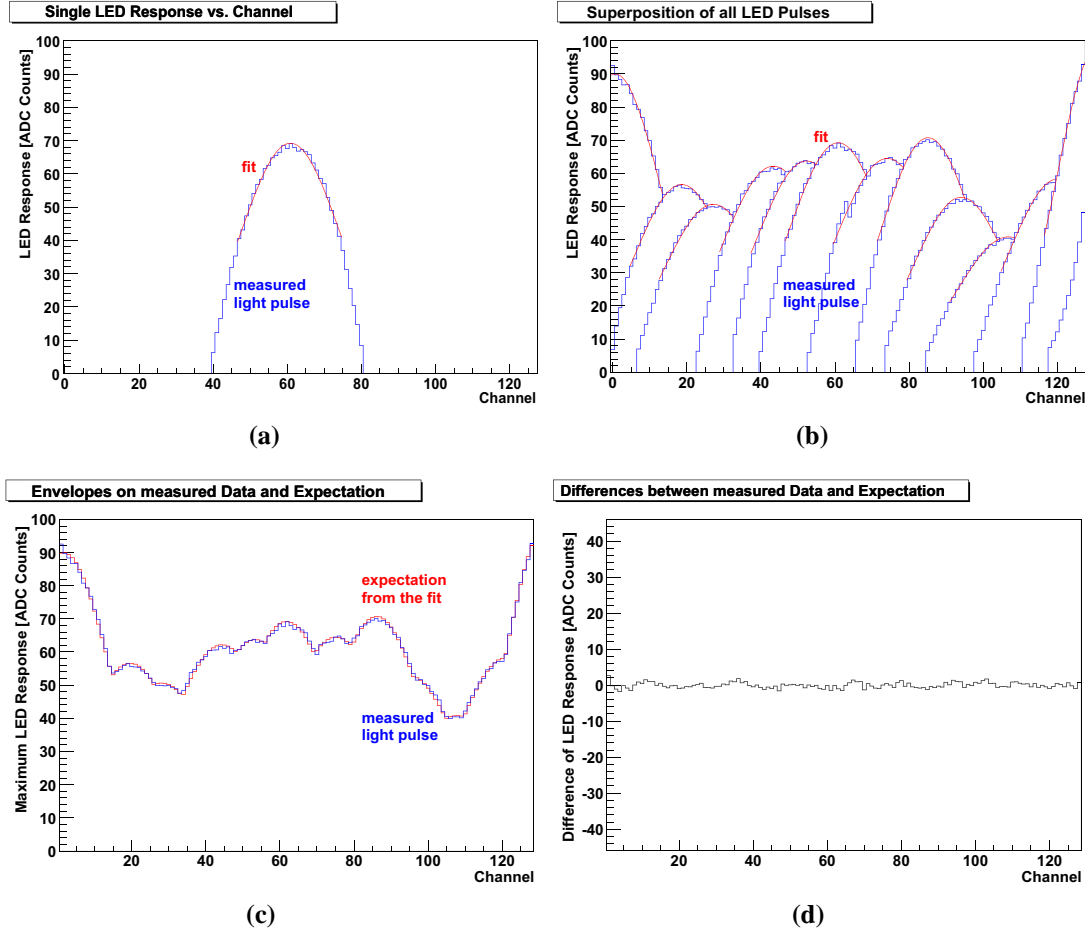


Figure 5.9: Illustration of the data processing in the LED test. (a) The data S_{ch,LED_i} for a single LED represent the region of the sensor illuminated by the LED. A Gaussian fit is applied to the data. (b) The superposition of the data of all LEDs. (c) The maximum envelope of the measured data and the expectation from the fit. (d) The difference between measurement and expectation gives a flat line for normal channels.

The p^+ -potential can be subdivided into two contributions. One is associated to the voltage drop across two external resistors, the other one to the voltage drop across the bias resistors of the strip.

The voltage drop across the two external resistors determines the potential V_{ring} of the bias ring of both sensors (see figure 5.7.1).

V_{ring} depends on the total module leakage current I_{leak} flowing through both sensors and the external resistors. Two resistors are connected in series on the front-end hybrid and switched in the high voltage return line between the bias ring and ground. One of these resistors is the 681Ω shunt resistor of the DCU (resistor R_S in figure 2.13), the other one is a $2.2 \text{ k}\Omega$ resistor. The potential of the bias rings can be calculated by:

$$V_{ring} = (I_{leak,S_1} + I_{leak,S_2}) \cdot 2.881 \text{ k}\Omega, \quad (5.26)$$

with I_{leak,S_i} , $i = 1$ or 2 , being the leakage current through the sensor i . Since both bias

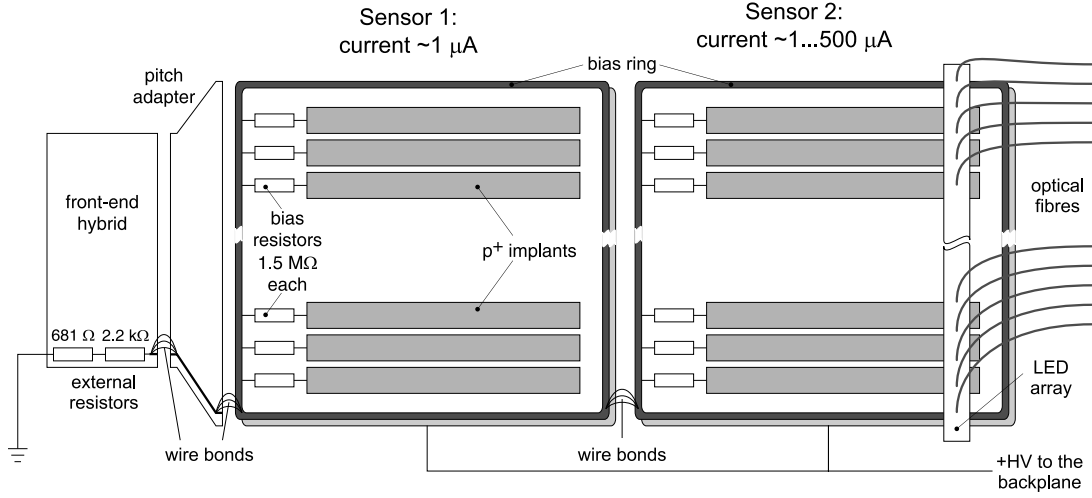


Figure 5.10: The pinhole test is based on the fact, that the potential of the p^+ -implants depends on the leakage current. Two contributions to that potential can be distinguished, originating from voltage drops across external resistors and bias resistors. The leakage current is influenced through different amount of light delivered by the fibre array.

rings are connected via micro bonds they have the same potential.

The potential of an individual p^+ -implant depends on the voltage drop across the bias resistor between the implant and the bias resistor, and the potential of the bias ring itself. The voltage drop $\Delta V_{ch,S_i}$, with i being 1 or 2, depends only on the leakage current through strip ch of sensor i . Assuming that all channels participate equally in the leakage current of a sensor the individual strip current can be estimated by

$$I_{ch,S_i} \approx \frac{1}{N_{strips}} \cdot I_{leak,S_i}, \quad i = 1 \text{ or } 2, \quad (5.27)$$

where N_{strips} is the number of strips of the sensor and I_{ch,S_i} is the single strip leakage through a strip ch of sensor i . Assuming a value of the bias resistor of $1.5 \text{ M}\Omega$ the voltage drop can be expressed by

$$\Delta V_{ch,S_i} = I_{ch,S_i} \cdot 1.5 \text{ M}\Omega \approx \frac{I_{leak,S_i}}{N_{strips}} \cdot 1.5 \text{ M}\Omega. \quad (5.28)$$

This voltage drop depends only on the leakage current through one sensor. The potential $V_{p^+,ch}$ of the p^+ -implant of strip ch on sensor i is the sum of the bias ring potential and the bias resistor voltage drop. It can be approximated by:

$$V_{p^+,ch} = V_{ring} + \Delta V_{ch,S_i} \quad (5.29)$$

$$\approx (I_{leak,S_1} + I_{leak,S_2}) \cdot 2.881 \text{ k}\Omega + \frac{I_{leak,S_i}}{N_{strips}} \cdot 1.5 \text{ M}\Omega. \quad (5.30)$$

If a pinhole is present on a strip the operating point of the amplifiers of the APV input lies on that potential $V_{p^+,ch}$. A shift of the potential by some hundredth of a volt has a

noticeable impact on the amplification of a signal. This impact is measured during the pinhole test. This is done by measuring the calibration pulse amplitude as a function of the leakage current. Only at a leakage current that effectuates an implant potential close to the nominal 0.75 V, the APV will measure the normal signal height.

The leakage current can be influenced by the illumination with infrared light of different intensities generated by the LEP 16 controller. Due to the fact that the fibre array is in general arranged above the sensor which is further away from the hybrid, an ideal pinhole on this sensor shows the normal signal height already at a lower module leakage current. On the other hand, this allows in principle, to determine the sensor on which a pinhole is present, from the leakage current that corresponds to the highest pulse amplitude. This point of maximum measured pulse amplitude corresponds to a p^+ -potential of 0.75 V. Table 5.1 exemplifies the necessary leakage currents for the cases of 512 and 768 strips on a two-sensor-module. Values for one-sensor-module resemble the case of the far sensor.

p^+-potentials as a function of the leakage current				
leakage current [μ A]	512 strips		768 strips	
	p^+ -potential [V]		p^+ -potential [V]	
	near sensor	far sensor	near sensor	far sensor
2	0.01	0.01	0.01	0.01
20	0.06	0.11	0.06	0.09
100	0.28	0.57	0.28	0.48
131	0.37	0.75	0.37	0.63
158	0.45	0.91	0.45	0.75
265	0.75	1.52	0.75	1.26

Table 5.1: Potentials of p^+ -implants of a two-sensor-module during the pinhole test. The values in the table are based on the assumption, that the fibre array is positioned above the sensor which is further away from the hybrid (far sensor) and that a constant leakage current of 1 μ A flows through the near sensor.

In reality pinholes have a certain resistance. The potential of the APV input depends also on the voltage drop across the pinhole, determined by the current that flows through the pinhole into the APV input and the resistance of pinhole. The leakage current corresponding to the highest measured calibration amplitude, can only give a hint for the sensor, havin a pinhole.

5.7.2 Data Acquisition Procedure

The leakage current is generated by the LEP 16 controller, operated in *continuous mode* with *all LEDs* being *switched on* at a time. The sequence of the data acquisition procedure during the pinhole test is implemented as follows:

- A certain LED intensity is set. This is done for 86 different intensities (equally spaced from 0 to 255).

- For a given LED intensity the pulse height is measured at a fixed point in time close to the maximum of the pulse shape for a specified number of events in the same way it is done during the gain test (cf. section 5.4.1). The average of these measurements is computed.

To allow a later attribution of LED intensities to leakage currents, the leakage current I_{leak} is measured for each LED intensity.

For each channel the average pulse amplitude for each LED intensity is stored. The pulse amplitude plotted versus the LED intensity gives a flat curve for normal channels. For a pinhole it gives a characteristic curve which starts at low values, reaches a maximum value and finally falls to lower values at very high LED intensities. This is illustrated on data of a real measurement in figure 5.11(a).

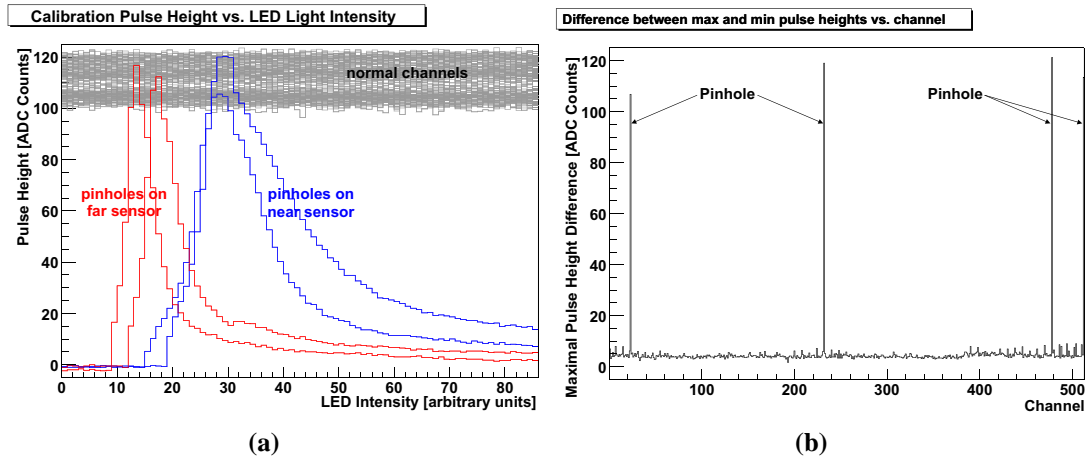


Figure 5.11: (a) The figure shows a typical result of a pinhole test for a number of channels at once. While the calibration pulse height of normal channels (grey) shows no dependency on the LED intensity (i.e. module leakage current), channels affected by a pinhole measure the full calibration pulse height only at a certain LED intensity. Channels with a pinhole on the sensor near the hybrid require a higher leakage current on average to reach the full calibration pulse amplitude. (b) The difference between the highest and lowest measured pulse height in figure (a) gives a good indicator for a pinhole.

5.7.3 Pre-Analysis of the Data

The difference between the maximum and minimum measured calibration amplitude of a channel is filled into a ROOT diagram (in the following denoted as *pinhole difference*). It can be used as an indicator for a pinhole. The difference is large for pinholes since the pulse amplitude varies strongly, whereas the difference is low for normal channels. This is indicated in figure 5.11(b). In addition, the maximum measured calibration amplitude is stored for each channel (in the following denoted as *pinhole maximum*). This is useful to distinguish pinholes from dead channels (cf. chapter 6.4).

5.8 The Backplane Pulse Test

In the backplane pulse test an external signal is induced by a fast step in the voltage that supplies the backplane of the sensors. The amplitude of the signal is determined by the gain on the ARC front-end adapter. The backplane pulse affects all channels at the same time and appears to the APV like a common mode signal of all channels. The APV internal common mode correction can thus correct the signal almost completely. An exception are channels which are affected by a faults like open bonds, that impede the transmission of the backplane pulse signal to the APV input of the respective channels. After the common mode subtraction such channels seem to have a high signal (see figure 5.12). This is the detection principle of the backplane pulse test.

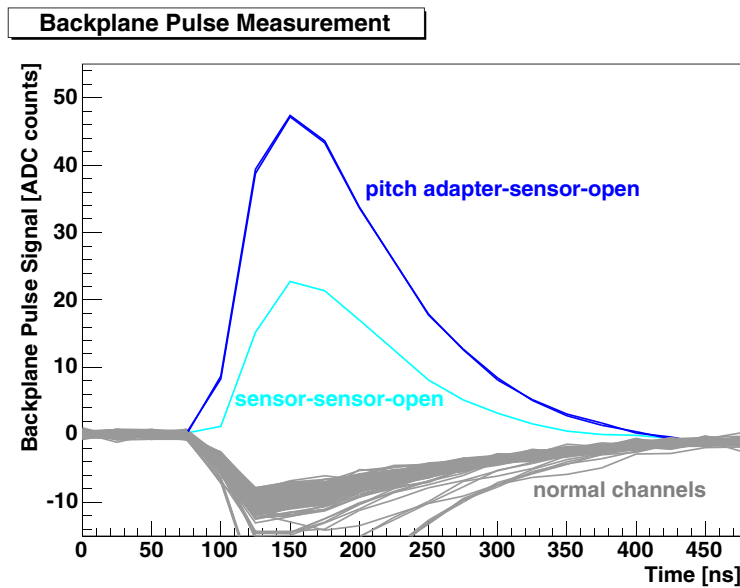


Figure 5.12: The behaviour of normal channels and open bonds in the backplane pulse test. While normal channels measure only a small signal, the signal of channels with an open bond is large. The pulse directs into the opposite direction.

5.8.1 Data Acquisition Procedure

The backplane pulse test measures the height of the backplane pulse signal at different sampling points in time. During the test a fixed latency of 20 is used. The sampling point in time is adjusted by adapting the spacer sp in the trigger pattern

$$0000.0000.(sp + sp_{min}).1000.0000.$$

In the pattern, sp_{min} is an adjustable minimum spacer. For each spacer value a specified number N of events is used to measure the pedestal $P_{ch,sp}$ for each channel with no backplane pulse being applied to the sensors. After the backplane pulse is enabled, the signals $S_{ch,sp}$ are determined for each channel ch and each adjusted spacer value sp by averaging over measurements of N events. For a certain channel ch the differences

$BPP_{ch,sp} = S_{ch,sp} - P_{ch,sp}$, $sp = sp_{min} \dots sp_{max}$ are filled in a diagram and stored in the ROOT data file. Such a diagram contains the full measured shape of the backplane pulse. An example of such a shape is shown in figure 5.12.

5.8.2 Pre-Analysis of the Backplane Pulse Data

For each channel the sum $\sum_{sp} BPP_{ch,sp}$ over the whole range of adjusted spacers sp is calculated for each channel ch and stored in the ROOT file. The sum is used instead of the extreme value since it is less affected by single point fluctuations.

5.9 The Functional Test

The functional test was originally designed as a fast test to give an assessment of the hybrid functionality by means of some significant tests. It is an integral part of the FHIT software. To avoid unnecessary costs during the production at the hybrid factories the test had to be easy to use and had to take less than 30 seconds. While the functionality of the fast test in the FHIT remained the same since the year 2002, the functional test in the ARC software was extended in later versions.

The functional test consists of several individual tests which are described in the following paragraphs. The results of each test are stored in the ROOT file. A human readable explanation is given in a dedicated display panel in the graphical user interface of the software, describing the test performed and possible faults which were found during the test.

ARC Self Test: The ARC self test was implemented to ensure the functionality of the ARC board during all subsequent tests. In particular, this is necessary to avoid misinterpretations of conspicuous test results. The ARC self test consists of four parts. At the beginning the access to the ARC board is checked by the comparison of register values, written into and read out of registers on the ARC board (so-called read/write test). The second step is a read/write test of the RAM modules. The third test checks the accessibility of the three I²C controllers of the ARC board. Finally a control sequence is processed that checks whether the ARC front-end adapters are connected to the correct ports. The distinction between ARC front-end adapters attributed to particular ports is done by different I²C addresses of the low voltage controller.

An ARC self test is also performed during the initialisation phase of the ARC software.

I²C Test: During the I²C test read/write cycles are performed for all different I²C devices on a front-end hybrid (TPLL, DCU, MUX and APVs).

Low Voltage Test: The low voltage test assesses the power consumption of a hybrid. The test uses the low voltage controllers on the ARC front-end adapter and measures voltages and currents, once with the data acquisition being switched off and once with the data acquisition running. The measured values are compared to predefined extreme

values which depend on the number of APVs the front-end hybrid houses. In case of an excess of the limits the hybrid supply voltage is switched off for reasons of security.

APV Data Output and Clock Distribution Test: The data of two APV are multiplexed onto a single differential output line. The de-multiplexing is done in the software. Data from a certain MUX channel are always routed to the same RAM module. This is checked in an *assignment test*. During the assignment test one APV is set to the three sample mode. If the assignment is correct one reads data of three frames from one specific RAM module.

In a further step the headers of all APV frames are checked for synchronisation and the error bit, indicating a FIFO error.

PLL Test: As soon as the PLL gets powered or after the reception of a reset command it should switch into an auto calibration mode, that determines default operation settings for the PLL. It should thus be the normal operating condition of the chip. In the test it is checked whether all I²C values read correspond to the settings expected after the auto calibration. If it does not, a reset command is sent.

MUX Resistor Test: The MUX resistor test measures the influence of the MUX resistors on the data read from the APVs. The height of the APV frames depends on the number of MUX resistors switched in parallel (cf. chapter 2.5.4). This height is measured by the height of the tick marks preceding the header of an APV data frame (see figure 2.11). Choosing a larger number of switched resistors decreases the amplitude of the APV frames. For a given number of MUX resistors the height of the tick mark should not depend on particular chosen resistors. This is checked by switching different combinations of the same number of resistors. The fluctuations of the height of the tick mark should not exceed a certain limit ($\mathcal{O}(\text{some ADC counts})$), otherwise an abnormal resistor value is assumed.

DCU Response Test: In this test all DCU registers are read. The acquired data are compared to expectation values for each of the properties the DCU monitors (cf. chapter 2.5.6).

In particular the DCU test includes a check of the DCU measurements of the hybrid supply voltages. For that purpose, the supply voltages are set to different values using the low voltage supply of the ARC front-end adapter. The change of the supply voltages should cause a change of the respective DCU value of the same relative amount.

Pedestal & Noise Test: The pedestal and noise test included in the functional test measures the pedestal and the noise for each channel according to the approximation algorithm explained in section 5.2.3. It is ensured that the calculation is based on at least 500 events.

Calibration Test: The calibration test uses the algorithms of the pulse shape test (cf. section 5.3), but the measurement is performed only for a fixed point in time (i.e. for one LATENCY and one CSEL value) close to the extremum of the calibration pulse.

Chapter 6

The Signatures of Faults in Module Tests

Different types of faults on a module (cf. chapter 2.6) show a significant, partially unique behaviour in a number of automated tests with the ARC software (cf. chapter 5). This chapter explains qualitatively how a certain type of fault shows up in different tests. The pipeline test will not be considered except for defective pipeline cells. The signature in the pipeline noise test equals the signature in the normal noise just as the signature in the pipeline calibration amplitude test equals the signature in the pulse height measurement.

It will be discussed which tests are feasible to discriminate different types of faults. Not all of them are equally suited for that purpose. A quantitative discussion that specifies the most appropriate ones will be elaborated in chapter 7.

Faults which can be detected with the ARC system must be faults that *affect the electrical behaviour* of the whole module, of a single strip, or of an ASIC. Other, mainly mechanical flaws like scratches, broken precision bushings, misaligned sensors, weak adhesion of glueing points etc., have to be found in other tests or optical inspections.

6.1 The Signature of Open and Missing Bonds

This section treats the signature of open or missing bonds. For the more general case of two-sensor-modules, opens can be classified as sensor-sensor-open and pitch adapter-sensor-opens. Opens between the APV input and the pitch adapter are counted among the pitch adapter-sensor-opens. Since mid-sensor-opens, which represent a substantial damage of a readout strip (see figure 2.16(a)), affect also the oxide layer underneath the aluminium strip, their behaviour is more difficult to classify. They are treated briefly at the end of this section.

Manifestation in the Pulse Shape Test: An open or missing bond implies a reduction of the capacitance connected to the APV input. The strip capacitances of the detector can be assumed to be about three orders of magnitude larger than any

capacitance within the APV. The reduction of that strip capacitance C_{strip} implies a significant *reduction of the shaping time* constant $\tau = R \cdot C_{tot}$ of the preamplifier of the APV which is determined by the effective resistance R and the total capacitance C_{tot} connected to the APV input.

Accordingly, also the shaped signal returned by the subsequent shaper, reaches its maximum value earlier than normal channels. For two-sensor-modules this effect scales with the number of sensors not connected to the APV input. The effect is less pronounced for the rise time. This is illustrated in figure 6.1(a), where the peak and the rise times of a part of a module with several opens of both types are shown.

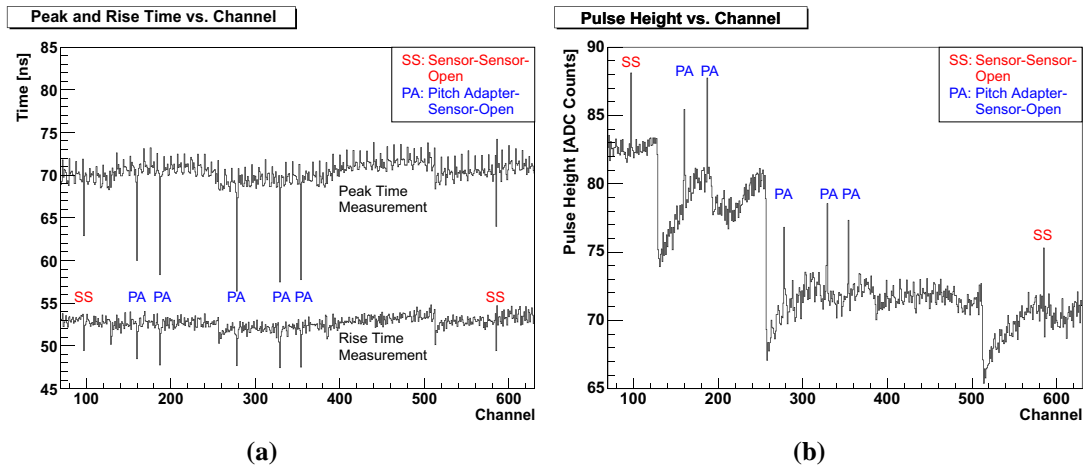


Figure 6.1: (a) The appearance of opens of different type in the measurements of rise time and peak time on the same module. The figure also illustrates the general observation, that the peak time is more appropriate to identify opens than the rise time. (b) The appearance of opens of different type in the pulse height measurement. Pitch adapter-sensor-opens are further separated from normal channels than sensor-sensor-opens. Both figures represent measurements in peak mode, inverter off.

A smaller capacitance connected to the APV input effectuates that a larger fraction of the calibration pulse charge flows to the APV input. Thus the *height* of the measured signal *increases*, as illustrated in figure 6.1(b). The figure also shows that the total pulse height gives no good measure for an open. The variations of the APV average pulse heights can be larger than the pulse height differences of channels with an open bond. It is more convenient to consider deviations of the pulse height with respect to the APV average.

Manifestation in the Gain Test: The influence of open bonds on the gain slope is comparable to their influence on the pulse height in the pulse shape test. Due to the smaller capacitance connected to the APV input, a larger fraction of charge flows into the APV preamplifier. Compared to normal channels a *higher signal* is thus present for all adjusted amounts of charge. The gain *slope* is thus *steeper* for open bonds.

Manifestation in the Noise Test: The smaller capacitance of a channel affected by an open bond is also evident in the noise measurements. According to [53] the equivalent noise charge ENC measured in units of the electron charge e depends on the capacitance C (cf. equation (2.9)) connected to an APV input according to:

$$\text{peak mode: } ENC_{peak}(C) = 270 + \frac{38}{\text{pF}} \cdot C, \quad (6.1)$$

$$\text{deconvolution mode: } ENC_{dec}(C) = 430 + \frac{61}{\text{pF}} \cdot C. \quad (6.2)$$

Thus a pitch adapter-sensor-open has a lower noise than a sensor-sensor-open which has again a *lower noise* than a normal channel. This is illustrated in figure 6.2.

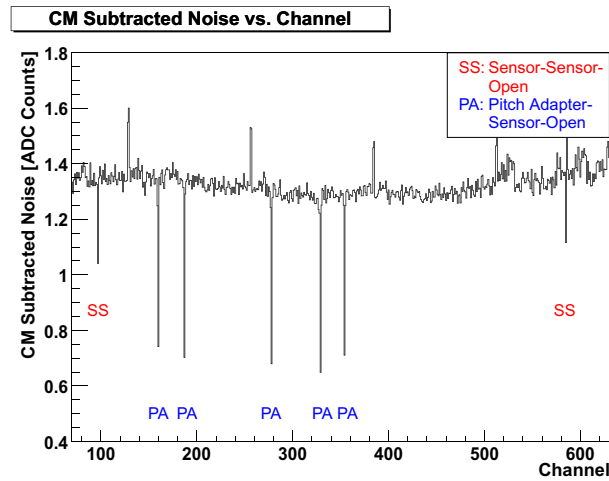


Figure 6.2: Illustration of the noise behaviour of open bonds (peak mode, inverter off) for the same module as in figure 6.1. In this measurement the sensor-sensor-opens have a lower noise than normal channels. Pitch adapter-sensor-opens have a very low and almost equal noise. APV edge channels (128, 129, 256, 257,...) have a slightly higher noise.

To observe this behaviour, it is of particular importance to keep the common mode low. The sensitivity of the noise on the width of the common mode distribution (cf. chapter 5.2.3) is depicted in figure 6.3. The noise of normal channels and APV edge channels is virtually independent of the width of the common mode distribution. The noise of sensor-sensor-opens increases slightly with an increasing common mode width. For pitch adapter-sensor-opens this dependency is much more pronounced, such that their noise can be even larger than the noise of normal channels.

The explanation for this dependency is as follows: A channel with an open does not participate in common mode shifts, induced by fluctuations on the HV line, to the same amount as normal channels. Nonetheless the whole common mode is subtracted from the raw data already by the APV internal common mode correction. On average the calculated signals and consequently the common mode corrected noise of channels with an open bond increases (cf. equations (5.12 and 5.13)). Although this effect is present for all values of the common mode, it becomes a dominant noise contribution

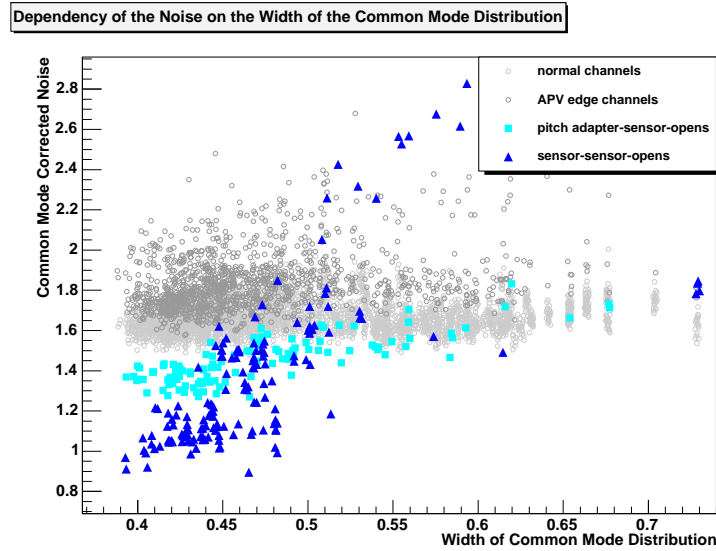


Figure 6.3: Illustration of the dependency of the noise on the common mode for ring 5 modules in deconvolution mode, inverter off. Each marker represents the noise of a channel and the corresponding width of the common mode distribution of the APV. The noise of normal channels and APV edge channels is not sensitive to the size of the common mode. The dependency of the noise of sensor-sensor-opens is much more pronounced than that of pitch adapter-sensor-opens.

only if the common mode exceeds a certain value. Since sensor-sensor-opens participate more in the common mode than pitch adapter-sensor-opens, their dependency lies between the one of normal channels and the one of pitch adapter-sensor-opens.

The effect is most pronounced in modes with deactivated inverter. In modes with activated inverter the noise of sensor-sensor-opens is not affected while the noise of pitch adapter-sensor-opens takes a wide range of values between normal noise and a noise below the sensor-sensor-open noise. Due to the APV internal common mode correction this effect is also present in the raw noise.

Manifestation in the LED Test: A missing bond prevents the transmission of the LED signal from the point of illumination to the APV input. Therefore virtually *no signal* can be measured on a channel with an open bond. A distinction between sensor-sensor-open and pitch adapter-sensor-open is not possible since the fibre array is positioned only above the far end of the sensor which is further away from the hybrid. The results of a LED measurement are shown in figure 6.4(a).

Manifestation in the Backplane Pulse Test: The size of the charge signal induced by the voltage pulse on the backplane scales with the length of the aluminium strip connected to the APV input. In case of a sensor-sensor-open the signal is halved, in case of a pitch adapter-sensor-open virtually no charge flows to the APV input. As the backplane pulse signal is applied to all channels at a time, normal channels recognize the backplane pulse as a pedestal shift. The APV internal common mode correction rectifies that shift. Since this correction is applied to all channels of an APV, it has the

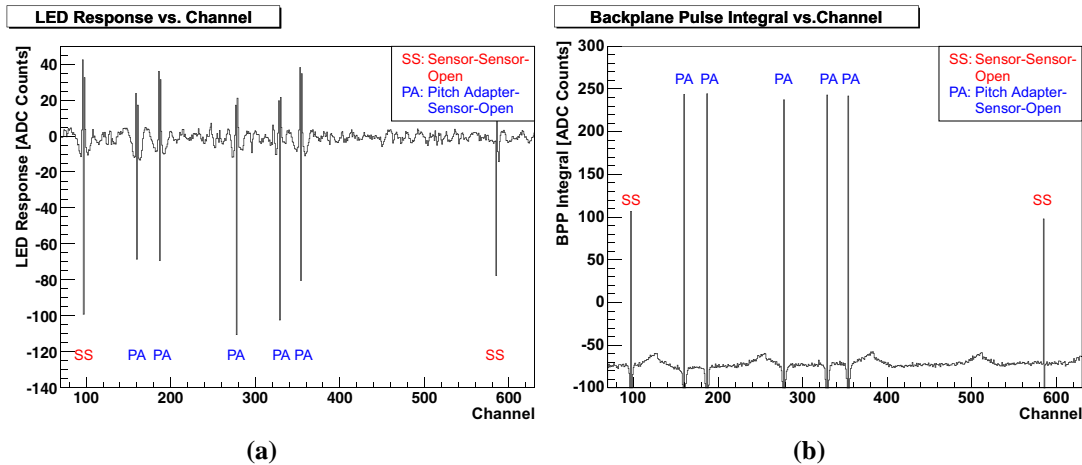


Figure 6.4: (a) The appearance of opens in the LED test. The height of the signal is determined primarily by the height of the LED pulse illuminating a strip. Thus a distinction of the type of open cannot be made. (b) The behaviour of opens in the backplane pulse test (peak mode, inverter off). The signal heights of sensor-sensor-opens and pitch adapter-sensor-opens are clearly different from each other and from normal channels. The module is in both cases the same as in figure 6.1.

opposite effect on channels that do not transmit the full backplane pulse signal to the APV input. Their small signals are shifted by the amount of the common mode and appear with a *high* signal during the backplane pulse test, see figure 6.4(b). The effect scales with the capacitance of the strip connected to the APV input.

Manifestation in the Pinhole Test: During the *pinhole test* the measured pulse height of open bonds is constantly higher than the pulse height of normal channels. The pulse height is in particular independent of the leakage current of the module (see figure 6.7).

Particular Signature of Mid-Sensor-Opens: From the low number of modules with a mid sensor open one can only find one significant criterion: the *noise is higher* in at least one of the APV operation modes. This behaviour is probably attributed to damages of the detector surface which cause further effects than just a change of the strip capacitance.

If a pitch adapter-sensor-open is measured with a high common mode, it also shows a higher noise. Thus, there is a certain probability to misidentify this channel as a mid-sensor-open.

The higher noise implies a certain probability to misidentify a pitch adapter-sensor-open, measured with a high common mode, for a mid sensor open.

6.2 The Signature of Short-Circuited Channels

A most important indication of a short-circuit is its influence on two neighbouring or next-to-neighbouring channels. A connection between strips separated by more than one strip is not considered, since their respective conductor paths are not adjacent at any point of the module. A signal induced in the bulk below two (or more) short-circuited strips induce charges in both p^+ -implants and thus in both aluminium strips. The charge division between both strips depends on the resistance of the aluminium strip, the resistance of the connection, and the position of the short-circuit along the strip.

Manifestation in the Pulse Shape Test: The capacitance of the short-circuited strips is approximately twice the capacitance of a single strip. The total impedance connected to the preamplifier of an APV input is halved, since the injected calibration charge flows through twice the number of resistors as indicated in figure 6.5. Thus no big effect on the time constant $\tau = R \cdot C_{tot}$ of the preamplifier is expected.

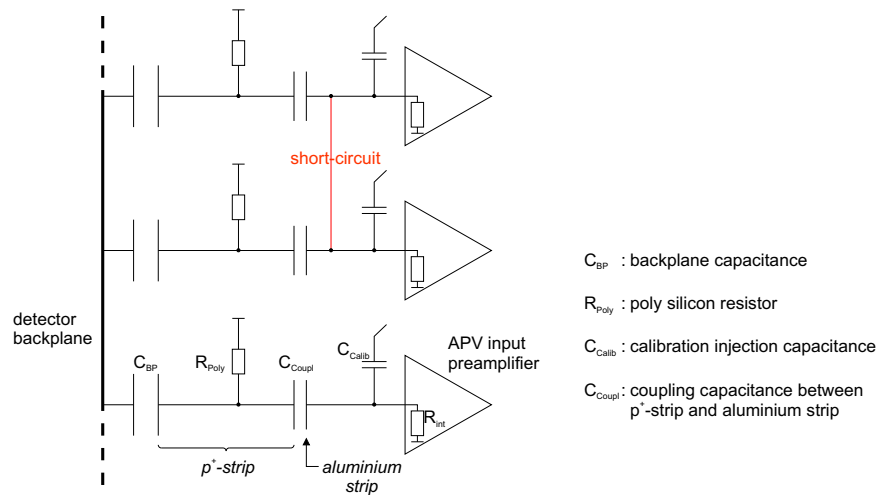


Figure 6.5: Simplified illustration of a short-circuit between two adjacent aluminium strips. A charge injected via one calibration injection capacitor is distributed to twice the capacitance and flows through twice the number of resistors switched in parallel.

During a pulse shape measurement the charge injected in one channel is distributed to two channels and two APV inputs. Therefore one measures a *lower pulse height* of approximately half the value of normal channels. This is illustrated in figure 6.6(a).

The charge division between both strips and the time constants of the preamplifiers are determined by the capacitance of the single strips, the resistance of the aluminium strip, the resistance of the connection between both, and the position of the short-circuit along the strip.

A further criterion for a short-circuit is given by the *crosstalk measurement* which measures the signal on a channel neighbouring the channel hit by the calibration charge. The crosstalk signal on a short-circuited, neighbouring strip is of the same size as the signal on the channel hit by the calibration signal. Both channels measure a signal that

corresponds roughly to half of the signal of a normal channel. In particular there is no counter motion (cf. chapter 5.3.2) observable on the neighbouring strip. This is illustrated in figure 6.6(b) for two short-circuited strips and one unaffected neighbouring strip.

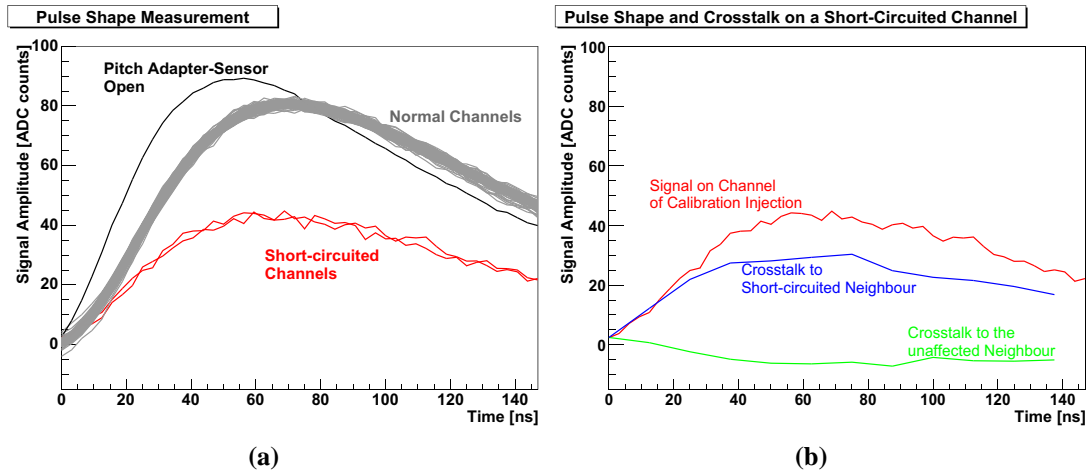


Figure 6.6: (a) The figure shows a superimposition of 128 pulse shapes of an APV. Two short-circuited channels have approximately half the pulse height of normal channels. A pitch adapter-sensor-open shows up with a larger pulse height and a shorter peak time. (b) Superimposition of the measured pulse shape on a short-circuited channel, the crosstalk to its short-circuited neighbouring string and the crosstalk to the other, unaffected neighbouring strip.

Manifestation in the Gain Test: The same considerations as for the pulse height apply to the gain slope. Since the division of the charge on two neighbouring channels effects a measured signal of approximately half the size of a normal channel the respective measured gain slope is about *half the slope* of normal channels.

Manifestation in the Noise Test: Doubling the capacitance increases the capacitive part of the noise contribution. As this increased noise is portioned to both strips, one does not expect a significant change of the noise. Nonetheless short-circuits are characterized by an *abnormal noise* on at least one of its channels *in at least one APV operation mode*. One observes, that the noise of both short-circuited channels is on average lower in APV modes with activated inverter. If the inverter is switched off, the noise is on average higher than the noise of normal channels. But there are also cases, where one of the short-circuited strips has a lower noise and the other one had a higher noise in various APV operation modes.

This behaviour is not completely understood. One reason for that observation can be the fact that the fluctuations on two neighbouring normal channels are in general anti-correlated [54] in a single event. A short-circuit disturbs this anti-correlation. A further reason can be damages of the sensor structure close to the surface, that are not incorporated in the simple model of an ohmic contact between both aluminium strips.

The different behaviour in modes with activated and deactivated inverter indicate also influences on the APV readout chain, e. g. of the APV internal common mode correction whose effectiveness depends on the inverter operation mode.

Manifestation in the LED and Backplane Pulse Test: Two short-circuited channels expose twice the area of a normal channel to the light. Accordingly the generated charge signal is doubled. If the charge is shared equally between both strips, there is no significant influence on the measured signal. If the charge is not equally shared between both strips, one strip shows a higher, the other strip a lower signal. The signal height is determined primarily by the amount of light extracted from the optical fibre above the strip.

A comparable situation is present in case of the backplane pulse test. If both channels share the charge equally, both transmit a similar signal to their respective APV input which equals the signal of normal channels. Otherwise the signals may be different of normal channels and can also have opposite signs with respect to the APV average.

Manifestation in the Pinhole Tests: In the pinhole test short-circuited channels appear as flat lines with a considerably lower level than normal channels (see figure 6.7).

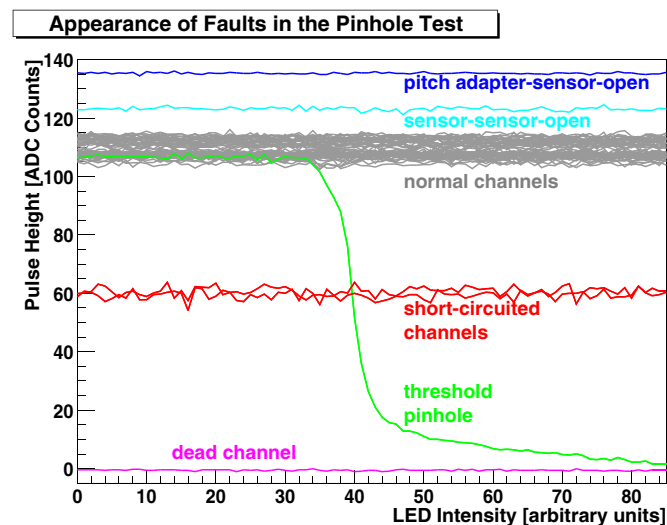


Figure 6.7: The behaviour of different faults in the pinhole test. Further signatures are shown in figures 5.11(a) and 6.12(c)

6.3 The Signature of Pinholes

Resistive pinholes show an abnormal behaviour in all tests. Resistive pinholes and threshold pinholes are identified best in the pinhole test. In fact it is such, that what ever shows the characteristic rise and loss of pulse height in the pinhole test, is called a pinhole. A detailed explanation of the pinhole test is given in chapter 5.7.

Manifestation in the Pinhole Test: Due to the increasing intensity of the light the leakage current in a module is increased, implying a change of the potential of the p^+ -implant. In case of a resistive pinhole, the potential at the APV input of the affected channel is nearly identical to the potential of the p^+ -implant. As the input amplifiers of the APV work properly only in a narrow range around the nominal potential of 0.75 V, the response to the calibration signal diminishes if the p^+ -potential takes significantly different values. A typical result for resistive pinholes is shown in figure 5.11(a).

Threshold pinholes show up differently. For low leakage currents the potential difference across the coupling capacitor made up of p^+ -implant and aluminium strip is low and the capacitor works properly. For higher leakage currents the potential difference rises such that a breakthrough in the oxide layer occurs. Thereby the coupling capacitor is short-circuited like a resistive pinhole. It is indicated by a breakdown of the measured pulse height as depicted in figure 6.7. The pinhole test is the only test that can identify threshold pinholes as they appear only at leakage currents which are not reached in any other test.

Manifestation in the Pulse Shape Test: As the APV input of a resistive pinhole is connected to the p^+ -implant, virtually no signal is measurable at low leakage currents. As low leakage currents are desirable for all tests except for the pinhole test, channels with resistive pinholes show up as flat lines with a pulse heights close to zero. Threshold pinholes appear like normal channels.

In the crosstalk measurement one observes a significantly higher crosstalk to both neighbours. This is due to an increased capacitance between both strips. Thus the fraction of charge flowing to the aluminium strips increases. Thereby a larger signal is induced on the neighbouring channels due to the coupling over the inter-strip capacitance. This effect is illustrated in figure 6.8(a). One should note that this is the only known mechanism besides a short-circuit, that generates a crosstalk with the same sign as the injected signal.

Manifestation in the Gain Test: The same considerations made for the pulse height apply also for the gain test. A resistive pinhole shows up as a flat line with a slope close to zero. Threshold pinholes appear like normal channels.

Manifestation in the LED Test: The considerations of the pulse shape test also apply to the LED test. No signal can be measured because the operating point of the APV input is shifted to the potential of the p^+ -implant. Threshold pinholes again show the behaviour of normal channels.

Manifestation in the Noise Test: If a resistive pinhole is present on a strip, the APV preamplifier does not respond to a charge signal. This applies also to small signal fluctuations, the noise. Thus affected channels have a *low noise*. From the few pinhole measurements available with a high common mode one can estimate (see figure 6.8(b)) that their noise also increases with a larger width of the common mode

distribution as this is the case for open bonds (cf. section 6.1). Threshold pinholes are not distinguishable from normal channels.

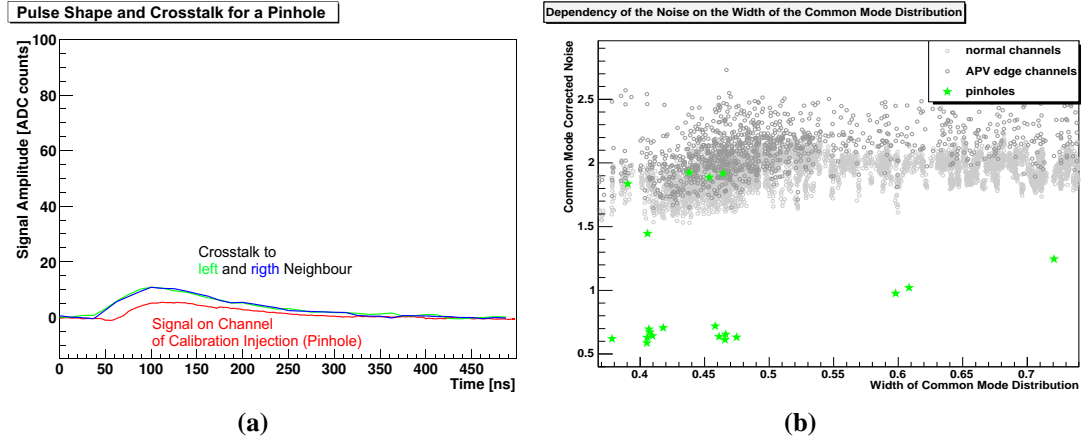


Figure 6.8: (a) The crosstalk signals on the channels adjacent to a pinhole do not show the typical counter motion. Their height even exceeds the low signal of the pinhole channel hit by the calibration signal. (b) Illustration of the dependency of the noise of pinholes on the common mode for ring 6 modules in deconvolution mode, inverter off. Each asterisk represents the noise of a channel and the corresponding width of the common mode distribution of the APV. The asterisks in the band of normal channels are measurements of threshold pinholes. The one near below is a resistive pinhole at a module edge. The other ones denote a slight dependency on the width of the common mode distribution.

6.4 The Signature of Dead Channels

Dead channels act in many aspects like pinholes as they show no response to any charge signal. At first the decisive difference—the behaviour in the pinhole test—is discussed. Commonalities are briefly discussed in the subsequent section.

Manifestation in the Pinhole Test: Unlike pinholes, dead channels show no response to a calibration signal at any leakage current. The criterion to identify dead channels is thus a very small response to the calibration signals during the whole pinhole test indicated by a low value in the diagram of the maximum measured pulse height.

Manifestation in Other Tests: At low leakage currents which are present in all tests but the pinhole test, dead channels are hardly distinguishable from pinholes. Both faults affect the APV preamplifier such that it does not respond to charge signals. Thus their behaviour matches in the following aspects:

- In the noise test, a low noise is evident in all APV modes. There is no evidence in the present data that this behaviour depends on the common mode.

- In the pulse shape test, one measures a signal close to zero in all APV modes.
- In the gain test, one measures a gain slope close to zero.

6.5 The Signature of Defective Inverters

Defective inverters become obvious, as they show a different behaviour in tests that are performed once with activated and once with deactivated inverter.

Manifestation in the Pulse Shape and Gain Test: The best method to spot a defective inverter is the comparison of two measurements of the pulse height with the inverter switched on and off. An example is shown in figure 6.9(a). Though the defective channels are clearly visible in the figure, they can be difficult to spot if their deviation from normal channels is of the order of pulse height differences due to the slope of the data. Dividing the absolute values (see figure 6.9(b)) of both measurements gives a slope independent measure, that is for normal channels close to 1. In case of a defective inverter this value is significantly different. The same considerations also apply to measurements of the gain slope.

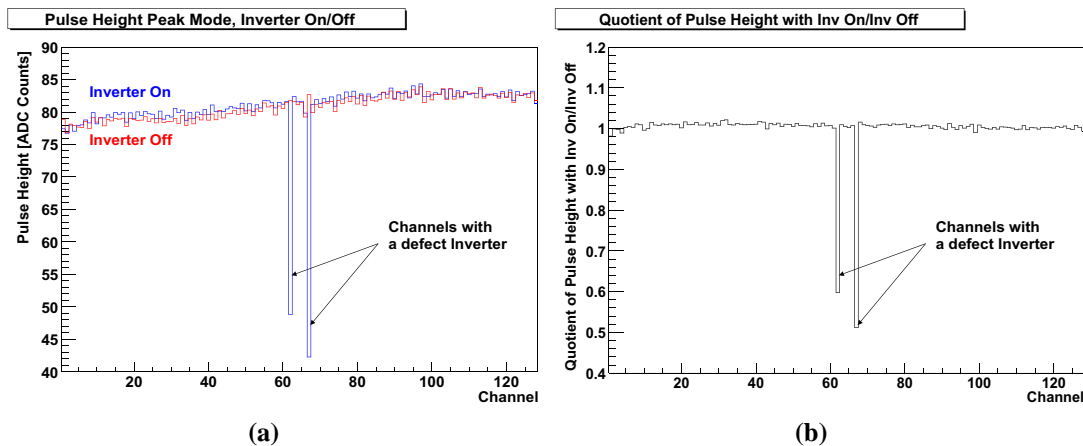


Figure 6.9: (a) Pulse height measurements in peak mode, inverter on and off, for an APV with two defective inverters. (b) The quotient of both measurements allows an easy identification of defective inverters.

Manifestation in the Noise Test: A defective inverter is also apparent in a different noise, if two measurements with inverter switched on and off are compared. The strip-wise quotient of both measurements gives a value close to 1 for normal channels and a significantly different value for defective inverters. As the noise depends on the setup specific common mode, the quotient of the pulse height measurements is taken as the more reliable indicator.

6.6 The Signature of Defective Pipeline Cells

In all tests but the pipeline tests data of a channel are read from randomly triggered pipeline cells. A single defective pipeline cell out of 192 cells belonging to a channel effects a different behaviour in these tests in every 192nd event on average. Depending on the number of events taken per channel this effect can be smoothed such that an anomaly is hardly observable, e. g. in the noise test. If the number of events is low, the results can be very different, depending on whether the average is computed based on data that include the defective pipeline cell or not. This is in particular the case for the pinhole test and the pulse shape measurement. These two measurements can thus indicate a defective pipeline cell if results from the pipeline test was not performed.

Manifestation in the Pipeline Test: Examples of deviations from the nominal behaviour are given in figure 5.8. By definition every significant deviation from the median¹ value of a channel is a defective pipeline cell. Very noisy pipeline cells can be spotted virtually only in the pipeline noise measurement. Pipeline cells with an abnormal calibration response have a chance to be discovered also in other tests which are described in the following sections.

Manifestation in the Pinhole Test: Due to the complexity of the pinhole test only a small number of events of $\mathcal{O}(10)$ is used per point. If data for a certain point include data from a defective pipeline which shows no calibration response, the computed average value will be significantly lower, as shown in figure 6.10(a). Therefore the difference between the maximum and minimum measured calibration amplitude of a channel (cf. chapter 5.7.3) can differ significantly from zero. Thereby this channel can imitate a pinhole signature. In fact, this imitation was one of the main reasons for the implementation of the pipeline calibration amplitude test.

Manifestation in the Pulse Shape Test: Due to the small number of events used for each point of a pulse shape measurement ($\mathcal{O}(10)$) the influence of a defective pipeline cell is also noticeable. If data from a defective pipeline cell is included in the calculation of the single point average, this average value is smaller than expected. In the curve progression, this is indicated by a kink in the smooth curve (see figure 6.10(b)). Since pulse shape data are evaluated using fit functions the influence of defective pipeline cells on the peak time and the pulse height is low.

6.7 Noisy Channels

Marking a noisy channel is more difficult than the marking of other faults, since there is in general no other conspicuous effect in the respective channel. Thresholds that

¹Median: The median of a list of entries is defined as the smallest number for which holds that at least half the numbers in the list are not larger than itself. In ARCS the median is calculated using ROOT. A histogram is filled and the median is the number that divides the area under the histogram in two equal halves.

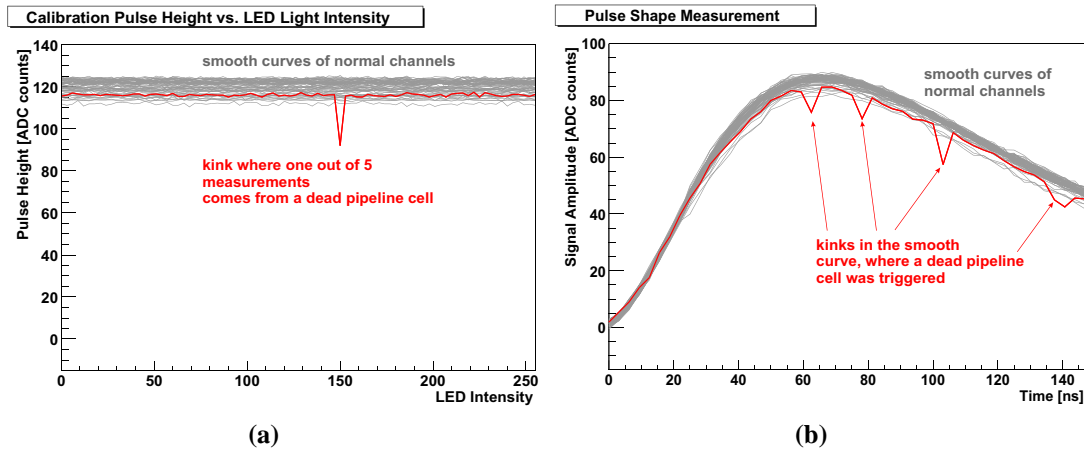


Figure 6.10: A defective pipeline cell causes characteristic kinks in the pinhole measurement (a) and in the smooth pulse shape curves (b).

determine the tolerable noise level have to be chosen carefully to keep the number of accidentally flagged normal channels low and on the other hand all noisy channels. Chapter 7.5 is dedicated to the definition of feasible noise thresholds.

Normally the noise of a channel is independent from its pedestal value. But a distorted noise figure of some strips can be observed, if the pedestal values of those strips are at the level of the digital zero of the corresponding APV (see figure 2.11). In such a case the value of the digital zero will be measured occasionally. The noise calculations can give a higher noise for those channels due to the common mode correction, as it was described for opens in section 6.1. An example of such a noise distortion is given in figure 6.11.

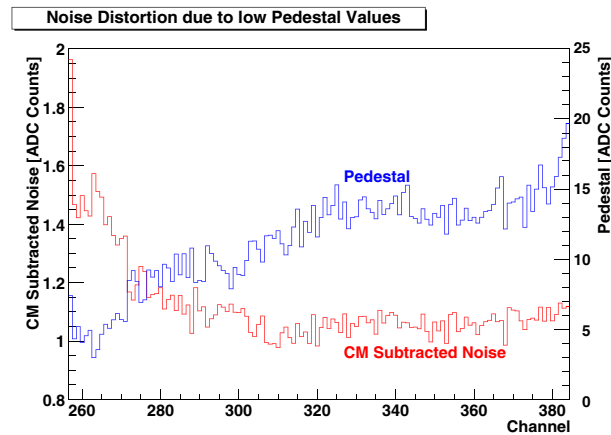


Figure 6.11: Noise distortion due to a low pedestal. The closer the pedestal value is to the level of the digital zero (here about 5 ADC counts) the higher is the noise of the channel.

A measurement with such a signature has to be repeated with an adapted pedestal which is adjustable via the APV I²C register VPSP.

In many cases the noise measurements of a whole module reveals a slightly increased noise on APV edge channels. This behaviour is attributed to crosstalk effects between adjacent APV edge channels. The noise of the outermost channels of a module (*module edge channels*) often exceeds the noise of “inner APV” edge channels. The main reasons are crosstalk effects with the bias ring, whose potential is also slightly fluctuating [54].

6.8 Micro-Discharges

Micro-discharges create a very large noise. Channels with a noise of up to 100 ADC counts have been observed. This noise is attributed to localized peaks in the electric field which can cause avalanche effects. Micro-discharges are characterised by a normal noise up to a certain bias voltage of the sensors. Above this voltage, the avalanche process starts and the noise rises. The influence of such a noisy strip is not limited to its neighbours. Even the noise of the whole APV can be affected, as illustrated in figure 6.12(a). Also pulse shape measurements are affected as shown in figure 6.12(b). A fit to data acquired in the pulse shape measurement is meaningless. Nonetheless the resulting peak time and pulse height can resemble the signature of another type of fault. During the pinhole test, extremely noisy channels can reach the amplitude differences of pinholes (see figure 6.12(c)).

6.9 Unknown Faults

Any conspicuousness in a test that is not associated to other signatures that would allow the attribution to one of the types of faults mentioned above, is denoted as an *unknown fault*. Examples are low or high pulse heights or peak times due to a failed fit or channels with a low noise in only one of the APV operation modes without any further conspicuousness.

6.10 Summary Table of Signatures

The signatures of all types of faults are summarized in table 6.1.

Summary Table of Signatures of Faults									
	Noise	Pulse Height	Crosstalk	Peak Time	Gain Slope	Backplane Pulse	Pinhole Difference	Pinhole Maximum	Pipeline
open bond	low	high	—	short	steep	high	—	high	—
mid-sensor-open	high	high	—	short	steep	?	—	high	—
short-circuit	low or high	$\approx \frac{1}{2}$	high	?	$\approx \frac{1}{2}$?	—	low	—
resistive pinhole	low	≈ 0	high	?	≈ 0	?	high	—	—
threshold pinhole	—	—	—	—	—	—	high	—	—
dead channels	low	≈ 0	—	?	≈ 0	?	—	≈ 0	—
defective inverter	inv. on \neq inv. off	inv. on \neq inv. off	—	?	inv. on \neq inv. off	?	—	—	—
defective pipeline cells	—	—	—	—	—	—	high	—	obvious
noisy channels	high	—	—	—	—	—	—	—	—
micro-discharge	very high	spoiled	large	spoiled	spoiled	?	high	—	—

Table 6.1: Summary table of all signatures of different faults in different tests. All faults do also affect the pipeline measurements, but the measurement is made such that only defective pipeline cells are marked. A question mark indicates an influence that is noticeable but not significant.

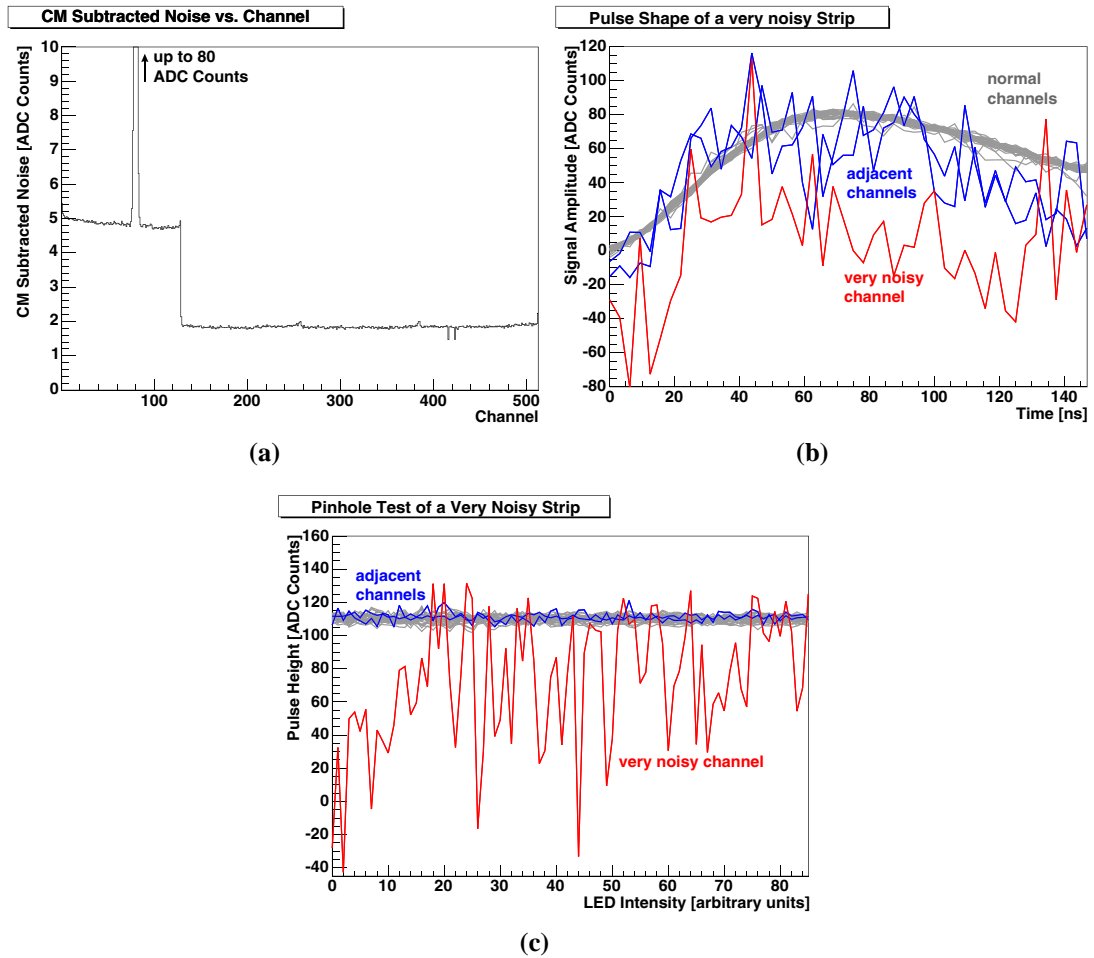


Figure 6.12: The influence of micro-discharges. (a) The noise of a whole APV (channels 1 to 128) and particularly the noise of the adjacent channels can be affected. (b) The pulse shape gets deteriorated. (c) In the pinhole test a micro-discharge channel can imitate the large difference of the pulse height that is typical for a pinhole.

Chapter 7

The Optimisation of the Fault Finding Algorithm

A safe identification of bad channels accompanied by a minimised rate of wrongly flagged good channels is essential for the grading of modules (cf. chapter 4.7). By means of the determined grade a module can be accepted for the insertion into the tracker or can be sorted out.

A safe automated identification of the type of fault is of importance during the production since decisions of potential reparations or deliberate removals of bonds depend on the type of fault.

An analysis algorithm for the identification of faulty channels as included in the XML Parser, generates a XML file that is sent to the database. The entries in the database will be used to exclude bad channels from the track reconstruction. But data of a channel with a sensor-sensor-open have to be excluded only in half of the cases for example. Thus a safe identification of the type of fault is also of some importance for the reliability of track reconstruction.

This chapter describes an analysis that determines the tests which are best suited to find a certain type of fault. For that purpose, the behaviour of all common types of faults in all different types of tests are investigated for all different TEC geometries. Two criteria for the assessment of the appropriateness of a test will be introduced. One criterion measures the distance of the mean values of two different distributions of results of faulty channels with respect to the width of the corresponding distributions. The second criterion measures the overlap between two distributions.

The determination of noisy channels requires a different approach. Therefore an extra analysis for the noise was made. Finally an algorithm will be presented that combines the test results to a reliable fault identification. The fault finding and identification efficiency and the stability of the grading will be evaluated.

7.1 Motivation for the Analysis

The aim of the analysis is the definition of a fault finding algorithm for the ROOT data of a standard module test. The fault finding algorithm has to create a list of all defective channels with the correct identification of the respective type of fault.

In chapter 6 the signatures of different types of faults were presented. It should be noted that in many cases the conspicuousness is less pronounced than in the examples presented there. To avoid misinterpretations of the results it is thus necessary to determine the *most appropriate tests* for the identification of a fault.

The interpretation of the results of a single test depends on *thresholds*, also denoted as *cuts*, that determine the acceptable range of values for normal, i. e. unaffected channels. These thresholds have to be tuned carefully.

Though a redundancy of results in different test is desirable, the identification can fail if an agreement on fault signatures is required for too many tests¹. There are many influences that can spoil the clearness of a signature, such as a high common mode, the slope in the pulse height etc. For an automated determination of the type of fault it is hence of the same importance to *combine the results* in an appropriate manner.

As the production of the CMS silicon microstrip modules is distributed among several centres, it is furthermore important to guarantee the consistence of the results at different locations. Though the ARC system is used as a standardized readout system, the test box design is left to the different test centres. The results of the analysis should nonetheless be applicable for *all test centres* and all test stands.

Previous Fault Finding Algorithm

A preliminary version of a fault finding algorithm existed already prior to this analysis [50]. The algorithm is based on the results of about fifty pre-production modules. It is listed in appendix A.1 for comparison. In that fault finding algorithm all channels which exceed a certain threshold in a test get a specific *flag*. Up to four different thresholds are used per test. If a channel exceeds certain thresholds in an exclusive subset of tests, this channel is flagged as a fault of a particular type. For a safe identification of the type of fault, the signatures in up to twelve tests (three tests, in all four APV operation modes) have to match.

Using this algorithm for the evaluation of modules in the commencing mass production an unsatisfactory large number of channels was falsely flagged as “noisy” or “likely open”. Though the identification of pinholes and short-circuits worked satisfactorily, the distinction of different types of opens failed in 10 to 50% of the cases. Rare defects like defective pipeline cells or inverters were not considered by the fault finding algorithm.

A first inspection of the data revealed the necessity for a threshold tuning. In addition it implied, that a match of fault signatures was required between inappropriate

¹To identify for example the type of an open bond, it is not advisable to require a certain noise AND a certain pulse height AND a certain peak time AND a certain backplane pulse signal etc., in all four APV operation modes.

tests. This gave reason to the present, more elaborated analysis of the thresholds and the proper combination of results.

The fault finding algorithm according to [50] determined the tests of a *standard module test*, necessary for the qualification of a module. The standard module test requires measurements of the noise, the pulse shape, the pinhole test, the pipeline test, the functional test, and the I-V curve. For many modules of the commencing mass production for the CMS tracker only these tests were performed. Data of additional tests are mainly acquired at one test centre (Aachen) and thus less representative. To allow for a re-analysis of older data it is desirable that a reliable fault identification is possible using only results of a standard module test.

7.2 Preparation of the Analysis

7.2.1 The Dataset

For the tracker end cap ten different module geometries are used (cf. chapter 1.3). The modules of ring 1, ring 2 and ring 5 exist in two different types, “normal” and “stereo” modules. Concerning the data analysis, a distinction between these two types is not necessary. In the analysis a distinction is made between *seven different module geometries* according to the seven rings of a tracker end cap. Data of modules from other sections of the tracker are not considered.

In total, the data of approximately 1,000 ARCS ROOT file records, belonging to approximately 500 different modules, are considered. Module tests at cold, performed by some centres, are not considered. Only measurements at room temperature before or after the thermal cycling are used. Some modules were measured twice in different test centres. In such a case both measurements are considered in the analysis, too. Hence, for a lot of modules more than one dataset exist. The detailed numbers of datasets and the respective numbers of modules are listed in table 7.1.

If a dataset contained inconsistent or spoiled data, this dataset was not used for the analysis. Inconsistent data are e. g. data, where test results are spread over several records in the ROOT file. Spoiled data are e. g. a distorted noise behaviour, due to a low pedestal (cf. chapter 6.9), or an obviously failed fit to the LED measurement. Thereby it is assured that on one hand, channels classified as normal indeed show a normal behaviour and on the other hand, normal channels with a spoiled dataset stand out and indicate a problem during the data acquisition or pre-analysis of the data.

7.2.2 Fault Classification

For each of the more than 1,000 records the following test results were inspected *individually* for all four APV operation modes:

- Pedestal (cf. chapter 5.2.3),
- Common mode corrected noise (cf. chapter 5.2.3),
- Pulse height (cf. chapter 5.3.2),

geometry	centre	number of records per centre	total number of records	number of different modules
ring 1	Hamburg	100	269	102
	Aachen	169		
ring 2	Vienna	95	131	53
	Aachen	36		
ring 3	Karlsruhe	23	89	56
	Hamburg	26		
	Aachen	40		
ring 4	Zurich	162	256	191
	Strasbourg	22		
	Aachen	72		
ring 5	Santa Barbara	73	111	54
	Aachen	38		
ring 6	Santa Barbara	32	155	85
	Aachen	123		
ring 7	Strasbourg	9	54	40
	Aachen	45		
sum		1,065		581

Table 7.1: Quantity and origin of datasets used for the analysis.

- Peak time (cf. chapter 5.3.2),
- Rise time (cf. chapter 5.3.2),
- Gain slope (cf. chapter 5.4.2), mainly from Aachen data,
- LED test (cf. chapter 5.6.2),
- Pinhole difference (cf. chapter 5.7.3),
- Pinhole maximum (cf. chapter 5.7.3), and
- Sum of backplane pulse signals (cf. chapter 5.8.2), mainly from Aachen data.

According to the characteristics described in chapter 6 each channel with a deviating behaviour in the tests mentioned above is classified as a fault of a certain type. If no such classification is possible the conspicuous channel is marked as “unknown fault”. Due to the experience in the noise test (cf. chapter 6.9) APV edge channels represent an extra class. This enables a separate investigation of their behaviour and circumvents interferences with the data of normal channels. All other channels are characterized as normal channels.

The classification by eye is involved but time consuming. Nevertheless it allows a correct classification especially for cases where the signature does not match completely the expected one. Some ambiguities are possible in case of two or more neighbouring channels with a very low response to the calibration pulse (either neighbouring

dead channels or short-circuit). The identified classifications were stored in a file called `modulefaults_RX.txt` for all datasets of modules of ring X.

In many cases the identification could be verified, either with a microscope (in case of opens) or by the comparison with result tables (if the data of other test centres were used). If data of the QTC measurements were available in the database, they could be cross-checked with the classification as well (in case of short-circuits or pinholes).

7.2.3 Processing of the Measured Data

In general, no or only a few number of channels per module are of a certain type of fault. To assess the general behaviour of a fault in a certain test, it is useful to fill the corresponding data into a histogram. This is done for each module type separately. A dedicated evaluation program was thus implemented that reads all the results mentioned above for each module of a ring from the ARCS ROOT file. The program reads the `modulefaults_RX.txt` file to know the position of faulty channels in the data and their respective type. Different types of faults are assigned to different histograms. The data are processed in the evaluation program to compare different ways of data interpretation. Processing of data in a special manner means, that one of the following manipulations of data are done, before the results are filled into the histograms:

- *Absolute values (ABS)*: The absolute value is e. g. useful for the comparison of the total noise in a setup.
- *Percentage evaluation with respect to the APV median (PERC_0)*: All data are divided by the median value of the corresponding APV. The median is used as it is less influenced by outliers compared to the mean value. This consideration is useful for tests where only the ratio of test results is of interest (e. g. the pulse height of short-circuits is about 50 % the height of normal channels).
- *Percentage evaluation with respect to a polynomial fit (PERC_1 to PERC_3)*: A polynomial fit (1st to 3rd degree) is applied to the data of each APV, disregarding channels that are further than 30 % apart from the APV average. The fitted values for each channel are used as a prediction of the expectation value. The measured values are divided by these predicted data. This consideration was implemented as the average value of a pulse height measurement is a bad approximation for the expectation value, since all pulse height measurements show a distinct slope (see figure 5.6(a)).
- *Computation of the absolute deviations from the APV median value (ABSDEV_0)*: This consideration is e. g. useful for the evaluation of peak time data, where the absolute and percentage values are less significant since they depend on the adjusted latency range used in the pulse shape test (cf. chapter 5.3.1).
- *Computation of the absolute deviations from a polynomial fit (ABSDEV_1 to ABSDEV_3)*: A polynomial fit (up to 3rd degree) is applied to the data of each APV disregarding channels that are further than 30 % apart from the APV average.

The deviations are the difference between the value predicted by the fit and the measured value.

- Computation of the *absolute deviations from the median of a calibration injection group (CALGR)*: In this calculation the median of the 16 channels within a calibration injection group is used as the expectation value. The deviations considered are the differences between this expectation value and the measured value. The intention of this evaluation is the removal of the structure repeating with every 8th strip (see e. g. figure 5.6(b)).
- *Sigma Evaluation (SIGMA)*: The width σ of the distribution of measured values of an APV with respect to their mean value is determined in this test. The deviation of the value of a single channel from the mean value of the APV is expressed in multiples of σ .

The results are stored in an evaluation ROOT file. The evaluation ROOT file is structured such that for each test and each type of processing in each APV mode a specified histogram exists for each type of fault (see figure 7.1). Thereby it is possible to

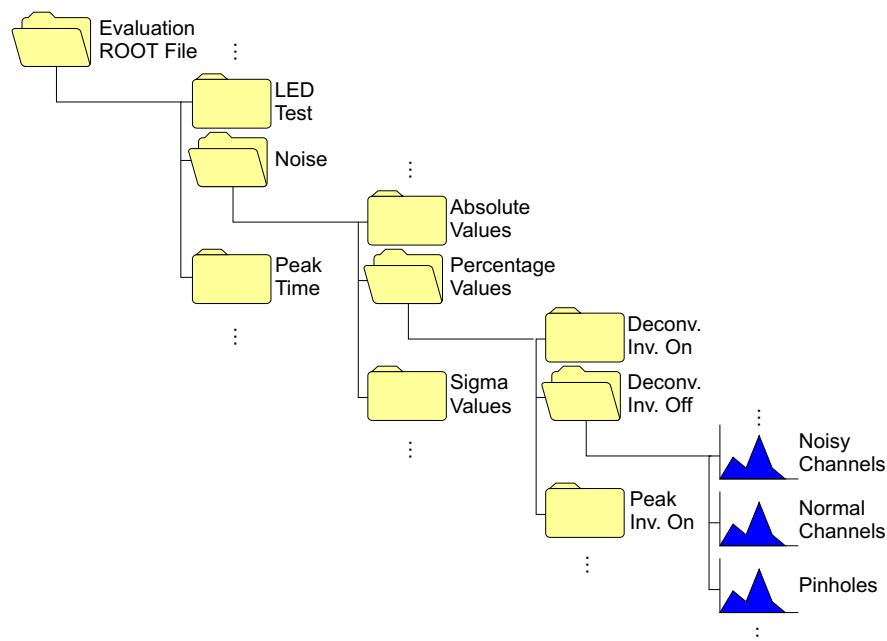


Figure 7.1: Structure of the evaluation ROOT file.

investigate the most appropriate way of processing the data, that gives the best separation between normal and faulty channels or between two different types of faults. Examples of different processing techniques of peak time data are shown in figure 7.2. Another example of resulting histograms is shown in figure 7.3, where the histograms of the absolute values of the noise (deconvolution mode, inverter off) of normal channels, sensor-sensor-opens and pitch adapter-sensor-opens are superimposed. Though a grouping of channels of a type is visible, the figure illustrates that the noise measurement is not well suited to distinguish between normal channels and the two different types of opens.

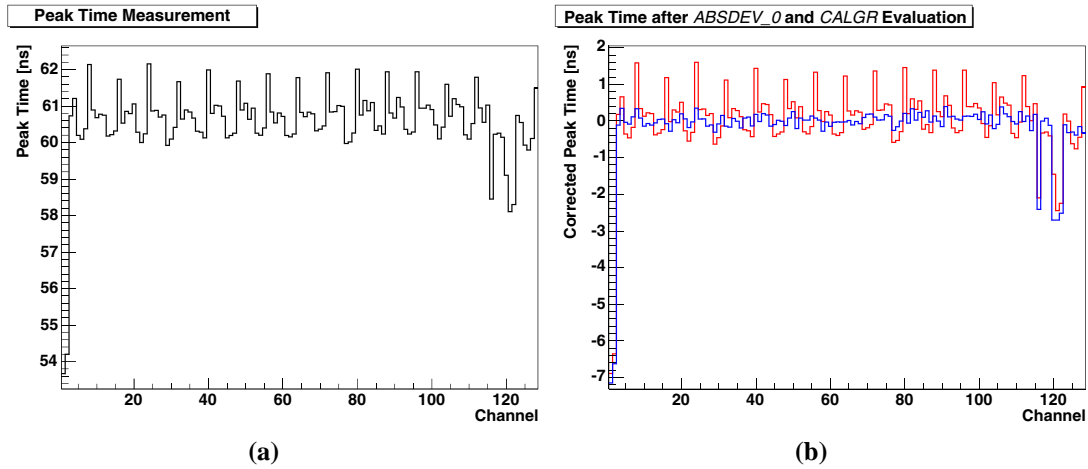


Figure 7.2: Different processing techniques of the peak time data. (a) The absolute values (ABS) of the measured peak time. (b) The absolute deviations from the APV median value of the peak time (red curve) in comparison to the data corrected by the median on the calibration injection group (blue curve). In the latter case the distribution of normal channels is narrower. This simplifies the separation of bad channels.

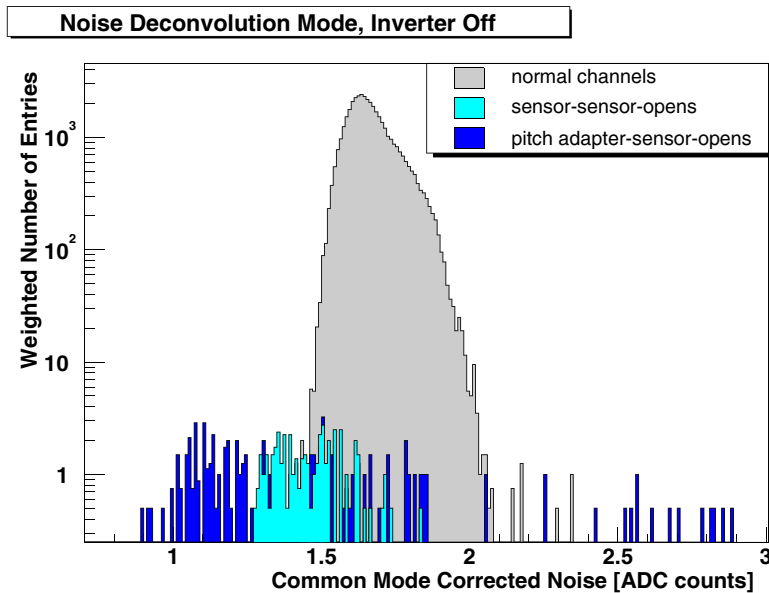


Figure 7.3: Superimposed noise histograms (deconvolution mode, inverter off) of normal channels, sensor-sensor-opens and pitch adapter-sensor-opens of ring 5. Knowing only the noise value of a channel gives no reliable information about the state of a channel.

7.2.4 Weighting of the Data

To avoid a dominant influence of a single module that was measured several times, each module is counted with an overall weight of 1. If a module is measured several times at different locations, the weight is portioned such that each centre gets the same overall weight. For each centre the weight is portioned such that each measurement gets the same weight. For example:

test centre	number of tests	overall weight	weight of a single measurement
Zurich	1	0.5	0.5
Aachen	2	0.5	0.25

Therefore the histograms contain also entries smaller than 1.

7.3 Evaluation of the Separation of Faults

To determine the most appropriate way to separate a fault from normal channels or two different faults from each other in some thousands of histograms² an objective quantification of the separation is required. For that purpose two criteria were introduced that quantify the separation of two distributions stored in the histograms in the evaluation ROOT file. The separation is quantified only for fault histograms belonging to the same ring, the same test, the same processing procedure, and the same APV mode. Both separation criteria are discussed in the following.

7.3.1 Distance Criterion

The first criterion assesses the distance between the mean values of two histograms with respect to their RMS. The criterion for the separation between both distributions is defined as:

$$F = \frac{|mean_1 - mean_2|}{RMS_1 + RMS_2}, \quad (7.1)$$

where $mean_i$ is the mean value and RMS_i is the RMS³ of histogram i ($i=1$ or 2). F is larger if the mean values of two distributions of a given width are further apart and if the RMS of one (or both) histograms is smaller for a given difference of mean values.

It is thus reasonable to attribute *large values of F to a good separation* between two distributions (see also figure 7.4).

² 27 different ring geometries \times 10 different test \times 11 different processing techniques \times 4 APV operation modes \times 10 different fault classifications \approx 30,000 different histograms.

³The RMS is used instead of a fit since most of the fault histograms have only a few entries. For a few number of entries a fit is meaningless. Even if a histogram contains some ten or hundred entries a meaningful fit requires an adequate binning that is difficult to automate.

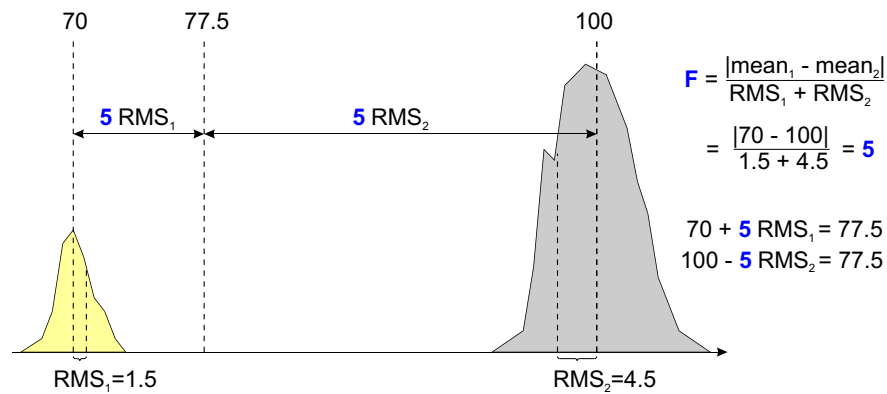


Figure 7.4: Distinction of two distribution according to the first separation criterion.

Properties of the Distance Criterion:

The measure F gives a number of results that match the experiences gained before, e. g.:

- F is (of all module geometries and all APV operation modes) below 0.25 on average for the separation of opens from normal channels in the pedestal test. Such a low value of F means that the pedestal test is not suited for the discrimination of opens from normal channels.
- F is about 2.5 on average for the distinction of opens (of any type) from normal channels in the noise test. This implies a noticeable but bad separation between opens and normal channels (see figure 7.3).
- F is about 5 on average for the distinction of pinholes from normal channels in the noise test. Pinholes are hence further separated from normal channels than opens (compare e. g. figure 6.3 with 6.8(b)).
- F is always larger than 7 for the distinction of pinholes from normal channels in the pinhole test. Thus the pinhole test is better suited to identify pinholes than the noise test.

Nonetheless the value F alone is not adequate since it discounts some important aspects of the measured distributions:

- The results of some tests are systematically non-Gaussian distributed, e. g. the absolute deviations from the APV average of the peak time (see figure 5.6(b)). The RMS of distributions with a few number of entries can be dominated by a few outliers. This is in principle the case for all histograms except for the normal and edge channel histograms which have hundreds or thousands of entries. In such a case the RMS value is large though the distribution can be constricted to a comparably small range. Thereby the value of F underestimates the chances for a separation of two histograms.

- If a histogram with a large mean value and a tail to larger values, is compared to a histogram with a small average value and a tail to smaller values, the measure F can be very low, though a clear separation of both histograms is possible.
- A reasonable threshold should be chosen such that as many values as possible belonging to different faults are on different sides of the threshold. The value of F contains no information about how well a threshold separates two histograms.

An overlap criterion was thus introduced which also takes the outliers into account and provides information about the adequacy of a chosen threshold.

7.3.2 Overlap Criterion

The second criterion assesses the fraction of a histogram that overlaps with data from another histogram. For each histogram in the evaluation ROOT file the position of the maximum and minimum entries is determined. These positions are denoted as min_i and max_i of the histogram i ($hist_i$). In the comparison of two histograms three different cases have to be distinguished:

1. *No overlap*, i. e. $min_1 < max_1 < min_2$:

This is the easiest case since both histograms do not overlap. Thus the measure of overlapping OL of histogram 1 with histogram 2 is zero. In such a case both histograms can be separated from each other by a threshold at any position between max_1 and min_2 .

2. *Partial overlap*, i. e. $min_1 < min_2 \leq max_1 < max_2$:

This case is illustrated in figure 7.5(a). In such a case the overlap of the histograms is calculated using thresholds at the overlap limits min_2 and max_1 . If a cut is now applied at max_1 , the value

$$OL_1 = \frac{\sum_{min_2}^{max_1} hist_2}{\sum_{min_2}^{max_2} hist_2} \quad (7.2)$$

indicates the fraction of channels of fault type 2 that would be flagged falsely as type 1. If a cut is applied at min_2 the value

$$OL_2 = \frac{\sum_{min_2}^{max_1} hist_1}{\sum_{min_1}^{max_1} hist_1} \quad (7.3)$$

indicates, the fraction of fault type 1, that would be flagged falsely as type 2.

3. *Total overlap*, i. e. $min_2 \leq min_1 < max_1 \leq max_2$:

In this case histogram 1 is completely included in histogram 2 (see figure 7.5(b)). In such a case the overlap of the histograms is evaluated using thresholds at the limits of the inner histogram min_1 and max_1 . If a cut is applied at max_1 the value

$$OL_1 = \frac{\sum_{min_2}^{max_1} hist_2}{\sum_{min_2}^{max_2} hist_2} \quad (7.4)$$

indicates the fraction of channels of the type of histogram 2 that would be flagged falsely as type 1.

If a cut is applied at min_2 the value

$$OL_2 = \frac{\sum_{min_1}^{max_2} hist_2}{\sum_{min_2}^{max_2} hist_2} \tag{7.5}$$

indicates again, how many of the channels of the type of histogram 2 would be flagged falsely as type 1.

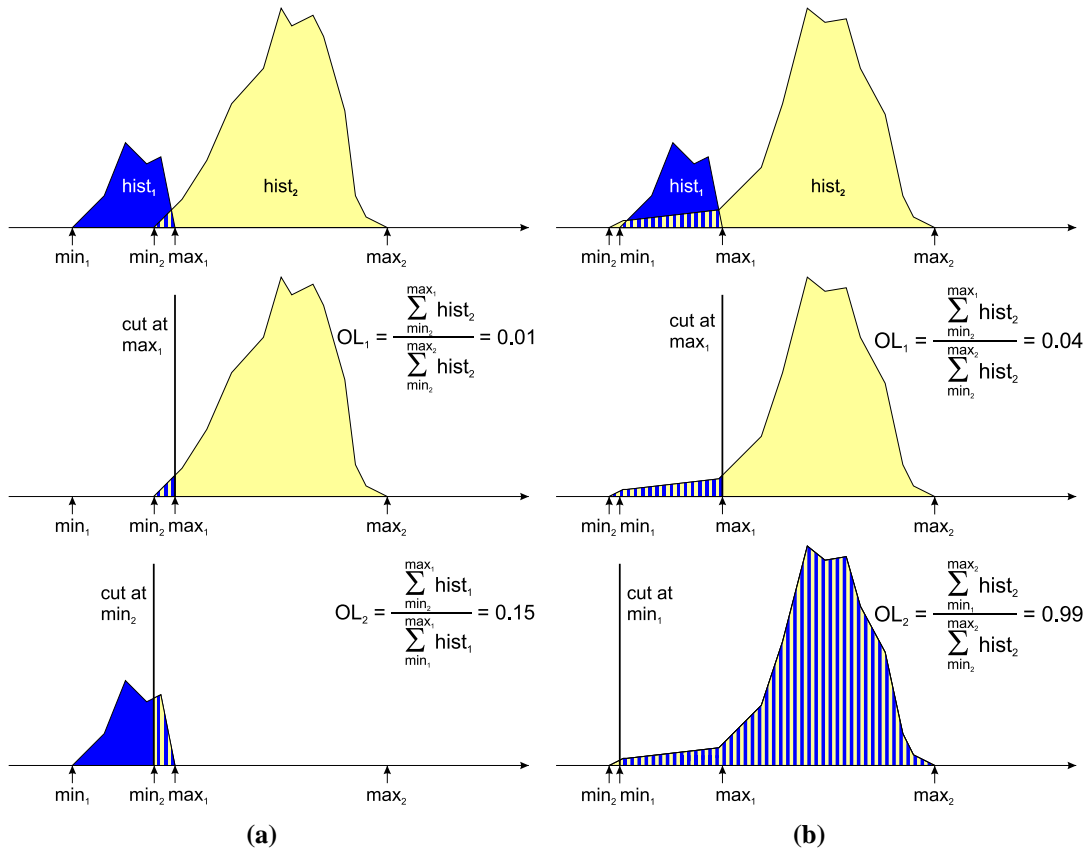


Figure 7.5: Illustration of the definition of the overlap criterion (a) for the case of a partial overlap, (b) for the case of a total overlap of two histograms.

Properties of the Overlap Criterion:

In case of an overlap between two histograms two different values of OL exist. A reasonable separation between two histograms can be obtained if one of the two values is low. The value of OL_i depends even more on outliers in the histograms. A single entry in the histogram can alter the situation from the non-overlapping to the total overlapping case. Though the definition of OL_i uses thresholds, there is no direct information about the appropriateness of the threshold for the separation of two histograms. A

proper threshold depends not only on the values of OL_i but also on the total number of falsely flagged channels and the compared histograms⁴. If one of the two histograms represents the normal channels, it is often advisable to apply a cut such that the number of wrongly flagged normal channels is minimized. Such a procedure is maintainable with the argument, that a channel that appears in all tests like a normal channel must be regarded as a normal channel, as long as no test exists where the channel shows a deviating behaviour. The criteria for the qualification of the separation are thus used to evaluate the suitability of a test but *not* for the threshold definition. For the best suited tests the thresholds must still be applied by hand.

In the comparison of two evaluations with equal overlap of the histograms of the same faults the one with the larger value of F is more appropriate. If the distance F between two histograms has the same value in two different tests, the one with the lower overlap is preferable. In particular the quantification allows the comparison of the application of different processing procedures to equal test results.

7.4 Results of the Analysis

The aim of the evaluation described in the previous sections is, to find a set of tests where a distinction between faulty and normal channels or two types of faulty channels is possible for all module geometries. Only those tests are considered for a pre-selection that fulfil certain selection criteria. The average value of F over all module geometries has to be larger than 3. The overlap between two investigated histograms must be below 5 % for at least one of the affected geometries.

7.4.1 Tests for the Safe Identification of Opens

The identification of opens is subdivided into three parts according to three different kinds of opens: pitch adapter-sensor-opens on one-sensor-modules, on two-sensor-modules and sensor-sensor-opens on two-sensor-modules. Only separations with respect to normal channels are considered.

Pitch Adapter-Sensor-Opens on One-Sensor-Modules:

The analysis is based on 128 pitch adapter-sensor-opens that are present on modules of ring 1 to ring 4. The analysis verified that the common mode subtracted noise is a feasible but not the best test for the identification of opens. Independent of the specific processing of the noise data, the separation is better in the peak modes. The best results can be obtained in tests that process the data with respect to the APV average noise. The separation in the absolute values of the noise is worse. Nonetheless the overlap values are close to zero for all methods of processing the data. Tests marked

⁴To flag 5 out of 20 opens falsely as normal channels is not as bad as flagging 1,000 out of 20,000 normal channels as faulty, though the fraction of wrongly identified channels is smaller in the latter case.

with an asterisk (*) are for comparison with tests required in the previous fault finding algorithm [50].

Separation: normal channels vs. pitch adapter-sensor-opens on one-sensor-modules				
test	processing	APV mode	distance criterion F	$OL_i < 0.05$ in % of the histograms
noise	<i>PERC_0</i> to 3	peak	4.2	75
	<i>ABSDEV_0</i> to 3	peak	4.1	75
	<i>ABS</i> (*)	dec/peak	1.9/3.0	50/75

A more appropriate test is the pulse height in the deconvolution modes. Measured in F , the best separation is given by percentage evaluations of data processed with a polynomial fit. The overlaps are the closest to zero for a polynomial fit of first degree (*PERC_1*). A correction with respect to the calibration group median (*CALGR*) has a worse distance criterion, but *no* overlap ($OL = 0$) between normal channels and opens in 100 % of the cases. Such cases of “perfect” separation are in the following indicated by a bold **100**.

Comparable results are obtained with the gain slope measurements. One gets the largest values of F in the deconvolution mode measurements which are corrected with a polynomial fit. The least overlap is present in *CALGR* processed data.

Separation: normal channels vs. pitch adapter-sensor-opens on one-sensor-modules				
test	processing	APV mode	distance criterion F	$OL_i < 0.05$ in % of the histograms
pulse height	<i>PERC_0</i> (*)	dec/peak	4.0/2.1	100/75
	<i>PERC_1</i> to 3	dec	~6.5	100
	<i>CALGR</i>	dec	4.8	100
gain slope	<i>PERC_0</i>	dec	3.4	75
	<i>PERC_1</i> to 3	dec	~5.9	75
	<i>CALGR</i>	dec	6.4	75

The most appropriate test is the peak time. The overlaps are zero, almost independent from the way of processing. The largest values of F can be obtained if the data are processed according to the *PERC_1* to 3 or the *CALGR* procedure. The rise time is less appropriate. F is about 2 to 3 times smaller in all modes although an overlap of zero is present in almost all processed data.

Separation: normal channels vs. pitch adapter-sensor-opens on one-sensor-modules				
test	processing	APV mode	distance criterion F	$OL_i < 0.05$ in % of the histograms
peak time	<i>ABSDEV_0</i> (*)	dec/peak	3.8/4.5	100/100
	<i>CALGR</i>	dec/peak	6.7/7.7	100/100
	<i>PERC_1</i>	dec/peak	8.2/9.6	100/100

Pitch Adapter-Sensor-Opens on Two-Sensor-Modules:

This analysis is based on the data of 327 pitch adapter-sensor-opens present in the ROOT file records of modules of ring 5 to ring 7. Due to the pronounced common mode dependency, the noise of pitch adapter-sensor-opens takes a wider range of values. Compared to one-sensor-modules the separation in the noise is worse. But the influence of the large missing strip capacitance, improves the separation for all tests using the APV calibration circuit. In particular this applies to the gain slope measurement with data processed according to the procedures *PERC_1* to *3* and all peak time evaluations. Appropriate tests are summarised in the following table.

Separation: normal channels vs. pitch adapter-sensor-opens on two-sensor-modules				
test	processing	APV mode	distance criterion F	$OL_i < 0.05$ in % of the histograms
noise	<i>ABS</i> (*)	dec/peak	0.5/2.8	0/67
pulse height	<i>PERC_0</i>	dec/peak	4.6/3.0	100/100
	<i>PERC_1</i>	dec/peak	~6.1/~4.1	100/100
peak time	<i>ABSDEV_0</i> (*)	dec/peak	3.6/7.1	100/100
	<i>CALGR</i>	peak	11.4	100
	<i>PERC_1</i>	peak	10.9	100
gain slope	<i>CALGR</i>	dec	11.2	100
	<i>PERC_1</i>	dec	11.6	100

Sensor-Sensor-Opens on Two-Sensor-Modules:

This analysis is based on 288 sensor-sensor-opens present in the data of modules of ring 5 to ring 7. Here the separation in the noise test is as bad as for the case of pitch adapter-sensor-opens. But the same tests that are appropriate for the identification of pitch adapter-sensor-opens are also suited for a separation of sensor-sensor-opens from normal channels. Nonetheless the separation in all tests using the APV calibration circuit is less pronounced compared to pitch adapter-sensor-opens. The best distinction can be derived from the peak time and the gain slope data. The results are summarised in the next table.

Separation: normal channels vs. sensor-sensor-opens on two-sensor-modules				
test	processing	APV mode	distance criterion F	$OL_i < 0.05$ in % of the histograms
noise	<i>ABS</i> (*)	dec/peak	1.1/2.0	0/67
pulse height	<i>PERC_0</i> (*)	dec/peak	2.7/2.0	100/33
	<i>PERC_1</i>	dec/peak	3.7/2.7	100/50
peak time	<i>ABSDEV_0</i> (*)	dec/peak	1.9/4.3	0/100
	<i>CALGR</i>	peak	7.3	100
	<i>PERC_1</i>	peak	7.1	100
gain slope	<i>CALGR</i>	dec	6.0	100
	<i>PERC_1</i>	dec	8.7	100

7.4.2 The Separation of Pitch Adapter-Sensor-Opens from Sensor-Sensor-Opens

The separation of pitch adapter-sensor-opens from sensor-sensor-opens was one of the most serious problems of the fault finding algorithm described in [50]. The problem is related to the fact, that all kinds of opens show a qualitatively similar behaviour in all tests. A reliable separation requires tests, in which both types show a significantly, quantitatively different behaviour. Among other things, in the previous fault finding algorithm [50] a match of the determined open type in the absolute values of the noise was required for all 4 APV modes, while the pulse height must not be low. The following table demonstrates the difficulty of separating both types of opens in the noise and the pulse height measurement.

Separation: pitch adapter-sensor opens vs. sensor-sensor-opens on two-sensor-modules				
test	processing	APV mode	distance criterion F	$OL_i < 0.05$ in % of the histograms
noise	<i>ABS</i> (*)	dec/peak	0.1/1.2	0/0
pulse height	<i>PERC_0</i> (*)	dec.	2.3/1.2	33/0

The separation in the noise measurement is bad due to the strong common mode dependency of the noise. That causes the overlaps and make the RMS of the histograms very large⁵. Some results of appropriately processed test results for the distinction of pitch adapter-sensor-opens and sensor-sensor-opens are given in the following table:

Separation: pitch adapter-sensor opens vs. sensor-sensor-opens on two-sensor-modules				
test	processing	APV mode	distance criterion F	$OL_i < 0.05$ in % of the histograms
peak time	<i>ABSDEV_0</i> (*)	peak	3.7	100
	<i>CALGR</i>	peak	5.3	100
	<i>PERC_1</i>	peak	5.4	100
gain slope	<i>CALGR</i>	dec	5.9	100
	<i>PERC_1</i>	dec	6.1	100

Obviously both, the correction with respect to the calibration group median and corrections with a polynomial fit, moderating the slope in the data of calibration measurements, improve the separation between the two types of opens significantly.

The backplane pulse test has a very good separation power of both types of opens (see figure 6.4(b)) only for a single setup, where the pulse has always the same size. If the setup is changed, the backplane pulse also changes. If data of different setups are considered in one analysis the separation between both types is of the order of $F \leq 2$. If a single setup is used, values of $F > 7$ can be obtained.

⁵At the time [50] was released, data from only a few modules on very homogeneous setups were available. These data implied a clear separation of faults in the noise test.

Conclusion:

The *CALGR* processed data of the peak time in peak mode are chosen as the *most appropriate* for the separation of both types of opens and from normal channels. For all geometries and all types of opens a gap of more than 2 ns is present between two types of faults. This allows a simple and save choice of a threshold close to the middle of the gap. Figure 7.6 shows an example of the good separations of normal channels from sensor-sensor-opens and pitch adapter-sensor-opens using the *CALGR* evaluation. This separation should be compared to the large overlaps between all three types of channels in the noise measurement (figure 7.3). In fact, also some short-circuited channels have a similar peak time. For the distinction from short-circuited channels one should thus require the pulse height not to be below a certain threshold (cf. section 7.4.3).

The good result in the *PERC_I* processed data of the peak time is due to the very consistent data acquisition (all measurements done in the same latency range). If this latency range would be changed at some point in time (e. g. to save testing time) the separation would not work properly. In that sense the *CALGR* processed data in peak time gives the more stable separation, as it is independent of these data acquisition parameters.

The gain slope measurements also allow for a good separation. The most plausible explanation for its advantage with respect to the pulse height measurement is the good linearity of the gain measurements and the simpler, linear fit that is applied to the data. If the algorithm would depend on the gain test data, the re-analysis of older ARCS ROOT files would not be possible. Therefore the gain slope is not used in the fault finding algorithm.

7.4.3 Tests for the Safe Identification of Short-Circuits

The behaviour of short-circuits is examined for all module types at once. In total 128 short-circuited channels are present in the data of rings 1 to 7. Short-circuits have a clear significance in only a few number of tests. The noise measurement in peak mode, inverter off, is the only feasible test with an at least acceptable separation, that does not make use of the APV calibration circuit. The clearest signature can be obtained in measurements of the pulse height and the gain slope. Percentage evaluations are best suited in both cases. The separation is always better in measurements with activated inverter. Results of feasible processing procedures are summarised in the next table.

Separation: normal channels vs. short-circuited channels on all modules				
test	processing	APV mode	distance criterion F	$OL_i < 0.05$ in % of the histograms
noise	<i>ABS</i> (*)	peak inv. off	2.0	28
pulse height	<i>PERC_I</i>	dec/peak	3.0/3.2	93/93
gain slope	<i>PERC_I</i>	dec/peak	3.2/3.8	80/100
	<i>CALGR</i>	dec/peak	3.2/3.7	90/100

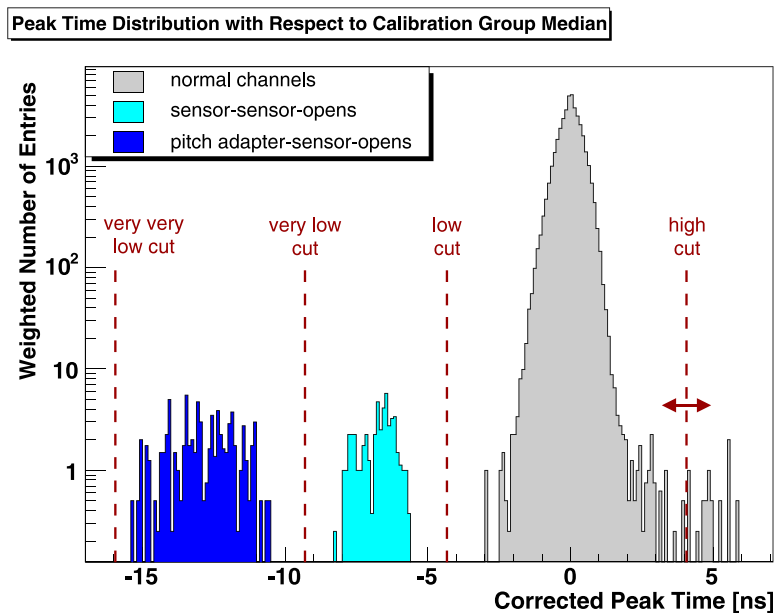


Figure 7.6: Superimposed peak time histograms (peak mode, inverter on) of normal channels, sensor-sensor-opens and pitch adapter-sensor-opens of ring 5 after the application of a *CALGR* correction. The three types are easily separable by the application of different low cuts. (These low cuts will be denoted as *LC_1*, *LC_2* or *LC_3*, cf. section 7.6). A high cut can be applied at the upper edge of the histogram of the normal channels to mark obvious deviations from the expected behaviour.

Crosstalk measurements cannot be evaluated within the analysis⁶. It can be stated that all normal channels show a crosstalk whose integral has an opposite sign than the average integral over the pulse shape. A crosstalk measurement having the same sign as the calibration signal thus indicates a failure on a (next-to-)neighbouring channel.

Conclusion:

Short-circuits can be identified safely only by their pulse height that has to be below a threshold for two or more (next-to-)neighbouring channels. A combination of the conspicuousness in all four APV operation modes is advisable, since the pulse height of short-circuited channels can be spread over a wide range (see figure 7.7).

The requirement for an abnormal noise behaviour on at least one of the two (or more) channels seems to be fulfilled already by the consideration of the noise in peak mode, inverter off. A combination of the conspicuousness in the noise measurements of all four APV operation modes is nonetheless advisable.

Though the gain slope is the best measure to separate short-circuited channels from opens, these data cannot be used since this would impede the re-analysis of older data.

⁶The crosstalk signal of a channel classified as short-circuited to another, is filled in the corresponding histograms for short-circuited channels independent from whether the next to right, the right, the left, or the next to left channel is the short-circuit partner. Thereby data get mixed and impede a correct evaluation.

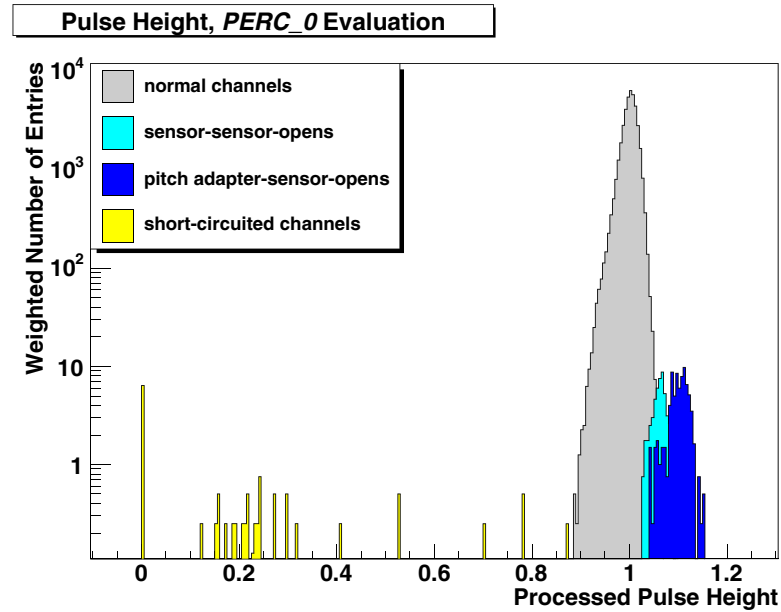


Figure 7.7: The relative pulse height (*PERC_0*) of short-circuited channels (Ring 5, peak mode, inverter on). The relative pulse height of pitch adapter-sensor-opens and sensor-sensor-opens is shown for comparison.

7.4.4 Tests for the Safe Identification of Dead Channels

This analysis is based on the data of 114 dead channels in all records.

Dead channels are comparably easy to separate from normal channels, due to their clear signature in a number of tests. Good separations from normal channels can be obtained in the noise test, the pulse height measurement and the gain slope measurement. In the noise measurements the separation is mostly better when the inverter is activated.

For dead channels the separation in the pulse height and gain slope measurements is very good. The clear separation in the pulse shape measurement is partially imitated by the fact, that the pulse height is set to zero, if a certain value is not exceeded. If this applies to all entries in a histogram, the mean value of the histograms and the RMS are both zero in all processing procedures based on percentage and absolute evaluations.

The distinction of dead channels from pinholes requires the consideration of the maximum measured pulse amplitude during the pinhole test (see section 7.4.6). If this value is close to zero, a dead channel is present. There exists no other fault with this signature in the pinhole test.

Results of feasible tests for the identification of dead channels are listed in the next

table.

Separation: normal channels vs. dead channels on all modules				
test	processing	APV mode	distance criterion F	$OL_i < 0.05$ in % of the histograms
noise	<i>ABS</i> (*)	dec/peak	7.3/7.3	100/100
pulse height	<i>PERC_0</i> (*)	dec/peak	36/56	100/100
gain slope	<i>PERC_0</i>	dec/peak	19/28	100/100
pinhole maximum	<i>ABS</i>	peak inv. off	15	100

Conclusion:

Dead channels are easy to spot as bad channels in the noise, the pulse height, the gain slope and the pinhole test. The signature of dead channels in the pinhole maximum evaluation is in principle significant enough. Nonetheless, a low noise or a low pulse height should be required additionally.

7.4.5 Tests for the Safe Identification of Pinholes

This analysis is based on the data of 109 pinholes⁷ from modules of rings 1 to 7.

Pinholes, in particular resistive pinholes, have a clear signature in the noise test, the pulse height measurement and the gain slope measurement. In the noise measurements the separation is usually better, if the inverter is activated.

Compared with dead channels, pinholes have slightly worse separation values. This is due to threshold pinholes that show a behaviour of normal channels in all tests but the pinhole test. Thereby the RMS of the histograms and the overlaps are increased. Some average values are summarised in the next table. Pinholes have the clearest signature in the evaluation of the pinhole difference. In addition the pinhole test is the only test that allows the detection of threshold pinholes.

Separation: normal channels vs. pinholes on all modules				
test	processing	APV mode	distance criterion F	$OL_i < 0.05$ in % of the histograms
noise	<i>ABS</i> (*)	dec/peak	5.5/4.7	70/60
pulse height	<i>PERC_0</i> (*)	dec/peak	19/26	70/70
gain slope	<i>PERC_0</i>	dec/peak	19/26	80/80
pinhole difference	<i>ABS</i> (*)	peak inv. off	9	100

⁷Many pinholes known from the sensor database stay unbonded and appear as a open bond.

Determination of the Pinhole Location:

The leakage current of the module, at which a channel with a pinhole reaches its maximum pulse amplitude in the pinhole test, is correlated to the sensor on which a pinhole is located. Using the model described in chapter 5.7.1, the predicted currents corresponding to the maximum measured pulse amplitude, are about 130 μA for a pinhole on the far sensor and about 260 μA for a pinhole on the near sensor.

During the analysis also the leakage current at the maximum measured pulse amplitude is determined. Most expressively are the data of ring 7 modules, containing 70 pinhole measurements⁸. The distribution of the leakage currents is shown in figure 7.8.

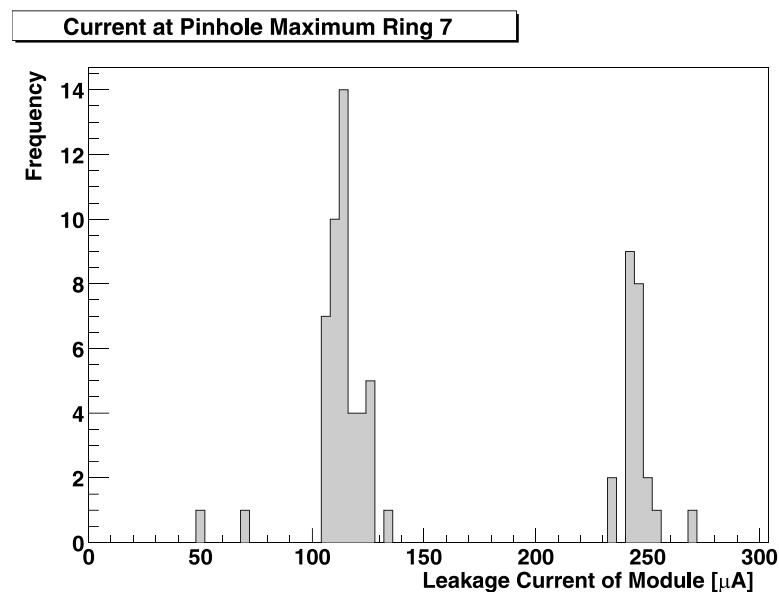


Figure 7.8: The currents corresponding to the maximum measured pulse height during the pinhole test of ring 7 modules. The two peaks are attributable to the two different sensors on which a pinhole is present.

Two clear peaks with mean values of 115 μA and 246 μA are observed. This matches well with the expectations. The little discrepancies between measured and expected mean values can be due to different values of the poly-silicon resistors, slightly different operating points of the APV preamplifiers and the simple evaluation of the point of maximum measured pulse amplitude⁹.

The histogram contains entries from 16 different modules with pinholes. Sensor data of the C_{AC} and $I_{Di\text{el}}$ measurements (cf. chapter 2.6.1) were available in the database for twelve of these modules, corresponding to 49 of the 70 entries. Only 25 entries (on seven modules) could be attributed to defects that were present on the

⁸Contrary to other tests, modules which were measured two or three times are counted with two or three entries of weight 1 in this histogram. Many pinholes are thus counted twice.

⁹Only the point of the largest pulse amplitude is considered. Since each point is the average of only five measurements, the measured amplitude at a certain LED intensity (i. e. at a certain leakage current of the module) has an error of the order of one ADC count.

sensor at the time of the sensor test, i. e. before the module was assembled. For all these entries the measured current at the maximum measured pulse amplitude matches with the expectation due to the affected sensor. The remaining 24 pinholes were all intentionally created on six of the sensors for test purposes by a bond connection between the AC and DC of a strip.

Conclusion:

Pinholes have a unique signature in the pinhole test. Due to the simple evaluation of the pinhole difference, the test alone is nonetheless not adequate to identify pinholes. Extremely noisy channels or dead pipeline cells can cause large differences in the pinhole difference test (cf. chapter 6.6 and 6.8). For the identification of a pinhole it is therefore advisable to require in addition a low noise (for resistive pinholes) or a normal noise (for threshold pinholes) and properly working pipeline cells for the respective channel.

It seems possible to localize pinholes by the leakage current that corresponds to the maximum measured pulse height during the pinhole test. In case of a pinhole on the far sensor only this sensor has to be unbonded. The sensitive area on the near sensor remains connected.

7.4.6 The Separation of Dead Channels and Pinholes

Results of the separation between both types are based on much less data, since more than 100 pinholes are located on modules of ring 2, ring 6 and ring 7, while more than 100 dead channels are concentrated on modules of ring 1 and 4.

Due to their equal impact on the APV input preamplifier, the noise, pulse height and gain slope measurements are not suited for the distinction between dead channels and pinholes.

Threshold pinholes are detectable only in the pinholes test. In addition, this test is the only test, where dead channels and resistive pinholes show a different behaviour. In fact, the behaviour in the pinhole test is used for classification of the type of fault (cf. section 7.2.2). The separation values for various tests are summarised in the next table.

Separation: pinholes vs. dead channels on all modules				
test	processing	APV mode	distance criterion F	$OL_i < 0.05$ in % of the histograms
pinhole difference	<i>ABS</i> (*)	peak inv. off	32	100
pinhole maximum	<i>ABS</i>	peak inv. off	20	100

Conclusion:

Pinholes and dead channels can be distinguished by their different behaviour in the pinhole test. Pinholes have a large signal in the pinhole difference evaluation. Dead channels are the only type of fault that have a very low signal in the pinhole maximum evaluation.

7.4.7 Identification of Defective Inverters

The ratio of pulse height measurements with activated and deactivated inverter (for deconvolution and peak mode separately, cf. chapter 6.5) is an appropriate indicator of defective inverters. Good results can be obtained with all processing techniques. The *PERC_0* processing was found to be very suitable¹⁰. There, the pulse height of a channel is first divided by the median pulse height of the APV, giving for each channel a relative pulse height. The ratio of the relative pulse height of measurements with inverter on and off is computed. For normal channels and all other types of defects (except short-circuited channels and some noisy channels) this ratio is close to 1, with a variation of less than 10 % as indicated in figure 7.9.

A high noise during the data acquisition of the pulse shape data can spoil the pulse height measurement. Therefore a looser threshold of 25 % is chosen as appropriate, i.e. all ratios between 0.75 and 1.25 are considered as normal channel signatures.

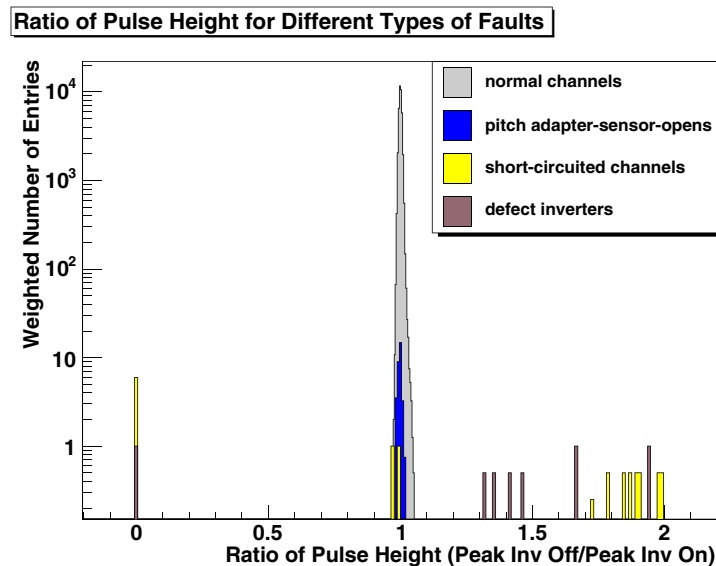


Figure 7.9: The signature of defective inverters in the evaluation of the ratio of pulse height measurements with activated and deactivated inverter. Entries at zero are due to the calculation algorithm.

¹⁰An evaluation of the overlap and distance criteria was not used to assess the appropriateness of a processing procedure, due to the fact, that a total overlap of the histograms is present in almost all cases. The calculated ratio is in general larger than 1. But it is set to 0, if the pulse height with activated inverter is 0 (to avoid division by zero).

Defective inverters can be distinguished from short-circuited channels by the fact that short-circuits affect two (next-to-)neighbouring strips. In addition defective inverters reach the pulse height of normal channels if the inverter is deactivated which is not the case for short-circuited channels.

7.4.8 Identification of Defective Pipeline Cells

The irregularities in the pinhole and the pulse shape tests (see figure 6.10) caused by dead pipeline cells are not used for their identification. For the determination of bad pipeline cells the pipeline noise and calibration amplitude matrices (see figure 5.8) are considered. The noise (calibration amplitude) of each cell is divided by the median noise (median calibration amplitude) of all cells of a channel, resulting in a relative noise (relative calibration amplitude). An analysis comparing different processing procedures was not made. The distribution of these relative values is much wider in case of the noise matrices. This is shown in figure 7.10 for a sample of 25 modules.

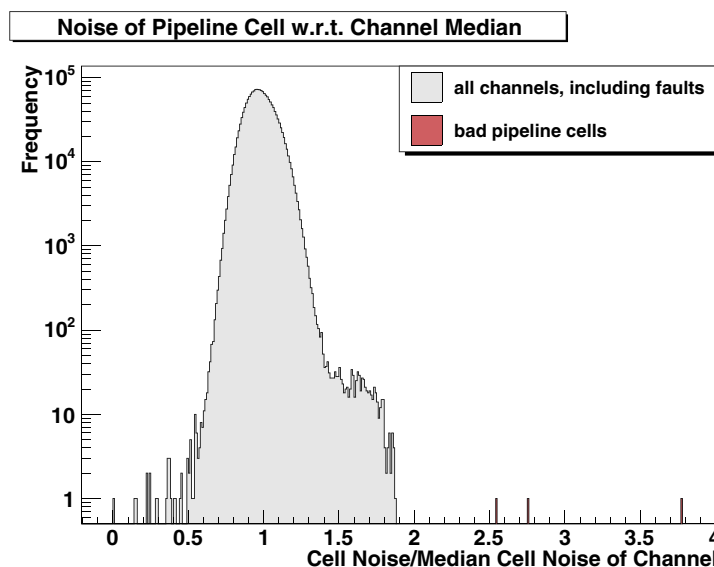


Figure 7.10: The distribution of the relative noise of pipeline cells with respect to the median noise of a channel. The distribution of normal cells contains a fraction of cells from noisy channels (in the range of 1.4 to 1.9).

The values range from approximately 0.5 to 2.0. Only a very low number of cells is outside this range. Cells with a noise below one half of the channel median noise are not marked since a low noise of a cell is in principle desirable. If the cell does indeed not respond to a charge signal, it will stand out in the calibration amplitude matrix. A cell is marked as a bad cell if the relative noise of that cell exceeds a value of 2.5.

In the calibration amplitude matrices the distributions of values are narrower. This is shown for a sample of 16 modules in figure 7.11. Channels with a median value smaller than 10 are excluded, since small fluctuations of the calibration amplitude of some ADC counts would give large relative amplitudes. The probability of missing a fault due to this exclusion criterion is not significant. Channels with such a low

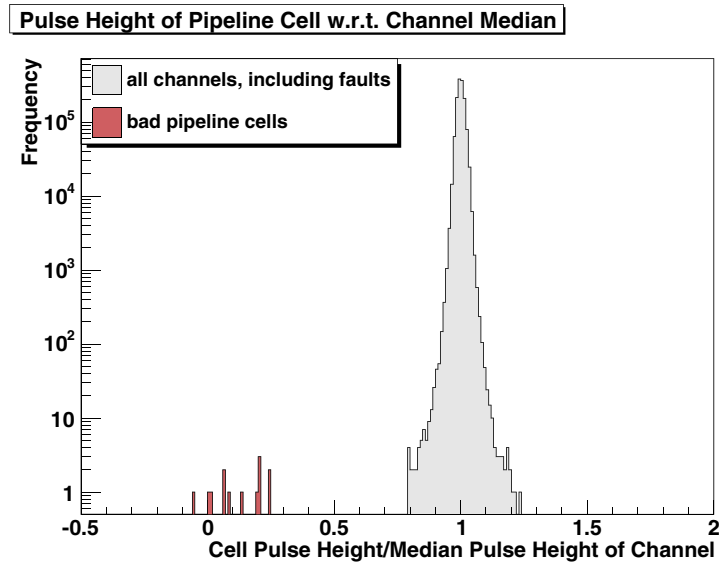


Figure 7.11: The distribution of the relative calibration amplitudes of pipeline cells with respect to the median amplitude of a channel.

calibration amplitude would be flagged as another type of fault anyway. Due to the good separation between defective and normal pipeline cells a loose cut can be applied at 0.5. Though a significant deviation to higher values was never observed, a cut at 1.5 is used as well.

7.5 Determination of Stable Noise Cuts

The definition of noise cuts requires a different approach, since noisy channels do not necessarily have a signature in any other test. According to the results of section 7.4 the separation of different types of faults is better for *PERC_0* to 3 than for *ABS* processed data. Nonetheless there is no necessity to use the noise for the identification of the type of fault. But there is an interest in the absolute value of the noise which is therefore a criterion for the qualification of a module. Moreover the absolute noise of an APV can be deteriorated by one or a few extremely noisy channels, as shown in figure 6.12(a). In this case, a percentage evaluation would flag only the noisy strips, though all channels of the APV have a high noise.

The noise of about 200 modules of all TEC geometries was investigated [55]. It was shown, that the absolute noise values of normal channels are approximately Gaussian distributed, if only modules of one geometry are considered and APV edge channels are neglected. A Gaussian distribution function was fitted to the data, giving a mean value M and a width σ . One conclusion of the analysis was, that all normal channels are distributed within a range of 5σ around the mean value. Thresholds for the absolute noise were thus defined at these 5σ limits.

The application of these thresholds (for ring 4 modules) on modules tested later qualified only 25 % of the modules as grade A, whereas 40 % were graded C [56]. All grade C modules failed due to a high number of noisy channels. The situation was

altered when all noise cuts were slightly increased by only 0.05 ADC counts¹¹. In this case the number of noisy channels was reduced by about 65%. Two third of the modules were graded A and no module was graded C.

To get rid of this unsatisfactory sensitivity of the grading, a new analysis was made, emphasizing the stability of the grading with respect to slight variations of the noise cut [57]. This analysis is described in the following.

7.5.1 The Noise Analysis

The noise analysis is made on a subset of 502 ROOT records¹². Consistent with [55], only the absolute noise values are used. The histograms of the noise values of normal channels (without APV edge channels) are taken from the evaluation ROOT files. In total 28 histograms (4 different APV operation modes for 7 different module geometries) are considered.

A Gaussian distribution fit (cf. equation 5.21) is applied to all noise histograms as indicated in figure 7.12. For most of the histograms the fit is well suited to describe

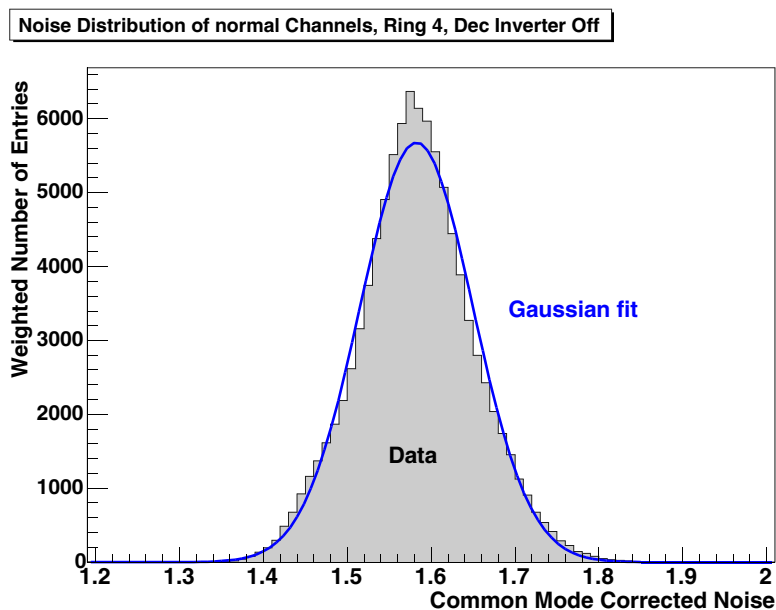


Figure 7.12: The histogram of absolute noise values for ring 4 modules, deconvolution mode, inverter off. The blue curve is the fit of a Gaussian distribution function.

the data. The fit returns a mean value M (corresponding to PT in equation (5.21)) and a value σ for the width of the distribution. The ring 6 data contained data from two different batches of modules (modules with HPK and ST sensors), with an obviously different noise behaviour. Thereby the width of the distribution was significantly increased. Ring 6 modules were hence excluded from the further analysis steps.

¹¹In this particular case no separate noise cut for the APV edge channels was used.

¹²The number of 502 accounts for the number of records without ring 6 modules which were excluded in a later step of the analysis.

Threshold values THR_X are determined for different multiples X of σ according to the equation

$$THR_X = M + X \cdot \sigma, \quad (7.6)$$

where X is varied from 2 (2 σ -cut) to 10 (10 σ -cut) in steps of 0.25. For each threshold THR_X the number of channels N_X above the threshold value is determined.

As a criterion for the stability of a noise cut, the ratio

$$R_x = \frac{N_{X=x}}{N_{X=(x-1)}}, \text{ with } x = 3 \dots 10 \quad (7.7)$$

is used. It compares the number of channels flagged as noisy by the application of noise cuts which are separated by 1σ . The choice of just one σ is arbitrary, though much larger or smaller steps would always result in ratios close to 0 or 1, respectively. The closer this ratio approximates 1, the better is the stability of the grading result with respect to variations of the threshold. The calculation procedure is exemplified in table 7.2 for the evaluation of ring 4 measurements in deconvolution mode, inverter on.

The noise analysis for the example of ring 5 peak mode, inverter off mean value $M = 1.326$, width $\sigma = 0.061$			
multiples X of σ	THR_X	N_X	$R_x = \frac{N_{X=x}}{N_{X=(x-1)}}$
2.00	1.449	1337	--
2.25	1.464	979	--
2.50	1.479	542	--
2.75	1.494	395	--
3.00	1.510	242	0.184
3.25	1.525	184	0.192
3.50	1.540	114	0.218
3.75	1.556	89	0.235
4.00	1.571	75	0.324
4.25	1.586	72	0.407
4.50	1.602	65	0.588
4.75	1.617	62	0.713
⋮	⋮	⋮	⋮
7.00	1.755	49	0.871
7.25	1.770	48	0.898
7.50	1.785	48	0.946
⋮	⋮	⋮	⋮

Table 7.2: Example for a table used in the noise analysis. For each multiple X of σ the number N_X of channels above a threshold THR_X is determined. The ratio R_x measures, how stable the number N_X is with respect to variations of X by 1σ .

In this table the value of R_x converges against 1 for higher values. For example the

value of $R_{4.75} = 0.713$ means, that a change of threshold value by one sigma, changes the number of channels flagged as noisy by $1 - 0.713 = 0.287$, i. e. 28.7 %.

The same calculations are done for all module geometries and all APV operation modes. Since the number of channels decreases rapidly for large values of x , the data of several evaluations have to be combined, to get an expressive result. Thus the data are averaged over all measurements in deconvolution mode, all measurements in peak mode, and all measurements in all modes. The resulting curve (see figure 7.13) indicates a strong dependency of the ratio R_x on the value of x . For values of $x < 4$

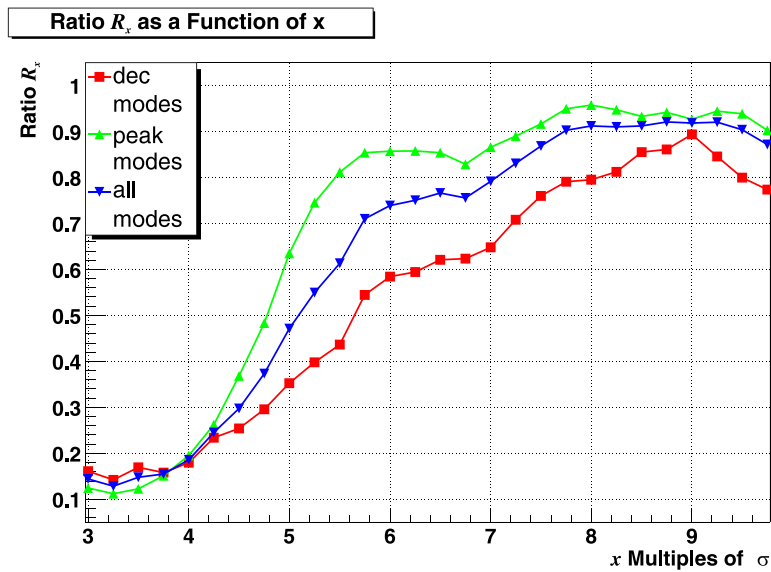


Figure 7.13: The ratio R_x as a function of x .

the ratio is below 0.2, i. e. the number of channels flagged as noisy varies by more than 80 % if the noise cut is varied by 1σ . For values $x > 4$ the ratio R_x increases significantly, i. e. the number of noisy channels gets less dependent on the choice of the threshold. At about $x = 6$ the ratio R_x saturates at a value of about 0.75, i. e. the number of noisy channels changes on average by 25 % if the threshold is changed by 1σ . For higher values of x small improvements up to $R_x = 0.9$ can be observed.

The total numbers of channels, that exceed a noise cut in at least one of the four APV operation modes, is listed in table 7.3. A channel that exceeds the noise cut in all operation modes is counted fourfold among the noisy channels. Thus, the numbers are to interpret as upper limits and the true number of noisy channels can be up to a factor of four smaller.

The table shows that the total number of flagged channels does not change by more than a factor of 2, if a 5σ cut is used instead of a 9σ cut. In both cases less than 0.2 % of the channels are affected on average. It was decided to take a 5σ cut (instead of a 6σ cut), despite the minor stability.

For single modules the number of noisy channels can vary much more if different cuts are applied. The strong dependency of the number of noisy channels on ring 4 modules observed in [56] is not present with the 5σ cut based on the present analysis. This is due to a larger width of the noise distributions, caused by the mixing of data

Number and fraction of channels flagged as noisy		
Total number of considered channels: 292320		
multiples X of σ	N_X	fraction of all channels
2.00	40004	13.69 %
3.00	5774	1.98 %
4.00	1073	0.37 %
5.00	506	0.17 %
6.00	374	0.13 %
7.00	296	0.10 %
8.00	270	0.09 %
9.00	248	0.08 %

Table 7.3: The table shows the total number of channels (sum of all APV operation modes) flagged as noisy as a function of the threshold value. Above 3.5σ less than one percent of all channels would be flagged as noisy. Above 7σ less than 0.1 of all channels would be flagged as noisy.

from different test centres with different test setups. A larger width of the distributions implies a larger value of σ and hence a looser noise cut.

The concept of the 5σ cut is also used for the determination of noise cuts for APV edge channels.

7.6 The Updated Fault Finding Algorithm

Sections 7.2 to 7.4 served to find the most appropriate tests and processing procedures. By the consideration of the resulting histograms thresholds are determined that define the expected range of values a channel can take in a certain test.

The fault finding algorithm presented in the following section, represents the same fault finding algorithm that is implemented in the latest version of the XML parser and the ARC software, respectively. It is based on the fault finding algorithm in [50]. The most important change is the reduced confidence in the results of the noise measurements. Different iterations of the algorithm have been tried. Each change of the algorithm required a re-analysis of all 1,065 ROOT records of the dataset. In combination with the determined cut values (see appendix A.2) the subsequently explained algorithm represents the best compromise. The algorithm is divided into three different parts. Firstly, flags are attributed to channels that exceed a threshold. Secondly, the flags are analysed and combined to a definite fault identification. Thirdly, a grade is attributed to the module, indicating the suitability of the module for the insertion into the CMS tracker.

7.6.1 Flagging of Bad Channels

At first all data are processed. The cut values are ordered according to the following relation:

$$LC_3 \leq LC_2 \leq LC_1 < \text{range of normal channels} < HC_1 \leq HC_2 ,$$

where LC_X are *Low Cuts* and HC_X are *High Cuts*, of which the distance to normal channels increases with the increasing number of the cut. A separation of test results according to all cuts is not always necessary such that different cuts can be combined in one cut.

The following processing procedures and cuts are applied:

- Noise data of all APV operation modes are considered as absolute values (*ABS* evaluation). Five different cuts are used for the evaluation of the noise data:
 - LC_3 (denoting the threshold for pinholes),
 - LC_2 (denoting the threshold for pitch adapter-sensor-opens),
 - LC_1 (denoting the threshold for the sensor-sensor-opens),
 - HC_1 (denoting the threshold for noisy channels),
 - HC_2 (denoting the threshold for noise APV edge channels).
- Peak time data are processed with respect to the calibration group median (*CALGR* evaluation). Four cuts are used:
 - LC_3 (to indicate channels with a peak time corresponding to a non-classified fault),
 - LC_2 (denoting the threshold for pitch adapter-sensor-opens),
 - LC_1 (denoting the threshold for the sensor-sensor-opens),
 - HC_1 (to indicate channels with a peak time corresponding to a non-classified fault).
- Absolute values of the pulse height data of all modes are processed with respect to the median pulse height of an APV (*PERC_0* evaluation). Two cuts are used:
 - LC_1 (denoting the threshold for shorts, dead channels, and resistive pinholes),
 - HC_1 (denoting the threshold for opens of any type).
- The absolute values of the pinhole difference data are used (*ABS* evaluation). Two cuts are applied:
 - HC_1 (denoting the threshold for potential pinholes),
 - HC_2 (denoting the threshold for pinholes).

- The absolute values of the pinhole maximum data are used (*ABS* evaluation). Only one cut is applied:
 - *LC_1* (denoting the threshold for dead channels).
- The ratio of the pulse height is evaluated using the *PERC_0* evaluation (cf. section 7.4.7). Two cuts are applied:
 - *LC_1* (for cases in which one of the measured pulse height values is zero),
 - *HC_1* (denoting the threshold for defective inverters).
- The noise of all columns of a channel in the pipeline noise test is evaluated with respect to the median value of a channel (*PERC_0*). One cut is used:
 - *HC_1* (denoting the threshold for noisy pipeline cells).
- The calibration amplitudes of all cells of a channel in the pipeline calibration amplitude test are evaluated with respect to the median amplitude of a channel (*PERC_0* evaluation). Two cuts are used:
 - *LC_1* (denoting dead pipeline cells),
 - *HC_1* (denoting an unknown problem due to a very large signal amplification).

Convention on the Combination of Flags

The thresholds subdivide the range of measured values. For each excess of a threshold in a certain test, the respective channel gets a separate flag. A channel can get only one flag in a single test. In that case the flag of the cut with the larger distance to normal channels is indicated. For example, if a value falls under the *LC_1* and the *LC_2* cut, but not under the *LC_3* cut, it gets a flag indicating the undershoot of *LC_2*. The value of a channel is said to be *low* if it falls under one of the three low cuts. The value of a channel is said to be *high* if it exceeds one of the two high cuts.

The flags of different APV operation modes in a certain test are combined in disjunction. Only the combined flags are transferred to the subsequent analysis procedure. An example of such a combination is shown in table 7.4.

7.6.2 Analysis of the Flags

To each channel that is assumed to be of a certain type, a textual output flag is assigned, that describes the type of fault in words. While the algorithm is processed, the possible type of fault gets rendered more precisely. If a more accurate identification is possible, the output flag of previous identifications is overwritten. At the end of the algorithm the textual output of all channels is returned to the graphical user interface of the ARC software and the XML parser, respectively. The textual output can be stored in a file. For the XML file, which has to be filled for the transmission to the database, an equivalent numerical output is created instead of the textual output.

Example for the flag combination					
	dec inv. on	dec inv. off	peak inv. on	peak inv. off	combined flag
below LC_3	no	no	no	yes	yes
between LC_3 and LC_2	yes	no	yes	no	yes
between LC_2 and LC_1	no	yes	no	no	yes
between HC_1 and HC_2	no	no	no	no	no
above HC_2	no	no	no	no	no

Table 7.4: Example of the combination of flags for the fault finding algorithm. Though only one cut can be set for a single APV mode, several flags can be set in the combined flag. The combined flag is transferred to the subsequent analysis.

Analysis Procedure

1. A channel is marked as an *unknown fault*, if it is flagged in any test. An additional textual output is added to specify the type of threshold excess.
2. If a channel (APV edge channel) exceeds the HC_1 cut (HC_2 cut), the channel is marked as *noisy*. Module edge channels cannot be marked as noisy.
3. A channel is marked as being *likely a pinhole or saturated (dead)*, if it has a noise below LC_3 , a peak time below LC_3 and a low pulse height. The latter two criteria make use of the fact, that no fit is applied to the data if the maximum acquired pulse height is less than 10 ADC counts.
4. A channel is marked as a *saturated (dead) channel*, if it has a signal below LC_1 in the pinhole maximum test, a low pulse height, and one of the three low noise flags is set. The requirements for the noise signature can be loosened since the signature in the pinhole maximum test is more trustworthy.
5. A channel is marked as being *likely an open between two sensors*, if the pulse height is not low and the LC_2 flag of either the noise or the peak time is set. This criterion allows at least an estimation of the type of fault if only noise data or only pulse shape data are available.
6. A channel is marked as *an open between two sensors*, if the pulse height is not low, the LC_1 flag of the peak time, and at least one of the three low noise flags is set. The requirements for the noise signature can be loosened since the peak time results are the most reliable results.
7. A channel is marked as being *likely an open between pitch adapter and sensor*, if the pulse height is not low and either the LC_2 flag of the noise or the peak time is set. This criterion allows at least an estimation of the type of fault if only the noise data or only the pulse shape data are available.
8. A channel is marked as *an open between pitch adapter and sensor*, if the pulse height is not low and the LC_2 flag of the peak time and one of the three low

noise flags is set. The requirements for the noise signature can be loosened since the peak time results are the most reliable results.

9. A channel is marked as a *possible mid-sensor open*, if one of the high noise flags and one of the low peak time flags is set. In addition it is required that the pulse height should not be low. The latter criterion avoids the false marking of noisy channels for which a pulse shape fit could not be applied.
10. A separation between sensor-sensor-opens and pitch-adapter-sensor-opens is not possible, if both, the *LC_1* and the *LC_2* flag of the peak time are set. If in addition the pulse height is not low and one of the low noise flags is set the channel is marked as an *open with conflicting location results*.
11. A channel is marked as having a *defective inverter*, if the ratio of the pulse height exceeds either the *LC_1* or the *HC_1* cut.
12. A channel is marked as *likely short-circuited* with its (next-to-)neighbouring channel, if the *LC_1* flag of the pulse height is set for the channel and its (next-to-)neighbouring channel. A channel is marked as *short-circuited* with its (next-to-)neighbouring channel, if in addition one of the noise flags (low noise flags or high noise flags) is set for at least one of the two channels.
13. A channel is marked as being *likely a pinhole*, if the *HC_1* cut of the pinhole difference is exceeded. This marks resistive pinholes, threshold pinholes, extremely noisy channels, and channels with defective pipeline cells. The type is changed to an *unidentified problem* if the *HC_1* noise cut is exceeded.
14. A channel is marked as *pinhole*, if in addition to the excess of the *HC_1* cut of the pinhole difference the pulse height is low and at least one of the low noise flags is set.

Two additional textual outputs can be added to any of the above mentioned fault identifications of a channel. Both are intended to give additional information on the identified fault. A channel that is marked with an additional textual output only is not counted among the bad channels. The additional informations are:

- *Crosstalk information*: A hint for a suspicious crosstalk is added if the sum of all crosstalk data points of a channel has the opposite sign of the median of the APV.
- *Pipeline information*: A hint for a bad pipeline cell is added if the *HC_1* cut of the pipeline noise or the pipeline calibration amplitude is exceeded or if the value of a cell falls below the *LC_1* cut on the pipeline calibration amplitude. By the information from the pipeline measurements many *unidentified problems* can be attributed to defect pipeline cells.

7.6.3 Grading

At the end of the fault finding algorithm a grading of the module is returned. The grading takes place according to the procedure stated in chapter 4.7 and takes also the results of the I-V measurement into account.

7.7 The Evaluation of the Fault Finding Efficiency

The fault finding algorithm returns for each of the 1,065 records of the analysed dataset a result file that contains the list of identified bad channels. These results have to be compared with the fault classification that was made prior to the analysis. As several iterations of the fault finding algorithm were tried, an automated program for the call of the XML Parser with the respective fault finding algorithm was implemented. Furthermore a program for the automated comparison of the former classification with the results of the fault finding algorithm was used.

With the final fault finding algorithm presented in the previous section, the following results have been obtained.

Identification of Opens

129 channels within the datasets of ring 1 to 4 were classified before as pitch adapter-sensor-opens. 126 (98 %) were identified correctly, the remaining 3 were marked as mid-sensor-opens due to a higher noise.

For the ring 5 to 7, data of 326 pitch adapter-sensor-opens were present. 288 of them (88 %) were identified correctly. The remaining 38 channels are all marked as mid-sensor-opens due to a noise that exceeded the threshold for the definition of noisy strips.

288 sensor-sensor-opens were present in the datasets of ring 5 to 7. 273 of them (95 %) were identified correctly. 15 were marked as being likely a sensor-sensor-open since the noise was not below the low noise threshold.

Out of 4 mid-sensor-opens in the datasets of all rings all were identified as mid-sensor-opens.

The identification of opens in this analysis can be improved if mid-sensor-opens are not considered as an extra type of opens. This is not done because almost all of the misidentified sensor-sensor-opens and pitch adapter-sensor-opens are attributable to one test setup with has a higher common mode.

Identification of Short-Circuits

134 channels have been classified as short-circuited to another channel prior to the application of the fault finding algorithm. 133 of them (99 %) were identified correctly. One of the channels was marked as a mid-sensor-open. The particular channel was one of 5 neighbouring channels showing a short-circuit like behaviour.

7.7.1 Identification of Pinholes

The data of 113 pinholes were present in the datasets of all rings, of which 108 were resistive pinholes and 5 threshold pinholes. All 108 resistive pinholes were marked correctly. 4 of the threshold pinholes were marked as being likely pinholes. In the remaining case, only the HC_1 cut in the pinhole difference test was exceeded instead of the HC_2 cut such that only a (weak) pinhole suspect was indicated.

Identification of Dead Channels

Out of the 115 classified dead channels 99 channels (86 %) were marked as dead channels by the fault finding algorithm. From the remaining 16 channels 13 were marked as a short-circuited. In all the cases the neighbouring channel was a pinhole or another dead channel. Under these circumstances also the classification prior to the analysis is ambiguous. 3 channels were marked as an unknown fault.

Number of Noisy Channels

Out of about 675,000 channels 489 channels are flagged as noisy. 92 of these channels are APV edge channels that exceeded their corresponding 5σ cut. 397 channels are “inner” APV channels, out of which 51 are adjacent to APV edges.

Flagging of Unknown Faults

In the datasets of all modules 96 channels showed a suspicious behaviour but were not attributable to a specific fault. 89 of these channels were found by the fault finding algorithm. For the remaining 7 channels the deviation of the average behaviour was not significant enough, such that they are treated as normal channels.

Additionally Flagged Channels

49 channels were marked additionally to the classified faults. In about 20 % of the cases it turned out that they were not classified as faults accidentally. In many of the remaining cases a threshold was exceeded only marginally. Thus these channels can be denoted as wrongly flagged good channels. Their total number is of the order of 40 out of 675,000 channels. This corresponds to a misidentification rate of about 0.01 %. If all unknown faults are assumed to be caused by failed fits applied to the pulse height measurements, one can estimate an upper limit for the misidentification rate of about 0.02 %.

7.8 Assessment of the Stability of the Grading

The dataset contained data of 581 different modules of which 280 were measured once, see table 7.5. The remaining 301 modules were measured two times or even more often. For those modules one can compare the grading. This implies a comparison

of the grading at different test centres, since in many cases the data are acquired at different sites.

Matching of the determined module grade between repeatedly measured modules						
Module tested	Number of cases	match	not graded	more noisy channels	different I_{leak}	repaired
once	280	–	–	–	–	–
2 times	135	113	14	1	1	6
3 times	150	127	16	4	2	1
4 times	15	14	–	–	1	–
5 times	1	1	–	–	–	–
repeatedly measured	301	255	30	5	4	7

Table 7.5: Comparison of the gradings of repeatedly measured modules.

In 255 of the cases the grading matched. For 30 modules a direct comparison was not possible since the grade of the module could not be determined for at least one of the records, because there was no information about the leakage current measurement in the ROOT file¹³. For 28 of these modules the grade matches if a similar leakage current is assumed as in the corresponding record that contained data of the I-V measurement. Six of the modules (ring 7 modules, cf. section 7.4.5) were measured once with intentionally introduced failures (for test purposes) and once after these failures were removed. Also in this case one can assume that the grading would have matched if no artificial faults would have been added. Therefore one can state that the grading of repeatedly measured modules matched in this analysis in $255+28+6=289$ out of 301, i. e. in 96% of the cases.

For two of the 30 modules for which a direct comparison was not possible the grading differs if only the number of defective channels is compared and an identical leakage current as in other measurements of that module is assumed. In one of the cases the mismatch is due to a wrong VPSP adjustment during the pulse shape measurement¹⁴.

In five of the mismatching cases the grade was changed from *A* to *B*, due to a larger number of noisy channels. In the single remaining case a module was repaired between two measurements. Thus the grading changed from *B* to *A*.

Four of the mismatching cases can be attributed to leakage current excesses in one of the measurements, where the module was graded *C* though the number of bad channels is low. This might be due to a higher humidity during the test or due to a less hermetic shielding against light from the environment.

¹³Some institutes used a different high voltage supply than the DEPP for the I-V measurements in the beginning of the mass production. Though a tool for the filling of these measurements into the ROOT file was available, not all ROOT files include I-V data. In a later stage of the mass production nearly all I-V measurements were done with the DEPP board. The absence of an I-V measurement was no criterion for the exclusion of a dataset.

¹⁴This module accidentally passed the selection criteria for the dataset.

7.9 Assessment of the Module Quality

Out of about 675,000 channels that were investigated, 1743 channels were marked as faulty. This corresponds to a fraction of 0.26%. Based on the 1,065 ARCS ROOT records a grading was determined. 920 of the records were assessed as grade *A*, 39 as grade *B*. 23 of the modules were marked as grade *C*, out of which 18 had more than 2% bad channels and 5 had an high leakage current. Among the 18 records that contained more than 2% bad channels 9 modules have been prepared with faults for test purposes. In 83 of the cases it was not directly possible to determine the grade, since there was no information about the leakage current in the ROOT record. Considering only the number of bad channels 63 of these modules would be grade *A*, 16 grade *B*, and 4 grade *C*.

Although this is not representative for the whole production of CMS silicon tracker modules it indicates a very good quality.

Chapter 8

Conclusion

The challenge of the production of the largest ever built all-silicon tracker requires an accurate and widely automated assembly of all mechanical and electrical components. More than 16,000 modules are needed for the tracker. Due to the distribution of the module production on a number of centres with different tasks, a fault has to be detected as soon as possible. An important contribution to the quality assurance during the production of the modules is achieved with the ARC system. The ARC system is used in all steps of the production that allow for a control of the electrical function of the modules. A whole spectrum of faults can be found and identified in these tests.

In this thesis all components of the ARC system are described. All tests implemented in a dedicated test software are explained. It is shown, by which significance certain types of faults show up in tests with the ARC system. A detailed analysis was made to determine the most appropriate tests for the identification of different types of bad channels. The analysis is based on a carefully examined dataset of more than 1,000 records of 500 different modules of all TEC geometries. To measure the degree of separation between different types of channels, two independent measures were introduced, assessing the distance and the overlap between two distributions of channels of different types in a certain test. The reliability of the identification depends on the correct definition of thresholds determining the range of expected values for a fault of a certain type.

Based on the analysis, an existing fault finding algorithm could be improved significantly with respect to the reliability of the identification of the respective type of fault. It is possible to implement the fault finding algorithm in such a way that only those test results have to be used that are available in all formerly measured module data files. Therefore also older data can be re-analysed.

The fraction of correctly identified faults varies between 85 and 99 percent, depending on the type of fault. The most important result is, that none of the faulty channels remained undiscovered by the fault finding algorithm. The requirement for a safe identification implies a certain probability to flag also healthy channels as bad. By the use of the most appropriate tests for the fault identification also the number of wrongly flagged normal channels could be reduced significantly.

Noisy channels make up the largest fraction of faulty channels. Due to a setup dependency of the measured noise, normal channels can be flagged as noisy if they

exceed a threshold. Only clearly noisy channels should be marked. A separate noise analysis was thus made, emphasizing the stability of the number of channels marked as noisy with respect to variations of the threshold.

The results of the analysis can be used to assess also the quality of the modules produced. In total a fraction of 0.26 % percent of the channels was marked as bad. In 93.7 % of the cases where a conclusive grading was possible, the data were assessed as being of grade *A*. In 4 % of the cases the resulting grade was *B*. Thus one can estimate that about 98 % of the modules can be used for the construction of the tracker.

Appendix A

Addendum to the Fault Finding Algorithms

A.1 The first version of the fault finding algorithm

In the following an abstract of the fault finding algorithm in [50] is listed.

The fault flagging algorithm gives the confidence level for the identification. Faults with multiple consistent bad channel flags are given stronger confidence levels than ones with only one bad channel flag. The current fault finding codes used are:

- OSO+: one sensor unbonded (confirmed by both noise and peak time tests)
- OSO-: likely one sensor unbonded (in either noise or peak time test)
- TSO+: two sensor unbonded (confirmed by both noise and peak time test)
- TSO-: likely two sensor unbonded (in either noise or peak time test)
- PHL+: pinhole (confirmed by all tests)
- PHL-: likely pinhole (saturated channel)
- MSO-: possible mid-sensor open (fast peak time with high noise)
- NOIS: high noise channel
- SHT+: short (low pulse shapes and at least one channel non-normal noise)
- SHT-: likely short (only low pulse shapes)
- OPN?: likely open (conflicting location results in noise and peak time tests)
- ????: unidentified problem (conflicting test results)

Fault finding algorithm

Here is the fault finding algorithm used in the analysis macro. Each step supersedes the previous ones.

1. A channel that fails any test is initially marked as an unknown problem (????).
2. If the channels is flagged as noisy in the noise test, the type of fault is changed to noisy channel (NOIS).
3. If the noise and peak-time flag a pinhole and the pulse height is low, then the type of fault is changed to a likely pinhole (PHL-). The channel may have been saturated, be a pinhole, have a broken preamplifier, or have a bad read/write amplifier for the pipeline.
4. Next opens are identified. In all cases the pulse height is required not to be flagged as low:
 - (a) If either the noise *or* peak-time flags marks a one sensor open, the type of fault is changed to a likely one sensor open (OSO-).
 - (b) If both the noise *and* peak-time flags mark a one sensor open, the type of fault is changed to a one sensor open (OSO+).
 - (c) If either the noise *or* peak-time flags marks two sensor open, the type of fault is changed to a likely two sensor open (TSO-).
 - (d) If both the noise *and* peak-time flags mark an two sensor open, the type of fault is changed to a two sensor open (TSO+).
 - (e) If the channel is flagged noisy and the peak-time is flagged as a one or two sensor open, the type of fault is changed to a likely mid-sensor open (MSO-).
 - (f) Finally, if the channel is flagged as a one sensor open in either the noise or peak-time test, and a two sensor open in the other, the type of fault is changed to an open of unknown location (OPN?).
5. The type of fault is changed to a likely short (SHT-), if the pulse height is marked low in two adjacent channels or next-to-adjacent channels.
6. The type of fault is changed to a short (SHT+), if the pulse height is marked low in two adjacent channels or next-to-adjacent channels *and* one of the two channels has a bad channel flag in the noise test.
7. The type of fault is changed to a likely pinhole (PHL-), if the channel is flagged as a pinhole in the pinhole test.
8. The type of fault is changed back to an unknown problem (????), if the channel is flagged as a pinhole in the pinhole test and as noisy in the noise test. A channel with an extremely high noise (> 10 ADC counts) can be falsely marked as a pinhole in the pinhole test.

9. Finally if a channel passes the requirements in 3. and is also marked as a pinhole in the pinhole test, the type of fault is changed to a pinhole (PHL+).

A.2 Cut Values for the new Fault Finding Algorithm

Here are the cut values, for those tests listed, that are used by the fault finding algorithm. Hints for the interpretation of the following tables:

Noise: All given cut values apply to the absolute values of the noise measurements (*ABS* evaluation). All results below the *LC_3* cut are pinholes or dead channels. All values below the *LC_2* cut are pinholes, dead channels, or pitch adapter-sensor-opens. All values below the *LC_1* indicate a pinhole, a dead channel, or an open. In case of an one-sensor-module *LC_2* and *LC_1* cut are identical. Values above the *HC_1* cut indicate a noisy channel. The *HC_2* cut is the threshold for the definition of noisy APV edge channels.

Pulse Height: All given cut values apply to the relative height with respect to the median pulse height of an APV (*PERC_0*). The *LC_3* cut is not used by the fault finding algorithm. *LC_1* and *LC_2* cut are identical. Values below the *LC_1* cut and above the *LC_3* cut indicate a pulse height typical for a short-circuit. The *HC_1* cut marks the upper limit of the normal channel histogram. All values above it indicate an open. The *HC_2* cut is not used.

Peak Time: All values are considered with respect to the median value of the calibration group (*CALGR*). All values below the *LC_3* cut are an unknown fault. A value between the *LC_3* and *LC_2* cut indicates a pitch adapter-sensor-open. A value between *LC_2* and *LC_1* cut indicates a sensor-sensor-open. In case of a one-sensor-module *LC_1* and *LC_2* are identical. The *HC_1* cut marks the upper limit of peak time distribution of normal channels. *HC_1* and *HC_2* cut are identical. Values above it indicate an unknown problem.

Independent of the specific ring geometry values of *HC_1*=15 and *HC_2*=40 determined with the *ABS* evaluation, are used for the assessment of the pinhole difference data. A value of *LC_1*=1 (*ABS* evaluation) is used for the determination of dead channels in the pinhole maximum test. Thresholds at $\frac{1}{2}$ and 2-fold of the median values of a channel are used in the determination of bad pipeline cells in the calibration amplitude matrices. A cut at the 2.5-fold of the median value of a channel is applied to measurements of the noise matrices.

Bold numbers indicate thresholds where a perfect separation with no overlap between two types of faults was possible (*OL* = 0.0).

Ring 1						
test	APV mode	very very low cut <i>LC_3</i>	very low cut <i>LC_2</i>	low cut <i>LC_1</i>	high cut <i>HC_1</i>	very high cut <i>HC_2</i>
noise	dec inv. on	0.80	1.10		1.74	1.86
	dec inv. off	0.80	1.10		1.70	1.86
	peak inv. on	0.55	0.79		1.31	1.48
	peak inv. off	0.55	0.77		1.30	1.50
pulse height	dec inv. on	–	-15.0		13.0	–
	dec inv. off	–	-15.0		13.0	–
	peak inv. on	–	-13.0		8.0	–
	peak inv. off	–	-13.0		8.0	–
peak time	dec inv. on	-6.5	-3.9...-1.2		1.5	
			-2.7			
	dec inv. off	-6.5	-3.9...-2.6		1.5	
			-2.7			
	peak inv. on	-10.0	-7.4...-2.5		3.0	
			-5.0			
	peak inv. off	-10.0	-7.9...-2.4		3.0	
			-5.0			

Table A.1: Optimized cut values for the fault identification on TEC ring 1 modules.

Ring 2						
test	APV mode	very very low cut <i>LC_3</i>	very low cut <i>LC_2</i>	low cut <i>LC_1</i>	high cut <i>HC_1</i>	very high cut <i>HC_2</i>
noise	dec inv. on	0.70	1.20		1.83	2.01
	dec inv. off	0.70	1.17		1.78	2.00
	peak inv. on	0.50	0.83		1.36	1.59
	peak inv. off	0.50	0.83		1.37	1.64
pulse height	dec inv. on	–	-16.0		16.0	–
	dec inv. off	–	-16.0		16.0	–
	peak inv. on	–	-12.0		8.0	–
	peak inv. off	–	-12.0		8.0	–
peak time	dec inv. on	-6.5	-3.3...-1.0		1.5	
			-2.2			
	dec inv. off	-6.5	-3.1...-1.3		1.5	
			-2.2			
	peak inv. on	-11.0	-6.5...-1.8		3.0	
			-4.2			
	peak inv. off	-11.0	-6.2...-2.2		3.0	
			-4.2			

Table A.2: Optimized cut values for the fault identification on TEC ring 2 modules.

Ring 3						
test	APV mode	very very low cut <i>LC_3</i>	very low cut <i>LC_2</i>	low cut <i>LC_1</i>	high cut <i>HC_1</i>	very high cut <i>HC_2</i>
noise	dec inv. on	0.70	1.25		2.02	2.18
	dec inv. off	0.70	1.25		1.98	2.23
	peak inv. on	0.51	0.84		1.42	1.60
	peak inv. off	0.55	0.84		1.41	1.60
pulse height	dec inv. on	–	-15.0		11.0	–
	dec inv. off	–	-15.0		11.0	–
	peak inv. on	–	-12.0		6.0	–
	peak inv. off	–	-12.0		6.0	–
peak time	dec inv. on	-7.0	-4.6...-1.2		1.5	
			-3.0			
	dec inv. off	-7.0	-4.8...-1.5		1.5	
			-3.0			
	peak inv. on	-12.0	-8.0...-2.0		2.5	
			-5.0			
	peak inv. off	-12.0	-7.9...-2.8		2.5	
			-5.0			

Table A.3: Optimized cut values for the fault identification on TEC ring 3 modules.

Ring 4						
test	APV mode	very very low cut <i>LC_3</i>	very low cut <i>LC_2</i>	low cut <i>LC_1</i>	high cut <i>HC_1</i>	very high cut <i>HC_2</i>
noise	dec inv. on	0.74	1.30		1.97	2.16
	dec inv. off	0.74	1.30		1.92	2.09
	peak inv. on	0.55	0.92		1.38	1.55
	peak inv. off	0.51	0.89		1.38	1.56
pulse height	dec inv. on	–	-16.0		13.0	–
	dec inv. off	–	-16.0		13.0	–
	peak inv. on	–	-12.0		8.0	–
	peak inv. off	–	-12.0		8.0	–
peak time	dec inv. on	-7.0	-4.4...-1.0		2.0	
			-2.7			
	dec inv. off	-7.0	-4.3...-1.2		2.0	
			-2.7			
	peak inv. on	-12.0	-8.5...-1.5		4.0	
			-5.0			
	peak inv. off	-12.0	-7.8...-2.1		4.0	
			-5.0			

Table A.4: Optimized cut values for the fault identification on TEC ring 4 modules.

Ring 5						
test	APV mode	very very low cut <i>LC_3</i>	very low cut <i>LC_2</i>	low cut <i>LC_1</i>	high cut <i>HC_1</i>	very high cut <i>HC_2</i>
peak time	dec inv. on	0.85	1.27	1.47	2.05	2.32
	dec inv. off	0.85	1.27	1.43	2.00	2.29
	peak inv. on	0.60	0.85	1.10	1.63	2.03
	peak inv. off	0.60	0.88	1.10	1.63	2.09
pulse height	dec inv. on	–	-30.0		14.0	–
	dec inv. off	–	-30.0		14.0	–
	peak inv. on	–	-12.0		7.0	–
	peak inv. off	–	-25.0		11.5	–
peak time	dec inv. on	-10.0	-3.5	-2.0	4.0	
	dec inv. off	-10.0	-3.4	-2.6	4.0	
	peak inv. on	-16.0	-10.5... -8.3	-5.6... -3.0	7.0	
			-9.4	-4.3		
	peak inv. off	-16.0	-10.8... -8.5	-5.2... -2.6	7.0	
			-9.6	-3.9		

Table A.5: Optimized cut values for the fault identification on TEC ring 5 modules.

Ring 6						
test	APV mode	very very low cut <i>LC_3</i>	very low cut <i>LC_2</i>	low cut <i>LC_1</i>	high cut <i>HC_1</i>	very high cut <i>HC_2</i>
noise	dec inv. on	1.01	1.34	1.51	2.50	2.50
	dec inv. off	0.90	1.27	1.50	2.50	2.50
	peak inv. on	0.68	0.87	1.10	2.50	2.50
	peak inv. off	0.63	0.85	1.13	2.50	2.50
pulse height	dec inv. on	–	-25.0		15.5	–
	dec inv. off	–	-30.0		27.0	–
	peak inv. on	–	-11.0		7.0	–
	peak inv. off	–	-15.0		112.0	–
peak time	dec inv. on	-12.0	-4.7	-2.5	5.0	
	dec inv. off	-12.0	-4.6	-2.5	5.0	
	peak inv. on	-17.0	-12.8... -8.9	-6.2... -4.5	8.5	
			-10.8	-5.3		
	peak inv. off	-17.0	-12.0... -9.0	-5.6... -4.9	13.0	
			-10.5	-5.3		

Table A.6: Optimized cut values for the fault identification on TEC ring 6 modules. The noise cut is a loose cut feasible for STM and HPK modules.

Ring 7						
test	APV mode	very very low cut <i>LC_3</i>	very low cut <i>LC_2</i>	low cut <i>LC_1</i>	high cut <i>HC_1</i>	very high cut <i>HC_2</i>
noise	dec inv. on	0.8...0.95 0.90	1.29...1.45 1.30	1.51	2.26	2.52
	dec inv. off	0.94	1.29...1.35 1.30			
	peak inv. on	0.61	0.96...1.00 0.96	1.25	1.80	2.15
	peak inv. off	0.60	1.00	1.21	1.79	2.19
pulse height	dec inv. on	—	-20.00	-20.00	15.00	—
	dec inv. off	—	-20.00	-20.00	15.00	—
	peak inv. on	—	-14.00	-14.00	10.00	—
	peak inv. off	—	-14.00	-14.00	10.00	—
peak time	dec inv. on	-10.0	-5.9...-3.0 -4.5	-1.6...-1.0 -1.6	5.0	
	dec inv. off		-5.9...-2.9 -4.5	-1.6...-1.0 -1.6		
	peak inv. on	-20.0	-14.9...-8.1 -11.7	-6.0...-2.8 -4.5	8.0	
	peak inv. off		-14.9...-8.9 -11.7	-5.5...-3.0 -4.5		

Table A.7: Optimized cut values for the fault identification on TEC ring 7 modules.

Appendix B

Additional Plots and Figures

B.1 Characteristics of the LED induced Leakage Current

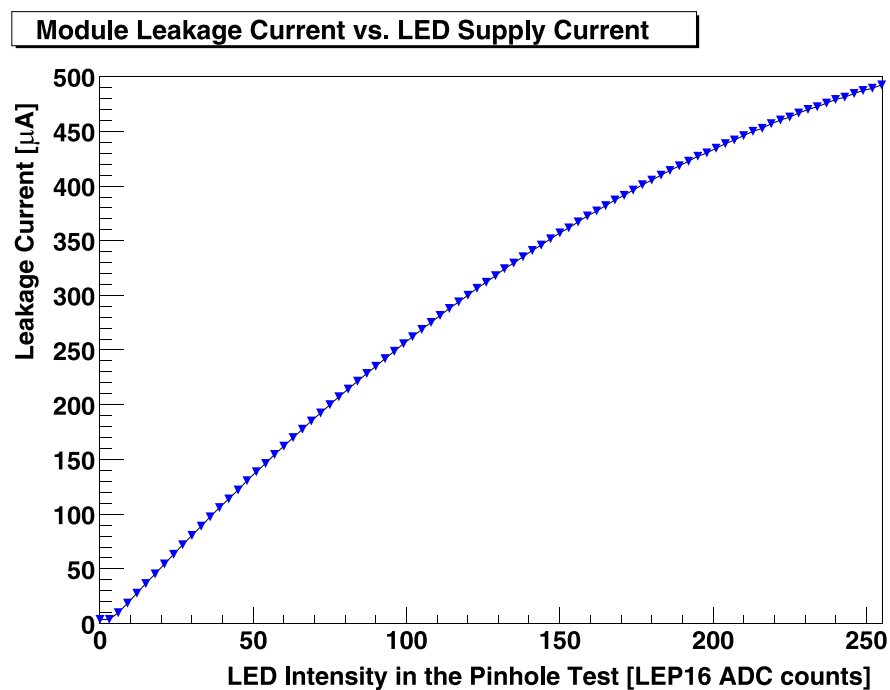


Figure B.1: Module leakage current as a function of the LED adjusted intensity. The curve shown is only an example to demonstrate the roughly linear relation between LED intensity and the leakage current. Depending on the sensor geometry, the illuminated area, and the specific fibre array the curve can take higher or lower values.

B.2 The Timing of the Backplane Pulse

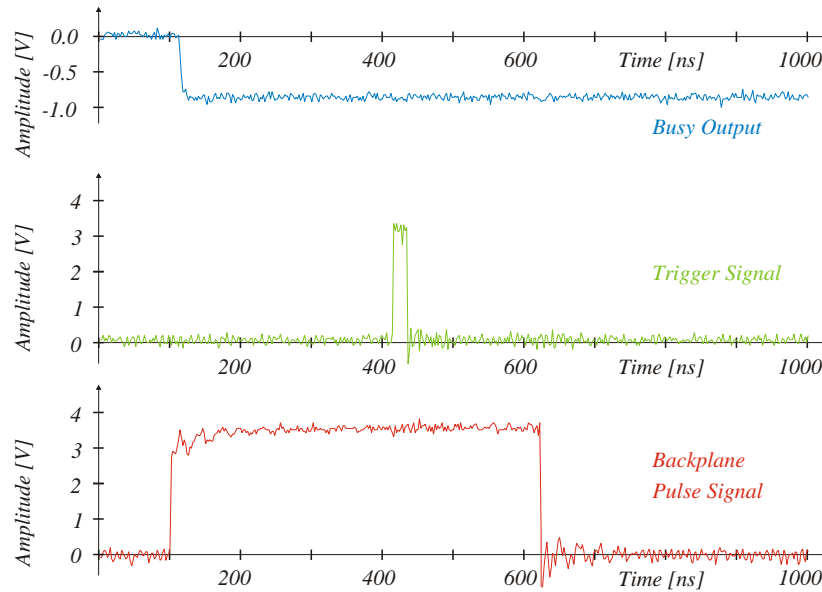


Figure B.2: Timing of the backplane pulse measured with an oscilloscope. The adjusted trigger pattern was 0000.0000.(spacer=5).1000.0000. The length of the backplane pulse signal is determined by the length of the trigger pattern (length = $(16 + \text{adjusted spacer} = 21) \times 25$ ns.). The busy signal is present within some ns after the start of the trigger output. The trigger (the 1 in the trigger pattern) appears 13×25 ns = 325 ns after the start of the the trigger output.

B.3 The Signal-to-Noise Ratio

The performance of a detector depends on the discrimination of signals from the detector noise. The measure that assesses the detector performance is the signal-to-noise ratio. The higher the signal $S_{ch,n}$ on that channel in event n (cf. equation (5.6)) or the lower the noise CMN_{ch} of a channel ch (cf. equation (5.7)), the better is the discrimination. A feasible requirement for the detection of a signal is an excess of a threefold noise threshold:

$$S_{ch,n} > 3 CMN_{ch}. \quad (\text{B.1})$$

A signal caused by a particle passage can be distributed over several channels. Therefore all neighbouring channels of which the signal exceed the threefold of the noise have to be considered as belonging to the same signal. Such a group of neighbouring channels from channel k to K is called a *cluster*. The signal-to-noise ratio S/N for such a cluster in an event n is defined as

$$\frac{S}{N} = \frac{\sum_{ch=k}^K S_{ch,n}}{\sqrt{\sum_{ch=k}^K CMN_{ch}}}. \quad (\text{B.2})$$

For the determination of the signal-to-noise ratio of a whole detector all measured values of S/N in a large number of events have to be filled into a histogram. For silicon detectors of a thickness below $500 \mu\text{m}$ the resulting histogram can be approximated by a Landau distribution, see figure B.3. The most probable value in such a histogram is the signal-to-noise ratio of the detector.

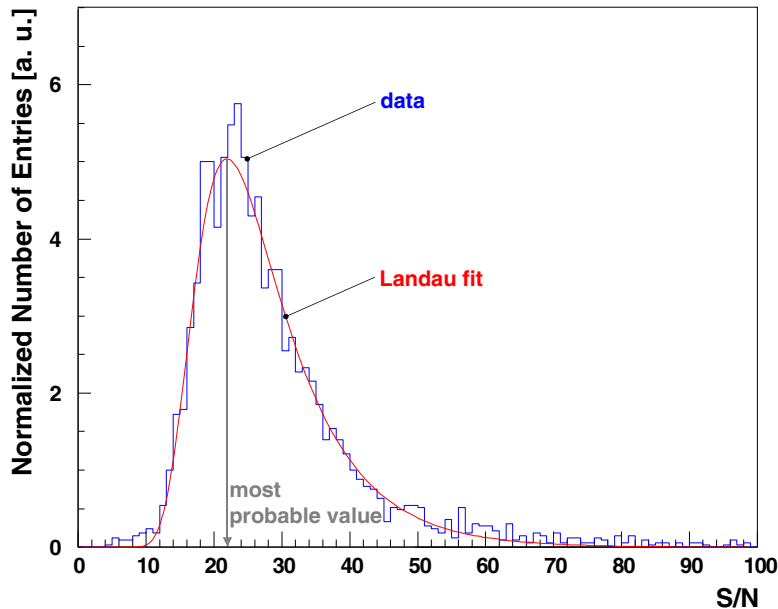


Figure B.3: Determination of signal-to-noise ratio of a detector. All values of S/N in single events are filled into the histogram. In this particular case the most probable value and hence the signal-to-noise ratio is 22 (from [52]).

B.4 Preferred Decay Channels for the Search for the Higgs Boson

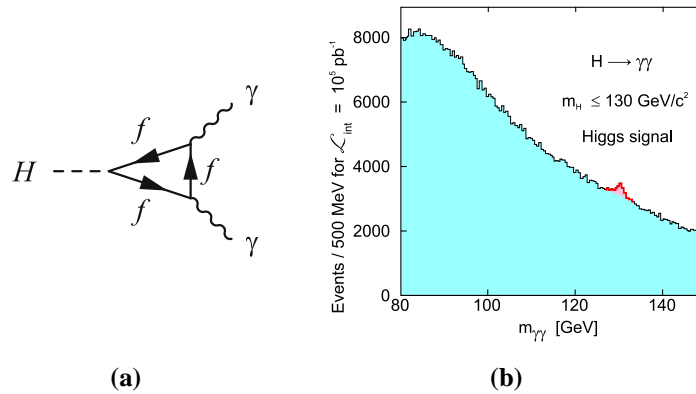


Figure B.4: The decay $H \rightarrow \gamma\gamma$ is the most promising process for the detection of a light Higgs boson ($m_H < 130 \text{ GeV}/c^2$). (a) The corresponding Feynman diagram. (b) Simulation of the significance of the decay in CMS for $m_H = 130 \text{ GeV}/c^2$ (from [58]). The significance of the Higgs signal with respect to the background depends on a precise measurement of the energy in the electromagnetic calorimeter. A worse energy resolution would smear the signal over a larger range.

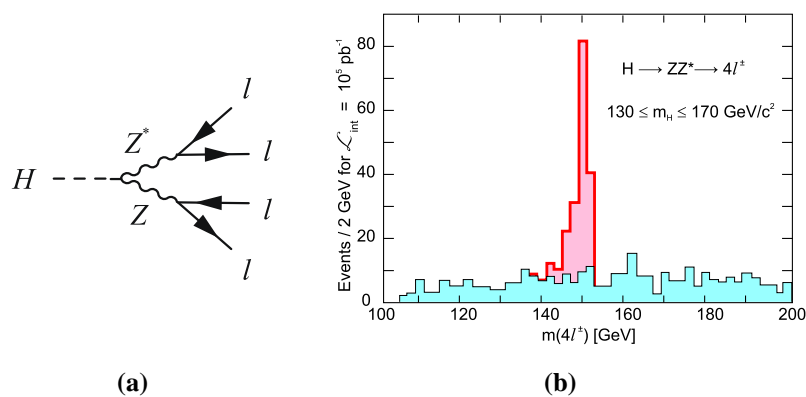


Figure B.5: The decay $H \rightarrow ZZ^* \rightarrow l^+ l^- l^+ l^-$ is the most important process for the detection of a Higgs boson of a mass in the range from 130 to 180 GeV/c^2 . (a) The corresponding Feynman diagram. (b) Simulation of the significance of the decay in CMS for $m_H = 150 \text{ GeV}/c^2$ (from [58]).

B.5 Branching Ratios and Cross Sections

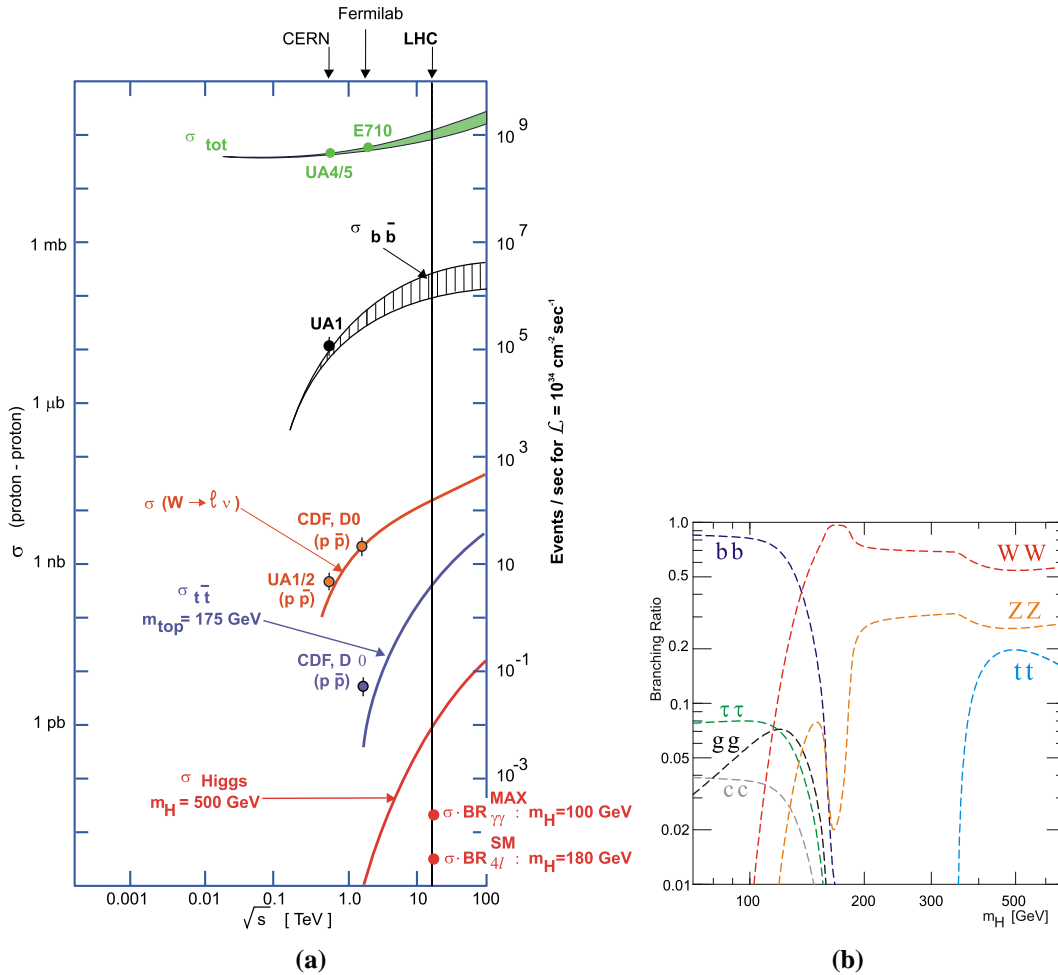


Figure B.6: (a) Dependence of some characteristic cross sections at hadron colliders as a function of the centre-of-mass energy \sqrt{s} (from [59]). (b) Branching ratios for different decay modes of the Higgs boson depending on the mass of the Higgs boson (from [60]).

Appendix C

Module Sizes and Quantities

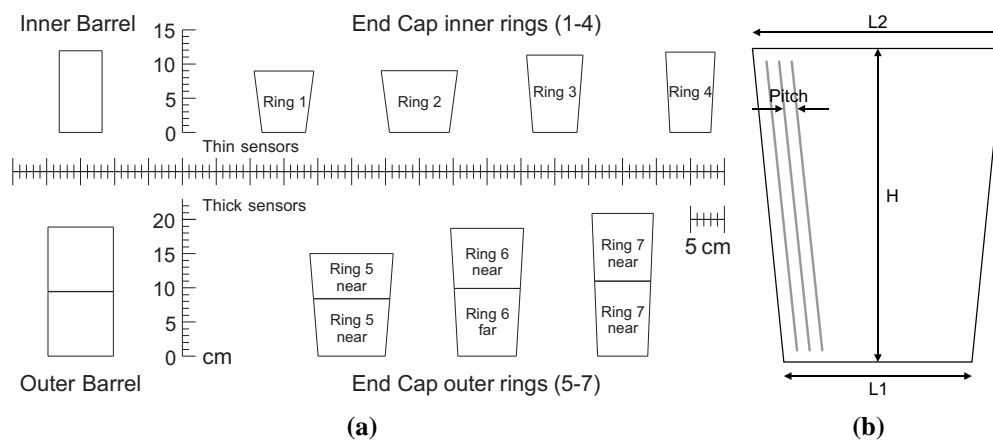


Figure C.1: (a) Graphical overview of the dimensions of modules used in the CMS tracker (according to [9]). (b) Explanation of measures used in table C.1.

Section	Type	L1 [mm]	L2 [mm]	H [mm]	Pitch [μ m]	No. of Strips	No. of Sensors	No. of Modules
TIB	IB1	61.5		116.9	80	768	1,536	1,536
	IB2	61.5		116.9	120	512	1,188	1,188
TOB	OB1	93.9		91.6	122	768	3,360	1,680
	OB2	93.9		91.6	183	512	7,056	3,528
TEC	R1	63.1	85.8	85.2	81...112	768	288	288
	R2	86.6	110.1	88.2	113...143	768	576	576
	R3	63.3	81.1	110.7	123...158	512	880	880
	R4	58.1	71.3	115.2	113...139	512	1,008	1,008
	R5 near	110.0	120.1	63.2	143...156	768	1,440	1,440
	R5 far	96.5	109.5	81.2	126...142	768	1,440	
	R6 near	94.5	104.7	84.9	185...205	512	1,008	1,008
	R6 far	83.6	94.6	96.1	163...185	512	1,008	
R7 near	71.5	80.1	106.9	140...156	512	1,440	1,440	
R7 far	80.4	88.0	94.9	156...172	512	1,440		
TID	R1	62.1	91.7	110.9	80.5...119	768	288	288
	R2	86.6	110.1	88.2	113...143	768	288	288
total number of sensors/modules							24,244	15,148

Table C.1: Module dimensions and quantities used for the CMS Tracker. The given dimensions describe the sensitive areas (from [21]). The meanings of L1, L2 and H are visualized in figure C.1(b). The frequently used number of 16,000 modules includes some percent spare modules.

Appendix D

Addendum to the APV Chip

D.1 The APV Internal Common Mode Correction

The inverter stages of all channels of an APV are supplied via a single external 50Ω resistor. A common mode signal recognised by all channels at a time causes a larger current through this resistor. Hence the a larger voltage drop is effected, such that the potential V_{CM} is lowered. Thereby the effect of the common mode is cancelled in the resulting signal V_{out} (see figure D.1).

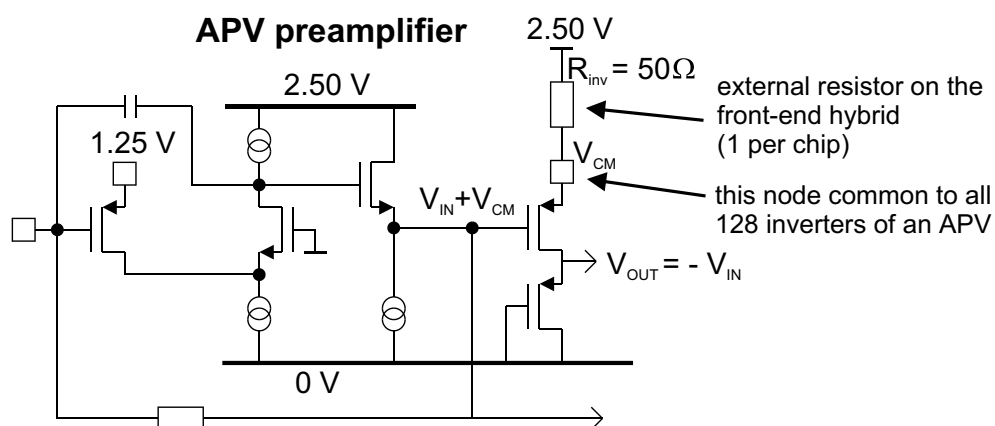


Figure D.1: The supply of all inverter stages via one external resistor causes a common mode correction.

D.2 APV Register Values

Bit number	Function	Value = 0	Value = 1
5	Preamp Polarity	Non-Inverting	Inverting
4	Read-out Frequency	20 MHz	40 MHz
3	Read-out Mode	Deconvolution	Peak
2	Calibration Inhibit	OFF	ON
1	Trigger Mode	3-sample	1-sample
0	Analogue Bias	OFF	ON

Table D.1: Coding of the bits defining the APV operation mode (from [32]). For example: APV mode 37 means: $37 = 1 \cdot 2^5 + 0 \cdot 2^4 + 0 \cdot 2^3 + 1 \cdot 2^2 + 0 \cdot 2^1 + 1 \cdot 2^0$, which denotes that bit 5, bit 2, and bit 0 are set to 1. APV mode 37 thus stands for: Inverting, 20 MHz Readout Frequency, Deconvolution Mode Calibration Inhibit On, 3-sample Mode, Analogue Bias Off. It is usually called “Deconvolution Mode, Inverter Off”.

Name	Range	Res.	Value	Description
IPRE	0 - 1020 μ A	4 μ A	n x 4 μ A	Preamplifier input fet bias current
IPCASC	0 - 255 μ A	1 μ A	n x 1 μ A	Preamplifier cascode current
IPSF	0 - 255 μ A	1 μ A	n x 1 μ A	Preamp source follower current
ISHA	0 - 255 μ A	1 μ A	n x 1 μ A	Shaper input fet bias current
ISSF	0 - 255 μ A	1 μ A	n x 1 μ A	Shaper source follower current
IPSP	0 - 255 μ A	1 μ A	n x 1 μ A	APSP current bias
IMUXIN	0 - 255 μ A	1 μ A	n x 1 μ A	Mux input current bias
ICAL	0 - 255 μ A	625 elec.	n x 625 electrons	Calibrate edge generator current bias
VFP	-1.25 to + 0.65V	7.5mV	-1.25V+(7.5mV \times n)	Preamplifier feedback voltage bias
VFS	-1.25 to + 0.65V	7.5mV	-1.25V+(7.5mV \times n)	Shaper feedback voltage bias
VPSP	-0.65 to +1.25V	7.5mV	+1.25V-(7.5mV \times n)	APSP voltage level adjust
CDRV	Channel 0-7	-	-	Calibrate output mask
CSEL	0 to 25ns	3.125ns	3.125ns / delay	Calibrate Delay Select

Table D.2: Overview of the APV I²C registers used for the configuration of the chip (from [32]). n denotes an adjustable value between 0 and 255.

Register	Default Value	Register	Default Value
IPRE	98	VFP	30
IPCASC	52	VFS	60
IPSF	34	VPSP	35
ISHA	34	CDRV	254
ISSF	34	CSEL	127
IPSP	55	MODE	15
IMUXIN	34	LATENCY	120
ISPARE	0	MUXGAIN	4
ICAL	29	ERROR	0

Table D.3: APV default values used by the ARC software in the all-test-sequences.

Bibliography

- [1] The LEP Electroweak Working Group. <http://lepewwg.web.cern.ch/LEPEWWG/>.
- [2] S. Hermann. *Präzisionsmessungen an Myondriftkammern für den CMS-Detektor und die Bedeutung des Myonsystems für die Higgs-Suche am LHC*. PhD thesis, RWTH Aachen, 2004. http://sylvester.bth.rwth-aachen.de/dissertationen/2004/102/04_102.pdf.
- [3] CMS, The Magnet Project, Technical Design Report. Technical Report CERN/LHCC-97-010, CERN, 1997.
- [4] CMS, the Hadron Calorimeter Project, Technical Design Report. Technical Report CERN/LHCC-97-031, CERN, 1997.
- [5] CMS, Data Acquisition and High Level Trigger, Technical Design Report. Technical Report CERN/LHCC-2002-026, CERN, 2002. <http://doc.cern.ch/archive/electronic/other/generic/public/cer-2336481.pdf>.
- [6] CMS, The Electromagnetic Calorimeter, Technical Design Report. Technical Report CERN/LHCC-97-033, CERN, 1997.
- [7] CMS, The Tracker System Project, Technical Design Report. Technical Report CERN/LHCC-98-006, CERN, 1998.
- [8] Addendum to the CMS Tracker TDR. Technical Report CERN/LHCC-2000-016, CERN, 2000. <http://doc.cern.ch/archive/electronic/other/generic/public/cer-2244540.pdf>.
- [9] D. Abbaneo. Layout and Performance of the CMS Silicon Strip Tracker. *Nuclear Instruments and Methods A 518*, pages 331–335, 2004.
- [10] D. Abbaneo. The tracker layout. <http://abbaneo.home.cern.ch/abbaneo/cms/layout/whole.html>.
- [11] Long term test setup gallery. <http://cms-ka.fzk.de/petals/LtGallery.htm>.
- [12] W. R. Leo. *Techniques for Nuclear and Particle Physics Experiments*. Springer Verlag, 1994.

- [13] S. Eidelmann et. al. Passage of particles through matter. In *Phys. Lett. B 592, 1 (2004), Chapter 27*. Particle Data Group, 2004. <http://pdg.lbl.gov/2004/reviews/passagerpp.pdf>.
- [14] C. Grupen. *Teilchendetektoren*. Bibliographisches Institut & F.A Brockhaus, 1993.
- [15] G. Lutz. *Semiconductor Radiation Detectors*. Springer Verlag, 1999.
- [16] A. Peisert. Silicon microstrip detectors. In F. Sauli, editor, *Instrumentation in High Energy Physics*. World Scientific, 1992.
- [17] G. Lindstrom et al. Radiation hard silicon detectors - developments by the RD48 (ROSE) collaboration. *Nuclear Instruments and Methods A 466*, pages 308–326, 2001.
- [18] H. Spieler. Introduction to Radiation-Resistant Semiconductor Devices and Circuits. http://www-physics.lbl.gov/~spieler/radiation_effects/rad_tutor.pdf.
- [19] J.-L. Agram et al. The Silicon Sensors for the Compact Muon Solenoid Tracker - Design and Qualification Procedure. CMS Note 2003/015, CERN, 2003. http://cmsdoc.cern.ch/documents/03/note03_015.pdf.
- [20] E. Migliore et al. Investigation of design parameters for radiation hard silicon microstrip detectors. *Nuclear Instruments and Methods A 485*, pages 343–361, 2002.
- [21] L. Borello et. al. Sensor design for the CMS Silicon Strip Tracker. CMS Note 2003/020, CERN, 2003. http://cmsdoc.cern.ch/documents/03/note03_020.pdf.
- [22] A. Honma et al. An Automated Silicon Module Assembly System for the CMS Silicon Tracker. CMS Note 2002/005, CERN, 2002. http://cmsdoc.cern.ch/documents/02/note02_005.pdf.
- [23] J. D’Hondt. Status Brussels Gantry. Presentation at CMS week, CERN, June 2004. <http://agenda.cern.ch/askArchive.php?base=agenda&categ=a042208&id=a042208s2t15/transparencies>.
- [24] S. König. *Deformation Studies on CMS Endcap Modules and Misalignment Studies on the CMS Tracker*. PhD thesis, RWTH Aachen, 2003. http://accms04.physik.rwth-aachen.de/Thesis/data/koenig_diss.pdf.
- [25] U. Goerlach. Front-End Hybrids for the CMS Silicon Tracker. In *CERN Report*, number 2002-003, page 170. CERN, 2002. <http://doc.cern.ch/archive/cernrep/2002/2002-003/p170.pdf>.

- [26] U. Goerlach. Industrial Production of Front-End Hybrids for the CMS Silicon Tracker. In *CERN Report*, number 2003-006, page 175. CERN, 2003. <http://doc.cern.ch/archive/cernrep/2003/2003-006/p175.pdf>.
- [27] M. J. French. Design and results from the APV25, a deep sub-micron CMOS front-end chip for the CMS tracker. *Nuclear Instruments and Methods A 466*, pages 359–365, 2001.
- [28] M. Raymond. APV25 Power Consumption, 2004. <http://www.hep.ph.ic.ac.uk/~dmray/pdffiles/APV25PowerConsumption.pdf>.
- [29] S. Gadomski et al. The deconvolution method of fast pulse shaping at hadron colliders. *Nuclear Instruments and Methods A 320*, pages 217–227, 1992.
- [30] L. L. Jones. The APV25 Deep Submicron Readout Chip for CMS Detector. In *CERN Report*, number 1999-09, page 162. CERN, 1999. <http://doc.cern.ch/archive/cernrep/1999/99-09/p162.pdf>.
- [31] Philips Company. *The I²C-bus specification, Version 2.1*, 2000. http://www.semiconductors.philips.com/acrobat_download/literature/9398/39340011.pdf.
- [32] L. Jones. *APV25-S1 User Guide Version 2.2*, 2001. http://www.te.rl.ac.uk/me/projects/High_Energy_Physics/CMS/APV25-S1/pdf/User_Guide_2.2.pdf.
- [33] P. Placidi. A 40 MHz clock and trigger recovery circuit for the CMS tracker fabricated in a 0.25 μm CMOS technology and using a self calibration technique. In *CERN Report*, number 1999-09, page 469. CERN, 1999. <http://doc.cern.ch/archive/cernrep/1999/99-09/p469.pdf>.
- [34] G. Magazzu et al. The Detector Control Unit: An ASIC for the Monitoring of the CMS Silicon Tracker. *IEEE Transaction on Nuclear Science*, 51(4):1333, 2004. http://ieeexplore.ieee.org/xpl/abs_free.jsp?arNumber=1323692.
- [35] J. Incandela. US Production Report. Presentation at CMS Tracker Steering Committee, September 2003. http://hep.ucsb.edu/people/incandela/US_production_TSC_030904.ppt.
- [36] Th. Bergauer, March 2005. personal e-mail communication.
- [37] Th. Bergauer. Tests of the Silicon Strip Sensors for the CMS Tracker. *Nuclear Instruments and Methods A 518*, pages 317–320, 2004.
- [38] M. Krammer. ST Thick Sensor Qualification. Presentation at CMS week, CERN, July 2004. <http://agenda.cern.ch/askArchive.php?base=agenda&categ=a043126&id=a043126s17t11%2Ftransparencies%2FSensors-General-Tracker23-7.pdf>.

- [39] B. Reinhold. Automatic Bonding Test of Front End Hybrids for the CMS Tracker. Diploma thesis, RWTH Aachen, 2004. http://www.physik.rwth-aachen.de/group/IIIphys/CMS/tracker/papers/thesis_reinhold.pdf.
- [40] C. Camps et al. *Flight Version SRD APV READOUT CONTROLLER Version 3.0*. RWTH Aachen. <http://www.physik.rwth-aachen.de/group/IIIphys/Electronics/PSRD/apv.htm>.
- [41] M. Axer. *Development of a Test System for the Quality Assurance of Silicon Microstrip Detectors for the Inner Tracking System of the CMS Experiment*. PhD thesis, RWTH Aachen, 2003. http://sylvester.bth.rwth-aachen.de/dissertationen/2004/011/04_011.pdf.
- [42] X. Rouby V. Lemaitre, L. Bonnet. Tests of hybrids circuits for the cms tracker : Fhit project. <http://www.fynu.ucl.ac.be/themes/he/cms/activities/tracker/hybrids.html>.
- [43] Th. Hermanns. Aufbau eines Systems für Kühltests zur Qualitätüberwachung von CMS Silizium-Modulen. Diploma thesis, RWTH Aachen, 2004. http://www.physik.rwth-aachen.de/group/IIIphys/CMS/tracker/papers/Diplomarbeit_Hermanns.pdf.
- [44] Supercool AB. *Model DL-290-24-00-00-00*. <http://www.supercool.se>.
- [45] Maxim Integrated Products, Inc. *DS18B20 Programmable Resolution 1-Wire Digital Thermometer*, 2002. <http://pdfserv.maxim-ic.com/en/ds/DS18B20.pdf>.
- [46] Sensirion AG, Eggbühlstrasse 14, CH-8052 Zürich. *SHT 1x/SHT 7x Humidity & Temperature Sensor*, 2002. http://www.sensirion.com/en/pdf/Datasheet_SHT1x_SHT7x.pdf.
- [47] G. Kaußen. Aufbau eines Hodoskops aus Siliziumstreifendetektoren. Diploma thesis, RWTH Aachen, 2005. <http://www.physik.rwth-aachen.de/group/IIIphys/TESLA/en/download.html#theses>.
- [48] M. Giffels. Entwicklung der Auslesesoftware für den Kalibrationsteststand einer TPC. Diploma thesis, RWTH Aachen, 2005. <http://www.physik.rwth-aachen.de/group/IIIphys/TESLA/en/download.html#theses>.
- [49] C. Camps et al. *SRD Test Readout V1.0*. RWTH Aachen, 2001. <http://www.physik.rwth-aachen.de/group/IIIphys/Electronics/PSRD/SOFTWARE/SRD.doc> and <http://www.physik.rwth-aachen.de/group/IIIphys/Electronics/PSRD/SOFTWARE/SRD080201.zip>.

- [50] Affolder et al. Procedures For CMS Silicon Tracker Module Testing using The ARC System. CMS Internal Note 2004/018, 2004. <http://hep.fi.infn.it/CMS/moduletest/note/in0418.pdf>.
- [51] Web page of the cms tracker database browser. <http://cmsdoc.cern.ch/~cmstrkdb/>.
- [52] St. Kasselmann. Untersuchung der Qualitätskriterien für die CMS-Silizium-Module anhand einer Prototypserie. Diploma thesis, RWTH Aachen, 2003. http://www.physik.rwth-aachen.de/group/IIIphys/CMS/tracker/papers/diplomarbeit_kasselmann.pdf.
- [53] M. Raymond. APV25S1 status. Presentation at CMS week, CERN, October 2000. http://icva.hep.ph.ic.ac.uk/~dmray/pptfiles/CMStracker24_10_00.ppt.
- [54] C. Civinini. Studies on noisy strips. Presentation at CMS week, CERN, January 2003. <http://hep.fi.infn.it/CMS/moduletest/tkwgen03/carlo.pdf>.
- [55] J. Fernandez Menendez. Cuts optimization for TEC modules. Presentation at Tracker week, CERN, July 2004. <http://hep.fi.infn.it/CMS/moduletest/tkwjul04/fernandez.pdf>.
- [56] Th. Hermanns. Results on 198 TEC-Modules. Presentation at CMS week, CERN, December 2004. <http://agenda.cern.ch/askArchive.php?base=agenda&categ=a045389&id=a045389s3t12/transparencies>.
- [57] T. Franke. Data Analysis & Cut Definition. Presentation at Tracker week, CERN, February 2005. http://agenda.cern.ch/askArchive.php?base=agenda&categ=a05834&id=a05834s0t3/transparencies/CutDiscussion_Franke_February05.pdf.
- [58] Higgs physics. Poster. <http://cmsinfo.cern.ch/Welcome.html/CMSdocuments/CMSposters/PDF/Higgs.pdf>.
- [59] M. Dittmar F. Pauss. Experimental Challenges at the LHC. In *CMS Conference Report*, number CMS CR 1999/008. CERN, 1999. http://cmsdoc.cern.ch/documents/99/cr99_008.pdf.
- [60] S. Eidelmann et. al. Searches for higgs bosons. In *Phys. Lett. B 592, 1 (2004), Chapter 27*. Particle Data Group, 2004. http://pdg.lbl.gov/2004/reviews/higgs_s055.pdf.

Index

- ACDC, 54
- Annealing, 18
- APSP, 24
- APV, 23
 - Data Output Test, 91
 - Edge Channels, 106
 - Latency, 24
 - OperationModes, 24
- APV Register
 - VPSP, 105
- ARC
 - Front-End Adapter, 42
 - Overview, 36
- ARC Board, 36
 - Data Acquisition, 40
 - Master/Slave Mode, 54
 - Self Test, 59, 90
 - Slow Control, 41
 - Trigger, 38
- ARCS, 57
 - Automated Test Procedures, 61
 - Data Acquisition, 58
 - Data Analysis, 63
 - Initialization, 59
 - Monitoring Panel, 60
 - SoftwareStructure, 58
- ASIC and Hybrid Problem, 32
- Assignment Test, 91
- Auto-Repeat Mode, 45, 83
- Automated Test Procedures, 61, 67
- Average Value, 69

- Backplane Pulse, 39, 44
- Backplane Pulse Test, 89
 - Open Bonds, 96
 - Short-Circuits, 100
- Bethe-Bloch Formula, 9

- C-V Curve, 30
- Calibration Request, 27, 74
- Calibration Test, 92
- Clock Distribution, 91
- Clock Divider, 46
- Cluster, 157
- CMS Experiment, 2
- Cold Box Setup, 52
- Common Mode, 69, 70
- Common Mode Corrected Noise, 70, 71
- Consistent Dataset, 62
- Continuous Mode, 45
- Crosstalk, 75

- Data Acquisition
 - Pulse Shape Test, 74
- Dataset, 111
- DCU, 28
 - Response Test, 91
- Dead Channel, 32
 - Signature, 102
- Deconvolution Mode, 24
- Defective Inverter, 32, 103
- Defective Pipeline Cell, 32, 104
- Depletion Voltage, 15
- DEPP, 48
- Detector Capacitances, 17
- DIL Switch, 45
- Distance Criterion, 116

- Electromagnetic Calorimeter, 4
- Energy Loss in Material, 9

- Fault Classification, 111
- Fault Finding Algorithm, 136
 - Cut Criteria, 149
- FHIT, 35, 90
- Fit Function
 - Deconvolution Mode, 77

- Peak Mode, 76
- Flag, 65, 110
- Front-End Adapter, 42
- Front-End Hybrid, 21
- Function Principle of a Silicon Strip Detector, 12
- Functional Test, 90
- Gain Test, 78
 - Open Bonds, 94
 - Pinholes, 101
 - Short-Circuits, 99
- Grading, 63
- Hadron Calorimeter, 4
- High Cut, 138
- High Luminosity Phase, 2
- HV Controller, 48
- Hybrid
 - Test Station, 55
- Hybrid-to-VUTRI Adapter, 36, 44
- I²C Test, 90
- I-V Test, 67
- Landau Distribution, 11
- Large Hadron Collider, 2
- Latency, 24
- Lattice Orientation, 17
- Leakage Current, 16
- LED, 46
- LED Controller, 45
- LED Test, 83
 - Open Bonds, 96
 - Pinholes, 101
 - Short-Circuits, 100
- LEP16, 45
- Level Shifter, 43
- LHC, 2
- Low Cut, 138
- Low Luminosity Phase, 2
- Low Voltage Test, 90
- Magnet, 4
- Master Mode, 54
- Mean Value, 69
- Micro Discharges, 30
- Micro-Discharges, 106
- Mid-Sensor-Open, 31
- Mid-Sensor-Opens
 - Signature, 97
- MIP, 10
- Missing Bond, 33
- Module, 20
 - Assembly Centre, 55
 - Bonding and Qualification Centre, 56
 - Edge Channels, 106
 - Geometries, 5
 - Grading, 63
 - Mechanical Design, 20
 - Normal, 5
 - Possible Faults, 29
 - Production Problems, 33
 - Stereo, 5
 - TestBox, 50
- Multi Board Setup, 54
- Multi Mode, 26
- Muon Detectors, 3
- MUX, 27
 - Resistor Test, 91
- Noise Test, 68
 - Defective Inverter, 103
 - in the Fast Test, 91
 - Open Bonds, 94
 - Pinholes, 101
 - Short-Circuits, 99
- Noisy Channel, 30, 104
- One-Sensor-Module, 21
- Open Bond, 33
 - Signature, 93
- Operation Modes, 24
- Optical Fibres, 47
- Overlap Criterion, 118
- Peak Mode, 24
- Peak Time, 76
- Pedestal, 68, 70
- Pedestal Test
 - in the Fast Test, 91
- Pinhole, 30

- Location, 128
- Signature, 100
- Pinhole Difference, 88
- Pinhole Maximum, 88
- Pinhole Test, 84
 - Dead Channels, 102
 - Defective Pipeline Cells, 104
- Pinholes
 - Identification, 127
- Pipeline, 32, 104
- Pitch adapter-Sensor-Open, 33
- PLL
 - Test, 91
- Possible Module Faults, 29
- Production Problems, 33
- Pulse Height, 76
- Pulse Shape Test, 73
 - Defective Inverter, 103
 - Open Bonds, 93
 - Pinholes, 101
 - Short-Circuits, 98
- Pulsed Mode, 45, 83
- QTC, 30
- Radiation Damage, 14
- Raw Noise, 69, 70
- Repetition Rate, 45
- Resistive Pinholes, 30
- Resistivity, 16
- Reverse Annealing, 18
- Rise Time, 76
- Rod, 6
- ROOT File, 62
- Saturated Channel, 32
 - Signature, 102
- Self Test, 59, 90
- Sensor
 - Annealing, 18
 - Depletion Voltage, 15
 - Design, 14
 - Detector Capacitances, 17
 - Function Principle, 12
 - Lattice Orientation, 17
 - Layout, 19
 - Leakage Current, 16
 - Problems, 29
 - Radiation Damage, 14
 - Resistivity, 16
 - Reverse Annealing, 18
 - Schematics, 19
 - Strip Capacitance, 18
 - Test, 29
 - Trapping of Signal Charge, 17
 - Type Inversion, 15
 - Width-to-Pitch Ratio, 18
- Sensor-Sensor-Open, 33
- Short-Circuit, 31, 98
 - Signature, 98
- Signal, 69, 71
- Signal Processing, 24
- Signal-to-Noise Ratio, 157
- Silicon Microstrip Sensors
 - cf. Sensor, 19
- Silicon Strip Tracker (SST), 5
- Slave Mode, 54
- Slow Control
 - APV, 27
 - ARC Board, 41
- Software Structure, 58
- Solenoid, 4
- Space Charge Region, 12
- SST Module, 20
- Standard Module Test, 111
- Summary Table
 - Fault Signatures, 107
 - Fault Types, 34
- Support Structure, 21
- System Overview, 36
- Test Box, 50
- Three Sample Mode, 26
- Threshold Pinholes, 30
- Tick Mark, 26
- Time Consumption, 61
- Time Offset, 76
- TPLL, 27
- Tracker, 5
 - Design, 5
 - End Cap, TEC, 5

- Inner Barrel, TIB, 5
- Inner Disc, TID, 5
- Outer Barrel, TOB, 5
- Trapping of Signal Charge, 17
- Trigger, 38
- Trigger Pattern, 27
- Two-Sensor-Module, 21
- Type Inversion, 15

- Unknown Fault, 106

- Vertex Detector, 5
- VUTRI Adapter Card, 36, 44

- Width-to-Pitch Ratio, 18

- XML File, 65
- XML Parser, 64

Acknowledgement

This thesis would not have been possible without the friendly help and support of many colleagues, friends and my family. That is why I would like to dedicate the remaining space to those people.

- First of all I would like to thank Prof. Dr. Günter Flügge and Prof. Dr. Joachim Mnich, who gave me the opportunity to work in an interesting field of physics in a challenging, international environment. Your style of leadership facilitated a very motivating and enjoyable atmosphere in the whole institute. From the very beginning you encouraged us developers. You always believed in our abilities and in the success of the test system. Thank you very much.
- Secondly, and may be even more importantly, I would like to thank Mr. Franz Beißel. The test system would not exist without your ingeniously and prospectively designed hardware. I really appreciated your patience when you shared some pieces of your knowledge of electronics with me. A special thank goes to you and your colleagues Eric Bock and Vladimir Ossovyi for all the little repairs you made for us.
- The ARC software is the result of an extremely fruitful and enthusiastic teamwork of Dr. Markus Axer, Michael Pöttgens, Jan Niehusmann, Andreas Nowack, Thomas Hermanns, Stefan Kassermann and myself. I cannot imagine to find better colleagues and a more pleasant working atmosphere than I found with you. Thank you all.
- All other members of the III. Physikalisches Institut B also contributed to the wonderful atmosphere.
- This thesis in its final version profited a lot from the helpful corrections and hints of Thomas, Markus, Oliver, Andreas, Franz Beißel and Reiner Schulte. Thanks for your patience and diligence.
- Thomas, you definitely had the hardest job, since you always had to read the first drafts. A special thank I owe you for all the extra measurements you performed for the completion of the datasets for this thesis and your patient explanations of particle physics.
- The success of the ARC system is also based upon the support and the feedback we got from many members of the CMS collaboration, for example from Marco

Meschini, Valery Zhukov, Anthony Allen Affolder, Steven Levy, Derek Barge, Leonard Christofek, Vincent Lemaitre, Xavier Rouby and Klaus Freudenreich. But also the contacts to our in-house colleagues from the I. Physikalisches Institut B, Prof. Dr. W. Braunschweig, Prof. Dr. St. Schael, Dr. D. Pandoulas, Roman Adolphi, Jan Olzem, Katja Klein were very helpful. Thanks to all of you for the friendly and fruitful cooperation.

- I am grateful for the help I got from members of the CMS collaboration during the preparation of this thesis, notably Thomas Bergauer, Marko Dragicevic, Anna Macchiolo, Ulrich Goerlach and Jean-Daniel Berst.
- My family always helped me to find my way and supported me on every way I decided to go. Thank you very, very much.
- Finally I would like to thank my wonderful wife Claudia who always supported and believed in me. You are the best thing that ever happened to me. I love you.

Lebenslauf

Persönliche Daten

Torsten Franke

geboren am 19.03.1975 in Rudolstadt

Schulbildung

Sept. 1981 - Nov. 1989 Besuch der Georg Schumann Oberschule in Rudolstadt

Jan. 1990 - Mai 1994 Besuch des Städtischen Gymnasiums in Herzogenrath

Juni 1995 Abitur (Gesamtnote 2,0)

Zivildienst

Juli 1994 - Sept. 1995 Zivildienst in einer Behinderten-Werkstatt in Aachen

Studium

Okt. 1995 - Nov. 2000 Studium der Mathematik und Physik, Lehramt-Sekundarstufe II

Apr. 1997 Zwischenprüfung Mathematik

Okt. 1997 Zwischenprüfung Physik

Apr. 1998 Zwischenprüfung Erziehungswissenschaften

Juni 2000 Examensarbeit bei Prof. Dr. A. Böhm, Thema:

”Simulation von Wechselwirkungen harter Photonen mit Materie“

Nov. 2000 1. Staatsexamen (Gesamtnote 1,7)

Feb. 2001 - Juli 2005 Promotion

25. Apr. 2005 Einreichen des Promotionsgesuchs

04. Juli 2005 Promotionsprüfung

